IOP Publishing Journal of Physics B: Atomic, Molecular and Optical Physics
J. Phys. B: At. Mol. Opt. Phys. **45** (2012) 245502 (8pp) doi:10.1088/0953-4075/45/24/245502

Ramsey effects in coherent resonances at closed transition $F_g = 2 \rightarrow F_e = 3$ of ^{87}Rb

Z D Grujić, M M Lekić, M Radonjić, D Arsenović and B M Jelenković

Institute of Physics, University of Belgrade, Pregrevica 118, 11080 Belgrade, Serbia

E-mail: milan.radonjic@ipb.ac.rs

Received 22 August 2012, in final form 8 October 2012
Published 30 November 2012
Online at stacks.iop.org/JPhysB/45/245502

Abstract
Experimental and theoretical investigations show the strong effect of the pump beam, spatially separated from the probe beam, on the probe's electromagnetically induced absorption (EIA) and nonlinear magneto-optical rotation (NMOR). Linearly polarized pump and probe laser beams are locked to the $F_g = 2 \rightarrow F_e = 3$ transition of the ^{87}Rb D_2 line and pass a vacuum Rb gas cell coaxially. We show that the observed narrowing of EIA and NMOR resonances is due to the Ramsey effect. Linewidths of the resonances decrease when the size of the dark region between pump and probe lasers increases. Variation of the angle between pump and probe linear polarizations strongly influences the phases of atomic coherences generated by the pump beam and consequently the line-shapes of the probe EIA and NMOR resonances. Complete change of the resonance sign is possible if the phases of the ground state coherences, $\Delta m_g = 2$, are altered by π. The central EIA fringe becomes less pronounced if the probe intensity increases, due to the larger probe contribution to atomic evolution. Ramsey-like interference is a manifestation of the evolution of ground state Zeeman coherences, required for EIA, in the dark region in the presence of a small magnetic field.

(Some figures may appear in colour only in the online journal)

1. Introduction

In the work of Akulshin *et al* [1], a new kind of resonance was observed, one in which atomic coherence produces an increase of laser absorption. This coherent phenomena is termed electromagnetically induced absorption or EIA. Conditions for observing EIA have been recently identified: a narrow absorption resonance can be obtained when the laser frequency is scanned across a degenerate two-level transition such that $F_g \rightarrow F_e = F_g{+}1$, where F_g and F_e are total angular momentum quantum numbers of hyperfine levels of ground and excited states, respectively. It is worth mentioning that Kazantsev *et al* [2] theoretically predicted that optical pumping in the case of such transitions leads to an enhanced absorption of the medium. It is now well known that EIA is a multilevel effect, meaning that the degeneracy of the ground level is necessary. In comparison to electromagnetically induced transparency (EIT) [3] EIA has an opposite sign of resonance. Unlike EIT, which is due to coherent population trapping (CPT) and ground level dark states [4], EIA has not been associated with a particular coherent superposition of atomic ground states. While both EIT and CPT were intensely investigated over the past decade, this is not the case for EIA. A better knowledge of the phenomena is necessary, including a better understanding of excitation and emission processes that lead to the development of EIA.

The first observations of EIA were performed by perpendicularly polarized pump and probe lasers, interacting with a cycling degenerate two-level transition in which $F_e = F_g + 1$ and $F_g > 0$ [1, 5]. In later experiments, EIA was also found in non-cycling degenerate two-level systems [6, 7]. Both two-photon resonances in a bichromatic light field (pump–probe spectroscopy) and magneto-optical resonances in the Hanle configuration have been explored. The influence of various parameters like laser intensity, light ellipticity and magnetic fields on EIA amplitudes and linewidths was studied in [8–11].

Assuming the simplest system presenting EIA, a four-level N-atomic system of a near degenerate two-level atom, Taichenachev *et al* [13] obtained an analytic expression for the probe light absorption. A direct link between the efficiency of spontaneous coherence transfer and the appearance of EIA indicates that the Zeeman coherence, after being developed in the excited level, is transferred to the ground level by spontaneous emission. Analytic expressions of different perturbation orders for Zeeman and optical coherences and populations have shown such ordering of events in the development of EIA [14].

EIA media have some similarities but also differences from EIT media. Since these two coherent phenomena have different origins, their temporal behaviour is different, as given in [15]. Slower development of EIA and its consequent narrowing after turning on the excitation pulse was notable in comparison with EIT. EIA media have a steep anomalous dispersion that is related to subluminal light propagation, as demonstrated in [16]. As a consequence, in EIA media light pulses can also be stored and retrieved like in EIT media, but only the storage of a smaller part of the initial pulse is possible [17]. In some open atomic systems, minor changes of the pump laser Rabi frequency can transform EIT to EIA (and vice versa) [18]. A modest change of the buffer gas cell's temperature can alter the sign of the transmission resonance from positive (EIT) to negative (EIA) [12].

Ramsey's method of separated fields is often used in atomic and molecular beam experiments [19]. Ramsey fringes that are induced by the two spatially or temporally separated excitation fields lead to a considerable narrowing of the corresponding resonances. In this work, we test if the Ramsey effects of separated pump and probe laser beams can be effective for narrowing EIA as they are for EIT. Repeated interaction of coherently prepared alkali-metal atoms with a pair of laser fields in Raman resonance leads to a strong Ramsey narrowing of EIT in cells with buffer gas [20, 21], and in vacuum gas cells if a specific pump–probe laser beam geometry is used [22, 23]. The Ramsey effects on EIA were recently explored in gas cells with anti-relaxation coating experimentally [24] and, using a four-level *N*-atomic system, theoretically [25]. We look for the Ramsey effects introduced by separated excitation fields in an EIA medium in a vacuum gas cell without anti-relaxation coating by measuring and calculating the probe's transmission and nonlinear magneto-optical rotation (NMOR) when the laser fields couple the $F_g = 2 \rightarrow F_e = 3$ transition of the ^{87}Rb D_2 line. In *V* atomic schemes supporting EIA, polarization rotation has the opposite sign to that in EIT atomic systems, e.g. Λ or *M* systems. There have been numerous studies of NMOR in EIT media in buffer-gas-free vapour cells and without anti-relaxation coating [26–29]. A change of the NMOR sign in the case of the closed transition $F_g = 4 \rightarrow F_e = 5$ of the Cs D_2 line was first reported in [27].

In our work, we use a pump laser beam to coherently prepare the atoms and a spatially separated probe laser beam to check the pump-induced atomic coherence. We studied the Ramsey effects on narrowing EIA and NMOR, theoretically and experimentally, using a similar pump–probe geometry as in [22]. Both pump and probe laser beams are linearly polarized and resonant to the closed transition, $F_g = 2 \rightarrow F_e = 3$ in ^{87}Rb. EIA measurements were carried out by monitoring the probe beam's transmission. NMOR of the linear probe polarization, for a given pump polarization, is obtained using a balanced polarimeter. The measurements were performed as a function of the external axial magnetic field for different angles between the electric vectors of the pump and probe beams. Obtained EIA and NMOR line-shapes are compared with the results of the theoretical model. The model solves time-dependent optical Bloch equations for the density matrix elements for all sublevels of the $F_g = 2 \rightarrow F_e = 3$ transition. The atomic state evolution is calculated when an atom passes the pump, the dark region and the probe beam. The probe's total transmission was calculated after averaging over all atom velocity components parallel and perpendicular to the laser beam and over all possible atomic trajectories. The probe beam's transmission and polarization rotation are obtained from the calculated change of the probe's electric field due to the Rb vapour polarization.

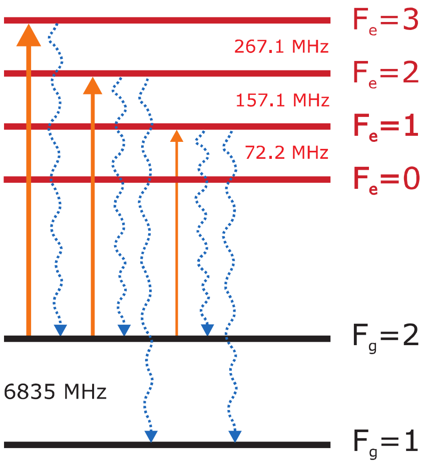

Figure 1. Energy level diagram for D_2 line transitions considered in the theoretical model. Solid arrows pointing up represent the transitions induced by the laser, while dotted wavy arrows pointing down correspond to possible spontaneous emission channels from excited levels. Frequency differences between adjacent hyperfine levels are shown.

2. Theory

We used a density-matrix formalism to model the dynamics of the interaction between Rb atoms and spatially separated pump and probe laser beams. Figure 1 shows a Rb D_2 line atomic level diagram, the hyperfine levels either coupled by the laser light, or populated via spontaneous emission.

The external magnetic field **B**, along the propagation direction of the laser beam, splits the adjacent Zeeman sublevels by the amount $\mu_B g_F B$, where μ_B is the Bohr magneton and g_F is the gyromagnetic factor of the level. The temporal evolution of the atomic density matrix is obtained from time-dependent optical Bloch equations for a moving atom

$$\frac{\mathrm{d}\hat{\rho}}{\mathrm{d}t} = -\frac{\mathrm{i}}{\hbar}[H_{\mathrm{atom}}(B) + H_{\mathrm{int}}(t), \hat{\rho}] + \left(\frac{\mathrm{d}\hat{\rho}}{\mathrm{d}t}\right)_{\mathrm{SE}}, \qquad (1)$$

where

$$H_{\mathrm{atom}}(B) = \sum_j \hbar\omega_j(B)|g_j\rangle\langle g_j| + \sum_k \hbar\omega_k(B)|e_k\rangle\langle e_k|, \qquad (2)$$

is the atomic Hamiltonian corresponding to ground (excited) states $|g_j\rangle$ ($|e_k\rangle$) with Zeeman-shifted energies $\hbar\omega_j(B)$ ($\hbar\omega_k(B)$). The laser–atom interaction is given by

$$H_{\mathrm{int}}(t) = -\sum_{j,k} \mathbf{E}(t)\cdot\mathbf{d}_{jk}(|g_j\rangle\langle e_k| + |e_k\rangle\langle g_j|), \qquad (3)$$

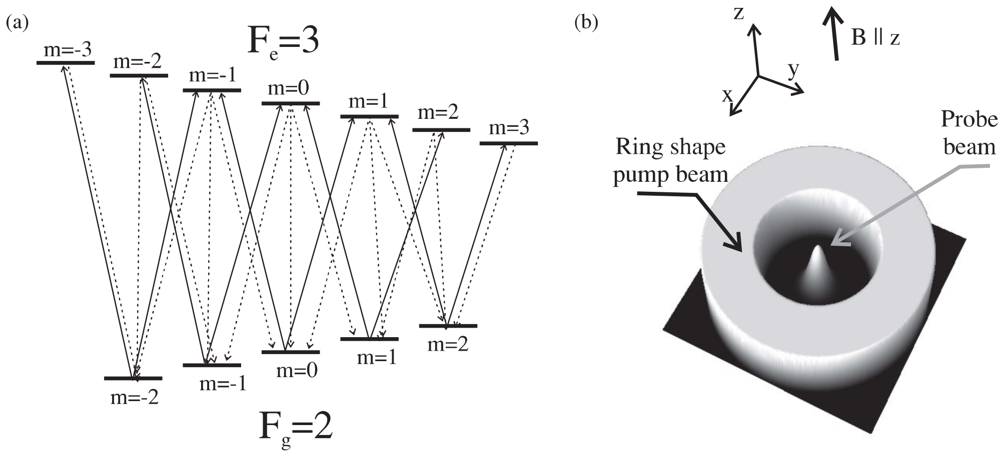

Figure 2. (a) The energy level diagram for magnetic sublevels of the $F_g = 2 \rightarrow F_e = 3$ transition and (b) pump and probe laser beam radial profiles used in the theoretical model. In (a) solid lines represent transitions induced by the linearly polarized laser fields, while dotted lines correspond to possible spontaneous emission channels from excited levels.

where $\mathbf{E}(t)$ is the time-dependent electric field of the laser seen by the atom and $\mathbf{d}_{jk}$ is the atomic electric dipole moment for the transition between states $|g_j\rangle$ and $|e_k\rangle$. Spontaneous emission is treated using the Lindblad-form term

$$\left(\frac{\mathrm{d}\hat{\rho}}{\mathrm{d}t}\right)_{\mathrm{SE}} = \sum_m 2\Gamma_m\hat{\rho}\Gamma_m^\dagger - \Gamma_m^\dagger\Gamma_m\hat{\rho} - \hat{\rho}\Gamma_m^\dagger\Gamma_m, \tag{4}$$

where Γ_m are operators related to dipole transitions from the excited to ground state manifold. Although the laser is frequency locked to the $F_g = 2 \rightarrow F_e = 3$ transition, due to Doppler broadening, the excited hyperfine levels $F_e = 2$ and $F_e = 1$ are also laser-coupled and therefore have to be included in the calculations. Equations for density matrix elements related to the $F_g = 1$ ground level are excluded since that level is not coupled by the laser. For additional details about the resulting equations please refer to [30].

Both the pump and probe are linearly polarized, have the same frequency ω_0 and propagate along the z axis. As schematically given in figure 2, the probe laser beam is at the centre of the coaxial hollow pump beam. The initial probe beam radial profile is a Gaussian

$$I_{\mathrm{probe}}(r) = 2\bar{I}_{\mathrm{probe}} \exp\left(-2r^2/r_0^2\right), \tag{5}$$

where r_0 is the $1/e^2$ radius of the probe beam and $\bar{I}_{\mathrm{probe}}$ is the probe beam's intensity (total probe power divided by $r_0^2\pi$). The pump beam's intensity profile along the radial distance r is modelled as

$$I_{\mathrm{pump}}(r) = \bar{I}_{\mathrm{pump}} a(\mathrm{erf}(p(r-r_1)) - \mathrm{erf}(p(r-r_2))), \tag{6}$$

where $\bar{I}_{\mathrm{pump}}$ is the pump beam's intensity, a is the normalization constant, p affects the steepness of the profile near the beam's edge determined by the parameters r_1 and r_2.

It is assumed that every collision with the cell wall resets the state of an atom. Therefore, the atoms entering the pump beam from the direction of the wall have equally populated Zeeman sublevels of both hyperfine levels of the ground state. The density of the rubidium vapour at room temperature is low enough, so that Rb–Rb collisions are negligible. Therefore, an atom moves through the laser beams with constant velocity $\mathbf{v} = \mathbf{v}_\parallel + \mathbf{v}_\perp$, where $\mathbf{v}_\parallel$ and $\mathbf{v}_\perp$ are velocity components parallel and perpendicular to the direction of laser propagation, respectively. When calculating the density matrix at a given value of z, we neglect longitudinal changes of the beam profiles compared to the transverse ones so that only the transverse direction of the trajectory matters. From the reference frame of the moving atom, the electric field varies and the rate of variation depends only on $\mathbf{v}_\perp$. Assume that the transverse projection of the atomic trajectory at some z is given by $\mathbf{r}_\perp(t) = \mathbf{r}_{0\perp} + \mathbf{v}_\perp t$, where $\mathbf{r}_{0\perp}$ is the transverse component of the atom position vector at $t = 0$. The temporal variation of the laser intensity seen by the atom is given by

$$I(t, z) \equiv I(\mathbf{r}_\perp(t), z) = I(\mathbf{r}_{0\perp} + \mathbf{v}_\perp t, z), \tag{7}$$

corresponding to the transverse laser intensity variation along the trajectory of the atom in the laboratory frame. Additionally, due to cylindrical symmetry of the beam profiles, the transverse dependence becomes a purely radial dependence.

The observed experimental resonances are the probabilistic average of contributions due to many individual, mutually non-interacting Rb atoms. The atoms traverse the laser beams at different paths with different velocities. The Maxwell–Boltzmann velocity distribution, diversity of atomic trajectories and custom cylindrical symmetric radial beam profiles are treated similarly as in [30]. Atomic trajectories having different distances from the centre of the probe beam are chosen so that the probe beam's cross-section is uniformly covered. For a suitable set of atomic velocities, the atomic density matrix $\hat{\rho}(B; \mathbf{v}; \mathbf{r})$ along a given trajectory is calculated assuming constant magnetic field B during the atomic transit through the laser beams. Numerical integration of the optical Bloch equations is carried out from the moment when the atom enters the pump beam's region until it exits the probe beam. To obtain the atomic ensemble density matrix $\hat{\rho}(B; r, z)$ across the beam's cross-section at some z and for a set of radial distances r, the calculated density matrices are averaged over the Maxwell–Boltzmann velocity distribution and integrated over trajectories containing points at given radial distance r.

The velocity-averaged density matrix will possess cylindrical symmetry arising from the cylindrical symmetry of the laser beam profiles and the atomic velocity distribution. Thus, the angular integral appearing in the averaging over velocity $\mathbf{v}(\theta) = (\theta, v_\perp, v_\parallel)$ can be replaced by an angular integral over space

$$\hat{\rho}(B; r, z) = \int_0^{2\pi} \frac{\mathrm{d}\theta}{2\pi} \int_0^{\infty} \mathrm{d}v_\perp W_\perp(v_\perp) \int_{-\infty}^{\infty} \mathrm{d}v_\parallel W_\parallel(v_\parallel) \times \hat{\rho}(B; 0, v_\perp, v_\parallel; r\cos\theta, r\sin\theta, z), \quad (8)$$

with the Maxwell–Boltzmann velocity distribution given by

$$W_\perp(v_\perp) = \frac{2v_\perp}{u^2}\,\mathrm{e}^{-(v_\perp/u)^2}, \qquad W_\parallel(v_\parallel) = \frac{1}{u\sqrt{\pi}}\,\mathrm{e}^{-(v_\parallel/u)^2}, \quad (9)$$

where $u = (2k_B T/m_{\mathrm{Rb}})^{1/2}$ is the most probable velocity.

In order to make a comparison with the experiment, we calculate the transmission and the angle of the polarization rotation of the linearly polarized probe laser's light as a function of the magnetic field. The effects of the probe beam's propagation and variation in its intensity along the Rb cell are treated using

$$\frac{\partial \mathbf{E}(B; r, z)}{\partial z} = \frac{\mathrm{i}\omega_0}{2\epsilon_0 c}\mathbf{P}(B; r, z), \quad (10)$$

where ϵ_0 is the vacuum dielectric constant and c the speed of light in vacuum. The accompanying initial condition is given by (5) and by the angle of the probe's incident linear polarization. The Rb vapour ensemble density matrix $\hat{\rho}(B; r, z)$ at some values of z is computed using the electric field $\mathbf{E}(B; r, z)$. The polarization of the Rb vapour is obtained from the ensemble density matrix

$$\mathbf{P}(B; r, z) = n(T)\,\mathrm{Tr}(\hat{\rho}(B; r, z)\hat{\mathbf{d}}), \quad (11)$$

where the ^{87}Rb concentration $n(T)$ at absolute temperature T is taken from [31]. Due to the trace operation including the dipole operator $\hat{\mathbf{d}}$, the polarization $\mathbf{P}$ depends only on the optical coherences between the ground and excited Zeeman sublevels. Using the computed Rb polarization, we are able to calculate the change of the probe's electric field due to propagation through the Rb vapour from (10). Following that procedure, we calculate the transmitted electric field $\mathbf{E}(B; r, z = L)$, where L is the cell length, used in the calculation of the transmission and the angle of the polarization rotation of the probe laser beam. During the calculation of the probe beam's propagation, we also treated the pump beam's propagation effects in an analogous manner.

The angle of the polarization's rotation is calculated in a similar manner as measured from signals of the two detectors S_1 and S_2 behind the polarizing beam-splitter rotated at 45° with respect to the incident probe's polarization. The polarization's rotation angle is given by

$$\varphi = \frac{1}{2}\arcsin\frac{S_1 - S_2}{S_1 + S_2}. \quad (12)$$

Values of S_1 and S_2 were obtained from

$$S_{1,2} = \int_{S_p} |\mathbf{u}_{1,2}\cdot\mathbf{E}(B; r, z = L)|^2 \mathrm{d}^2\mathbf{r}, \quad (13)$$

where $\mathbf{u}_{1,2} = (\sqrt{2}/2)(\mathbf{e}_x \pm \mathbf{e}_y)$ are unity vectors corresponding to the polarizing beam splitter's, s and p, polarization axes and S_p is the probe beam's cross-section.

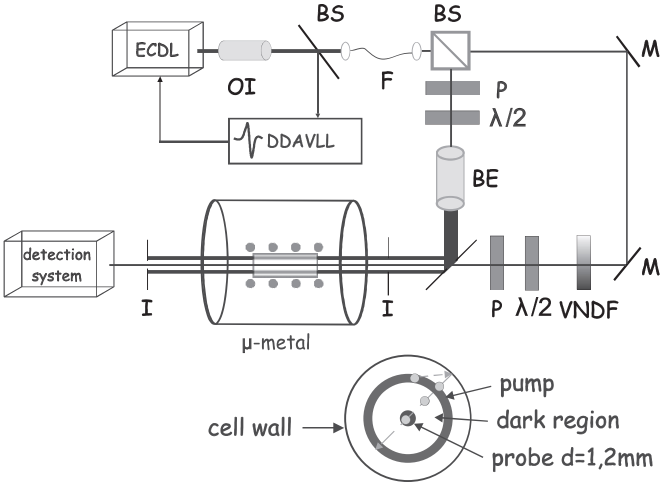

Figure 3. Experimental setup: ECDL-external cavity diode laser, OI-optical isolator, DDAVLL-Doppler free dichroic atomic laser lock, BS-beam splitter, F-optical fibre, M-mirrors, I-iris, P-polarizer, VNDF-variable neutral density filter, BE-beam expander, λ/2-retardation plate. Inset: transverse cross-section of the Rb cell with typical atomic trajectory.

3. Experimental setup

Figure 3 shows the experimental setup. An external cavity diode laser with a linewidth of about 1 MHz was used in the experiment. The laser frequency was locked to the D_2 transition $F_g = 2 \to F_e = 3$, in ^{87}Rb, using the Doppler-free dichroic atomic vapour laser lock (DDAVLL) technique [33]. The Gaussian laser beam is split into two beams, the pump beam and the probe beam. The diameter of the pump beam is enlarged and sent through a 12 mm diameter iris. The linear polarizations of the pump and probe beams, and the angle between their polarizations, are adjusted by a linear polarizer and λ/2 retardation plate. The important element for generating a laser beam like a hollow cylinder, as shown in figure 3(b), is a mirror with a hole [34]. The diameter of the hole thus determines the inner diameter of the hollow pump beam. We used two mirrors with central holes of 5 and 7 mm in diameter, respectively. The probe beam, 1.2 mm in diameter, comes from behind the mirror and passes through the hole's centre. The vacuum Rb gas cell is 85 mm long and its diameter is 25 mm. The cell is at room temperature. A scanning magnetic field along the laser beam's propagation is generated by the solenoid around the gas cell. Magnetic shielding from stray laboratory fields is achieved by three layers of μ-metal cylinders around the Rb cell. Behind the cell, the probe beam first passes through a pair of irises (in order to minimize the contribution of the pump beam) and then passes through the polarizing beam splitter with the fast axis oriented at 45° with respect to the direction of the initial polarization of the probe beam. Two beams emerging from the polarizing beam splitter were detected with two photodiodes. The sum $S_1 + S_2$ and the difference $S_1 - S_2$ of these two signals were recorded by a digital oscilloscope, while B was scanned around its zero value. The sum signal gives Hanle EIA, while the difference

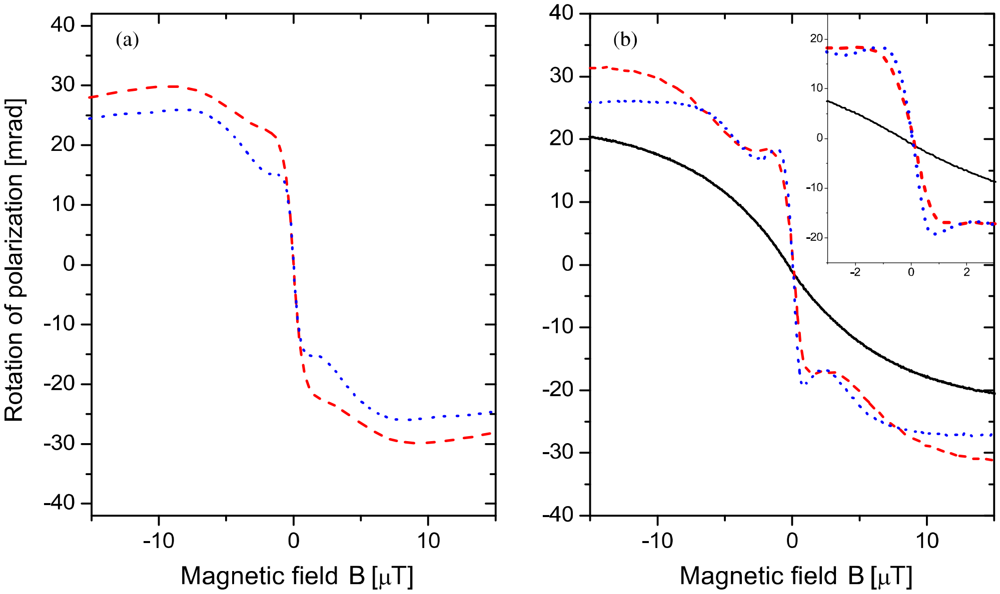

Figure 4. Calculated (a) and measured (b) probe NMOR for the $F_g = 2 \rightarrow F_e = 3$ transition in ^{87}Rb as a function of the axial magnetic field B. Dashed and dotted lines are for two inner pump beam diameters of 5 and 7 mm (corresponding to the 'dark region' size of 2 and 3 mm), respectively. Both pump and probe beams have the same linear polarization. The probe laser power is 10 μW, while the pump laser power is 1.2 mW. Solid line in (b) is NMOR for single wide laser beam having power of 10 μW and diameter of 7 mm. Inset in (b) shows the recorded resonances near $B = 0$.

signal gives NMOR. In this configuration, the rotation angle of the probe's polarization is given by

$$\phi = \frac{1}{2} \arcsin \frac{S_1 - S_2}{S_1 + S_2}. \qquad (14)$$

4. Discussion

In this section, we present results concerning the probe laser's transmission and polarization rotation when the probe laser interacts with Rb atoms prepared into coherent superposition of Zeeman sublevels of the $F_g = 2$ ground hyperfine level by the spatially separated pump beam. We intend to demonstrate that the Ramsey effects play a role here as they do for dark resonances [22] by measuring and calculating the line-shapes of EIA and NMOR resonances for different sizes of the dark region, and for different atomic states generated by the pump beam. Both probe and pump beams are linearly polarized and resonant to the $F_g = 2 \rightarrow F_e = 3$ transition in ^{87}Rb. The pump beam fills almost the entire 25 mm diameter Rb cell except for the hole at its centre, which is either 5 or 7 mm in diameter. The probe beam of 1.2 mm in diameter is collinear with the pump beam and passes along the axis of the hollow pump beam. This configuration allows, like in the Rb cells with anti-relaxation coating or buffer gas, repeated interaction of atoms and laser fields. It provides higher influx of atomic states prepared by the pump beam that reach the probe beam passing through the central hole, in comparison with co-propagating parallel but spatially separated Gaussian laser beams in [21]. In addition, the use of two separate laser beams gives the ability to independently control the properties of the beams, like polarization and power. Our experimental geometry is similar to the geometry used in [32], where the sub-Doppler feature was observed in the transmission of the hollow probe, through the very thin (10 μm) cell, while the pump beam is placed in the centre of the probe.

We first present theoretical and experimental line-shapes of the probe's NMOR, calculated and measured from the signals at the two detectors of the balanced polarimeter as a function of the external magnetic field B. The direction of the magnetic field is along the laser beam's propagation. In the experiment, the magnetic field varies slowly (50 Hz) so that the period of a magnetic sweep is much longer than typical atom transit time across the cell. This validates the assumption made in the theoretical model that B is constant while the atom passes through three regions of the Rb cell: the pump laser beam, the dark region and the probe laser beam. In all figures, spatially displaced pump and probe beams have the same frequency. Figures 4(a) and (b) present the calculated and measured angle of rotation of the linear probe polarization as a function of the axial magnetic field. The linear polarizations of the pump and probe beams are parallel. When the pump laser is turned on, the probe's NMOR resonance has a central dispersive shape and a pair of much weaker sidebands around the centre. Results are given for the two inner diameters of the pump beam, 5 and 7 mm. The resonance width decreases with the distance between the pump and the probe laser beam, which is a characteristic of the Ramsey effect. For dark regions of sizes 2 and 3 mm, the NMOR width is 2.4 and 1.6 μT, respectively. The results given in figures 4(a) and (b) show good agreement between theoretical predictions and experimental measurements. The solid curve in figure 4(b) corresponds to NMOR resonance of a single wide laser beam of 7 mm in diameter and 10 μW of power. It is notably wider and has smaller amplitude than the probe resonances obtained in pump–probe configuration, although the probe beam's diameter is much smaller, 1.2 mm. The amplitudes of NMOR and EIA are larger than for an open

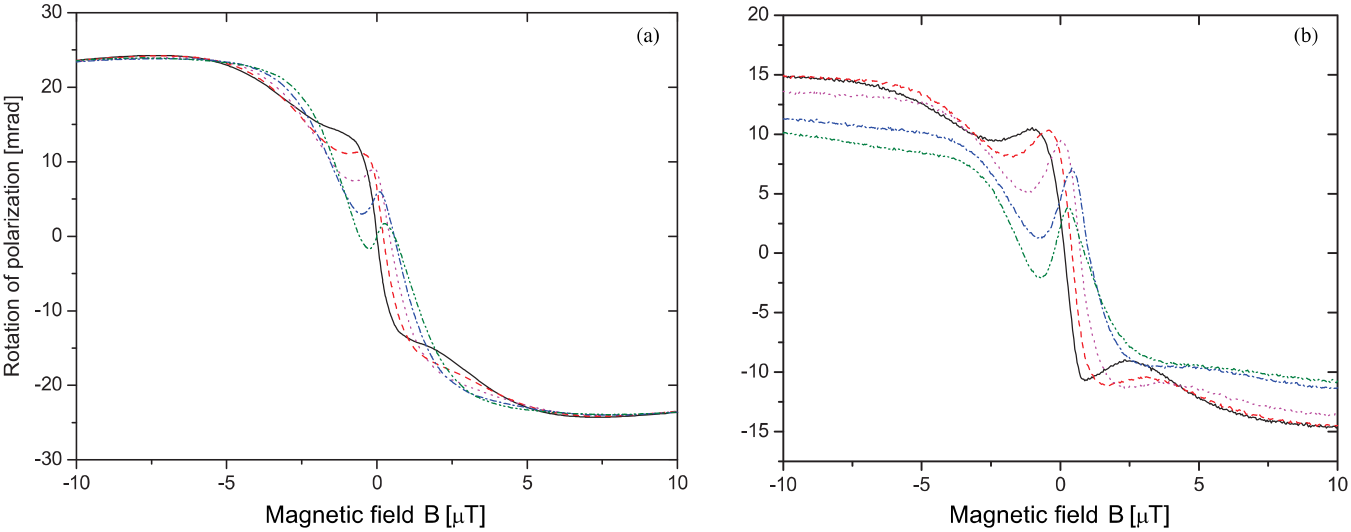

Figure 5. Theoretical (a) and experimental (b) results for the angle of rotation of the probe polarization for different angles between linear polarization of the pump and probe beams (0° black, 22.5° red, 45° green, 67.5° blue and 90° magenta). The pump and probe beams couple the $F_g = 2 \rightarrow F_e = 3$ transition in ^{87}Rb. The probe and pump laser powers are 20 μW and 1.2 mW, respectively. The pump beam's inner diameter is 7 mm.

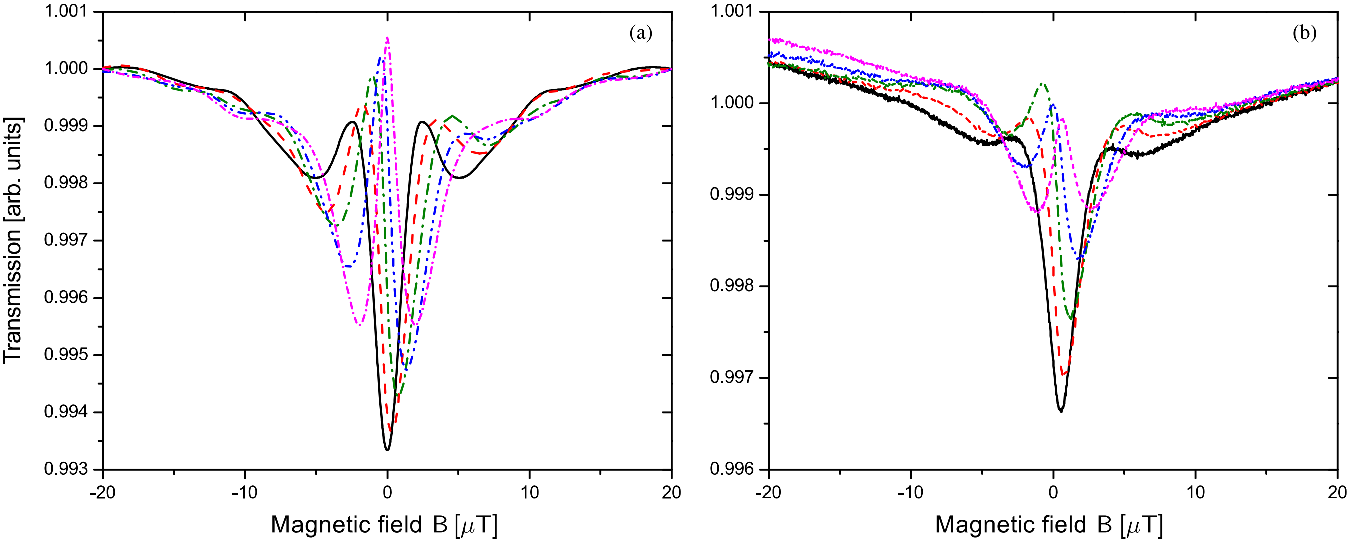

Figure 6. Theoretical (a) and experimental (b) results of the probe's absorption spectra for the $F_g = 2 \rightarrow F_e = 3$ transition in ^{87}Rb, for linearly polarized pump and probe beams and different probe beam polarization angles with respect to the pump beam's polarization (0° black, 22.5° red, 45° green, 67.5° blue and 90° magenta). The probe and pump powers are 20 μW and 1.2 mW, respectively. The pump beam's inner diameter is 7 mm.

EIT transition [23] because the closed transition limits losses of population to the hyperfine level of the uncoupled ground state.

The initial phases of atomic ground state coherences created in the pump beam can be controlled by varying the relative angle between pump and probe beam polarizations. Rotating the polarization of the pump beam by the angle φ, the phase between the circular components of the pump beam is changed by 2φ. This leads to the change of the phase of the atomic ground state coherences entering the probe beam by 2φ, for a constant magnetic field. In figure 5, we present the results for the probe beam's polarization rotation for several angles between the electric vectors of linearly polarized pump and probe beams. When we set the angle between the two electric field vectors to $\varphi = \pi/2$, we obtain the opposite sign for the probe beam's polarization rotation ($2\varphi = \pi$). For the angle φ between 0 and $\pi/2$, the dispersion-like curves for the probe NMOR beam are centred at an external magnetic field different from zero. The magnetic field corresponding to the centre of the NMOR resonance increases with the angle between the polarizations of two beams because different phases of the coherence require a different magnetic field for the constructive interference to occur. The comparison between results in figures 5(a) and (b) shows that calculated and measured line-shapes have very similar behaviour.

Figure 6 presents the Ramsey interference effects on the shape of EIA resonances. It shows the probe beam's transmission for several angles between the electric vectors

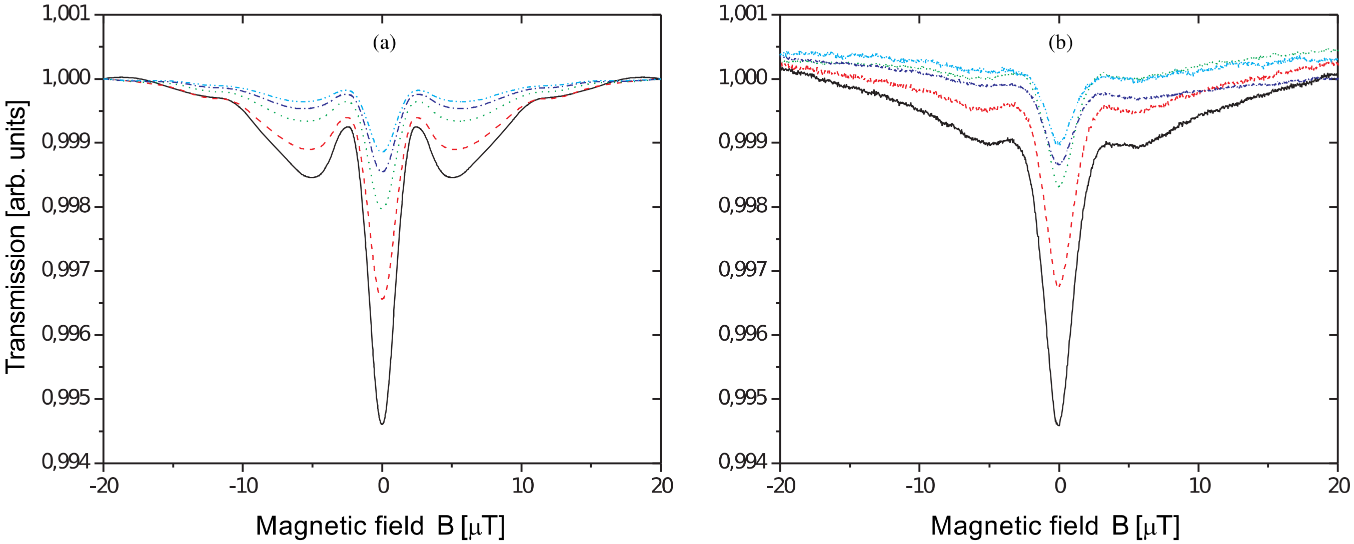

Figure 7. Theoretical (a) and experimental (b) results of the probe's absorption spectra for the $F_g = 2 \rightarrow F_e = 3$ transition in ^{87}Rb, for linearly polarized pump and probe beams and different powers of the probe beam (10 μW solid, 20 μW dashed, 40 μW dotted, 60 μW dash-dot, 80 μW dash-dot-dot lines). The pump laser power is 1.2 mW. The inner pump beam's diameter is 7 mm.

of linearly polarized pump and probe beams. Interference between the coherently prepared atoms and the probe field will give a probe transmission dip (for $2\varphi = 0$) or transmission gain (for $2\varphi = \pi$) around the same magnetic field values. These two cases are presented by solid and dash-dot-dot lines, respectively. For other values of φ, the transmission has a dispersion-like shape. As the angle between two polarizations increases, the main transmission dip shifts towards higher values of B, since a larger magnetic field is necessary for the occurrence of constructive interference. The comparison between the results in figures 6(a) and (b) shows that calculated line-shapes are very similar to the measured line-shapes. Similar dispersion-like line-shapes for an arbitrary angle between the linear polarizations of two laser fields have been theoretically predicted for EIA in a bichromatic laser field [35]. The behaviour observed from figures 5 and 6 supports the fact that the atomic ground state coherences essentially determine the development of EIA and NMOR in the considered atomic system.

The effects of the probe laser's power on the probe's transmission are given in figure 7. Both theory and experiment show that the increase of the probe beam's power lowers the amplitudes of the narrow central transmission dip. Higher probe beam power increases the probe beam's contribution to EIA resonance and at the same time lowers the effects of the pump beam induced atomic coherence. As long as the effect of atomic coherence entering the probe beam dominates over the probe's contribution, the resonance width of the central dip remains the same.

5. Conclusion

Experimental and theoretical evidences imply that probe EIA and NMOR in a vacuum Rb gas cell at room temperature are strongly affected by interference effects between the probe beam and atomic states prepared by the spatially separated pump beam in the presence of a small magnetic field. By increasing the size of dark region between the pump and probe, the resonances become narrower. By changing the initial phase of the atomic coherence in the pump beam, fully constructive interference with the probe beam can change into fully destructive interference yielding the change of the sign of the resonances. Moreover, the Ramsey effects seem to be even more pronounced on the EIA linewidth and amplitude than for EIT (developed on atomic transition $F_g \rightarrow F_e = F_g - 1$), as found by comparing the results for both phenomena using the same geometry of the laser beams [22, 23]. Among many differences between EIT and EIA, these results show that the response of ground state Zeeman coherences in an atomic system showing EIA to Ramsey-type excitation is very similar to the previously observed response of Zeeman coherences in atomic systems showing EIT [22, 23].

Acknowledgments

This work was supported by the Ministry of Education and Science of Serbia, under grant nos III45016 and OI171038 and also by SCOPES JRP IZ73Z0_127942.

References

[1] Akulshin A M, Barreiro S and Lezama A 1998 *Phys. Rev.* A **57** 2996
[2] Kazantsev A, Smirnov V, Tumaikin A and Yagofarov I 1984 *Opt. Spectrosc. (USSR)* **57** 116
Kazantsev A, Smirnov V, Tumaikin A and Yagofarov I 1984 *Opt. Spektrosk.* **57** 189
[3] Harris S E 1997 *Phys. Today* **50** 36
[4] Arimondo E and Orriols G 1976 *Lett. Nuovo Cimento Soc. Ital. Fis.* **17** 333
[5] Lezama A, Barreiro S and Akulshin A M 1999 *Phys. Rev.* A **59** 4732
[6] Dancheva Y, Alzetta G, Cartaleva S, Taslakov M and Andreeva C 2000 *Opt. Commun.* **178** 103

[7] Kim S K, Moon H S, Kim K and Kim J B 2003 *Phys. Rev.* A **68** 063813
[8] Brazhnikov D V, Tumaikin A M, Yudin V I and Taichenachev A V 2005 *J. Opt. Soc. Am.* B **22** 57
[9] Dimitrijević J, Arsenović D and Jelenković B M 2007 *Phys. Rev.* A **76** 013836
[10] Dimitrijević J, Krmpot A, Mijailović M, Arsenović D, Panić B, Grujić Z and Jelenković B M 2008 *Phys. Rev.* A **77** 013814
[11] Dimitrijević J, Grujić Z, Mijailović M, Arsenović D, Panić B and Jelenković B M 2008 *Opt. Express* **16** 1343
[12] Failache H, Valente P, Ban G, Lorent V and Lezama A 2003 *Phys. Rev.* A **67** 043810
[13] Taichenachev A V, Tumaikin A M and Yudin V I 1999 *Phys. Rev.* A **61** 011802
[14] Dimitrijević J, Arsenović D and Jelenković B M 2011 *New J. Phys.* **13** 033010
[15] Valente P, Failache H and Lezama A 2003 *Phys. Rev.* A **67** 013806
[16] Akulshin A M, Barreiro S, Sidorov A I, Hammaford P and Opat G I 2003 *Phys. Rev.* A **67** 011801
[17] Akulshin A M, Sidorov A I and Hannaford P 2006 *Phys. Rev.* A **73** 033806
[18] Goren C, Wilson-Gordon A D, Rosenbluh M and Friedmann H 2003 *Phys. Rev.* A **67** 033807
[19] Ramsey N 1956 *Molecular Beams* (London: Oxford University Press)
[20] Xiao Y, Novikova I, Phillips D F and Walsworth R L 2006 *Phys. Rev. Lett.* **96** 043601
[21] Zibrov A S and Matsko A B 2001 *Phys. Rev.* A **65** 013814
[22] Grujić Z D, Mijailović M, Arsenović D, Kovacević A, Nikolić M and Jelenković B M 2008 *Phys. Rev.* A **78** 063816
[23] Mijailović M M, Grujić Z D, Radonjić M, Arsenović D and Jelenković B M 2009 *Phys. Rev.* A **80** 053819
[24] Kim H-J and Moon H S 2011 *Opt. Express* **19** 168
[25] Kim H-J and Moon H S 2012 *Opt. Express* **20** 9485
[26] Barkov L M, Melik-Pashayev D and Zolotorev M 1989 *Opt. Commun.* **70** 467–72
[27] Kanorsky S I, Weis A, Wurster J and Hänsch T W 1993 *Phys. Rev.* A **47** 1220
[28] Budker D, Kimball D F, Rochester S M and Yashchuk V V 2000 *Phys. Rev. Lett.* **85** 2088
[29] Budker D, Gawlik W, Kimball D F, Rochester S M, Yashchuk V V and Weis A 2002 *Rev. Mod. Phys.* **74** 1153
[30] Radonjić M, Arsenović D, Grujić Z and Jelenković B M 2009 *Phys. Rev.* A **79** 023805
[31] Nesmeyanov A N 1963 *Vapour Pressure of the Chemical Elements* (Amsterdam: Elsevier)
[32] Briaudeau S, Saltiel S, Leite J R R, Oria M, Weis A, Bloch D and Ducloy M 2000 *J. Phys.* IV *France* **10** Pr8–145
[33] Corwin K L, Lu Z T, Hand C F, Epstein R J and Wieman C E 1998 *Appl. Opt.* **37** 3295
[34] Chang Chun Bo Xin Photoelectric Co. Ltd. (Chang Chun, Ji Lin, China), www.bxoptic.com/
[35] Zhukov A A, Zibrov S A, Romanov G V, Dudin Y O, Vassiliev V V, Velichansky V L and Yakovlev V P 2009 *Phys. Rev.* A **80** 033830

PHYSICAL REVIEW A **90**, 023845 (2014)

Formation of complex two-dimensional dissipative solitons via spontaneous symmetry breaking

V. Skarka,[1,2,3,*] N. B. Aleksić,[2,3] M. Lekić,[2] B. N. Aleksić,[2,3] B. A. Malomed,[4] D. Mihalache,[5] and H. Leblond[1]
[1] *Laboratoire de Photonique d'Angers, EA 4464, Université d'Angers, 2 Boulevard Lavoisier, 49045 Angers Cedex 01, France*
[2] *Institute of Physics, University of Belgrade, 11000 Belgrade, Serbia*
[3] *Texas A&M University at Qatar, PO Box 23874, Doha, Qatar*
[4] *Department of Physical Electronics, Faculty of Engineering, Tel Aviv University, Tel Aviv 69978, Israel*
[5] *Horia Hulubei National Institute for Physics and Nuclear Engineering, 407 Atomistilor, Magurele-Bucharest, 077125, Romania*

(Received 12 May 2013; published 25 August 2014)

We propose a complex Ginzburg-Landau equation (CGLE) with localized linear gain as a two-dimensional model for pattern formation proceeding via spontaneous breaking of the axial symmetry. Starting from steady-state solutions produced by an extended variational approximation, simulations of the CGLE generate a vast class of robust solitary structures. These are varieties of asymmetric rotating vortices carrying the topological charge (TC), and four- to ten-pointed revolving stars, whose angular momentum is decoupled from the TC. The four- and five-pointed stars feature a cyclic change of their structure in the course of the rotation.

DOI: 10.1103/PhysRevA.90.023845 PACS number(s): 42.65.Tg, 42.65.Sf, 47.20.Ky

I. INTRODUCTION

The generation of self-organized dissipative structures in nonlinear systems is driven by external energy and/or matter supplies [1]. Various species of self-trapped localized structures are represented by dissipative solitons acting as *attractors* [2,3]. The self-organization is based on the balance of antagonistic effects, with gain compensating losses, and nonlinearity-induced self-contraction arresting the linear diffraction and/or dispersion. The ensuing formation of vast varieties of patterns is apparently spontaneous, and in many cases its origins are not yet understood well, in spite of the great deal of work done on this subject. Generically, the pattern formation proceeds via spontaneous breaking of an underlying continuous symmetry, followed by the emergence of novel forms which feature reduced symmetries [4]. Since the pioneering work of Turing [5], many works have been dealing with models for spontaneous pattern formation in diverse settings; see, e.g., Refs. [6,7].

Complex Ginzburg-Landau equations (CGLEs) constitute a class of ubiquitous models to describe the generation of dissipative-solitonic structures in plenty of systems ranging from nanophotonics, plasmonics, nonlinear optics, fluids, and plasmas through superconductivity, superfluidity, quantum field theory, and biological systems [2,3,8–11]. The great deal of work done in this field has demonstrated cogently that CGLEs are appropriate models for studying the spontaneous pattern formation *per se*.

In this work, we demonstrate that the above-mentioned crucially important aspect of the pattern formation, viz., the spontaneous breaking of the continuous symmetry, leading to the emergence of localized structures featuring reduced symmetries, may be adequately modeled by a suitably chosen two-dimensional (2D) CGLE with the competing cubic-quintic (CQ) nonlinear terms. We resort to the synergy of the variational approximation (VA) and parallelized numerical simulations to demonstrate spontaneous formation of previously unexplored solitonic structures, which have diverse counterparts in nature. Using the CGLE with a spatially modulated linear loss, which features a minimum at the center, we have previously demonstrated that vortices may spontaneously evolve into stably rotating ellipsoidal or crescent vortical structures [12]. The CGLE model developed in the present work offers a vast potential for modeling transitions between different types of spontaneously established patterns, through the generation a broad class of localized states, such as periodically metamorphosing and rotating four- to ten-pointed stars, which resemble complex natural objects, but were not produced by previously studied models.

As mentioned above, the dissipative-soliton pattern formation is the result of the concurrent balance between losses and gain, and between diffraction and cubic self-focusing, which must be supplemented by the quintic self-defocusing, to prevent the collapse in the 2D geometry. The creation of (2+1)D optical solitons (two transverse coordinates x and y, with $+1$ standing for the propagation distance z, which plays the role of the evolutional variable) in a CQ medium has been recently directly demonstrated in an experiment [13]. Dissipative solitons have been found in many varieties of CGLEs [2,3,8,14–16]. In particular, (2+1)D solitons with embedded vorticity m, featuring zero intensity at the center, carry the angular momentum, $M = mP$, where P is their total power (norm); see Eq. (3) below [17]. As a result of the spontaneous pattern change, the intrinsic angular momentum can transmute into explicit rotation of solitonic patterns, as shown in the movie in the Supplemental Material [18] (examples of this are known, e.g., in the form of *azimuthons* [19] and vortex gap solitons [20]).

II. MODEL FOR SELF-ORGANIZED PATTERN FORMATION

The present model is based on the (2+1)D CGLE with the CQ nonlinearity that governs the evolution of wave amplitude $E(x,y,z)$ in the nonlinear medium:

$$iE_z + (1/2)(E_{xx} + E_{yy}) + (1 - i\varepsilon)|E|^2E - (\nu - i\mu)|E|^4E = ig(r)E, \tag{1}$$

---

[*] vladimir.skarka@univ-angers.fr

where positive coefficients ε, μ, and ν, account, respectively, for the cubic gain, quintic loss, and quintic saturation of the cubic self-focusing. A crucially important ingredient of the model is represented by an "iceberg of the gain," $g(r) = \gamma - \Gamma r^2$ (with radial variable $r = \sqrt{x^2 + y^2}$, gain amplitude $\gamma > 0$, and gain curvature $\Gamma > 0$) *protruding above* the surface of the "loss sea," contrary to the above-mentioned model with the "submerged iceberg," where the main control parameter γ is negative [12]. A straightforward physical implementation of Eq. (1) is provided by optically pumped laser cavities (especially end-pump solid-state ones). The pumped beam is focused in order to increase the gain, hence the gain is localized [21]. The transverse localization of the laser beam known as "gain guiding" is used in titanium-sapphire, solid-state, Raman, free-electron, and x-ray lasers [22]. The pump beam is typically Gaussian with intensity $I(r) = I_0 \exp(-r^2/R^2)$, where R is its waist. The gain curvature $\Gamma \propto 1/R^2$ depends mainly on R, so that the localized gain is determined by the Taylor expansion of intensity $I(r)$, which makes the model generic [21–23]. The laser cavity can be adjusted by selecting parameters of the saturable absorber [2,8,9,12,21–23]. Thus, the pattern-formation scenarios reported below can be directly realized in the lasers, as well as in other self-organized systems.

Barring rare exceptions [24], the CGLEs, due to their complexity, do not admit exact solutions. Nevertheless, an analytical approximation for dissipative solitons has been developed using the VA adapted to dissipative systems [11,12], see also Ref. [25]. The VA makes use of the following Gaussian trial function representing the electric field of an axisymmetric Gaussian laser beam with vorticity (topological charge, TC) $m = 1$:

$$E = A(r/R)\exp[-r^2/(2R^2) + iCr^2 + i\theta + i\Psi], \qquad (2)$$

where amplitude A, radius R, wave-front curvature C, and phase Ψ have to be optimized. θ is the angular coordinate. The total power and angular momentum of the vortex are, respectively,

$$\begin{aligned} P &= \int_0^\infty r dr \int_0^{2\pi} d\theta\, |E(r,\theta)|^2 = \pi A^2 R^2, \\ M &= i\int_0^\infty r dr \int_0^{2\pi} d\theta \frac{\partial E^*}{\partial \theta} E. \end{aligned} \qquad (3)$$

Skipping straightforward details, the following system of evolution equations is produced by the VA (although formally similar to the one derived in Ref. [12], it produces essentially different results, as shown below):

$$dA/dz = \gamma A - \Gamma R^2 A + 5\varepsilon A^3/16 - 8\mu A^5/81 - 2AC, \quad (4)$$

$$dR/dz = 2CR - \Gamma R^3 - \varepsilon A^2 R/16 + 2\mu A^4 R/81, \quad (5)$$

$$dC/dz = -2C^2 + 1/(2R^4) - A^2/(16R^2) + 2\nu A^4/(81R^2), \quad (6)$$

$$d\Psi/dz = -2/R^2 + 3A^2/8 - 10\nu A^4/81, \quad (7)$$

with Eq. (7) decoupled from (4)–(6). Fixed points (FPs) of these equations correspond to steady-state solutions with a small wave-front curvature. Setting $dR/dz = 0$ in Eq. (5) leads to $C = \Gamma R^2/2 + \varepsilon A^2/32 - \mu A^4/81$. In Eq. (6) with $dC/dz = 0$, small C^2 may be neglected giving $R^2 = 8(A^2 - 32\nu A^4/81)^{-1}$. The remaining relation for the FP, following from Eqs. (4) with $dA/dz = 0$, is $\gamma + \varepsilon A^2/4 - 2\mu A^4/27 = 2\Gamma R^2$, which gives rise to two physically relevant steady-state solutions for amplitude A (solutions for which both A and R are real and positive). According to general principles of the analysis of dissipative systems [24,11], the solution with larger A may be stable, while the one with smaller A is always unstable. The former solution satisfies condition $C < 0$, which is necessary for the simultaneous stable balance of the diffraction and CQ nonlinearity, and of the gain and loss, thus rendering the dissipative solitons stable stationary modes [14,26].

The linear stability analysis of the FPs against small perturbations of amplitude, radius, and wave-front curvature within the framework of Eqs. (4)–(6) was performed via the computation of eigenvalues produced by the respective equation $\lambda^3 + \alpha_1\lambda^2 + \alpha_2\lambda - \alpha_3 = 0$,

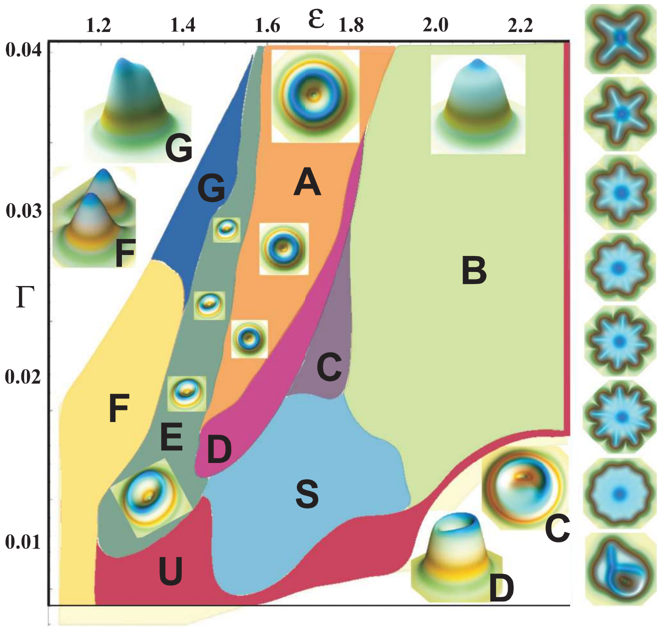

FIG. 1. (Color online) Stability domains produced by the VA-generated fixed points, which are used as the input for direct simulations of Eq. (1), in the plane of the nonlinear-gain strength, ε, and the linear-gain curvature, Γ (dimensionless units). Stable axisymmetric vortices are established in region A. In region B, the spontaneous symmetry breaking expels the vortical phase dislocation, resulting in the transition to a bell-shaped axisymmetric mode without the central crater. In intermediate area C, the vortex mutates into a rotating crescent-shaped soliton that fills only half of the original crater, thus breaking the inner circular symmetry. In region D, the vortex crater gets slanted but remains centrosymmetric. In area E, the modulational instability spontaneously breaks the axial symmetry, converting the circular vortex into a rotating elliptic one. In area F, the ring splits into two bell-shaped fragments. For larger Γ in region G, they merge into a stable double-hump shape. In the region of star-shaped patterns, S, small variations of Γ and ε result in the self-trapping of revolving four-, five-, six-, seven-, eight-, nine-, and ten-pointed stars with zero TC (examples are shown on the right). The strongly asymmetric steadily rotating "cobra" pattern, shown at the bottom of the right column, appears in interstices between different regions. Structure fails to form only in region U.

stable FPs being identified by the Routh-Hurwitz conditions [11]: $\alpha_1 \equiv 2\Gamma R^2 - 5\varepsilon A^2/8 + 32\mu A^4/81 > 0$, $\alpha_2 \equiv 8\nu A^4 R^{-2}/81 - \Gamma A^2 R^2(3\varepsilon/2 - 80\mu A^2/81) > 0$, $\alpha_3 \equiv (A^2 - 16R^{-2})\Gamma - (\varepsilon - 16\mu A^2/9)A^2 R^{-4} > 0$, and $\alpha_1\alpha_2 - \alpha_3 > 0$. They cover the entire area charted in Fig. 1 in the plane of the nonlinear-gain and linear-gain curvature parameters, ε and Γ, which are most essential for the control of the patterns and transitions between them. For effective saturable absorbers in laser cavities, such as those created by means of a Kerr lens, nonlinear polarization rotation, or an appropriate dopant, these parameters can be easily adjusted in the experiment [21–23]. For instance, different concentrations of the rhodamine dye in ethanol, used as a dopant, can be used in order to recover different values of the nonlinear-gain parameter, ε in Fig. 1. The linear-gain curvature parameters Γ can be adjusted to fit values in Fig. 1 by changing the pump-beam intensity. Other coefficients are fixed here as $\nu = 0.4$, $\mu = 1.4$, and $\gamma = 0.08$, which adequately represent the generic situation (varying these parameters does not entail essential changes). Steady-state solutions do not exist in the white corners of Fig. 1.

Next, Gaussian electric field (2) with parameters of the stable FP adopted by the VA was used as the input for parallelized [27] simulations of Eq. (1). As a result, a variety of stable patterns have been generated, some of them similar to the one assumed by Eq. (2), and some completely different, as summarized in Fig. 1.

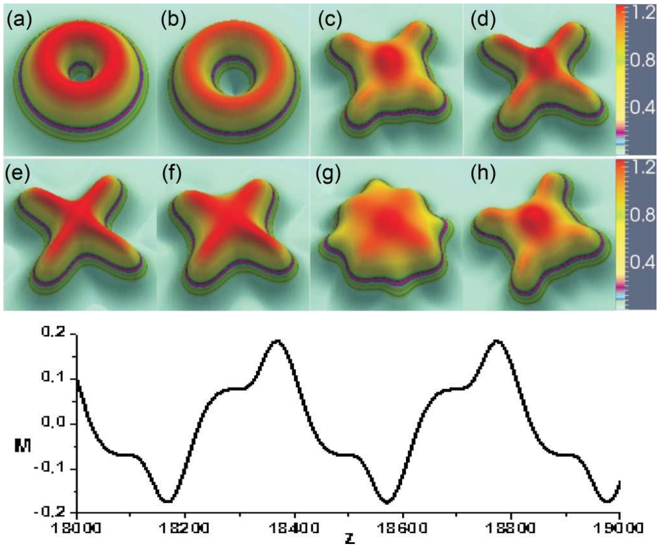

FIG. 2. (Color online) The spontaneous formation of four-pointed patterns. The input ring structure (a) evolves into a vortex soliton at $z \approx 40$ (b), whose spontaneous symmetry breaking in (c) produces a Celtic-cross structure (at $z \approx 1400$) that subsequently transmutes into other varieties of cross patterns from $z \approx 1440$ until $z \approx 1560$ (d)–(g). (h) After a half period ($T_M \approx 400$), a rotated Celtic-cross reappears at $z \approx 1600$. Graph M shows oscillations of the angular momentum between $M = -0.18$ and $M = +0.18$ (dimensionless units).

III. SELF-GENERATED DISSIPATIVE VORTEX SOLITONS

In area A of Fig. 1, stable axisymmetric vortex solitons (shown by insets) quickly self-trap by $z = 10$. In fact, only in this area does the model give rise to the simple vortex solitons assumed by Eq. (2), while in other domains unique patterns appear. First, in "filamentation" region F, the modulation instability breaks the vortices into two fragments (see the inset also labeled F), as the total power P given by Eq. (3) is not strong enough to keep the vortex structure stable. In contrast, in area G, the power and strength of the pinning to the localized gain (provided by the pump laser) are much larger, leading to coalescence of the fragments into a revolving double-hump soliton above an "effective threshold" for the pattern formation (see movie [18]); cf. Ref. [17]. An example of this stable pattern is shown in inset G.

In region E adjacent to F, with larger cubic-gain coefficient ε, the modulational instability is not strong enough to destroy the vortex, but it breaks the axial symmetry and deforms it into a stable elliptic rotating vortex. Adjacent to A, but on the opposite side (region D), the vortex remains centrosymmetric, but with a slanted shape (see inset D in Fig. 1). At still larger ε, in region C, the circular symmetry of the vortex is broken by its transformation into a crescent mode, featuring a half-filled vortical ring.

The common feature of these modes is that they start the self-organization as axisymmetric vortices, and the spontaneous symmetry breaking sets in after a period of a quasistable evolution, which may last for up to thousands of propagation units (unless a symmetry-breaking perturbation is added initially). The robustness of the finally established symmetry-reduced modes has been confirmed by the propagation over $z > 20\,000$. On the other hand, small gain curvature Γ cannot prevent quick destruction of vortices in the bottom region U ("unstable") of Fig. 1.

At larger values of Γ and ε (in region B), the original mode undergoes a faster transient evolution, lasting for several hundreds of units, in the form of oscillating breathers, before losing the intrinsic vorticity. Thus, a spontaneous change of the shape occurs, expelling the phase dislocation [see also Fig. 4(a)] and filling the corresponding "crater," while the former vortex transmutes into a stable fundamental (2+1)D soliton (with $m = 0$), as seen in inset B (a detailed dynamical picture is provided in the movie in the Supplemental Material [18]).

The most remarkable manifestation of the spontaneous formation of complex patterns induced by the symmetry breaking above the effective threshold is the transmutation of vortices into various *stars* (see the right-hand-side column in Fig. 1), caused by small changes of Γ and ε in region S. How the circular symmetry is broken can be seen in detail in movies S1–S6 [18] that display the dynamics of the spontaneous emergence of four-, five-, six-, eight-, and ten-pointed stars, as well as of double-hump localized structures. For instance, at $\varepsilon = 1.7$ and $\Gamma = 0.018$, close to the junction of domains C and D, the input vortex [Fig. 2(a)] at first self-traps into a vortex soliton [Fig. 2(b)]. Then, the vortex loses its inner circular symmetry at $z \approx 140$, transforming into a crescent, while the phase dislocation continues to drift, until it escapes at $z \approx 730$ [18]. Therefore, the outer circular symmetry is gone too. At $z > 900$, persistent oscillations commence, corresponding to a robust breather with period $T_A \approx 5$ and a superimposed beat period, $T_B \approx 40$. During another, much longer, beat period, $T_M \approx 400$, the angular momentum oscillates between

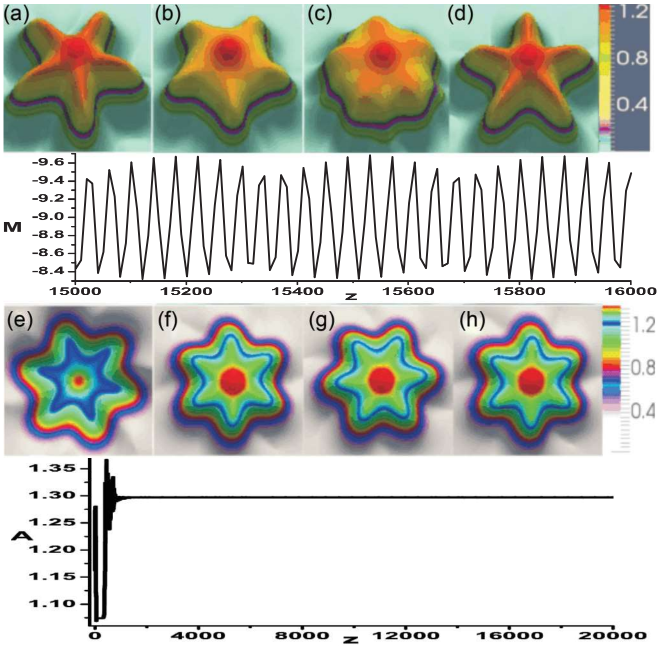

FIG. 3. (Color online) The evolution of the revolving five- and six-pointed stars. The five-pointed star at $z = 1000$ (a) gets fatter from $z \approx 1010$ until $z \approx 1020$ (b) and (c), before rotating by 30° at $z \approx 1040$ (d). The period of the cyclic evolution is $T_C \approx 40$. Angular momentum M oscillates between $M = -8.3$ and $M = -9.7$, with period $T_M \approx 360$ (dimensionless units). (e) The transient six-pointed star self-traps into the permanent shape. (f)–(h) The rotation of the star in the course of $T/6 \approx 36$ from $z \approx 1080$ until $z \approx 1116$ (only one sixth of the period is displayed, as the symmetry of the star makes the subsequent evolution tantamount to that shown here). Variations of amplitude A in the course of the soliton self-formation are displayed in the bottom plot (dimensionless units).

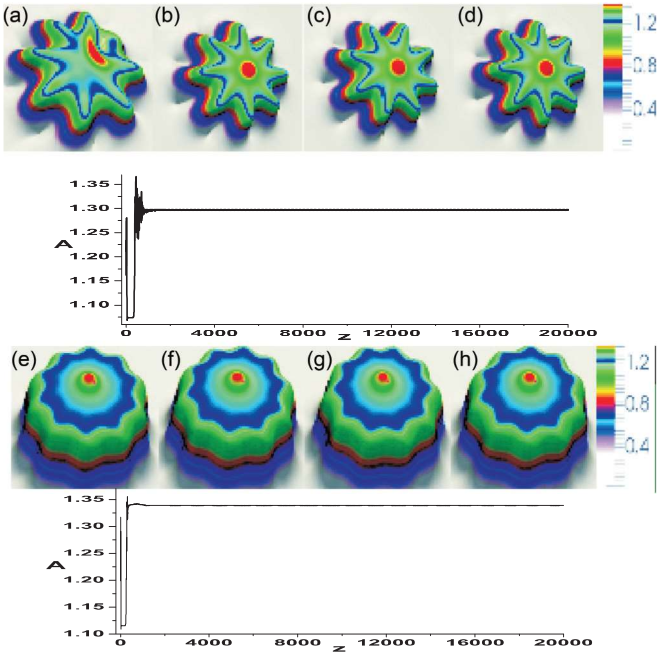

FIG. 4. (Color online) The evolution of the revolving eight- and ten-pointed stars. To establish the reduced symmetry, the phase dislocation is expelled from the vortical structure (a), and an "octopus" soliton emerges at $z \approx 960$ (b), which rotates, in the course of $T/8 \approx 24$, through (c) at $z \approx 972$ into an identical configuration at $z \approx 984$ (d). Its spontaneous self-organization is illustrated by the bottom plot displaying the evolution of the amplitude, $A(z)$. (e)–(h) The rotation of a ten-pointed star ("decapod"), from (e) at $z \approx 1200$ to (h) at $z \approx 1248$ in the course of $T/10 \approx 48$. Its self-generation is illustrated by the bottom plot for $A(z)$.

$M = -0.18$ and $M = +0.18$ (see graph M in Fig. 2). In the course of beatings, a "Celtic-cross" shape transmutes into a sequence of crosslike ones [see Figs. 2(c)–2(g)], and eventually returns to a rotated "Celtic cross" [Fig. 2(h)] [18]. The robustness of the cyclic shape transmutations in this regime was tested up to $z = 70\,000$. Reducing the gain curvature to $\Gamma = 0.014$, at the same $\varepsilon = 1.7$, increases the number of arms in the pattern, converting it into a five-pointed star, as shown in Figs. 3(a)–3(d) [18]. The scenario of breaking the axial symmetry to the reduced (fivefold) form is the same as in the previous case. However, the angular momentum now oscillates between $M = -8.3$ and $M = -9.7$, with period $T_M \approx 360$ as in diagram M in Fig. 3. This star rotates and simultaneously changes its shape, with period $T_C \approx 40$, between four particular five-pointed configurations.

Gradually decreasing the gain curvature (Γ), and increasing the nonlinear gain (ε), a sequence of six-, seven-, eight-, nine-, and ten-pointed stars is generated. After a transient period, each of them rotates at a constant angular velocity, keeping a permanent shape, unlike the cyclic "metamorphosis" featured by the four- and fivefold solitons. An example of a revolving six-pointed star (which resembles snowflakes [28]) is displayed in Figs. 3(e)–3(h), for $\Gamma = 0.013$ and $\varepsilon = 1.75$ (see movie in Supplemental Material [18]). The evolution of amplitude A in the course of the soliton self-organization is presented in the same figure. In this case, the angular momentum, defined as per Eq. (3), is $M = -24$. Further, a typical eightfold "octopus" is presented in Figs. 4(a)–4(d), for the same ε but a smaller gain curvature, $\Gamma = 0.007$, featuring a smaller radius of the pattern's core [18]. The self-formation of the eight-pointed soliton star is shown in diagram A. Finally, the spontaneous self-organization of a ten-pointed star for $\varepsilon = 1.95$ and $\Gamma = 0.01$ is shown in Figs. 4(e)–4(h), and additionally illustrated by the plot for amplitude A versus propagation distance z, which is displayed beneath panels 4(e)–4(h) [18]. All the stars are stable objects with a nonzero angular momentum but zero TC.

Structures with more than ten rays turn out to be transients evolving towards axially symmetric bell-shaped solitons in area B of Fig. 1. Lastly, at borderlines between B, S, and U areas there occur strongly asymmetric steadily rotating structures in the form of "cobras" (shown in the right bottom corner of Fig. 1).

It is precisely the spatially inhomogeneous linear gain ($\gamma > 0$) *protruding above* the loss sea, which drives, above an effective threshold, in synergy with the nonlinear gain, the spontaneous transition from vortices with topological charge $m = 1$ to the various species of fundamental solitons with $m = 0$, including the above-mentioned class of the star-shaped solitons. Such a spontaneous transition is not possible with the gain *submerged* into the sea of loss, which was the distinctive feature of the model considered in Ref. [12]. Therefore, the two models are substantially different, although they include similar terms. As a result, in the model with $\gamma < 0$, i.e., without the explicit linear gain, the stability chart in the same parameter plane is totally different [12].

It is relevant to stress the difference of the variety of patterns produced by the spontaneous breaking of the axial symmetry in systems of the CGLE type from their conservative counterparts, based on nonlinear Schrödinger equations (NLSEs). In the latter case, the angular momentum is always related to the TC, while the CGLE allows decoupling of the momentum from the TC, and (2+1)D NLSEs do not give rise to star-shaped patterns [29].

IV. CONCLUSIONS

In conclusion, we have established that the evolution of the 2D complex Ginzburg-Landau equation with the cubic-quintic nonlinearity and localized linear gain gives rise to spontaneous formation of many species of patterns, including asymmetric vortices, modes which feature cyclic metamorphosis, and revolving stars without intrinsic TC (topological charge). Starting from the input provided by the variational approximation, systematic simulations have generated the localized structures whose stability areas are charted in Fig. 1 (only in a small part of the parameter space, the input decays without initiating the pattern formation). The instability-induced spontaneous reduction of the continuous rotational symmetry to a discrete subsymmetry is the generic route to the pattern formation in the present setting. In particular, the modulational instability breaks the vortex into two fragments, which fuse into a double-hump pattern above an effective threshold for the pattern formation, depending of the pump-beam intensity. More sophisticated species of the robust localized modes include four- and fivefold ones, which evolve through cycles of periodically changing forms. On the other hand, six-, seven-, eight-, nine-, and ten-pointed stars steadily revolve, keeping the constant shape and constant angular momentum, with zero TC, unlike vortices, whose angular momentum is proportional to the TC. Stable, oddly shaped rotating patterns (cobras) occur in interstices between stability domains of the different species.

The proposed (2+1)D CGLE model establishes the complex pattern-formation phenomenology in laser cavities and other nonlinear photonic systems. As a consequence, it may be used to monitor real-time stability, and to detect fluctuations causing slight changes of the cavity (ε) and pump (Γ) control parameters in operating lasers, that can be visualized by the change of patterns (e.g., the increase of the number of arms in the star structures). The model may also help in understanding generic features of the pattern formation in other areas, with potential applications to the design of information-processing analog schemes [30].

ACKNOWLEDGMENTS

This work was supported, in part, by the Ministry of Science of Serbia through Projects No. OI 171006 and No. III 45016. This publication was partially made possible by NPRP Grants No. 5-674-1-114 and No. 6-021-1-005 from the Qatar National Research Fund (a member of Qatar Foundation). D.M. was supported by the Romanian Ministry of Education and Research (Project No. PN-II-ID-PCE-2011-3-0083).

---

[1] G. Nicolis and I. Prigogine, *Self-Organization in Non-Equilibrium Systems* (Wiley, New York, 1977).
[2] I. S. Aranson and L. Kramer, Rev. Mod. Phys. **74**, 99 (2002); N. Rosanov, *Spatial Hysteresis and Optical Patterns* (Springer, Berlin, 2002); *Dissipative Solitons: From Optics to Biology and Medicine*, Lecture Notes in Physics Vol. 751, edited by N. N. Akhmediev and A. Ankiewicz (Springer, Berlin, 2008).
[3] B. A. Malomed, Physica D **29**, 155 (1987); S. Fauve and O. Thual, Phys. Rev. Lett. **64**, 282 (1990); W. van Saarloos and P. C. Hohenberg, *ibid.* **64**, 749 (1990); V. Hakim, P. Jakobsen, and Y. Pomeau, Europhys. Lett. **11**, 19 (1990); B. A. Malomed and A. A. Nepomnyashchy, Phys. Rev. A **42**, 6009 (1990); A. Komarov, H. Leblond, and F. Sanchez, Phys. Rev. E **72**, 025604 (2005); J. N. Kutz, SIAM Rev. **48**, 629 (2006); W. H. Renninger, A. Chong, and F. W. Wise, Phys. Rev. A **77**, 023814 (2008); E. Ding and J. N. Kutz, J. Opt. Soc. Am. B **26**, 2290 (2009); M. Tlidi, A. G. Vladimirov, D. Pieroux, and D. Turaev, Phys. Rev. Lett. **103**, 103904 (2009); D. Mihalache, Proc. Rom. Acad. Ser. A **11**, 142 (2010); J. Jimenez, Y. Noblet, P. V. Paulau, D. Gomila, and T. Ackemann, J. Opt. **15**, 044011 (2013); C. Fernandez-Oto, M. G. Clerc, D. Escaff, and M. Tlidi, Phys. Rev. Lett. **110**, 174101 (2013).
[4] P. W. Anderson, Science **177**, 393 (1972).
[5] A. M. Turing, Philos. Trans. R. Soc. London **237**, 37 (1952).
[6] P. Tracqui, Rep. Prog. Phys. **72**, 056701 (2009); S. Kondo and T. Miura, Science **329**, 1616 (2010).
[7] M. Eiraku, N. Takata, H. Ishibashi, M. Kawada, E. Sakakura, S. Okuda, K. Sekiguchi, T. Adachi, and Y. Sasai, Nature **472**, 51 (2011).
[8] Y. S. Kivshar and G. P. Agrawal, *Optical Solitons: From Fibers to Photonic Crystals* (Academic Press, San Diego, 2003).
[9] F. T. Arecchi, S. Boccaletti, and P. L. Ramazza, Phys. Rep. **318**, 83 (1999); F. Lederer, G. I. Stegeman, D. N. Christodoulides, G. Assanto, M. Segev, and Y. Silberberg, *ibid.* **463**, 1 (2008).
[10] D. Mihalache, D. Mazilu, F. Lederer, Y. V. Kartashov, L.-C. Crasovan, L. Torner, and B. A. Malomed, Phys. Rev. Lett. **97**, 073904 (2006).
[11] V. Skarka and N. B. Aleksić, Phys. Rev. Lett. **96**, 013903 (2006).
[12] V. Skarka, N. B. Aleksić, H. Leblond, B. A. Malomed, and D. Mihalache, Phys. Rev. Lett. **105**, 213901 (2010).
[13] E. L. Falcao-Filho, C. B. de Araujo, G. Boudebs, H. Leblond, and V. Skarka, Phys. Rev. Lett. **110**, 013901 (2013).
[14] V. Skarka, N. B. Aleksić, and V. I. Berezhiani, Phys. Rev. A **81**, 045803 (2010).
[15] N. N. Akhmediev and A. Ankiewicz, *Solitons, Nonlinear Pulses and Beams* (Chapman and Hall, London, 1997).

[16] B. A. Malomed and H. G. Winful, Phys. Rev. E **53**, 5365 (1996); P. V. Paulau, *ibid.* **84**, 036213 (2011).

[17] L.-C. Crasovan, B. A. Malomed, and D. Mihalache, Phys. Rev. E **63**, 016605 (2001); V. Skarka, N. B. Aleksić, M. Derbazi, and V. I. Berezhiani, Phys. Rev. B **81**, 035202 (2010).

[18] See Supplemental Material at http://link.aps.org/supplemental/10.1103/PhysRevA.90.023845 for Movies S1–S6 which display the real dynamics of the self-organized pattern formation of four-, five-, six-, eight-, and ten-pointed stars, as well as of the double-hump structures (with the same color bars as in corresponding figures).

[19] A. S. Desyatnikov and Yu. S. Kivshar, Phys. Rev. Lett. **88**, 053901 (2002); A. S. Desyatnikov, A. A. Sukhorukov, and Y. S. Kivshar, *ibid.* **95**, 203904 (2005); V. M. Lashkin, E. A. Ostrovskaya, A. S. Desyatnikov, and Y. S. Kivshar, Phys. Rev. A **80**, 013615 (2009).

[20] H. Sakaguchi and B. A. Malomed, J. Phys. B: At. Mol. Opt. Phys. **37**, 2225 (2004).

[21] T. Y. Fan, A. Sanchez, and W. E. DeFeo, Opt. Lett. **14**, 1057 (1989); W. Koechner and M. Bass, *Solid-State Lasers: A Graduate Text* (Springer, New York, 2003).

[22] F. Salin, J. Squier, and M. Piche, Opt. Lett. **16**, 1674 (1991); X. Yan, Q. Liu, D. Wang, and M. Gong, Opt. Express **19**, 6883 (2011); Z. Xiang, D. Wang, S. Pan, Y. Dong, Z. Zhao, T. Li, J. Ge, Ch. Liu, and J. Chen, *ibid.* **19**, 21060 (2011); P. R. Battle, J. G. Wessel, and J. L. Carlsten, Phys. Rev. A **48**, 707 (1993); J. E. La Sala, D. A. G. Deacon, and J. M. J. Madey, Phys. Rev. Lett. **59**, 2047 (1987); E. E. Fill, Opt. Commun. **67**, 441 (1988).

[23] F. Salin and J. Squier, Opt. Lett. **17**, 1352 (1992).

[24] N. N. Akhmediev, V. V. Afanasjev, and J. M. Soto-Crespo, Phys. Rev. E **53**, 1190 (1996); J. Atai and B. A. Malomed, Phys. Lett. A **246**, 412 (1998); W. J. Firth and P. V. Paulau, Eur. Phys. J. D **59**, 13 (2010).

[25] D. J. Kaup and B. A. Malomed, Physica D **87**, 101 (1995).

[26] V. Skarka, D. V. Timotijević, and N. B. Aleksić, J. Opt. A: Pure Appl. Opt. **10**, 075102 (2008).

[27] B. N. Aleksić, N. B. Aleksić, V. Skarka, and M. Belić, Phys. Scr. T **149**, 014036 (2012).

[28] T. Bartels-Rausch, V. Bergeron, J. H. E. Cartwright, R. Escribano, J. L. Finney, H. Grothe, P. P. J. Gutiérrez, J. Haapala, W. F. Kuhs, J. B. C. Pettersson, S. D. Price, C. I. Sainz-Díaz, D. J. Stokes, G. Strazzulla, E. S. Thomson, H. Trinks, and N. Uras-Aytemiz, Rev. Mod. Phys. **84**, 885 (2012).

[29] B. A. Malomed, D. Mihalache, F. Wise, and L. Torner, J. Opt. B: Quantum Semiclassical Opt. **7**, R53 (2005).

[30] *Spontaneous Symmetry Breaking, Self-Trapping, and Josephson Oscillations*, edited by B. A. Malomed (Springer-Verlag, Berlin and Heildelberg, 2013).

Raman–Ramsey electromagnetically induced transparency in the configuration of counterpropagating pump and probe in vacuum Rb cell

**Ivan S. Radojičić,* Milan Radonjić, Marina M. Lekić, Zoran D. Grujić,
Dragan Lukić, and Branislav Jelenković**

Institute of Physics, University of Belgrade, Pregrevica 118, 11080 Belgrade, Serbia
**Corresponding author: ivan.radojicic@ipb.ac.rs*

Received November 19, 2014; revised January 22, 2015; accepted January 22, 2015;
posted January 22, 2015 (Doc. ID 226841); published February 13, 2015

Counterpropagating, spatially separated hollow pump and coaxial probe laser beams generate narrow Zeeman electromagnetically induced transparency (EIT) resonances in the vacuum Rb cell. The lasers are locked to D_2 line transition $F_g = 2 \rightarrow F_e = 1$ of ^{87}Rb. For the probe laser beam intensity between 0.1 and 3.0 mW/cm^2 this Ramsey-type configuration yields dual-structured resonances having a narrow peak on top of a broader pedestal. Linewidths of the narrow peak are nearly independent of the probe laser beam intensity and of the probe diameter (for diameters 0.8 and 2.7 mm), provided that the dark region between the pump and the probe beams is fixed. At the probe laser beam intensities below 0.1 mW/cm^2 Zeeman EIT is a single narrow resonance. With this geometry of laser beams, and at low probe intensity, the presence of the pump enables the probe EIT, i.e., the probe transmission becomes enhanced in a narrow spectral window. Accompanying theoretical model showed good quantitative agreement with the measurements.

OCIS codes: (270.1670) Coherent optical effects; (300.3700) Linewidth.
http://dx.doi.org/10.1364/JOSAB.32.000426

1. INTRODUCTION

Electromagnetically induced transparency (EIT) is a laser(s) transmission peak due to coherences between atomic levels induced by the same laser(s) whose transmission is monitored [1]. EIT as a quantum phenomenon has its classical analog [2]. In a typical interaction scheme, two lasers couple two hyperfine levels (hyperfine coherence) or Zeeman sublelevels (Zeeman coherence) with the common excited-state hyperfine level. Hyperfine (Zeeman) level (sublevels) are long lived and degeneracy of the ground-state angular momentum is larger or equal to that of the excited state. Alkali atoms with two long-lived hyperfine levels in the ground state, and optical transitions to excited-state hyperfine level in a suitable wavelength region are most often used in EIT experiments. Quantum EIT, the subject of this investigation, is a manifestation of the coherent superposition of Zeeman sublevels of the ground hyperfine level due to interactions with the laser field. Superposition called dark state [3–5] is decoupled from the interaction and presents foundation of EIT. EIT has gained considerable interest because of nonlinear response and steep dispersion around the atomic resonance at reduced absorption.

A method analog to the Ramsey method of separated oscillatory fields [6] can be utilized for narrowing dark resonances in alkali atoms using thermal atomic beam [7–9] or atoms contained in vacuum glass cells, by spatially separating pump and probe beams [10,11]. Ramsey-like mechanisms yield very narrow EIT resonances in alkali-metal vapor cells with buffer gas (or with antirelaxation wall coating), even with a single laser beam [12,13].

In experiments with vacuum gas cells it is necessary to apply a particular geometry of a hollow pump and a narrow coaxial probe in order to see narrow fringes on the probe EIT [14], or to implement a multizone spectroscopy like in [15]. Instead of spatially separating continuous wave pump and probe, pulses of the pump and probe were used in a Ramsey-like method for narrowing EIT by switching the laser beams on and off. Hyperfine EIT produced in the double Λ scheme with the pump and the weak probe pulse have produced high contrast, very narrow fringes (≈100 Hz) in the probe EIT in Cs buffer gas cell [16,17].

In this work we use counterpropagating pump and probe beams to study Ramsey effect on linewidths and amplitudes of the probe Zeeman EIT in Rb vacuum cell. Zeeman coherences are generated in the $F_g = 2$ hyperfine level of the ground state of ^{87}Rb by the pump beam, made in the form of a hollow cylinder. The atomic coherence is carried by the atomic thermal motion to a small-diameter probe beam that passes through the center of the hollow pump laser. There is dark region between the pump and probe beam, which we keep constant in the study. This counterpropagating geometry allows EIT with much weaker probe intensity as opposed to the copropagating pump and probe [14] due to reduced multiple scattering of pump light into the direction of the probe and toward the photodetector. Therefore in this work we cover much lower probe laser beam intensities than in [14]. Also, differently than in [14], here we investigate EIT line shapes for D_2 line of ^{87}Rb. We examine how different probe diameters, for the same dark region, change the shape of the dual-structured probe EIT resonances having a narrower central peak (due to atomic coherence coming from the pump) and a wider pedestal (due to probe beam influence). The dependence of narrow resonances as a function of the probe laser beam intensity and diameter is studied. Experimental results are compared with the detailed theoretical model based on time-dependent optical Bloch equations (OBEs). We determine the range of the probe intensity when Zeeman EIT has only narrow structure, i.e., the transmission of the probe beam becomes enhanced when the pump is turned on. EIT resonances in vacuum cells, even with the Ramsey method, are wider than EIT in buffer gas cells. However, there is an interest for narrow EIT in vacuum cells at room temperature because atomic collisions, and temperature fluctuations are reduced, which is important for EIT applications.

2. EXPERIMENTAL SETUP

The schematic of the experiment, given in Fig. 1, describes the geometry of laser beams we have used to investigate effects of spatially separating the probe and pump beam on the EIT line shapes. A large-diameter hollow pump beam and narrow coaxial probe beam counterpropagate through the Rb cell. The two beams are generated from the same external cavity diode laser (ECDL). Employing counterpropagating probe and pump beams requires precise laser frequency tuning to the optical transition; otherwise the probe and pump will not be able to interact with the same atoms (atomic velocity is not expected to change in the region between the pump and probe). The laser is locked using the Doppler free dichroic atomic laser lock (DDAVLL) technique [18] on D_2 line transition $F_g = 2 \rightarrow F_e = 1$ of ^{87}Rb, and is linearly polarized. The vacuum Rb cell, 85 mm long and of 25 mm in diameter, is kept at room temperature. The Rb cell is inside cylindrical solenoid that provides longitudinal magnetic field. The triple layers of μ-metal, around the cell, minimize effects of stray magnetic fields. In the experiment we measure the probe transmission as a function of the external magnetic field. Pump intensity is $11.5\ \mathrm{mW/cm^2}$ and the probe intensity varies from 0.1 to $3.0\ \mathrm{mW/cm^2}$.

We have measured Zeeman EIT by sweeping the magnetic field for two probe $1/e^2$ diameters, 2.7 and 0.8 mm. The pump beam inner diameter is changed from 5 to 7 mm when the probe diameter is changed from 0.8 to 2.7 mm, respectively. Thus, the distance between pump and the probe, or "dark region," is the same and equals 2.1 mm.

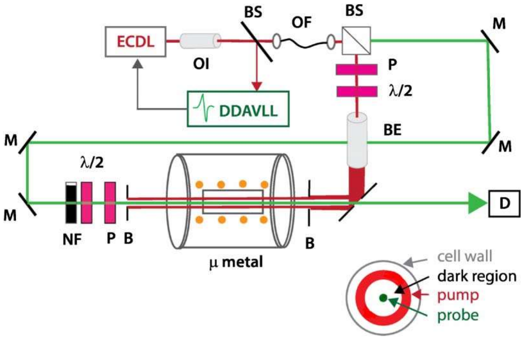

Fig. 1. Experimental setup: ECDL, external cavity diode laser; OI, optical isolator; DDAVLL, Doppler free dichroic atomic laser lock; BS, beam splitter; OF, optical fiber; M, mirrors; P, polarizer; NF, variable neutral density filter; BE, beam expander; $\lambda/2$, retardation plate; B, blade iris diaphragm; D, photodetector.

3. THEORY

The model is similar to one described in more detail in [19]. The difference stems from the fact that in this case the pump and probe are counterpropagating. The evolution of Rb atoms interacting with spatially separated pump and probe laser beams is described using time-dependent OBEs for the atomic density matrix

$$\frac{d\hat{\rho}}{dt} = -\frac{i}{\hbar}[\hat{H}_{\mathrm{atom}}(B) + \hat{H}_{\mathrm{int}}(t), \hat{\rho}] + \left(\frac{d\hat{\rho}}{dt}\right)_{\mathrm{SE}} + \left(\frac{d\hat{\rho}}{dt}\right)_{\mathrm{relax}}, \quad (1)$$

where

$$\hat{H}_{\mathrm{atom}}(B) = \sum_j \hbar\omega_j(B)|g_j\rangle\langle g_j| + \sum_k \hbar\omega_k(B)|e_k\rangle\langle e_k| \quad (2)$$

is the Hamiltonian of an atom in the external magnetic field **B**, aligned with the laser beam propagation direction. Zeeman-shifted energies $\hbar\omega_j(B)$ ($\hbar\omega_k(B)$) correspond to ground (excited) states $|g_j\rangle$ ($|e_k\rangle$). The interaction of an atom with laser is treated in dipole approximation

$$\hat{H}_{\mathrm{int}}(t) = -\sum_{j,k} \mathbf{E}(t) \cdot \mathbf{d}_{jk}(|g_j\rangle\langle e_k| + |e_k\rangle\langle g_j|), \quad (3)$$

where $\mathbf{E}(t)$ is the laser electric field (in the atomic reference frame) and $\mathbf{d}_{jk}$ is the atomic electric dipole moment for the transition between states $|g_j\rangle$ and $|e_k\rangle$. Spontaneous emission is given by

$$\left(\frac{d\hat{\rho}}{dt}\right)_{\mathrm{SE}} = \sum_m 2\hat{\Gamma}_m\hat{\rho}\hat{\Gamma}_m^\dagger - \hat{\Gamma}_m^\dagger\hat{\Gamma}_m\hat{\rho} - \hat{\rho}\hat{\Gamma}_m^\dagger\hat{\Gamma}_m, \quad (4)$$

where $\hat{\Gamma}_m$ are Lindblad operators related to dipole transitions from the excited- to ground-state manifold. In order to obtain good agreement with experimental line shapes, and in addition to [19], we include relaxation of ground-state populations toward the equilibrium

$$\left(\frac{d\hat{\rho}}{dt}\right)_{\mathrm{relax}} = -\gamma\sum_j\left(\rho_{g_j,g_j} - \frac{1-\pi_e}{8}\right)|g_j\rangle\langle g_j|, \quad (5)$$

where π_e is the total excited-state population. When considering D_2 line transition $F_g = 2 \rightarrow F_e = 1$, the excited hyperfine levels $F_e = 2$ and $F_e = 3$ are also populated due to the Doppler broadening and therefore have to be taken into account. Equations for $F_g = 1$ ground-level density matrix elements are disregarded since that level is not laser-coupled. OBEs are numerically integrated for a collection of atoms passing through the laser beams at different trajectories with velocities sampling Maxwell–Boltzmann distribution. The cylindrical symmetric atomic ensemble density matrix is obtained after averaging over velocities and suitable angular integration. This enables the calculation of atomic vapor polarization, the laser electric field after propagation through the Rb cell and, eventually, Zeeman EIT resonances. Additional details can be found in [20,21].

Pump and probe laser beams have linear polarization and the same frequency. Their propagation directions are

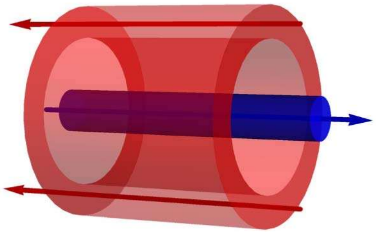

Fig. 2. Radial profiles of counterpropagating hollow pump and coaxial probe laser beams used in the theoretical model.

opposite. As schematically presented in Fig. 2, the probe laser beam passes coaxially through the center of the hollow pump beam. The probe beam profile along radial distance r at the Rb cell entrance is modeled by a Gaussian,

$$I_{\text{probe}}(r) = 2\bar{I}_{\text{probe}} \exp(-2r^2/r_0^2), \tag{6}$$

where r_0 is $1/e^2$ the radius of the probe beam and $\bar{I}_{\text{probe}}$ is the probe beam intensity (total probe power divided by $r_0^2\pi$). The pump beam radial intensity profile is taken to be the same along the cell length and ring-shaped:

$$I_{\text{pump}}(r) = \bar{I}_{\text{pump}} a(\operatorname{erf}(p(r-r_1)) - \operatorname{erf}(p(r-r_2))), \tag{7}$$

where $\bar{I}_{\text{pump}}$ is the pump beam intensity and a is the normalization constant. Parameter p controls the steepness of the profile near the beam inner and outer edge that are determined by the parameters r_1 and r_2, respectively.

4. RESULTS AND DISCUSSION

We show results of interactions of the probe beam with atoms prepared in the dark state by the spatially separated pump beam. Both the pump and probe have linear and mutually parallel polarizations. Sweep of the magnetic field provides detuning of two circular components from the two photon resonance among Zeeman sublevels for which $\Delta m_F = 2$. In the following we present EIT line shapes, amplitudes, and linewidths obtained by measuring the probe transmission at different magnetic fields. In this work we are not concerned with absolute values of the probe transmission. Therefore, we present EIT line shapes normalized such that maximal transmission is set to unity.

Figure 3(a) shows measured and Fig. 3(b) calculated Zeeman EIT resonances for two probe laser beam intensities, 0.2 mW/cm^2 (upper rows) and 1.4 mW/cm^2 (lower rows), and two probe laser beam diameters, 0.8 mm (left column) and 2.7 mm (right column). EIT line shapes for both laser beam intensities have dual structure, a narrow peak with fringes appearing on top of a broader pedestal. A broader pedestal is generated by the probe itself, while narrow peak and fringes result from Ramsey interference. Ramsey fringes are well pronounced for the narrower probe beam because of the shorter interaction time of Rb atoms with the probe light, i.e., smaller probe influence. When the probe laser beam intensity is increased, or its diameter is increased, the Ramsey fringes lose their visibility. Theoretical results in Fig. 3(b) are in quite good agreement with the experiment.

EIT widths and amplitudes of the narrow and wide structures are obtained after resolving the two structures in EIT line shapes. Figure 4 presents widths of the narrow structure

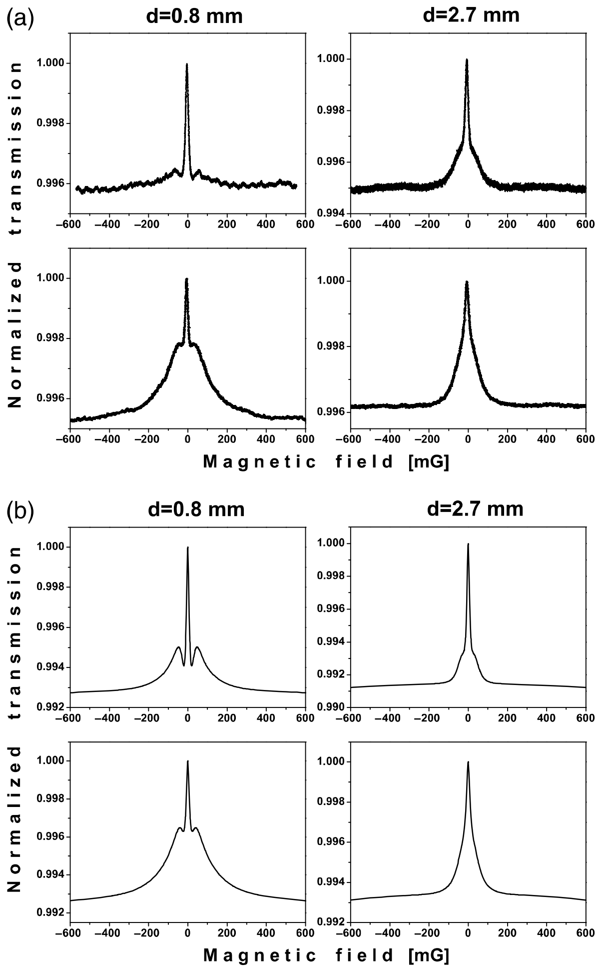

Fig. 3. (a) Experimental and (b) theoretical Zeeman EIT at D_2 line, for two probe laser beam intensities, 0.2 mW/cm^2 (upper rows) and 1.4 mW/cm^2 (lower rows), and two probe laser beam diameters, 0.8 mm (left column) and 2.7 mm (right column).

of EIT resonances, for two probe laser beam diameters. Experimental results are in Fig. 4(a), and theoretical in Fig. 4(b). The linewidth of the narrow structure in our experiment is ≈15 mG or ≈18 kHz. This is similar to the narrowest EIT obtained in vacuum alkali gas cells with multizone Ramsey technique [15]. As seen from Fig. 4, the narrow structure EIT linewidth is narrower and also more robust against probe intensity for the narrower probe beam. The behavior of the pedestal width is as expected for a single beam EIT [22]: it is narrower for the wider probe, and it changes much more rapidly with the probe laser beam intensity. Calculated linewidths follow the same trend and the narrower probe beam also gives narrower linewidth.

In the experiment with a single laser beam and coated cell [13], EIT has also dual structure. Similar to our result, narrow structure of EIT in [13] is narrower for the smaller laser beam diameter. Moreover, intensity dependence of the linewidths of the narrower peak is similar as in our setup: EIT linewidth obtained with the narrower beam is less dependent on the laser intensity. Such intensity dependence given in [13] is due to the geometry of the cell and the Ramsey effect of a multiple interaction of atoms with the same laser beam—narrowing the laser increases the dark region, i.e., time that the atom spends in the dark. The similar behavior of the

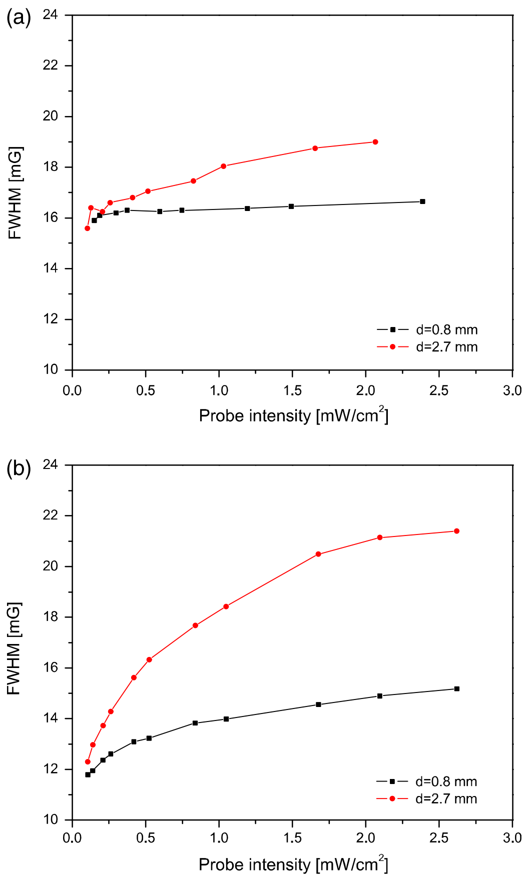

Fig. 4. (a) Experimental and (b) theoretical full width at half-maximum of the narrow structure of EIT as a function of the probe laser beam intensity, for two probe laser beam diameters, 0.8 and 2.7 mm.

narrow peak of the EIT in our work has a different explanation. The probe laser beam, apart from probing the atoms coherently prepared in the pump beam, influences the atomic evolution, which affects the narrow structure linewidth. During atomic passage through the laser beams the atomic state changes due to competitive effects of the laser electric field and the external magnetic field. The laser field continuously prepares the atoms into the dark state. The external magnetic field causes oscillations of the atomic ground-state coherences at the corresponding Larmor frequency and alters the atoms from the dark state. When the external magnetic field is zero the atoms reach the dark state inside the strong pump beam, which consequently leads to a maximum in the probe transmission. At nonzero magnetic field the state of the atoms passing through the probe beam differs from the dark state, so that the probe transmission decreases. However, this decrease in probe transmission due to the influence of the magnetic field is partially compensated by preparation of the atoms into the dark state within the probe beam. Hence, the actual probe transmission at some magnetic field is somewhat larger than the one expected without the probe influence. This causes broadening of the narrow structure in Zeeman EIT resonances that becomes more pronounced as the probe intensity and/or diameter increases.

Figure 5 shows measured and calculated amplitudes of the narrow structure of EIT resonances, for probe laser beam diameters 0.8 mm [Fig. 5(a)] and 2.6 mm [Fig. 5(b)]. As both

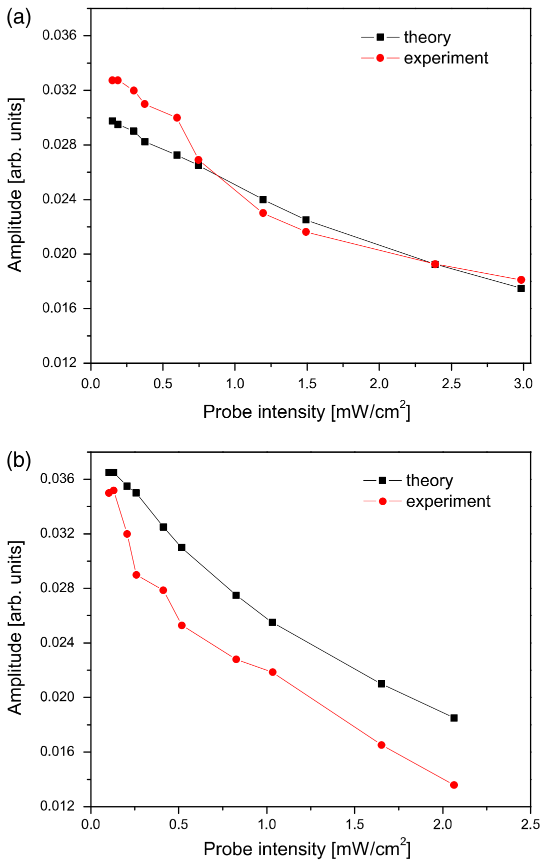

Fig. 5. Experimental and theoretical results for the amplitudes of the narrow structure of EIT resonances for two probe laser beam diameters: (a) 0.8 mm and (b) 2.7 mm.

experiment and theory show, amplitudes of narrow peaks of the probe EIT are nearly independent on probe beam diameter. Their dependence on the probe intensity and diameter is different than the amplitude of the wide structure EIT.

Amplitudes of the narrow peak of the probe EIT (obtained when the pump laser beam is turned on) have different dependence on the probe laser beam intensity than a single beam EIT, tuned to the same Raman resonance and with the same diameter. This is demonstrated in Fig. 6 where we plot amplitudes of both narrow and wide structure as a

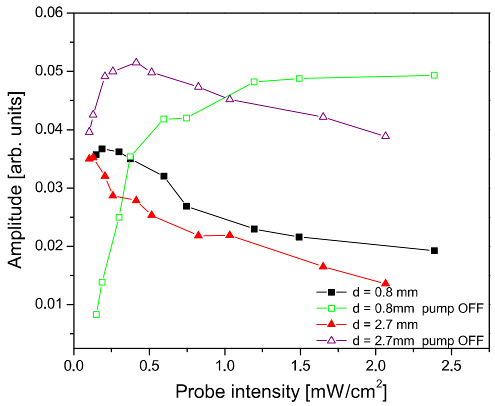

Fig. 6. Amplitudes of the probe EIT with and without pump laser beam, for two probe laser beam diameters: 0.8 and 2.7 mm. Amplitudes of wide (narrow) structures are shown for the pump laser beam turned off (on).

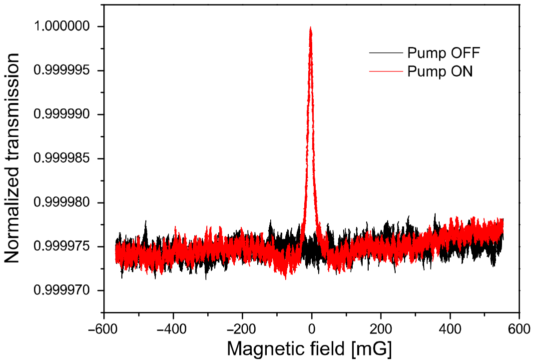

Fig. 7. Probe beam Zeeman EIT at D_2 line, with and without the pump beam. Intensities of the probe and pump beams are $0.1\ \mathrm{mW/cm^2}$ and $11.5\ \mathrm{mW/cm^2}$, respectively.

function of probe intensity, for two probe diameters. The maximum of the narrow structure of the probe EIT in the Raman–Ramsey configuration is at very low laser intensities, below values that we can detect in the experiment.

At very low probe laser beam intensities, below $0.1\ \mathrm{mW/cm^2}$, the probe EIT has only narrow structure. The transmission of the weak probe can be controlled in a narrow spectral range around zero magnetic field by switching the pump beam on/off. For small magnetic fields and when the pump laser beam is present, the atoms coming into the probe beam are already coherently prepared into the dark state. This leads to the increase of the probe transmission, as presented in Fig. 7, where we show probe EIT for 0.8 mm probe beam diameter and for probe beam intensity of $0.1\ \mathrm{mW/cm^2}$, without or with pump beam of intensity $11.5\ \mathrm{mW/cm^2}$. Enhancement of the probe transmission is better for larger pump beam intensities.

5. CONCLUSION

We presented effects of the counterpropagating spatially separated pump and probe laser beam configuration on the probe Zeeman EIT. Both pump and probe beams are tuned to the D_2 line of ^{87}Rb. For the geometry of the experiment, with the probe coaxial with the surrounding hollow pump and small dark region between the pump and probe, we showed that in the vacuum cell, like in cells with antirelaxation coating, resonances can be narrower when the probe diameter is smaller. For the probe of 0.8 mm in diameter we observed and calculated narrower linewidths, almost independent of the probe laser beam intensity. Also, for this small probe diameter, when its intensity is below $0.1\ \mathrm{mW/cm^2}$, dual structure of Zeeman EIT turns in to a single narrow EIT. Probe transmission is enhanced in a narrow range of small magnetic fields when the pump laser beam is present, which is akin to optical switch behavior.

ACKNOWLEDGMENTS

This work was supported by the Ministry of Education and Science of Serbia, under grants III45016 and OI171038, and also by SCOPES JRP IZ73Z0_127942.

REFERENCES

1. S. E. Harris, “Electromagnetically induced transparency,” Phys. Today **50**(7), 36–42 (1997).
2. C. L. Garrido Alzar, M. A. G. Martinez, and P. Nussenzveig, “Classical analog of electromagnetically induced transparency,” Am. J. Phys. **70**, 37–42 (2002).
3. G. Alzetta, A. Gozzini, L. Moi, and G. Orriols, “An experimental method for the observation of r.f. transitions and laser beat resonances in oriented Na vapour,” Nuovo Cimento B **36**, 5–20 (1976).
4. E. Arimondo and G. Orriols, “Nonabsorbing atomic coherences by coherent two-photon transitions in a three-level optical pumping,” Lett. Nuovo Cimento Soc. Ital. Fis. **17**, 333–338 (1976).
5. F. Renzoni, W. Maichen, L. Windholz, and E. Arimondo, “Coherent population trapping with losses observed on the Hanle effect of the D_1 sodium line,” Phys. Rev. A **55**, 3710–3718 (1997).
6. N. F. Ramsey, *Molecular Beams* (Oxford University, 1956).
7. B. Schuh, S. I. Kanorsky, A. Weis, and T. W. Hänsch, “Observation of Ramsey fringes in nonlinear Faraday rotation,” Opt. Commun. **100**, 451–455 (1993).
8. J. E. Thomas, P. R. Hemmer, S. Ezekiel, C. C. Leiby, Jr., R. H. Picard, and C. R. Willis, “Observation of Ramsey fringes using a stimulated, resonance Raman transition in a sodium atomic beam,” Phys. Rev. Lett. **48**, 867–870 (1982).
9. G. Theobald, V. Giordano, N. Dimatcq, and P. Cerez, “Observation of narrow Ramsey-type resonances in a caesium beam due to Zeeman coherences,” J. Phys. B **24**, 2957–2966 (1991).
10. S. Nakayama, G. W. Series, and W. Gawlik, “Larmor precession in polarization spectroscopy with spatially separated beams,” Opt. Commun. **34**, 389–392 (1980).
11. A. S. Zibrov and A. B. Matsko, “Optical Ramsey fringes induced by Zeeman coherence,” Phys. Rev. A **65**, 013814 (2001).
12. Y. Xiao, I. Novikova, D. F. Phillips, and R. L. Walsworth, “Diffusion-induced Ramsey narrowing,” Phys. Rev. Lett. **96**, 043601 (2006).
13. M. Klein, M. Hohensee, D. F. Phillips, and R. L. Walsworth, “Electromagnetically induced transparency in paraffin-coated vapor cells,” Phys. Rev. A **83**, 013826 (2011).
14. Z. D. Grujić, M. Mijailović, D. Arsenović, A. Kovačević, M. Nikolić, and B. M. Jelenković, “Dark Raman resonances due to Ramsey interference in vacuum vapor cells,” Phys. Rev. A **78**, 063816 (2008).
15. H. Failache, L. Lenci, and A. Lezama, “Raman-Ramsey multizone spectroscopy in a pure rubidium vapor cell,” Phys. Rev. A **81**, 023801 (2010).
16. T. Zanon, S. Guerandel, E. de Clercq, D. Holleville, N. Dimarcq, and A. Clairon, “High contrast Ramsey fringes with coherent-population-trapping pulses in a double lambda atomic system,” Phys. Rev. Lett. **94**, 193002 (2005).
17. X. Liu, J.-M. Mérolla, S. Guérandel, E. de Clercq, and R. Boudot, “Ramsey spectroscopy of high-contrast CPT resonances with push-pull optical pumping in Cs vapor,” Opt. Express **21**, 12451 (2013).
18. K. L. Corwin, Z. Lu, C. F. Hand, R. J. Epstein, and C. E. Wieman, “Frequency-stabilized diode laser with the Zeeman shift in an atomic vapor,” Appl. Opt. **37**, 3295–3298 (1998).
19. Z. D. Grujić, M. Lekić, M. Radonjić, D. Arsenović, and B. M. Jelenković, “Ramsey effects in coherent resonances at closed transition $F_g = 2 \rightarrow F_e = 3$ of ^{87}Rb,” J. Phys. B **45**, 245502 (2012).
20. M. Radonjić, D. Arsenović, Z. Grujić, and B. M. Jelenković, “Coherent population trapping linewidths for open transitions: cases of different transverse laser intensity distribution,” Phys. Rev. A **79**, 023805 (2009).
21. A. J. Krmpot, M. Radonjić, S. M. Ćuk, S. N. Nikolić, Z. D. Grujić, and B. M. Jelenković, “Evolution of dark state of an open atomic system in constant intensity laser field,” Phys. Rev. A **84**, 043844 (2011).
22. E. Figueroa, F. Vewinger, J. Appel, and A. I. Lvovsky, “Decoherence of electromagnetically induced transparency in atomic vapor,” Opt. Lett. **31**, 2625–2627 (2006).

Materials Research Bulletin 83 (2016) 284–289

Contents lists available at ScienceDirect

Materials Research Bulletin

journal homepage: www.elsevier.com/locate/matresbu

Influence of femtosecond pulsed laser irradiation on bismuth germanium oxide single crystal properties

Aleksander Kovačević[a], Jasna L. Ristić-Djurović[a,*], Marina Lekić[a], Branka Hadžić[a], Giuma Saleh Isa Abudagel[b], Slobodan Petričević[b], Pedja Mihailović[b], Branko Matović[c], Dragan Dramlić[a], Ljiljana M. Brajović[d], Nebojša Romčević[a]

[a] Institute of Physics, University of Belgrade, Pregrevica 118, 11080 Belgrade, Serbia
[b] School of Electrical Engineering, University of Belgrade, Bulevar kralja Aleksandra 73, 11000 Belgrade, Serbia
[c] Vinča Institute of Nuclear Sciences, University of Belgrade, P.O. Box 522, 11000 Belgrade, Serbia
[d] Faculty of Civil Engineering, University of Belgrade, Bulevar kralja Aleksandra 73, 11000 Belgrade, Serbia

ARTICLE INFO

Article history:
Received 5 December 2015
Received in revised form 16 May 2016
Accepted 12 June 2016
Available online 14 June 2016

Keywords:
A. Optical materials
B. Laser annealing
C. Raman spectroscopy
D. Optical properties
D. Color centers

ABSTRACT

High quality bismuth germanium oxide single crystals were irradiated by a femtosecond pulsed laser beam of increasing power. Analyses performed on irradiated and unirradiated samples showed significant changes in transmittance, transmission spectra, sample color, Raman spectra, X-ray diffraction (XRD) pattern, Verdet constant, magneto-optical property, and absorption coefficient. After irradiation, the transmission spectra values increased whereas anisotropy detected in the transmission spectra of unirradiated samples disappeared. The change of color caused by irradiation was noticeable to the naked eye. The XRD measurements confirmed structural changes induced by laser irradiation, i.e., the laser-beam-incident side of the sample became almost amorphous, whereas the side opposite to the incident can be indexed to the $Bi_{12}GeO_{20}$ compound. Irradiation caused increase of Raman spectra peaks with the exception of crystal peaks of type E, which disappeared. The femtosecond pulsed laser irradiation can be used to improve bismuth germanium oxide single crystal optical properties.

1. Introduction

Bismuth germanium oxide ($Bi_{12}GeO_{20}$), commonly abbreviated as BGO, or more specifically as s-BGO, belongs to the sillenite group of cubic crystals of the $I23$ space group. The chemical formula of cubic crystals with the sillenite-type structure is $Bi_{12}M^{n+}O_{20\pm d}$ where M may be an element from the II–V group of the Periodic Table or a combination of such elements [1–3]. Analysis of the experimental data on the component interaction and the phase equilibrium in the Bi_2O_3-M_xO_y systems revealed the possibility to achieve phases of the sillenite-type structure with oxides of Rb, Mg, Zn, Cd, B, Al, Ga, In, Tl, Si, Ge, Ti, Pb, P, V, As, Nb, Cr, Mo, W, Fe, Co, Ni, Ru, and Ir [4]. In [2], the atomic structure of $Bi_{12}M^{n+}O_{20\pm\delta}$ was discussed in detail for $Bi_{12}M^{4+}O_{20}$ (M = Si, Ge, Ti, Mn), $Bi_{12}(A^{3+}_{1/2}B^{5+}_{1/2})O_{20}$ (A = Fe, B = P), $Bi_{12}M^{2+}O_{20}$ (M = Zn, Co), $Bi_{12}M^{3+}O_{20}$ (M = Al, Ga, Fe, Tl), $Bi_{38}B_2O_{39}$, γ–Bi_2O_3, and $Bi_{12}VO_{20\pm\delta}$. A more recent study of sillenites $Bi_{12}SiO_{20}$, $Bi_{25}FeO_{39}$, and $Bi_{25}InO_{30}$ gave a representative sillenite structure using Si^{4+}, Ti^{4+}, Fe^{3+}, and In^{3+} as examples for M cation [5] and refered to [6] for more details about the sillenite structure. In [6], a general structural formula for the stoichiometric sillenites, $Bi_{12}(Bi_{4/5-nx}M^{n+}_{5x})O_{19.2+nx}$, was developed and discussed in detail for sillenites with M^{2+} ions (Cd, Co, Zn), M^{3+} ions (Ga, Fe, Cr, Tl, In, Al), M^{4+} ions (Si, Ti, Ge, Mn, $B_{1/2}P_{1/2}$), and M^{5+} ions (V, As, P).

For BGO, BSO, and BTO crystals the structural formula becomes $Bi_{12}MO_{20}$, where M is Ge, Si, and Ti, respectively. The cubic cell unit of $Bi_{12}GeO_{20}$ is composed of two formula units, namely 24 Bi, 40 O and 2 Ge. The Ge atoms occupy the center and the vertices of a cube and are tetrahedrally coordinated by oxygen atoms. The Bi atoms, due to their massiveness, constitute the core of the cell, they are heptacoordinated as BiO_5E, where $E = 6s^2$ is the non-shared electron pair in Bi, and the common edges form dimers. The five oxygen atoms compose an incomplete octahedral arrangement and the remaining two oxygen atoms are electrostatically coordinated on a side of E [1,3]. Due to its photoconductivity,

---

* Corresponding author.
E-mail addresses: aleksander.kovacevic@ipb.ac.rs (A. Kovačević), jasna@stanfordalumni.org (J.L. Ristić-Djurović), marina.lekic@ipb.ac.rs (M. Lekić), branka.hadzic@ipb.ac.rs (B. Hadžić), giuma05@yahoo.com (G.S.I. Abudagel), slobodan@etf.bg.ac.rs (S. Petričević), pedja@etf.bg.ac.rs (P. Mihailović), mato@vinca.rs (B. Matović), dragan.dramlic@ipb.ac.rs (D. Dramlić), aleksander.kovacevic@ipb.ac.rs (L.M. Brajović), aleksander.kovacevic@ipb.ac.rs (N. Romčević).

http://dx.doi.org/10.1016/j.materresbull.2016.06.023
0025-5408/

photochromism, photorefractivity, piezoelectricity, as well as to electro-optic and magneto-optic effects it supports [7,8], $Bi_{12}GeO_{20}$ is suitable for a broad range of applications and devices such as optical limiting, holography, spatial light modulation, optical phase conjugation, optical memories, fiber optic sensors, Pockels cells [8–12]. The properties of non-doped as well as doped $Bi_{12}GeO_{20}$ were investigated and reported in a number of studies, for example in [13–21]. Characteristics of $Bi_{12}GeO_{20}$ single crystals after exposure to thermal treatment [16–19,22], to beams of electrons [23], uranium ions [24], fluorine ions [15], γ-ray [19] or light [9,18,22,25–28] were investigated. Nonlinear properties of $Bi_{12}GeO_{20}$ crystals were measured with pulsed laser beams in the nanosecond range in [9], whereas in [26–28] BGO crystals were irradiated by picosecond laser pulses. Transmission, absorption [16,19], and Raman spectra [19] were found to be significantly influenced by doping and annealing. Thermally stimulated currents as a function of both the temperature at which the crystals are photoexcited and the density of energy used to photoexcite them were reported in [18]. Influences of laser irradiation, thermal treatment [22], and electron beam [23] on luminescence of $Bi_{12}GeO_{20}$ are reported. Photo-induced absorption in $Bi_{12}TiO_{20}$ was thoroughly studied in [29], whereas significant influence of doping and annealing on transmission and absorption of BGO were addressed in [16] and [19]. However, to the best of our knowledge, photo-induced increase in BGO transmission has not been reported so far. Therefore, following the determination of magneto-optical quality and refractive index of BGO single crystals presented in [20], we studied the influence of the femtosecond laser irradiation on $Bi_{12}GeO_{20}$ single crystals. The irradiation caused permanent changes visible to the naked eye, as can be seen in Fig. 1. In order to quantitatively define visually observed changes, we measured the transmittance, transmission spectra, color, Raman spectra, X-ray diffraction patterns, Verdet constant, absorption coefficient, and magneto-optical quality of $Bi_{12}GeO_{20}$ single crystals.

2. Experimental

2.1. Preparation of crystal samples

Single crystals of $Bi_{12}GeO_{20}$ with diameters of 12–13 mm and length of 70–80 mm were grown by the Czochralski technique. As explained in detail in [20], the critical crystal diameter and critical rotation rate were calculated to be 12 mm and 20 rpm, respectively, whereas the pulling rate was determined experimentally to be 2.8–3 mm/h. The crystal puller MSR 2 combined with the Eurotherm temperature controller was used to grow the crystals. The crystal diameter size was controlled by monitoring the crucible weight, and its deviation from the chosen value was kept below 0.1 mm. The system as a whole provided protection from excessive radiative heat losses and granted melting temperature fluctuations typically smaller than 0.2 °C. The crystals were grown in the air, without crucible rotation during the growth, using the $Bi_{12}GeO_{20}$ seed oriented in the $\langle 111 \rangle$ direction, and a mixture of Bi_2O_3 and GeO_2 in the stoichiometric ratio 6:1 as a charge. After its growth, the crystal boule was cooled to room temperature at the rate of approximately 50 °C/h. The crystals were not annealed after the growth. Crystal samples of size 4 mm × 4 mm × 10 mm were cut from the boule and mechanically as well as chemically polished. The crystal samples were chemically etched using the solutions HF + HNO_3 in the ratio 2:1, HCl + H_2O in the ratio 1:2, and HCl + H_2O in the ratio 1:5, whereas chemical polishing was performed with the solution HCl + HNO_3 + H_2O in the ratio 1:1:5. Observance of the polished crystal surfaces under polarized light confirmed the absence of the core. The purity of Bi_2O_3 and GeO_2 was 99.5 wt.% and 99.98 wt.%, respectively. The technique used to prepare the samples insured maximal sample quality within the limits corresponding to their purity [20].

2.2. Crystal irradiation and characterization

Crystal samples were exposed to a femtosecond laser irradiation of increasing power. The femtosecond pulsed laser beam was produced with the Coherent Mira 900 F femtosecond laser using as an input a 532 nm continuous wave pump beam obtained with the Coherent Verdi V-10 pump laser, Fig. 2. The irradiating beam wavelength of 800 nm was determined with the spectrometer Ocean Optics HR2000CG UV-NIR. Crystal samples were irradiated along their longest axis, z, i.e., along the crystal growth direction. The beam radius provided partial irradiation of the exposed crystal facet. The beam power on a sample was adjusted by a graded filter and was increased from 50 mW to 950 mW, which corresponds to the fluence range of 75–1425 nJ/cm^2. The samples were irradiated by each beam power for 3 s, which was measured by a stopwatch with 0.2 s accuracy. The repetition rate of 90 fs long laser pulses was 76 MHz. The total irradiation time and energy were intentionally kept low to avoid significant contribution of an accumulative process caused by repopulation of the traps [28]. The Ophir powermeter with thermal and photometric heads was used to perform beam power measurements.

Sample transmittance in the wavelength range between 200 and 1100 nm with the resolution of 1 nm was determined in the spectrometric device Beckman Coulter DU 720 General Purpose UV/VIS spectrometer. The obtained transmission spectra were used to calculate sample color, as well.

The X-ray diffraction patterns were measured with the Rigaku Ultima IV Multipurpose X-ray diffraction system. The system was operated at 40 kV and 40 mA to produce nickel-filtered Cu$K\alpha_1$ X-ray with $\lambda = 0.1540$ nm. The XRD data were collected in the 2θ

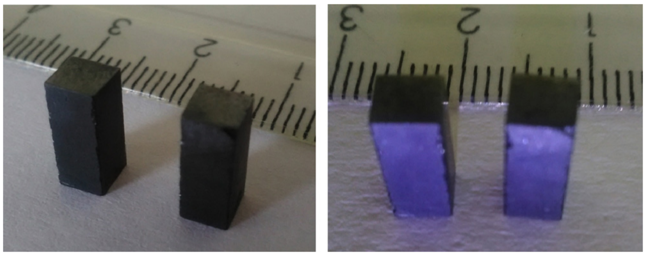

Fig. 1. Photographs of unirradiated and laser irradiated samples. The photographs are taken without (left) and with (right) a flash. In each photo the irradiated sample is placed to the right. The femtosecond laser irradiation was incident to the upper base of the prism. The visible laser induced changes span to approximately one quarter into the sample depth.

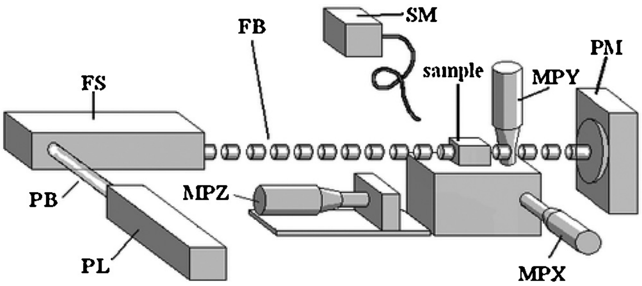

Fig. 2. Experimental setup for sample irradiation and power transmission measurements. PL – pump laser, PB – pump beam, FS – femtosecond laser, FB – femtosecond beam, MPX, MPY, MPZ – micro-positioners in x, y, and z direction respectively, SM – spectrometer, PM – powermeter.

range between 20 and 70° at the scanning rate of 5°/min. The phase analysis was performed using the PDXL2 software, version 2.0.3.0 [30], with reference to the patterns of the International Centre for Diffraction Database (ICDD), version 2012 [31].

Using the backscattering configuration and the 532 nm line of Verdi G optically pumped semiconductor laser as an excitation source, the micro-Raman spectra of crystal samples were obtained with the Jobin Yvon T64000 spectrometer, which has nitrogen cooled charge-coupled-device detector. The spectra were recorded at room temperature in the spectral range between 100 and 1100 cm^{-1} with 1 cm^{-1} resolution.

Optical activity and Faraday rotation were measured at the wavelength of 632.8 nm by an orthogonal polarization detection polarimetric method described in detail in [20]. Output signal voltages U_1 and U_2, obtained respectively from vertically and horizontally polarized component of the laser beam transmitted by the $Bi_{12}GeO_{20}$ crystal sample, after transimpedance stages are

$$U_1 = \frac{k_1\Gamma_0}{2}(1+\sin(2\theta)),\ U_2 = \frac{k_2\Gamma_0}{2}(1-\sin(2\theta)),$$

where Γ_0 is the beam irradiation, k_1 and k_2 are constants that include optical losses and optoelectronic conversion efficiency. The linear polarization rotation angle θ was determined using the difference over sum method that is independent of light source fluctuations. Use of the birefringent crystal instead of polarizing prism led to parallelism of separate optical paths that allowed employment of quadrant photodiode and further enabled matching of optoelectronic conversion gains as much as possible. Setting $k_1 = k_2$, the angle θ can be calculated as

$$\theta = \frac{1}{2}\sin^{-1}\left(\frac{U_1-U_2}{U_1+U_2}\right).$$

In the absence of magnetic field component parallel to the laser beam, the angle $\theta = \theta_0$ represents the optical activity. When $Bi_{12}GeO_{20}$ crystal sample is placed in a magnetic field generated by an alternating current through the Helmholtz coils, the angle θ becomes the sum of the optical activity and Faraday rotation, and can be used to calculate the Verdet constant [32]. The Hall probe was used to measure magnetic induction and to establish its linear relation to the coil current, namely

$$B[T] = 0.001282 \times I[A]$$

The Verdet constant is calculated from

$$V = \frac{\theta_{0AC}}{B_0 l} = \frac{1}{2B_0 l}sin^{-1}\left(\frac{U_1-U_2}{U_1+U_2}\right)_{0AC},$$

where θ_{0AC} is the amplitude of the AC signal and B_0 is the amplitude of magnetic induction. The coils were powered by a 50 Hz sine wave constant amplitude current that creates magnetic induction of the same frequency. Consequently, FFT was used to separate spectral components of U_1 and U_2. The Faraday rotation was determined from the magnitude of 50 Hz component.

Bulk absorption measurement was normalized using the reference beam created by the $CaCO_3$ birefringent crystal that was used for beam separation. Absorption coefficients were obtained by measuring the difference in beam intensities at the quadrant photodiode with and without $Bi_{12}GeO_{20}$ crystal in the beam path. Background light influence was eliminated by measuring the photodiode output without the laser beam and subtracting it from the two previous measurements.

3. Results and discussion

The change of sample transmittance with the increase of irradiating laser power for the two considered crystal samples is shown in Fig. 3. The error bars were calculated from the uncertainties of measured values of the incident and transmitted power, ΔP_0 and ΔP_1. The transmittance generally undergoes initial growth followed by a decrease. The maximal transmittance of 25.1% occurs at the irradiating laser power of 455 mW. It seems that curve exhibits local irregularities which occur at 197.4–249.7 mW, 552–605 mW and 800–857 mW. Similarly to our findings about transmittance dependence on the irradiating laser power, initial growth followed by a decrease in transmittance is found to be an outcome of annealing, as well [16]. Skorikov et al. in [16] reported that annealing of $Bi_{12}SiO_{20}$, $Bi_{12}GeO_{20}$, and $Bi_{12}TiO_{20}$ crystals in vacuum or inert atmosphere at 500–750 °C for 2–12 h typically raises the transmittance near the intrinsic edge and observed the most pronounced effect for $Bi_{12}SiO_{20}$ annealed at 650 °C for 2 h. Increase in temperature and/or annealing time was found to be associated with a decrease in transmittance to its initial or an even lower level, particularly in $Bi_{12}GeO_{20}$ and $Bi_{12}SiO_{20}$.

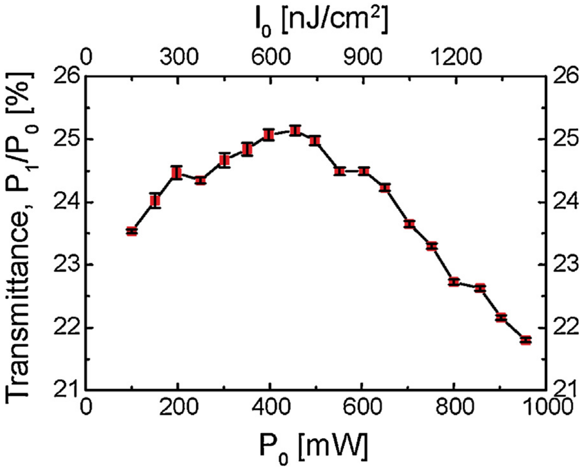

Fig. 3. Change of crystal transmittance during increase of irradiating laser power. Each data point corresponds to a 3 s long sample irradiation by the femtosecond laser beam with the incident power P_0, given in the bottom axis, and the corresponding incident fluence, I_0, depicted in the top axis. The transmittance is given as P_1/P_0, where P_1 is the transmitted power. The irradiating beam wavelength was 800 nm.

Transmission spectra of samples were determined along both directions of the longest sample axis and are shown in Fig. 4. In addition to the treated samples, i.e., the samples irradiated by the femtosecond laser beam of increasing power, the unirradiated samples were examined, as well. The unirradiated crystal exhibits

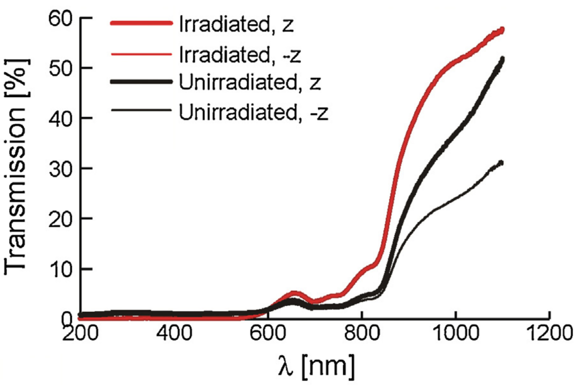

Fig. 4. Transmission spectra of irradiated and unirradiated samples. The transmission spectra of all samples were measured in the direction of crystal growth as well as in the direction opposite to it. The unirradiated sample exhibits significant anisotropy, which disappears after irradiation. Irradiation also causes transmission increase.

noticeable anisotropy. The transmissions of the crystal have small irregularities, which are probably caused by impurities, at 655 nm and 800 nm and a steep growth after 850 nm. For the unirradiated crystal the transmission corresponding to the *z* direction is larger than the one in the $-z$ direction. For wavelengths larger than 1000 nm the transmission is larger than 37 % and 24 % in the *z* and $-z$ direction, respectively. After irradiation the anisotropy disappeared, and the transmission of the crystal increased becoming larger than 51 % for wavelengths above 1000 nm. Measurements repeated after prolonged period of time confirmed full reproducibility of the obtained results and verified that the detected light-induced changes are permanent.

Our results are in agreement with the conclusion given in [16] that doping as well as annealing has significant effect on transmission and absorption spectra. They found that annealing at 650 °C for 12 h and at 740 °C for 2 h each cause decrease of absorption spectra throughout the considered range of 300–900 nm, when compared to the absorption spectrum of non-annealed $Bi_{12}GeO_{20}$ crystal. However, after absorption decrease in the low-wavelength range, annealing at 650 °C and 700 °C for 2 h resulted in local absorption minimum at approximately 450 nm and local maximum around 530 nm, followed by the absorption values somewhat larger than those of non-annealed case for wavelengths larger than 530 nm. The absorption spectra of untreated, annealed in N_2 for 8 h at 450 °C and 550 °C, γ-ray irradiated, and Mo doped $Bi_{12}GeO_{20}$ were studied in [19]. They found that the absorption was higher for annealed and yet higher for doped crystals. The absorption peaks for all studied cases were located at 390 nm followed by local maxima around 400 nm, steep linear decreases between 400 and 500 nm, and approximately constant absorbance values above 550 nm. Absorbance values above 550 nm listed in the increasing order correspond to the untreated, annealed in N_2 for 8 h at 450 °C, annealed in N_2 for 8 h at 550 °C, γ-ray irradiated, and Mo doped $Bi_{12}GeO_{20}$. Consequently, it can be concluded that annealing can be used to alter absorption of $Bi_{12}GeO_{20}$ crystals; however, nature and intensity of the change depend on the temperature and duration of annealing [16,19]. An asymmetric transmission through a photorefractive crystal, shown in Fig. 4, could be attributed to the nonlinear interaction between a beam and its own reflection from the back face of the crystal, as suggested in [33]. Impurities along the beam path, such as defects or color centers, surface irregularities caused by cutting and polishing, as well as mechanical imperfections and structural changes confirmed by XRD measurements given in Fig. 6, may contribute to the asymmetry detected in transmission spectra.

Changes in sample color caused by irradiation were quantified by calculating CIE chromaticity coordinates. The obtained results given in Fig. 5 revealed that the change of crystal color was significant.

The X-ray diffraction (XRD) patterns of prismatic unirradiated and irradiated single crystal samples, as well as of powdered samples taken from unirradiated and irradiated $Bi_{12}GeO_{20}$ crystals are given in Fig. 6. The XRD patterns of the two prism-shaped samples shown in graphs (a) and (b) in Fig. 6 were recorded along the *z* as well as along the $-z$ direction, i.e., using both bases of the prism as the incident facet. The relative shift between the XRD spectra that correspond to the *z* and $-z$ direction indicates that there is an offset between the prism axis and the crystal axis, regardless of the parallelism between the prism's bases, i.e., between the facets used as incident for XRD measurements. In addition, the *z* XRD spectrum of laser irradiated prism sample reveals that the side of the crystal sample that was not incident with regard to the laser beam, can be indexed to the $Bi_{12}GeO_{20}$ compound. The XRD spectrum of irradiated prism sample that corresponds to the $-z$ direction implies that the laser-beam-incident side of the sample is almost amorphous, indicating fragmentation of a monocrystal into disoriented fractals. This is in good agreement with the defect structure of $Bi_{12}GeO_{20}$ crystal [1], which is sensitive to any extreme conditions.

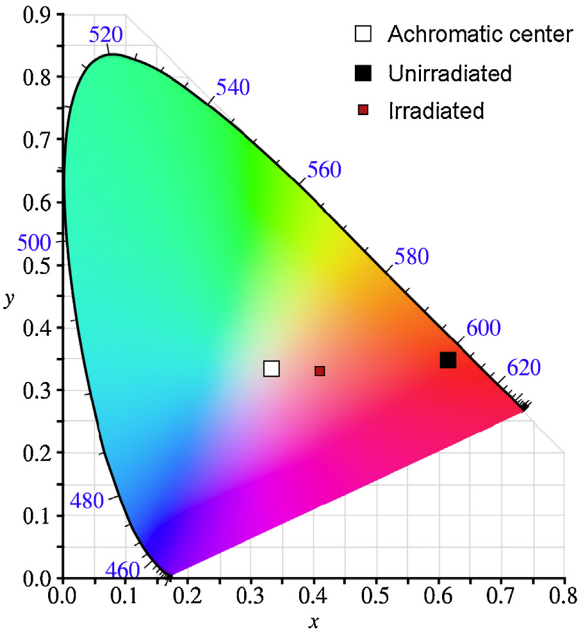

Fig. 5. Sample colors in CIE chromaticity diagram. The change in the crystal color was visible to the naked eye.

All the peaks in the powdered unirradiated $Bi_{12}GeO_{20}$ XRD pattern given in Fig. 6(c) correspond to the denoted $Bi_{12}GeO_{20}$ phases, which is in good agreement with the JCPDS Cards No. 34-0096. More details about this spectrum are given in [20].

The comparison between X-ray diffraction patterns of the powdered slices of irradiated prism, collected from the laser-beam-incident side, $-z$, and from the side opposite to it, *z*, shows significant general decrease in peak intensity as well as disappearance of some peaks in the $-z$ spectrum, with the exception of peaks (222), (622), and (613) that are somewhat stronger, see Fig. 6(d). This may be explained by an amorphization caused by laser irradiation. The lattice parameter values calculated for unirradiated and irritated materials confirmed this assumption. Namely, the lattice parameter of the laser-beam-incident side of powdered irradiated sample, $a_0 = 10.1411$, is smaller than the one of the powdered unirradiated sample, $a_0 = 10.1456$, whereas the lattice parameter of the *z*–side of powdered irradiated sample, $a_0 = 10.1454$, is very close to that of the powdered unirradiated sample.

The Raman spectra of $Bi_{12}GeO_{20}$ single crystals at room temperature in the spectral range from 150 to 800 cm^{-1} are shown in Fig. 7. The results obtained for unirradiated crystals are in agreement with those given in [2,20]. Irradiation of the crystal caused all the peaks of symmetry type E, i.e., the peaks at 234, 454, and 619.6 cm^{-1}, to disappear and intensity increase of all other peaks. The change in the same Raman spectrum peaks of $Bi_{12}GeO_{20}$ was reported in [19]; however, the most, medium, and least intense peaks discussed there correspond to the annealed, doped, and untreated samples, respectively.

The dominant role in formation of peaks at 234, 454 and 619.6 cm^{-1} is played by oxygen. Generally, it has been shown that all the peaks in the low-frequency region, i.e., below 650 cm^{-1}, are caused by excitations of the bismuth-oxygen sub-lattice, whereas the main contributors to the high-frequency region, i.e., above 650 cm^{-1}, are oscillations of $[GeO_4]$ tetrahedron [2]. In sillenites all E

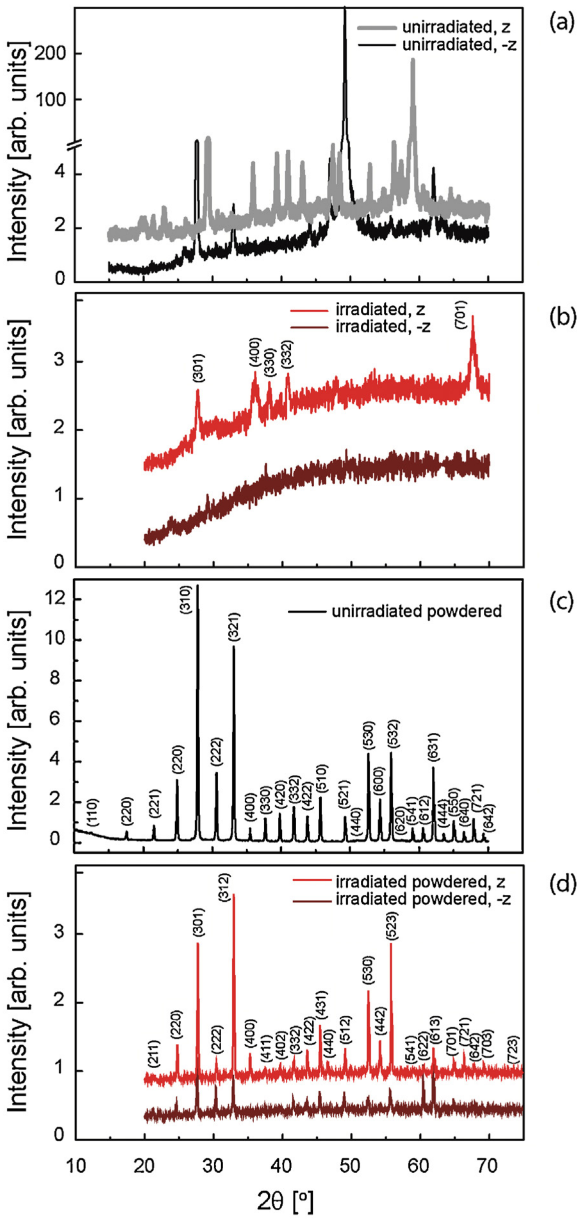

Fig. 6. X-ray diffraction spectra of $Bi_{12}GeO_{20}$. The XRD patterns correspond to the (a) unirradiated prism, (b) irradiated prism, (c) powdered unirradiated prism slice, and (d) powdered irradiated prism slices of $Bi_{12}GeO_{20}$. The $-z$ and z spectra in (d) correspond to the powdered slices taken from the laser-beam-incident side of the irradiated sample and the side opposite to it, respectively. The relative shift between spectra recorded in the z and $-z$ direction in (a) and (b) indicates offset between the prism and crystal axes. The laser-beam-incident side of the irradiated sample became almost amorphous, as can be seen from the $-z$ spectrum in (b) as well as from a significant decrease in $-z$ spectrum peaks in (d). From the spectra corresponding to the z direction in (b) and (d) it can be concluded that this side of irradiated crystal prism can be indexed to the $Bi_{12}GeO_{20}$ compound.

modes consist of oxygen vibrations, which elongate the cluster by stretching, rocking, and bending of Bi—O bonds [34–36]. Our results indicate that, under the influence of femtosecond laser irradiation, bonds of this kind are broken, some others are newly formed, and some oxygen have evaporated from the surface, causing the E type peaks at 234, 454, and 619.6 cm^{-1} to disappear. Similarly, high pressure is reported in [37] and references therein to cause breakage of some of the bonds and formations of new ones. Note that these conclusions are confirmed by the XRD measurements given in Fig. 6.

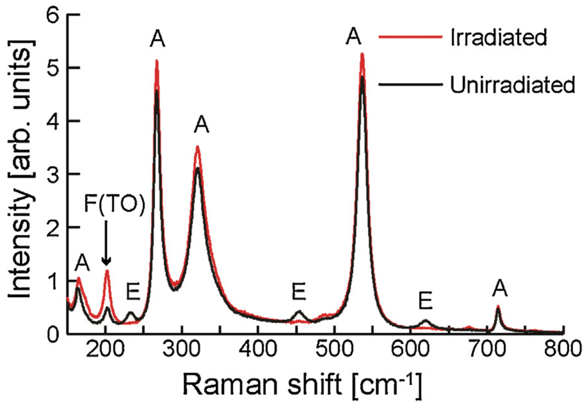

Fig. 7. Raman spectra. The E type peaks at 234, 454, and 619.6 cm^{-1} disappeared after irradiation, whereas all other peaks, i.e., A and F type peaks, underwent a small enhancement.

Table 1
Optical properties at 632.8 nm.

Property	Unirradiated sample	Irradiated sample
Verdet constant (rad T^{-1} m^{-1})	47.34	62.64
Absorption coefficient (cm^{-1})	3.3	2.7
Magneto-optical quality (rad T^{-1})	0.143	0.23

Optical properties of unirradiated and irradiated $Bi_{12}GeO_{20}$ crystal samples are compared in Table 1. The unirradiated sample has 24.38% lower Verdet constant compared to the irradiated sample. The absorption coefficient of unirradiated sample is 22.22% higher than the one of the irradiated crystal. The increased Verdet constant and lower absorption of irradiated sample led to its better magneto-optical quality, which is by 37.8% higher than the magneto-optical quality of the sample that has not been irradiated.

Previous work [38] suggests that $Bi_{12}GeO_{20}$ crystal exhibits continuous decrease in Verdet constant with increasing wavelength, which begins with 140 rad/(T m) at 480 nm and drops down to 50 rad/(T m) at 700 nm. A typical value for the Verdet constant is around 60 rad/(T m) at 632.8 nm. Another study [39] suggests an increase in the Verdet constant for undoped and Cr doped BSO and BTO:Cu crystals when exposed to white light for 20 min. The Verdet constant dependence on the wavelength remains monotonically decreasing with illumination causing a few percent increase of the Verdet constant at lower visible wavelengths.

All measurements were performed several months after irradiation, i.e., long after full post-irradiation relaxation of crystal samples; therefore, all the detected changes are stable and permanent.

4. Conclusions

The 800 nm, femtosecond pulsed laser irradiation of increasing power caused significant permanent changes in optical properties of $Bi_{12}GeO_{20}$ single crystals. The transmittance dependence on the applied irradiation power undergoes initial growth, reaches maximum, and then decreases. The maximal transmittance of 25.1% occurred at 455 mW. In the transmission spectra of unirradiated sample anisotropy was detected. After irradiation, the transmission increased, whereas the anisotropy disappeared. To the best of our knowledge, photo-induced increase in BGO transmission has not been reported before. The XRD measurements performed on the prismatic crystal samples as well as on the powdered slices taken from the crystal facets confirmed mechanical imperfections as well as femtosecond laser induced structural changes. The laser-beam-incident side of the sample became almost amorphous, indicating fragmentation of a monocrystal into disoriented fractals, whereas the side of the crystal sample that was not incident with regard to the laser beam, can be indexed to the $Bi_{12}GeO_{20}$ compound. The Raman spectra peaks became somewhat stronger, except for the E type peaks at 234, 454, and 619.6 cm^{-1}, which disappeared. Irradiation also caused significant change of the crystal color. The irradiation improved magneto-optical quality by 37.8%, and resulted in 24.4% increase of the Verdet constant as well as 22.2% decrease of the absorption coefficient. Optical properties of $Bi_{12}GeO_{20}$ single crystals can be improved by irradiation with the femtosecond pulsed laser beam. For the best results, the wavelength, duration, and power of irradiating laser beam, need to be optimized.

Acknowledgements

This work is financially supported by the Serbian Ministry of Education, Science, and Technological Development through the projects III45003 and III45016. We thank Z. Velikić for his assistance with transmission spectra measurements and A. Valčić for his help with sample preparation.

References

[1] S.C. Abrahams, P.B. Jamieson, J.L. Bernstein, Crystal structure of piezoelectric bismuth germanium oxide $Bi_{12}GeO_{20}$, J. Chem. Phys. 47 (1967) 4034–4041.

[2] V.I. Burkov, V.S. Gorelik, A.V. Egorysheva, Y.F. Kargin, Laser Raman spectroscopy of crystals with the structure of sillenite, J. Russ. Las. Res. 22 (2001) 243–267.

[3] S.F. Radaev, V.I. Simonov, Y.F. Kargin, New data on structure and crystal chemistry of sillenites $Bi_{12}M_xO_{20\pm\delta}$, Eur. J. Solid State Inorg. Chem. 29 (1992) 383–392.

[4] Kargin YuF, Syntheses, Composition, and Properties of Oxide Compounds of Bismuth with the Structure of Sillenite, Institute of general and inorganic chemistry, Moscow, 1998 (PhD thesis).

[5] C.A. Scurti, N. Auvray, M.W. Lufaso, S. Takeda, H. Kohno, D.J. Arenas, Electron diffraction study of the sillenites $Bi_{12}SiO_{20}$, $Bi_{25}FeO_{39}$ and $Bi_{25}InO_{39}$: evidence of short-range ordering of oxygen-vacancies in the trivalent sillenites, AIP Adv. 4 (2014) 087125, doi:http://dx.doi.org/10.1063/1.489334.

[6] M. Valant, D. Suvorov, A stoichiometric model for sillenites, Chem. Mater. 14 (2002) 3471–3476.

[7] M. Simon, F. Mersch, C. Kuper, Refractive indices of photorefractive bismuth titanate, barium-calcium titanate, bismuth germanium oxide, and lead germanate, Phys. Status Solidi A 159 (1997) 559–562.

[8] V.M. Skorikov, Kargin YuF, A.V. Egorysheva, V.V. Volkov, M. Gospodinov, Growth of sillenite-structure single crystals, Inorg. Mater. 41 (2005) S24–S46.

[9] R.A. Ganeev, A.I. Ryasnyansky, B. Palpant, S. Debrus, Third-order nonlinearities of $Bi_{12}GeO_{20}$ crystal measured by nanosecond radiation, J. Appl. Phys. 97 (2005) 104303, doi:http://dx.doi.org/10.1063/1.1891280.

[10] Introduction to Photorefractive Nonlinear Optics, in: P. Yeh (Ed.), 1st ed., Wiley-Interscience, New York, 1993.

[11] M.J. Weber, Inorganic scintillators: today and tomorrow, J. Lumin. 100 (2002) 35–45.

[12] M. Itoh, T. Katagiri, H. Mitani, M. Fujita, Y. Usuki, Comparative study of excitonic structures and luminescence properties of $Bi4Ge_3O_{12}$ and $Bi_{12}GeO_{20}$, Phys. Status Solidi B 245 (2008) 2733–2736.

[13] N.C. Deliolanis, I.M. Kourmoulis, G. Asimellis, A.G. Apostolidis, E.D. Vanidhis, N. A. Vainos, Direct measurement of the dispersion of the electrogyration coefficientof photorefractive $Bi_{12}GeO_{20}$ crystals, J. Appl. Phys. 97 (2005) 023531.

[14] C.G.P. Moraes, F.A.A. Jesus, Z.S. Macedo, Electrical and dielectric characterization of $Bi_{12}GeO_{20}$ prepared by modified Pechini method, Adv. Cond. Matter Phys. 2014 (2014) 968349, doi:http://dx.doi.org/10.1155/2014/968349.

[15] O. Peña-Rodríguez, J. Olivares, I. Bányász, Optical properties of crystalline and ion-beam amorphized $Bi_{12}GeO_{20}$: Relevance for waveguide applications, Opt. Mater. 47 (2015) 328–332.

[16] V.M. Skorikov, I.S. Zakharov, V.V. Volkov, E.A. Spirin, Transmission and absorption spectra of $Bi_{12}GeO_{20}$, $Bi_{12}SiO_{20}$, and $Bi_{12}TiO_{20}$ single crystals, Inorg. Mater. 38 (2002) 172–178.

[17] Z.S. Macedo, C.S.S. Oliveira, A.C. Hernandes, Dielectric relaxation mechanism of single crystal and polycrystal bismuth germinate, J. Appl. Phys. 102 (2007) 034105.

[18] H. Marquet, J.-C. Merle, J.-G. Gies, Charge transfer mechanisms between some shallow-trap centres involved in the photochromism of $Bi_{12}GeO_{20}$, Opt. Mater. 14 (2000) 277–285.

[19] P.S. Yu, L.B. Su, H.L. Tang, X. Guo, H.Y. Zhao, Q.H. Yang, J. Xu, Study on photoluminescence of thermally treated $Bi_{12}GeO_{20}$ and Mo:$Bi_{12}GeO_{20}$ crystals, Sci. China Technol. Sci. 54 (2011) 1287–1291.

[20] ZŽ Lazarević, P. Mihailović, S. Kostić, M.J. Romčević, M. Mitrić, S. Petričević, J. Radunović, M. Petrović-Damjanović, M. Gilić, NŽ. Romčević, Determination of magneto-optical quality and refractive index of bismuth germanium oxide single crystals grown by Czochralski technique, Opt. Mater. 34 (2012) 1849–1859.

[21] S. Kumaragurubaram, S. Moorthy Babu, C. Subramanian, P. Ramasamy, Growth and characterization of $Bi_{12}SiO_{20}$ and $Bi_{12}GeO_{20}$ crystals, Indian J. Eng. Mater. Sci. 7 (2000) 331–335.

[22] A. Cremades, J. Piqueras, A. Remón, J.A. García, M.T. Santos, E. Diéguez, Luminescence study of thermal treated and laser irradiated $Bi_{12}GeO_{20}$ and $Bi_{12}SiO_{20}$ crystals, J. Appl. Phys. 83 (1998) 7948–7952.

[23] A. Cremades, M.T. Santos, A. Remón, J.A. García, E. Diéguez, J. Piqueras, Cathodoluminescence and photoluminescence in the core region of $Bi_{12}GeO_{20}$ and $Bi_{12}SiO_{20}$ crystals, J. Appl. Phys. 79 (1996) 7186–7190.

[24] I. Stefaniuk, P. Potera, I. Rogalska, D. Wróbel, EPR investigations of defects in $Bi_{12}GeO_{20}$:Cr single crystal irradiated by high energy uranium ions, Curr. Topics Biophys. 33 (2010) 231–235.

[25] N. Benjelloun, M. Tapiero, J.P. Zielinger, F. Marsaud, J.C. Launay, Characterization of deep levels in $Bi_{12}GeO_{20}$ by photoinduced current transient spectroscopy, J. Appl. Phys. 64 (1988) 4013–4023.

[26] R.A. Ganeev, A.I. Ryasnyansky, R.I. Tugushev, M.K. Kodirov, F.R. Akhmedjanov, T. Usmanov, Nonlinear optical characteristics of BSO and BGO photorefractive crystals in visible and infrared ranges, Opt. Quant. Electron. 36 (2004) 807–818.

[27] M. Sylla, D. Rouède, R. Chevalier, X. Nguyen Phu, G. Rivoire, Picosecond nonlinear absorption and phase conjugation in BSO and BGO crystals, Opt. Commun. 90 (1992) 391–398.

[28] B. Taheri, S.A. Holmstrom, R.C. Powell, J.J.F. Song, F. Antonio Munoz, I. Földvári, A. Péter, Nonlinear absorption of laser light in $Bi_{12}GeO_{20}$ single crystals, Opt. Mater. 3 (1994) 251–255.

[29] A. Matusevich, A. Tolstik, M. Kisteneva, S. Shandarov, V. Matusevich, A. Kiessling, R. Kowarschik, Investigation of photo-induced absorption in a $Bi_{12}TiO_{20}$ crystal, Appl. Phys. B 92 (2008) 219–224.

[30] PDXL Version 2.0.3.0 Integrated X-ray Powder Diffraction Software. Rigaku Corporation, Tokyo, Japan, 2011, pp. 196–8666.

[31] Powder Diffraction File, PDF-2 Database, announcement of new database release 2012, International Centre for Diffraction Data (ICDD).

[32] P. Mihailovic, S. Petricevic, S. Stankovic, J. Radunovic, Temperature dependence of the $Bi_{12}GeO_{20}$ optical activity, Opt. Mater. 30 (2008) 1079–1082.

[33] K.R. MacDonald, J. Feinberg, Z.Z. Ming, P. Günter, Asymmetric transmission through a photorefractive crystal of barium titanate, Opt. Commun. 50 (1984) 146–150.

[34] B. Mihailova, D. Toncheva, M. Gospodinov, L. Konstatinov, Raman spectroscopic study of Mn-doped $Bi_4Ge_3O_{12}$, Solid State Commun. 112 (1999) 11–15.

[35] B. Mihailova, L. Konstatinov, D. Petrova, M. Gospodinov, Effect of doping on Raman spectra of $Bi_{12}SiO_{20}$, Solid State Comun. 102 (1997) 441–444.

[36] B. Mihailova, M. Gospodinov, L. Konstatinov, Raman spectroscopy study of sillenites I. Comparsion between $Bi_{12}(Si, Mn)O_{20}$ single crystals, J. Phys. Chem. Solids 60 (1999) 1821–1827.

[37] L. Wiehl, A. Friedrich, E. Haussühl, W. Morgenroth, A. Grzechnik, K. Friese, B. Winkler, K. Refson, V. Milman, Structural compression and vibrational properties of $Bi_{12}SiO_{20}$ sillenite from experiment and theory, J. Phys. Condens. Matter 22 (2010) 505401 16pp.

[38] A. Feldman, W.S. Brower Jr., D. Horowitz, Optical activity and faraday rotation In bismuth oxide compounds, Appl. Phys. Lett. 16 (1970) 201–202.

[39] V. Tassev, M. Gospodinov, M. Veleva, Faraday effect of BSO and BTO crystals doped with Cr, Mn and Cu, Cryst. Res. Technol. 35 (2000) 213–219.

Improvement of magneto-optical quality of high purity $Bi_{12}GeO_{20}$ single crystal induced by femtosecond pulsed laser irradiation

G. S. I. ABUDAGEL[a], S. PETRIČEVIĆ[a], P. MIHAILOVIĆ[a], A. KOVAČEVIĆ[b], J. L. RISTIĆ-DJUROVIĆ[b], M. LEKIĆ[b], M. ROMČEVIĆ[b], S. ĆIRKOVIĆ[b], J. TRAJIĆ[b,*], N. ROMČEVIĆ[b]
[a]*School of Electrical Engineering, University of Belgrade, Bulevar kralja Aleksandra 73, 11000 Belgrade, Serbia*
[b]*Institute of Physics, University of Belgrade, Pregrevica 118, 11080 Belgrade, Serbia*

Femtosecond pulsed laser irradiation can improve optical properties of $Bi_{12}GeO_{20}$ single crystals. We investigate if the effect occurs if the crystals are grown from high purity components. The samples are irradiated by a femtosecond pulsed laser beam of increasing power. The maximal transmittance of 44% occurs at the irradiating laser power of 451 mW. After irradiation, intensity of Raman spectra peaks increase, except for the peak at 203 cm^{-1}, whose intensity decreases. The irradiation also changes the sample colour. Although the Verdet constant does not change, the absorption coefficient decreases significantly, which leads to magneto-optical quality improvement of approximately 70%.

(Received March 3, 2017; accepted August 9, 2017)

Keywords: Bismuth germanium oxide, Laser annealing, Raman spectroscopy, Crystal colour, Magneto-optical quality

1. Introduction

Bismuth germanium oxide ($Bi_{12}GeO_{20}$) from the sillenite group of cubic crystals is commonly abbreviated as BGO or s-BGO. Due to its fitting optical characteristics, such as photoconductivity, photochromism, photorefractivity, piezoelectricity, as well as to electro-optic and magneto-optic effects it supports [1, 2], it has been used in a wide range of optical applications and devices [2–6]. Its cubic cell unit is composed of two formula units, namely of 24 Bi, 40 O and 2 Ge. The Ge atoms positioned in the centre and the vertices of a cube are tetrahedrally coordinated by the oxygen atoms, whereas the Bi atoms are heptacoordinated [7–9]. There are numerous studies that considered properties of doped and un-doped BGO, see for example [10–18], as well as those investigating property changes induced by a wide variety of exposure types such as thermal treatments, particle beams or light treatments [3, 12–16, 19–25].

BGO is a good example of a Faraday rotator crystal possibly applicable in sensor systems. In order to evaluate usability of a crystal for sensing purposes not only its Faraday rotation capability, but its ability to be integrated into a sensing optical system must be considered. In general, in fiber-optic sensing systems optical beams used to sense the measured quantity are guided through the fibers, giving rise to the absorption coefficient as the most important optical property. Crystals with high absorption coefficient are in general less useful for sensor systems because they absorb much of the light and cause low signal-to-noise ratio at the receiving photo diode. If the magnetic field is to be detected, the intensity of light caused by magnetic field modulation is proportional to the Verdet constant, whereas the intensity of light reaching the photodiode as well as the photocurrent is inversely proportional to the crystal absorption. The noise in a fiber optic sensing system is predominantly determined by the noise in the processing electronics and can be expressed as the noise present in the photocurrent. Therefore, the signal-to-noise ratio of the magnetic field sensor is proportional to the Verdet constant and inversely proportional to the absorption coefficient of a crystal. Consequently, due to its proportionality to the signal-to-noise ratio, the magneto-optical quality of a crystal defined as a ratio of the Faraday rotation, which is proportional to the Verdet constant, and the absorption coefficient can be used as a measure of a crystal's applicability in a magnetic field sensing system.

When $Bi_{12}GeO_{20}$ crystals were exposed to pulsed laser beam irradiation, there are examples of laser beam operating in the nanosecond [3], picosecond [23–25], or femtosecond range [26]. In [26] it was determined that femtosecond pulsed laser irradiation of increasing power causes significant changes in the transmittance, transmission spectra, sample colour, Raman spectra, X-ray diffraction pattern, Verdet constant, magneto-optical property, and absorption coefficient of lower quality black $Bi_{12}GeO_{20}$ single crystals. Here we analyze if the same increasing power pattern of femtosecond pulsed laser irradiation has similar effect on the high quality yellow $Bi_{12}GeO_{20}$ single crystals, i.e., on the crystals that were grown from the components whose purity is higher than that of the black crystals, and whose magneto-optical quality is the maximal obtainable by the applied crystal growth technique.

2. Experimental procedure

2.1. Preparation of crystal samples

Single crystals of $Bi_{12}GeO_{20}$ were grown in the air by the Czochralski technique using the MSR 2 crystal puller, Eurotherm temperature controller and the calculated critical crystal diameter, critical rotation rate and pulling rate, as explained in detail in [17, 26]. The system provided small fluctuations in crystal diameter size as well as in melting temperature. The $Bi_{12}GeO_{20}$ seed was oriented in the ⟨111⟩ direction and the charge was a mixture of Bi_2O_3 and GeO_2 in the stoichiometric ratio 6:1. The light yellow crystal samples were obtained using the Bi_2O_3 and GeO_2 purity of 99.999 wt.% and 99.9999 wt.%, respectively. Crystal samples of size 4 mm × 4 mm × 10 mm were cut from the boule and mechanically as well as chemically polished. The technique used to prepare the samples insured maximal sample quality within the limits corresponding to their purity [17].

2.2. Crystal irradiation and characterization

The equipment used to produce the femtosecond pulsed laser beam and establish its wavelength was the Coherent Mira 900F femtosecond laser, Coherent Verdi V-10 pump laser that provided a 532 nm continuous wave pump beam, and Ocean Optics HR2000CG UV-NIR spectrometer. Crystal samples were irradiated along the crystal growth direction (z), i.e. along the samples' longest axis. The irradiating laser beam radius provided partial irradiation of the exposed crystal facet. The beam wavelength was 800 nm, whereas its power was increased from 50 mW to 950 mW and was adjusted by a graded filter. The pulses were 90 fs long and had repetition rate of 76 MHz. The samples were irradiated by each beam power for 3 s. The beam power was measured with the Ophir power meter with the thermal and photometric heads. In order to enable comparison of the irradiation effects on the single crystal samples of different purity, i.e., on yellow and black $Bi_{12}GeO_{20}$ samples, the irradiation conditions were intentionally chosen to be identical to those applied to the lower purity black crystals in [26].

The sample colour was calculated from the transmission spectra measured by the Beckman Coulter DU 720 General Purpose UV/VIS spectrometer.

The micro-Raman spectra were recorded at room temperature in the spectral range between 100 and 1100 cm^{-1} with 1 cm^{-1} resolution using the backscattering configuration and the 532 nm line of Verdi G optically pumped semiconductor laser as an excitation source, and the Jobin Yvon T64000 spectrometer, which has nitrogen cooled charge-coupled-device detector.

The Faraday rotation and optical activity were measured by Δ/Σ method at the wavelength of $\lambda = 632.8$ nm. After the BGO crystal the orthogonal polarizations of the light beam were separated by the $CaCO_3$ crystal into two parallel beams 3 mm apart. The quadrant photodiode connected into transimpedance stages was used for optoelectronic conversion. This method is described in more details in [26].

3. Results and discussion

The irradiation pattern applied here to the higher purity yellow crystals is identical to the one utilized in [26] to irradiate black crystals grown from the components of lesser purity. Consequently, the obtained results can be compared and the differences can be attributed solely to different sample purity. With the increase of irradiating laser power, the transmittance of irradiated sample undergoes initial growth followed by a decrease, as can be seen in Fig. 1. Comparison with the dependence corresponding to the black crystal given in [26] reveals that the transmittance curves for the black as well as for the yellow crystal has the same shape and that the slopes of the two curves appear to be approximately equal. The curve corresponding to the yellow crystal is shifted to the larger values by approximately 18.8% compared to the curve corresponding to the black crystal. For the yellow crystal, the maximal transmittance of 44.0% occurs at the irradiating laser power of 451 mW, whereas the lower purity black crystal was reported in [26] to have the smaller maximal transmittance value of 25.1% corresponding to 455 mW. It seems that both curves exhibit local irregularities which occur at 197.4–249.7 mW, 552–605 mW and 800–857 mW for the black crystal and at 593–641 mW for the yellow crystal. It is possible that the irregularity in the yellow sample curve for large values of incident power P_0 is not visible because it is outside the considered range of irradiating laser power, or due to insufficient measurement accuracy achieved for yellow crystal data points above 700 mW.

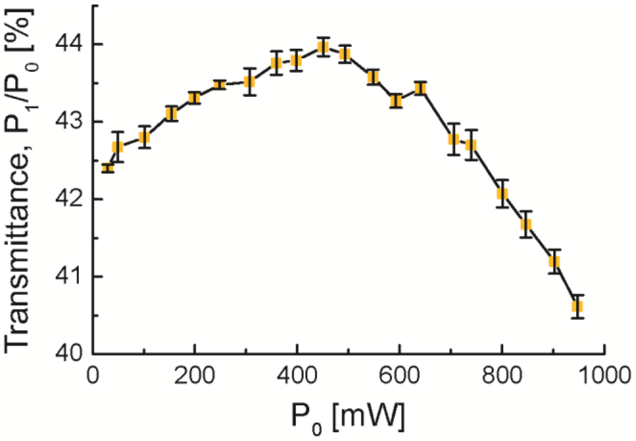

Fig. 1. Change of crystal transmittance with increase of irradiating laser power. For each value of the incident power P_0, a sample is irradiated by the femtosecond laser beam for 3 s. The transmittance is given as P_1/P_0, where P_1 is the transmitted power. The error bars were calculated from the uncertainties of measured values of the incident and transmitted power, ΔP_0 and ΔP_1.

The sample colours before and after irradiation were calculated using the CIE chromaticity coordinates and are given in Fig. 2. Comparison with the results corresponding to the black crystal given in [26] revealed that the change of black crystal colour was more pronounced than that of the yellow crystal presented here.

The Raman spectra of unirradiated and irradiated samples are recorded at room temperature in the spectral range from 150 to 800 cm^{-1} and are shown in Fig. 3. The results obtained for unirradiated crystals are in agreement with those given in [8, 17]. After irradiation the intensity of the $F(TO)$ peak at 203 cm^{-1} decreased, whereas all other peaks became more pronounced. Despite the difference in purity between the yellow samples studied here and the black crystals considered in [26] the Raman spectra of unirradiated crystals do not differ significantly. As reported in [26], irradiation of the black crystal caused all the peaks of symmetry type E, i.e., the peaks at 234, 454, and 619.6 cm^{-1}, to disappear and intensity increase of all other peaks. The change in the same Raman spectrum peaks of $Bi_{12}GeO_{20}$ was reported in [16]; however, the most, medium, and least intense peaks correspond to the annealed, doped, and untreated samples, respectively.

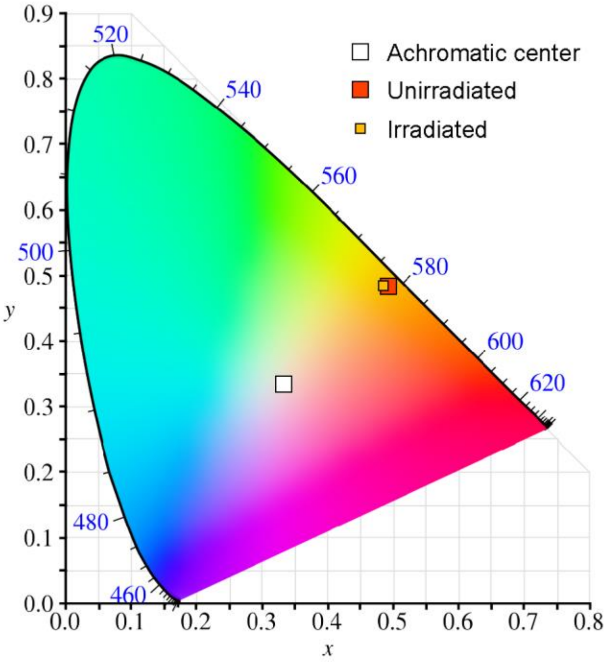

Fig. 2. Colours of irradiated and unirradiated samples in CIE chromaticity diagram.

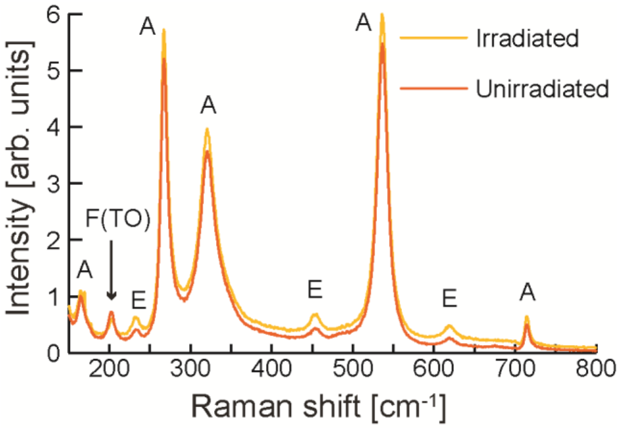

Fig. 3. Raman spectra. Irradiation caused a small upward shift of the crystal spectrum except for the F(TO) type peak at 203 cm^{-1}.

The Verdet constant is calculated from

$$V = \frac{\theta_{0\mathrm{AC}}}{B_0 l} = \frac{1}{2B_0 l}\sin^{-1}\left(\frac{U_1 - U_2}{U_1 + U_2}\right)_{0\mathrm{AC}} \tag{1}$$

where θ_{0AC} is the amplitude of the AC signal, B_0 is the amplitude of the magnetic induction, whereas U_1 and U_2, are the output signal voltages obtained after transimpedance stages from the vertically and horizontally polarized components, respectively. The FFT was used to separate spectral components of U_1 and U_2. The Faraday rotation was determined from the magnitude of the 50 Hz component.

The absorption coefficients were obtained by measuring the difference in beam intensities at the quadrant photodiode [26] with and without BGO crystal in the beam path. The reflection on the BGO crystal was calculated using the normal incidence and BGO refraction index of $n_{BGO} = 2.55$.

The absorption coefficient, α, was calculated from the beam intensities with and without the crystal present in the beam path, $I(x)$ and $I(0)$, and the known crystal length l = 9.8 mm as

$$I(l) = I_0 e^{-\alpha l} \Rightarrow \alpha = -\frac{1}{l}\ln\frac{I(l)}{I_0} \tag{2}$$

The magneto-optical quality is calculated by dividing the Verdet constant by the absorption coefficient. The obtained results are given in Table 1.

Table 1. Magneto-optical properties of irradiated and unirradiated high purity crystal samples.

Property	Unirradiated sample	Irradiated sample
Verdet constant (rad $T^{-1}m^{-1}$)	72	72
Absorption coefficient (cm^{-1})	0.58	0.34
Magneto-optical quality (rad T^{-1})	1.24	2.1

The data given in Table 1 show the effects of femtosecond laser irradiation on the magneto-optical properties of the high purity BGO crystal. The irradiation caused 41.4% decrease in the absorption coefficient and did not influence the Faraday constant. Consequently, the increase in crystal transparency resulted in a significant 70% increase in the magneto-optical quality. As explained earlier, increase in crystal transparency is an important gain from the point of view of a sensor system since the system-level signal-to-noise ratio is directly proportional to the magneto-optical quality of a crystal. Therefore, it is expected that the signal-to-noise ratio of a sensor system would be improved by the same amount as the improvement in the magneto-optical quality induced by the irradiation. Consequently, it can be concluded that the femtosecond pulsed laser irradiation affects the crystal in a positive manner.

4. Conclusions

Femtosecond pulsed laser irradiation of increasing power caused significant changes in optical properties of $Bi_{12}GeO_{20}$ single crystals grown from the components of high purity, as was the case in [26] when the component purity was not so high. The transmittance dependence on the applied irradiation power had the same shape regardless of the purity of the components the crystals were grown from. The curve corresponding to the higher purity crystal, i.e., the yellow crystal, is shifted to the larger values by approximately 18.8%. For the black and yellow crystal, the maximal transmittance of 25.1% and 44.0% occurred at 455 mW and 451 mW, respectively. The Raman spectra peaks became somewhat stronger, except for the E type peaks at 234, 454, and 619.6 cm^{-1} in the lower purity black crystal, which disappeared and the yellow crystal peak at 203 cm^{-1} whose intensity decreased. Irradiation also caused slight colour change of the yellow crystal and significant change of the black crystal colour. The Verdet constant did not change; however, the absorption coefficient significantly decreased leading to equally significant increase of the magneto-optical quality of the sample. Consequently, it can be concluded that optical properties of high quality $Bi_{12}GeO_{20}$ single crystals can be improved by irradiation with the femtosecond pulsed laser beam.

Acknowledgements

This work is financially supported by the Serbian Ministry of Education, Science, and Technological Development through the project III45003. We thank Z. Velikić and D. Dramlić for their assistance with transmission spectra measurements and A. Valčić for his help with sample preparation.

References

[1] M. Simon, F. Mersch, C. Kuper, Phys. Status Solidi A. **159**(2), 559 (1997).
[2] V. M. Skorikov, Yu. F. Kargin, A. V. Egorysheva, V. V. Volkov, M. Gospodinov, Inorg. Mater. **41**(1), S24 (2005).
[3] R. A. Ganeev, A. I. Ryasnyansky, B. Palpant, S. Debrus, J. Appl. Phys. **97**, 104303 (2005),
[4] P. Yeh, Introduction to Photorefractive nonlinear optics, first ed., Wiley-Interscience, New York, 1993.
[5] M. J. Weber, J. Lumin. **100**, 35 (2002).
[6] M. Itoh, T. Katagiri, H. Mitani, M. Fujita, Y. Usuki, Phys. Status. Solidi B, **245**(12), 2733 (2008).
[7] S. C. Abrahams, P. B. Jamieson, J. L. Bernstein, J. Chem. Phys. **47**(10), 4034 (1967).
[8] V. I. Burkov, V. S. Gorelik, A. V. Egorysheva, Y. F. Kargin J. Russ. Las. Res. **22**, 243 (2001).
[9] S. F. Radaev, V. I. Simonov, Y. F. Kargin, Eur. J. Solid. State Inorg. Chem. **29**(2), 383 (1992).
[10] N. C. Deliolanis, I. M. Kourmoulis, G. Asimellis, A. G. Apostolidis, E. D. Vanidhis, N. A. Vainos, J. Appl. Phys. **97**(2), 023531 (2005).
[11] C. G. P. Moraes, F. A. A. Jesus, Z. S. Macedo, Adv. Cond. Matter. Phys. **2014**, 968349 (2014), http://dx.doi.org/10.1155/2014/968349.
[12] O. Peña-Rodríguez, J. Olivares, I. Bányász, Opt. Mater. **47**, 328 (2015).
[13] V. M. Skorikov, I. S. Zakharov, V. V. Volkov, E. A. Spirin, Inorg. Mater. **38**(2), 172 (2002).
[14] Z. S. Macedo, C. S. S. Oliveira, A. C. Hernandes, J. Appl. Phys. **102**(3), 034105 (2007).
[15] H. Marquet, J-C. Merle, J-G. Gies, Opt. Mater. **14**, 277 (2000).
[16] P. S. Yu, L. B. Su, H. L. Tang, X. Guo, H. Y. Zhao, Q. H. Yang, J. Xu, Sci. China Tech. Sci. **54**(5), 1287 (2011).
[17] Z. Ž. Lazarević, P. Mihailović, S. Kostić, M. J. Romčević, M. Mitrić, S. Petričević, J. Radunović, M. Petrović-Damjanović, M. Gilić, N. Ž. Romčević, Opt. Mater. **34**, 1849 (2012).
[18] S. Kumaragurubaram, S. Moorthy Babu, C. Subramanian, P. Ramasamy, Indian J. Eng. Mater. Sci. **7**(5-6), 331 (2000).
[19] A. Cremades, J. Piqueras, A. Remón, J.A. García, M. T. Santos, E. Diéguez, J. Appl. Phys. **83**(12), 7948 (1998).
[20] A. Cremades, M. T. Santos, A. Remón, J. A. García, E. Diéguez, J. Piqueras, J. Appl. Phys. **79**(9), 7186 (1996).

[21] I. Stefaniuk, P. Potera, I. Rogalska, D. Wróbel, Current Topics in Biophysics **33**, 231 (2010).

[22] N. Benjelloun, M. Tapiero, J. P. Zielinger, F. Marsaud, J. C. Launay, J. Appl. Phys. **64**(8), 4013 (1988).

[23] R. A. Ganeev, A. I. Ryasnyansky, R. I. Tugushev, M. K. Kodirov, F. R. Akhmedjanov, T. Usmanov, Opt. Quant. Electron. **36**(9), 807 (2004).

[24] M. Sylla, D. Rouède, R. Chevalier, X. Nguyen Phu, G. Rivoire, Opt. Commun. **90**, 391 (1992).

[25] B. Taheri, S. A. Holmstrom, R. C. Powell, J. J. Song, A. M. F. I. Földvári, A. Péter, Opt. Mater. **3**, 251 (1994).

[26] A. Kovačević, J. L. Ristić-Djurović, M. Lekić, B. Hadžić, G. S. I. Abudagel, S. Petričević, P. Mihailović, B. Matović, D. Dramlić, L. M. Brajović, N. Romčević, Mater. Res. Bull. **83**, 284 (2016).

---

[*] Corresponding author: jelena@ipb.ac.rs

Opt Quant Electron (2018) 50:37
https://doi.org/10.1007/s11082-017-1298-7

Solitons generated by self-organization in bismuth germanium oxide single crystals during the interaction with laser beam

Vladimir Skarka[1,2,3] · **Marina M. Lekić**[1] · **Aleksander G. Kovačević**[1] · **Boban Zarkov**[4] · **Nebojša Ž. Romčević**[1]

Received: 8 November 2017 / Accepted: 19 December 2017 / Published online: 3 January 2018

Abstract We present here the experimental, theoretical, and numerical investigations of Kerr solitons generated by self-organization in black and yellow high quality bismuth germanium oxide ($Bi_{12}GeO_{20}$) single crystals. A picosecond laser beam of increasing power induces competing cubic and quintic nonlinearities. The numerical evolution of two-dimensional complex cubic-quintic nonlinear Schrödinger equation with measured values of nonlinearities shows the compensation of diffraction by competing cubic and quintic nonlinearities of opposite sign, i.e., the self-generation and stable propagation of solitons. Experiments as well as numerical simulations show higher nonlinearity in the black $Bi_{12}GeO_{20}$ than in the more transparent yellow one.

Keywords Solitons · Bismuth germanium oxide single crystals · Cubic-quintic Schrödinger equation · Experimental measurements

---

This article is part of the Topical Collection on Focus on Optics and Bio-photonics, Photonica 2017.

Guest Edited by Jelena Radovanovic, Aleksandar Krmpot, Marina Lekic, Trevor Benson, Mauro Pereira, Marian Marciniak.

✉ Vladimir Skarka
vladimir.skarka@univ-angers.fr

[1] Institute of Physics, University of Belgrade, Belgrade 11000, Serbia

[2] Texas A&M University at Qatar, P.O. Box 23874, Doha, Qatar

[3] Laboratoire de Photonique d'Angers, EA 4464, University of Angers, 49045 Angers Cedex 01, France

[4] Directorate of Measures and Precious Metals, Mike Alasa 14, Belgrade 11000, Serbia

1 Introduction

Dissipative structures far from the thermodynamic equilibrium, need external energy and/or matter supply in order to be self-organized (Nicolis and Prigogine 1977). The self-trapping of robust localized structures, i.e., solitons is based on the balance of antagonistic effects, with e.g. nonlinearity-induced self-contraction arresting diffraction and/or dispersion (Kivshar and Agrawal 2003; Crasovan et al. 2000; Mihalache et al. 2006). The complex nonlinear Schrödinger equation (NLS) adequately models the solitons generation and propagation in plenty of systems including nonlinear optics, nanophotonics, and nanoplasmonics (Aranson and Kramer 2002). The focusing cubic nonlinearity (e.g. Kerr nonlinearity) conpensates either difraction or dispersion generating stable spatial or temporal solitons in conservative (1 + 1)-dimensional systems (one standing for the transverse coordinate x or t, while the remaining one for the propagation coordinate z). However, the same focusing cubic nonlinearity dominates the diffraction and/or dispersion leading to the catastrophic collapse in (2 + 1)- and (3 + 1)-dimensional systems (two and three standing for the transverse coordinates). The collapse can be prevented in media having, for instance, negative quintic nonlinearity in addition to the positive cubic one, as it was established using synergy of variational method and numerical simulations (Skarka and Aleksić 2006; Skarka et al. 2010, 2014, 2017). Such Kerr solitons are hard to obtain experimentally especially in solid state systems.

The experimental generation of two-dimensionnal (2D) spatial optical solitons in a cubic-quintic medium has been recently directly demonstrated only in liquid carbon disulfide (CS_2) (Falcao-Filho et al. 2013). The excitation beam at 920 nm was obtained from an optical prametric amplifier pumped by a Ti:sapphire laser (100 fs, 1 kHz).

We present here the theoretical, experimental, and numerical investigations of Kerr solitons generated by self-organization in black and yellow high quality bismuth germanium oxide ($Bi_{12}GeO_{20}$) single crystals. A laser beam of increasing power induces competing cubic and quintic nonlinearities. The numerical evolution of (2 + 1)D complex cubic-quintic nonlinear Schrödinger equation (CQNLS) with measured values of nonlinearities shows the compensation of diffraction by competing cubic and quintic nonlinearities of opposite sign, i.e., the self-generation and propagation of stable solitons.

2 Theoretical model

Self-organization, propagation, and stability of solitons can be adequately modelled by the (2 + 1)D CQNLS that governs the evolution of normalized slowly-varying complex envelope E of electic waves in nanophotonic or nanoplasmonic media (Skarka et al. 1997, 1999):

$$i\frac{\partial E}{\partial z} + \gamma\left(\frac{\partial^2 E}{\partial x^2} + \frac{\partial^2 E}{\partial y^2}\right) + \kappa E + \sigma|E|^2 E - \nu|E|^4 E = 0 \tag{1}$$

where γ, σ, and ν are respectively the parameters characterizing the diffraction, cubic Kerr nonlinearity, and quintic nonlinearity. Barring rare exceptions, the (2 + 1)D CQNLS, due to it complexity, do not admit exact solutions. Nevertheless, an analytical approximation for solitons has been developed using the variational method adapted to dissipative systems (Skarka et al. 1997, 1999; Skarka and Aleksić 2006). The variational method makes use of the following Gaussian trial function representing the electric field of an axisymmetric Gaussian laser beam:

$$E = A\exp[-r^2/R^2 + iCr^2 + i\Psi] \tag{2}$$

where amplitude A, radius R, wave-front curvature C, and phase Ψ have to be optimized.

Skipping straightforward details, the following system of evolution equations is produced by the variational method:

$$dA/dz = -\gamma 4CA, \tag{3}$$

$$dR/dz = \gamma 4CR, \tag{4}$$

$$dC/dz = -4\gamma C^2 + \gamma/R^4 - \left(\sigma A^2 - (8/9)\nu A^4\right)/(4R^2), \tag{5}$$

$$d\Psi/dz = -2\gamma/R^2 + 3\sigma A^2/4 - 5\nu A^4/9 + \kappa, \tag{6}$$

with Eq. (6) decoupled from (3) to (5). Fixed points of these equations correspond to steady-state solutions with a zero wave-front curvature. Setting $dA/dz = dR/dz = 0$ leads to the expression for radius

$$R = 2\sqrt{\gamma}\left(\sigma A^2 - 8\nu A^4/9\right)^{-1/2} \tag{7}$$

and the limitation of amplitude

$$0 < A < \sqrt{\frac{9\sigma}{8\nu}}. \tag{8}$$

3 Experimental results

We present here not only theoretical but also experimental investigations of Kerr solitons generated by self-organization in black and yellow high quality bismuth germanium oxide ($Bi_{12}GeO_{20}$) single crystals. Although yellow and black crystals have the same chemical formula, their properties may be quite different (Lazarević et al. 2012; Kovačević et al. 2016; Abudagel et al. 2017). At 1064 nm a Neodymium Yag (17 ps, 10 Hz). laser of increasing power induces competing cubic and quintic nonlinearities into samples. Taking into account that intensity $I \sim |E|^2$ the corresponding output beam intensity can be deduced from Eq. (1)

$$I_{out} = \kappa I + \sigma I^2 - \nu I^3 \tag{9}$$

(Skarka et al. 2017).

Increasing incoming beam intensity I_{in} the outgoing beam intensity I_{out} for yellow and black crystals are charted respectively in Figs. 1 and 2. Fitting these experimental curves by cubic polynomial we obtain the values of parameters in Eqs. (1) and (9). The fit for yellow semi transparent crystal yields

$$I_{out} = 1.003 + 0.6492I + 0.4636I^2 - 0.0242I^3. \tag{10}$$

Due to the opacity of the black crystal the values of nonlinear parameters are increased

$$I_{out} = 1.6201 + 1.4731I + 0.7186I^2 - 0.0709I^3. \tag{11}$$

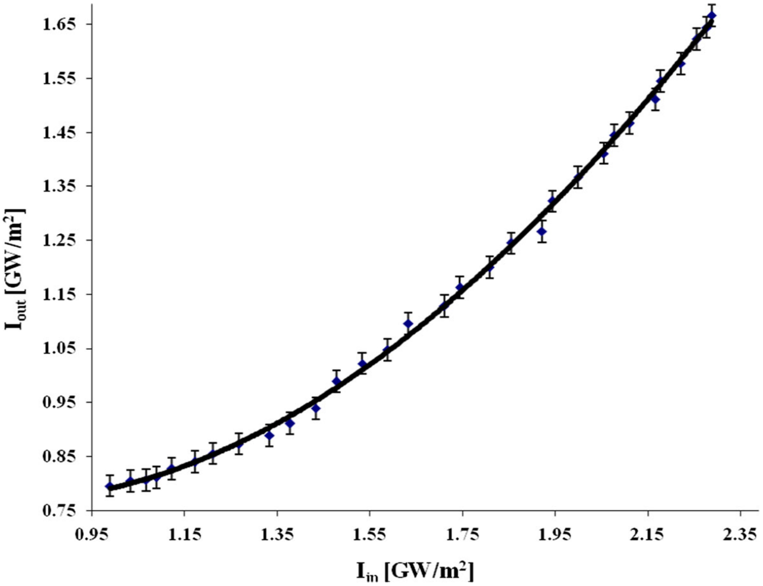

Fig. 1 Increasing of output beam intensity out of yellow crystal as a function of the increase of input laser intensity

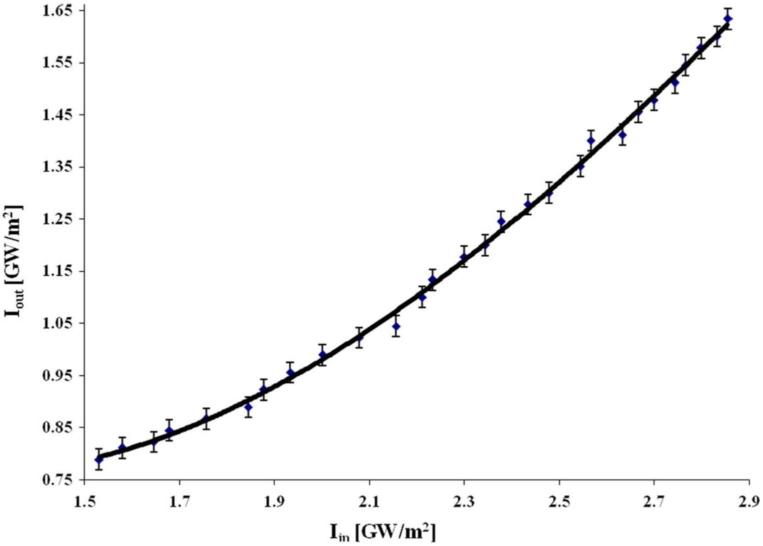

Fig. 2 Increasing of output beam intensity out of black crystal as a function of the increase of input laser intensity

Notice that the positive sign of quadratic intensity in both equations means the self-focusing of the laser beam induced due to the Kerr effect. In contrast, the negative sign of cubic intensity corresponds to the self-defocusing effect of negative quintic nonlinearity in CQNLS in agreement with our theoretical modeling.

Therefore, experimental results demonstrate that the propagation of laser beam across both yellow and black samples induces positive cubic and negative quintic nonlinearity. In turn, the light beam is modified due to this crossing as can be seen on the output intensity in Figs. 1 and 2. Such a behavior is the example of the control and structuring of light by light due to its crossing of nonlinear medium. The corresponding light-mater interaction leads to the self-organized structuring of laser beam. Following the pioneering work of Prigogine and his team, the self-organization far from thermodynamic equilibrium causes the appearance of dissipative structures (Nicolis and Prigogine 1977). In the case of the structuring of light by light, such a dissipative structure is a soliton. Solitons are completely localized in space and in time. They propagate long distance without altering.

In an experiment long distance propagation cannot be achieved in some solid sample, in particular if it is a crystal. Long crystals are simply not available. However we can resort to a numerical propagation that, under same conditions, may mimic real experiment.

The nonlinear effects are enhanced in black crystal due to its opacity with respect to yellow one, as can be concluded comparing curves in Figs. 1 and 2, as well as the results of their fits [see Eqs. (10) and (11)].

4 Confirmation of experimental results by numerical simulations of the Schrödinger model

In order to identify a pattern as a soliton, this structure has to be self-maintained during a long distance propagation. Obviously, such a drastically restrictive condition cannot be satisfied in an experiment. Both crystals we used for experiment are only 1 cm long. However, even such short samples allow the determination of linear and nonlinear parameters that enter in CQNLS [see Eqs. (1) and (9)–(11)]. Therefore, it is enough to perform numerical simulation of Eq. (1) with experimentally obtained parameters in order to investigate long distance propagation. If during such a evolution the beam profile presents the same form without the alteration, it can be concluded that it is a soliton. In Figs. 3, 4, 5 and 6 are charted results of the numerical propagation in black sample with the parameters from Eq. (11). Following the condition in Eq. (8) imposed by the variational method, the input amplitude is chosen to be three ($A = 3$) in dimensionless units. The input laser beam is initially always Gaussian and it is given by the trial function Eq. (2). In

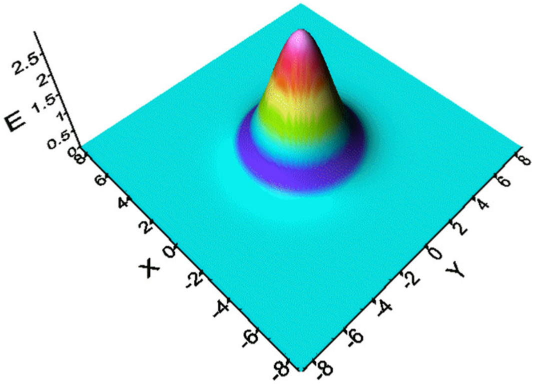

Fig. 3 The Gaussian output beam for z = 0

Fig. 4 The output beam becomes a soliton after z = 40

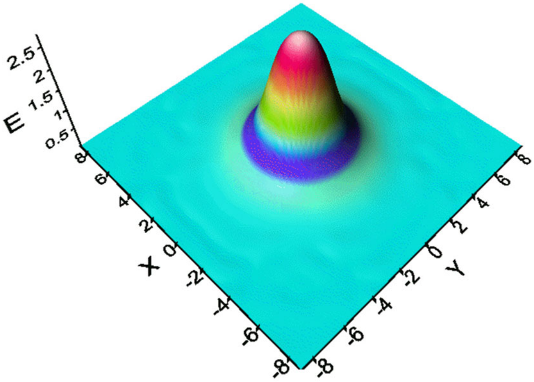

Fig. 5 The beam is still soliton after z = 10,000 steps

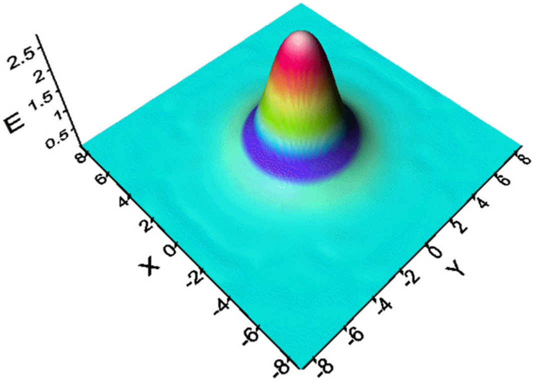

Fig. 6 Even after z = 20,000 steps the soliton remains stable

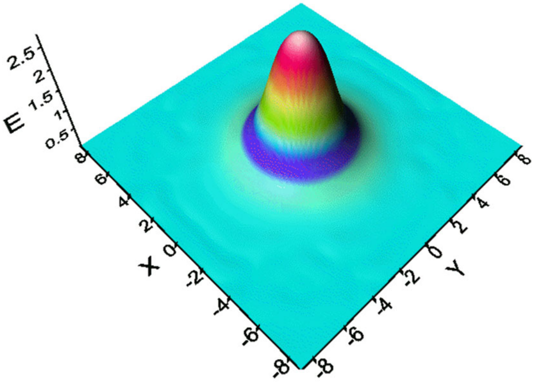

the beginning of propagation, e.i. for propagation step z = 0 this Gausian beam profile is given in Fig. 3.

The initial Gaussian laser beam is modified evolving through the nonlinear medium that itself alteres. This is precisely the effect of self-organization (Skarka and Aleksić 2006; Skarka et al. 2010). Already after z = 40 propagation steps, such a laser beam becomes soliton.

The laser beam is still soliton after 10,000 propagation steps, as in Fig. 5.

No changes even after 20,000 propagation steps (see Fig. 6).

Such an extraordinary stability of laser beam during numerical propagation without any alteration is the confirmation of its solitonic nature. Taking into account that the numerical propagation is performed with parameters obtained from an experiment, this confirms that in black $Bi_{12}GeO_{20}$ crystal a stable soliton is self-trapped. The numerical propagation of the laser beam in yellow sample gives sensibly the same results, so that on the figures no difference can be notified.

5 Conclusions

In order to study theoretically the propagation of the laser beam through yellow and black $Bi_{12}GeO_{20}$ single crystals the Schrödinger model is used. The variational method gives the conditions for stable propagation of spatial solitons. Indeed, a balance between the diffraction and the competing cubic and quintic nonlinearity insures the self-organization of a soliton. Experimental investigations using propagation of Neodymium Yag laser beam through crystals allow charting of input output-power curves. Fitting these experimental curves, parameters in Schrödinger equation are determined showing cubic-quintic nonlinearity. Very long numerical propagations of beams through crystals are performed demonstrating self-trapping of robust spatial solitons. Consequently, in turn in the experiments, the self-generation of solitons is confirmed. Self-organization of solitons in solid samples open many possibilities for applications.

Acknowledgements This publication was made possible by the National Priorities Research Program Grant No. 9-020-1-006 from the Qatar National Research Fund (a member of Qatar Foundation). Work at the Institute of Physics Belgrade is supported by the Ministry of Education and Science of the Republic of Serbia, under Projects OI 171,006 and III 45016.

References

Abudagel, G.S.I., Petričević, S.J., Mihailović, P.M., Kovačević, A.G., Ristić-Djurović, J., Lekić, M.M., Romčević, M.J., Cirković, S., Trajić, J.M., Romčević, N.Ž.: Improvement of magneto-optical quality of high purity Bi12GeO20 single crystal induced by femtosecond pulsed laser irradiation, Optoelectronics and advanced materials—rapid. Communications **11**, 477–481 (2017)

Aranson, I.S., Kramer, L.: The world of the complex Ginzburg-Landau equation. Rev. Mod. Phys. **74**, 99–144 (2002)

Crasovan, L.-C., Malomed, B.A., Mihalache, D.: Stable vortex solitons in the two-dimensional Ginzburg-Landau equation. Phys. Rev. E **63**, 0166051–6 (2000)

Falcao-Filho, E.L., de Araujo, C.B., Boudebs, G., Leblond, H., Skarka, V.: Robust two-dimensional spatial solitons in liquid carbon disulfide. Phys. Rev. Lett. **110**, 0139011–5 (2013)

Kivshar, Y.S., Agrawal, G.P.: Optical Solitons: From Fibers to Photonic Crystals. Academic, San Diego (2003)

Kovačević, A.G., Ristić-Djurović, J., Lekić, M.M., Hadzić, B., Abudagel, G.S.I., Petričević, S.J., Mihailović, P.M., Matović, B.Z., Dramlić, D.M., Brajović, L.M., Romčević, N.Z.: Influence of femtosecond pulsed laser irradiation on bismuth germanium oxide single crystal properties. Mater. Res. Bull. **83**, 284–289 (2016)

Lazarević, Z.Ž., Mihailović, P., Romčević, M.J., Kostić, S., Mitrić, M., Romčević, N.Ž.: Determination magnetno-optical quality and refractive index of bismuth germanium oxide single crystals grown by Czochralski technique. Opt. Mater. **34**, 1849–1859 (2012)

Mihalache, D., Mazilu, D., Lederer, F., Kartashov, Y.V., Crasovan, L.-C., Torner, L., Malomed, B.A.: Stable vortex tori in the three-dimensional cubic-quintic Ginzburg-Landau equation. Phys. Rev. Lett. **97**, 0739041–4 (2006)

Nicolis, G., Prigogine, I.: Self-organization in Nonequilibrium Systems. Wiley, New York (1977)

Skarka, V., Berezhiani, V.I., Miklaszewski, R.: Spatiotemporal soliton propagation in saturating nonlinear optical media. Phys. Rev. E **56**, 1080–1087 (1997)

Skarka, V., Berezhiani, V.I., Miklaszewski, R.: Generation of light spatiotemporal soliton from asymmetric pulses in saturating nonlinear media. Phys. Rev. E **59**, 1270–1273 (1999)

Skarka, V., Aleksić, N.B.: Stability criterion for dissipative soliton solutions of the one-, two-, and three-dimensional complex cubic-quintic Ginzburg-Landau equations. Phys. Rev. Lett. **96**, 0139031–4 (2006)

Skarka, V., Aleksić, N.B., Leblond, H., Malomed, B.A., Mihalache, D.: Varieties of stable vortical solitons in Ginzburg-Landau media with radially inhomogeneous losses. Phys. Rev. Lett. **105**, 2139011–4 (2010)

Skarka, V., Aleksić, N.B., Lekić, M., Aleksić, B.N., Malomed, B.A., Mihalache, D., Leblond, H.: Formation of complex two-dimensional dissipative solitons via spontaneous symmetry breaking. Phys. Rev. A **90**(2), 0238451–6 (2014)

Skarka, V., Aleksić, N.B., Krolikowski, W., Christodoulides, D.N., Rakotoarimalala, S., Aleksić, B.N., Belić, M.: Self-structuring of stable dissipative breathing vortex solitons in a colloidal nanosuspension. Opt. Express **25**, 10090–10102 (2017)

Optical and Quantum Electronics (2020) 52:301
https://doi.org/10.1007/s11082-020-02398-2

Inducing LIPSS on multilayer thin metal films by femtosecond laser beam of different orientations

Aleksander G. Kovačević[1] · **Suzana M. Petrović**[2] · **Branislav Salatić**[1] · **Marina Lekić**[1] · **Borislav Vasić**[1] · **Radoš Gajić**[1] · **Dejan Pantelić**[1] · **Branislav M. Jelenković**[1]

Received: 3 November 2019 / Accepted: 12 May 2020

Abstract

The occurrence of laser-induced periodic surface structures (LIPSS) has been known for a while. Multilayer thin films, like Al/Ti, are suitable for LIPSS formation and attractive for applications—due to their wearing behavior and corrosion resistance; LIPSS generation may improve their properties as well. LIPSS properties depend not only on the material but also on the beam characteristics, like wavelength, polarization and scanning directions, etc. After exposing with NIR femtosecond pulses from Coherent Mira 900 laser system in several beam exposures, we have analyzed the samples of thin metal film systems with Tescan Mira3 SEM and NTegra AFM. The formation of LIPSS is most probably due to the generation of surface plasmon polariton, through the periodic distribution of energy in the interaction zone which lead to thermal processes in layers and interfaces. Two types of LIPSS were generated, which differ in shape, orientation and in ablation pronounced or not. For consecutive interactions in the same direction, LIPSS maintained its orientation, while for orthogonal passes LIPSS with mutually orthogonal orientation were generated. LIPSS period fluctuated between 320 and 380 nm and structures with pronounced ablation have significantly smaller width. Probable mechanism is that for greater accumulated energy pronounced ablation takes place giving LIPSS in the form of trenches or grooves, while for less accumulated energy the buildup of the material—probably due to pronounced oxidation—lead to LIPSS in the form of hills or ridges.

Keywords Laser nanostructuring · Thin metal films · LIPSS · Structures orientation

---

This article is part of the Topical Collection on Advanced Photonics Meets Machine Learning.

Guest Edited by Goran Gligoric, Jelena Radovanovic and Aleksandra Maluckov.

✉ Aleksander G. Kovačević
Aleksander.Kovacevic@ipb.ac.rs

[1] Institute of Physics, University of Belgrade, Belgrade, Serbia

[2] Institute of Nuclear Sciences "Vinča", University of Belgrade, Belgrade, Serbia

1 Introduction

Interaction of pulsed laser beam with surfaces yields the appearance of LIPSS (laser-induced periodic surface structures). The occurrence of LIPSS has long been known and studied (Birnbaum 1965; Van Driel et al. 1982; Sipe et al. 1983; Young et al. 1984; Ursu et al. 1985). It has been studied on variety of materials: metals (Ursu et al. 1985; Wang and Guo 2005; Vorobyev and Makin 2007; Vorobyev and Guo 2008, 2013), semi-conductors (Von der Linde et al. 1997; Bonse and Krüger 2010; Bonse et al. 2011; Varlamova et al. 2014), dielectrics (Reif et al. 2008), graphite (Golosov et al. 2011), compounds (Kautek et al. 2005; Gakovic et al. 2011), diamond (Shinoda et al. 2009), graphene (Beltaos et al. 2014). LIPSS properties depend not only on the material but also on the beam characteristics, like wavelength, polarization and scanning directions, etc. (Kovačević et al. 2017).

Surface morphology is a key factor in controlling the optical, mechanical, wetting, chemical, biological, and other properties of a solid surface. LIPSS may improve material properties by functionalization and may widen applications: structural coloring, absorptance enhancement, antireflective films, biomedical applications, optofluidics applications, holography, anti-counterfeiting, decorating, sensing, catalysis, optical data storage (Vorobyev and Guo 2013).

The occurrence of LIPSS can be viewed as an inherent phenomena of the interaction of the ultrafast beam with solid surface, with main characteristics that the spatial period of LIPSS is less than the beam wavelength. The orientation depends on the incident beam polarization direction. Generation is explained by self-organization or by surface plasmon polaritons (SPP) (Vorobyev and Makin 2007; Reif et al. 2008). Incident wave induces oscillations of charges (surface plasmon) and SPP forms as the coupling between incident and induced waves; in this way periodic distribution of energy is formed on the surface.

Two types of LIPSS are reported: low spatial frequency LIPSS (LSFL) and high spatial frequency LIPSS (HSFL) (Bonse et al. 2005). LSFL period $\lesssim$ wavelength and HSFL period < wavelength/2. Named after their size (magnitude of spatial frequency), their orientation in respect to the polarization direction is not yet fully understood. It seems that LSFL orientation is perpendicular to polarization for metals and semiconductors (Bonse et al. 2012). Due to SPP, periodical distribution of thermal energy on the surface can instigate thermal processes. The occurrence of metal-oxide, or thermochemical type of LIPSS has been reported on Ti, Ni, Cr and NiCr surfaces, as well as ablative LIPSS and models have been proposed (Öktem et al. 2013; Dostovalov et al. 2017, 2019a).

When creating LIPSS on multilayer thin metal films, the underneath layer has an important role. In the example of Al/Ti multilayer film (Kovačević et al. 2015), Ti and Al have different electron heat conductivity and electron–phonon coupling. Top layer (Al) electrons accept energy and quickly transfer to the next layer (Ti). Strong coupling keeps the energy in Ti and away from topmost Al. In this way, the damage threshold for Al increases which preserves LIPSS for longer expositions. In this work, we have examined the LIPSS generated upon consecutive scanning over the same area of same and of different scanning orientations. By changing the parameters of the beam (fluence, scanning speed, scanning number and directions over the same area) the formation of LIPSS was affected. Two types of LIPSS, which differ in shape, orientation to the incoming beam polarization and in ablation pronounced or not, are generated and examined during repeated consecutive scanning of same and orthogonal directions. For lower accumulation on energy, LIPSS in the form of ridges formed while for higher fluences and accumulated energies, the generation of LIPSS gave prevalence to the ablation. After repeated consecutive scanning along the same trajectory LIPSS preserved to some extent. Also, during scanning along close parallel lines, LIPSS from one line affected generation of LIPSS from neighboring line. Overlapping scanning lines should generate LIPSS mutually perpendicular. We have examined the three cases of LIPSS: repeated consecutive scanning along same trajectory, scanning with close parallel lines, and scanning with perpendicular lines. The results can be of use in functionalization of materials by LIPSS forming with possible impact in wetting and biomedical applications.

2 Experiment and methods

The samples were prepared by D.C. ion sputtering in a single vacuum run, using Ar ions and switching from one target to the other. Targets were 99.9% pure Al and Ti deposited on a Si(100) wafer as a substrate. In this way, 5×(Al/Ti) multilayer structures have been generated, where each layer was 13 nm thick and total thickness of the multilayer structure was 130 nm.

Coherent Mira 900 laser system was a source of NIR femtosecond pulses (wavelength 730–840 nm, repetition rate 76 MHz, fluence 145–260 mJ/cm^2) pumped by Verdi V10 Nd:YVO4 CW laser (wavelength 532 nm, power 10 W) for exposition of the samples. Steering and focusing was a part of a modified optical microscope with 2D mirror scanner (objective 40×, NA 0.65). Ocean optics HR2000CG UV-NIR fiber spectrometer was used for spectral detection. The samples have been analyzed with Tescan Mira3 SEM and NTegra Prima AFM under ambient conditions. The numerical simulations have been performed by COMSOL Multiphysics package, with one-dimensional two-temperature (1D TTM) model. Basic relations underlying the TTM model were proposed by Anisimov (Anisimov et al. 1974). The model observes the electron and lattice subsystems. TTM model has been used for many years to calculate the temperature of the electrons and lattice during interaction of ultrashort laser pulses with different materials. All necessary physical quantities and constants that we used in the simulation can be found in the literature (Majchrzak et al. 2010a, b). The fs beam from laser was introduced into the modified microscope onto the steering two-axis scanning mirror system and transferred through the objective of the microscope to the sample.

Patterns used for interaction are presented in Fig. 1. For consecutive repeated scanning over same trajectory, the pattern in the form of letter “N” is used (Fig. 1a). The laser beam traverses over the sample surface following the pattern of the letter. At first location, it “writes” one letter. At second (neighboring) location, it traverses the same trajectory twice, writing two letters one over another. At third location, it writes three letters, and so on. The pattern used for perpendicular overlapped scanning is composed of set of parallel lines and the sample is rotated by 90° (Fig. 1b).

3 Results and discussion

The samples were exposed to laser beam of 730, 800 and 840 nm of wavelength with different fluences. Irradiated areas were examined by SEM and AFM. For specified parameters, simulations of 1D temperature distribution were performed.

In Fig. 2, the results after beam of 800 nm wavelength and 153 mJ/cm^2 of fluence repeatedly scanned from 1 to 10 times over the surface are presented. The area where beam

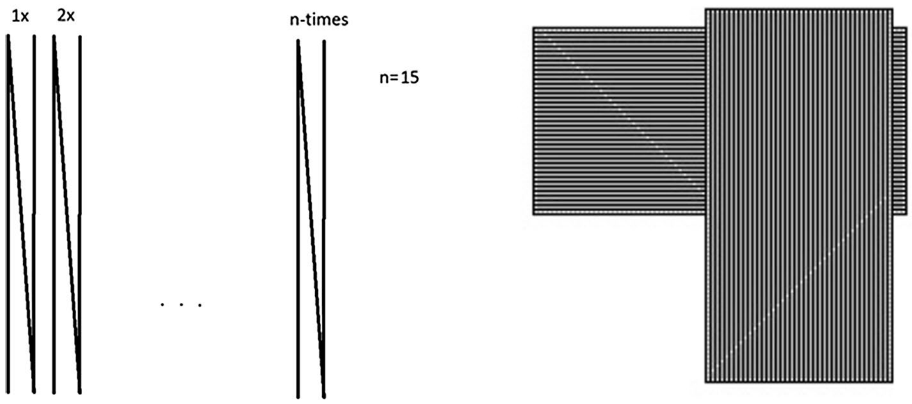

(a) (b)

Fig. 1 Implemented patterns of scanning: **a** for consecutive repeated scanning; **b** for perpendicular overlapped scanning

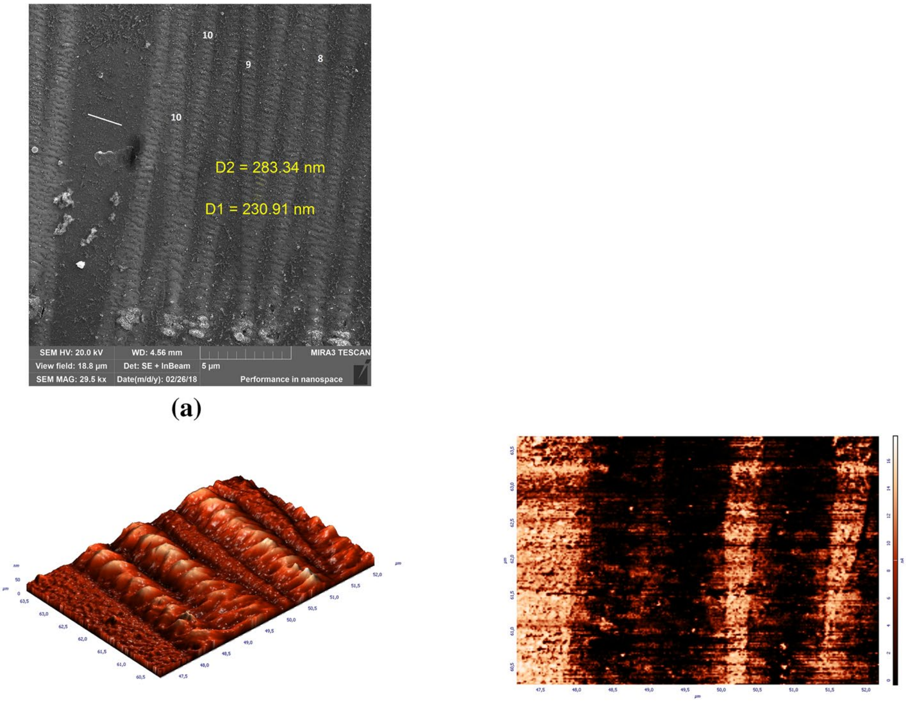

(a)

(b)

(c)

Fig. 2 LIPSS generated after beam of 153 mJ/cm^2 repeatedly scanned over the same trajectory: **a** SEM of the area of 8–10 passes: **b** AFM, detailed portion of the area in **a**—rendered area is (3×5) µm and maximal height is 50 nm; **c** graphical presentation of the AFM current (a.u.) of the area in **b**

scanned 8, 9 and 10 times along the same trajectory, following the shape of the letter "N", is shown in Fig. 2a. White line on the left side of the image presents polarization direction. The beam repetition rate was 76 MHz, diameter ~ 1.2 μm, scanning speed 242 μm/s. Effective number of pulses (number of pulses which affect the area of a beam spot) for one pass is 317,000. LIPSS in the form of ridges parallel to the polarization direction with spatial period of ~ 283 nm are generated and preserved up to 10 passes. In Fig. 2b, detailed AFM view of a part of the area from Fig. 2a which shows 10 passes is presented. AFM current of the area from Fig. 2b is shown in Fig. 2c.

The simulation of the lattice temperature from the surface to the bulk is shown in Fig. 3. Odd layers (Al) are presented with light grey bars, even layers (Ti) are presented with grey bars, while substrate (Si) is presented with dark grey bar. After 1.25 ps (Fig. 3a), the temperature reaches maximum in the second (Ti) layer. After 20 ps (Fig. 3b), the temperature reaches maximum in the first (Al) layer.

In Fig. 4, the results after beam of: (a) 730 nm wavelength and 145 mJ/cm^2 fluence (repetition rate 76 MHz, diameter ~ 1 μm) scanned 15 times (scanning speed 1.14 mm/s, effective number of pulses for one pass 67,000) and (b) 800 nm wavelength and 215 mJ/cm^2 fluence (repetition rate 76 MHz, diameter ~ 1.1 μm) scanned 10 times (scanning speed 24 μm/s, effective number of pulses for one pass 667,000) along the same trajectories are presented. In Fig. 4a, LIPSS are in the form of ridges (spatial period of ~ 278 nm) parallel to the polarization direction. In Fig. 4b, LIPSS are in the form of grooves (spatial period of ~ 370 nm and groove width of ~ 80 nm) perpendicular to the polarization. In both cases LIPSS are preserved up to 15 and 10 passes, consecutively. Higher fluence provoked the appearance of groove-type of LIPSS. Spatial temperature distribution is similar in shape to the distributions shown in Fig. 3.

In order to create structures of mutual perpendicular direction at the same area, we performed perpendicular consecutive scanning of two (same) patterns by sample rotation (Fig. 1b). The beam was of 840 nm wavelength and the fluence was set to ~ 182 mJ/cm^2 in order to generate groove-type of LIPSS. The beam repetition rate was 76 MHz, scanning speed 1.5 mm/s. diameter ~ 1.1 μm, Effective number of pulses for one pass is 51,000.

In Fig. 5a, the interaction area of the sample with two consecutive beam scanning of the same pattern (Fig. 1b) is presented. The right-hand and lower parts of the image present areas where patterns don't overlap, while central, upper and left parts present overlapped patterns. Magnified portion of the right-hand part, Fig. 5b, shows that grooves of two

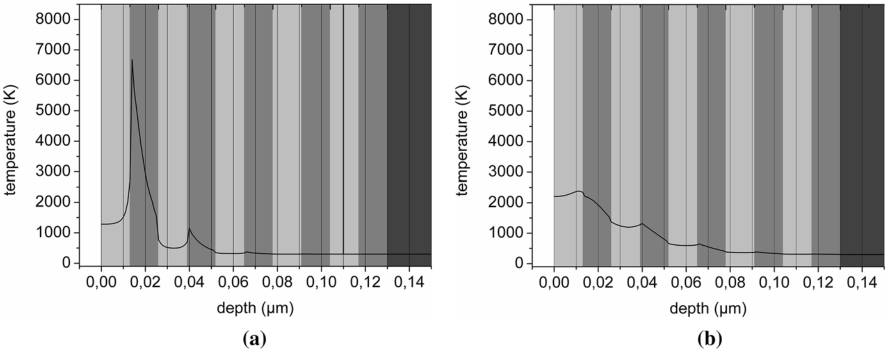

Fig. 3 Spatial temperature distribution from the surface to the bulk after exposition to the beam of 800 nm wavelength and 153 mJ/cm^2 of fluence: **a** after 1.25 ps; **b** after 20 ps

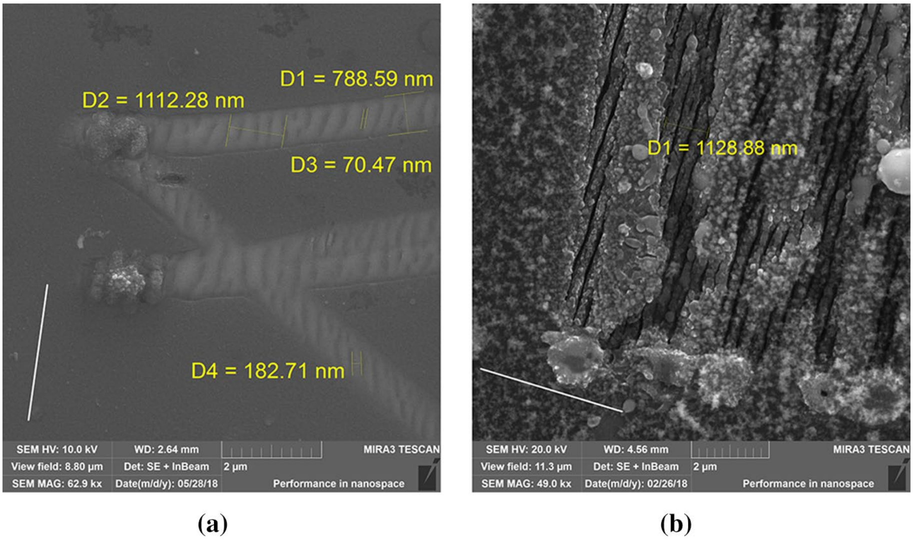

Fig. 4 SEM micrographs of LIPSS generated after beam of: **a** 145 mJ/cm^2 scanned 15 passes and **b** 215 mJ/cm^2 scanned 10 passes. White line on the left side shows polarization orientation

neighboring lines connect when patterns do not overlap. Where patterns overlap, Fig. 5c, grooves don't form in connected perpendicular directions; their width ranges from 98 to 126 nm.

The decrease in the AFM current (Fig. 2c) in the areas of laser exposition could be explained by increased resistivity of the exposed areas. Interaction with the beam fostered the penetration of nitrogen and/or oxygen into the first (Al) layer increasing the resistivity, which goes well with the three-step model (Öktem et al. 2013). The lattice temperature distribution from the surface to the bulk (Fig. 3) shows the influence of the multi-layer structure. After 1.25 ps (Fig. 3a), the temperature reaches maximum in the second layer (Ti). Moreover, the temperatures are higher in Ti layers than in neighboring Al layers. This is explained by the difference between two materials characteristics (Kovačević et al. 2015). Electrons from Al can quickly transfer energy to Ti layer away from the interaction zone due to the difference in electron–phonon coupling. This increases the damage threshold in Al leading to more regular ripples. The repetition rate also influences the regularity of the LIPSS, as noted in (Dostovalov et al. 2019b): higher the repetition rate, more ordered structures are formed.

The LIPSS in the form of ridges (Figs. 2a, 4a) are most probably generated by the penetration of the nitrogen and/or oxygen from the ambient (air) into the material—thermochemical LIPSS (Öktem et al. 2013; Dostovalov et al. 2017). For higher fluences, LIPSS formed in the form of grooves by ablation mechanisms, which can be deduced by scattered ejected material seen in Fig. 4b. Slower scanning speed and low melting point of Al induced energy accumulation sufficient for Al melting and ablation, which gave the prevalence of the generation of grooves (ablative LIPSS) over ridges (thermochemical LIPSS). The comparison of the spatial periods—283 nm (Fig. 2a) and 278 nm (Fig. 4a) for ridges versus 370 nm (Fig. 4b) for grooves—suggests grooves could be classified into LSFL and ridges into HSFL; this could be also supported by their orientation in respect to the beam polarization direction (Bonse et al. 2013).

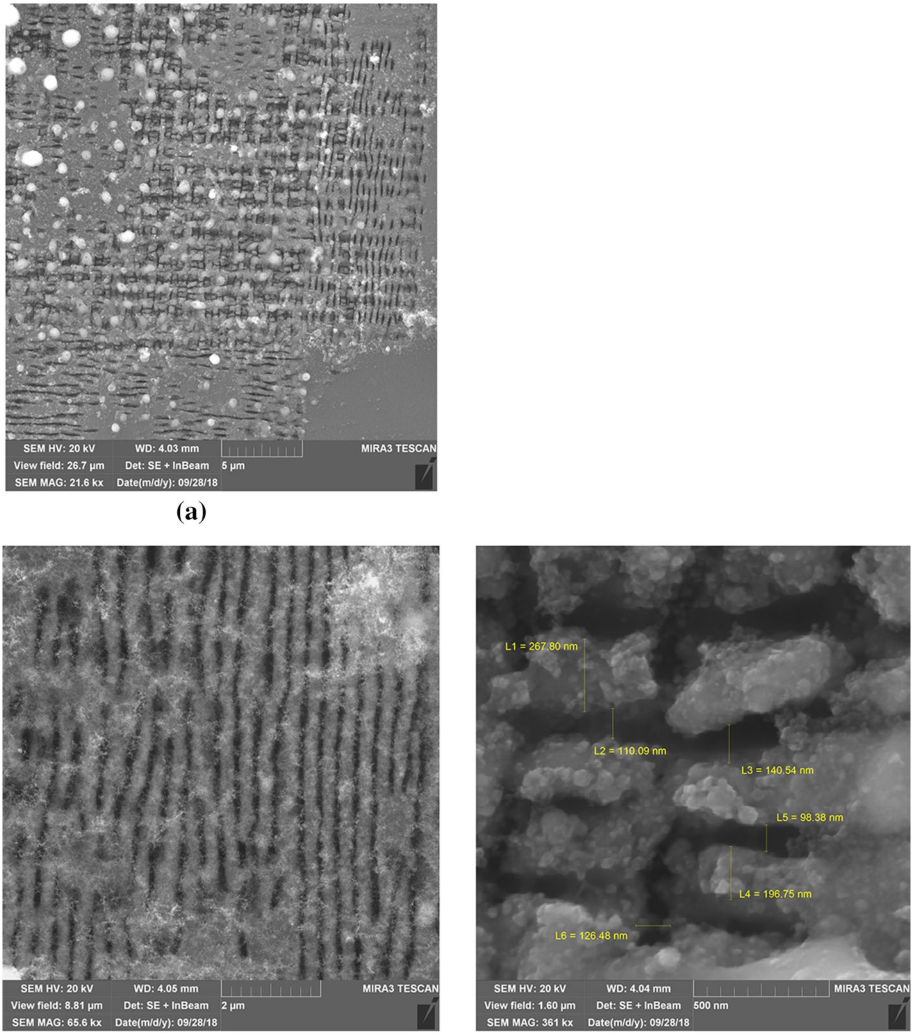

(a)

(b) (c)

Fig. 5 SEM micrograph of LIPSS generated by consecutive pattern scanning and sample rotation: **a** wide area; **b** right-hand part of the area in **a**; **c** magnified part of the central area in **a**

The attempt to generate intersecting perpendicular grooves was not successful. The reason is twofold. First generated LIPSS pattern distracts the formation of the second LIPSS pattern. Also, the formation of the second LIPSS pattern smears the first LIPSS pattern due to the accumulation of energy.

4 Conclusion

We have exposed 5×(Al/Ti) multilayer thin film metal structures to fs laser beam of various wavelengths and fluences. Due to differences in materials characteristics, the temperatures are higher in Ti layers than in neighboring Al layers, which was illustrated by simulations. The appearance of LIPSS indicates lateral periodical distribution of temperature in second layer (Ti). Two types of LIPSS emerged depending on the beam fluence. For fluence lower than ~ 170 mJ/cm^2, LIPSS in the form of ridges are generated most probably by the penetration of nitrogen and/or oxygen into the sample material (thermochemical LIPSS), which can be deduced by the decrease in the AFM current indicating the increase in resistivity. For higher fluences (above 170 mJ/cm^2), LIPSS in the form of grooves are generated by ablation mechanisms (ablative LIPSS). Both types are preserved after 10–15 consecutive beam scanning along the same trajectory. Intersecting perpendicular LIPSS can't be successfully formed because of competing influences of perpendicular patterns causing smearing of LIPSS.

Acknowledgements The work was supported by the Ministry of Science of the Republic of Serbia under No. III45016, OI171038 and OI171005. The authors appreciate the valuable help from: Dr. Davor Peruško (Institute of Nuclear Sciences "Vinča", University of Belgrade), Dr. Aleksandar Krmpot, Dr. Mihajlo Rabasović, Dr. Svetlana Savić-Šević and Vladimir Lazović (Institute of Physics, University of Belgrade), Dr. Đorđe Veljović and Dr. Željko Radovanović (Faculty of Technology and Metallurgy, University of Belgrade).

References

Anisimov, S.I., Kapeliovich, B.L., Perel'man, T.L.: Electron emission from metal surface exposed to ultrashort laser pulses. Sov. Phys. JETP **39**, 375–377 (1974)

Beltaos, A., Kovačević, A.G., Matković, A., Ralević, U., Savić-Šević, S., Jovanović, Dj, Jelenković, B.M., Gajić, R.: Femtosecond laser induced periodic surface structures on multi-layer graphene. J. Appl. Phys. **116**, 204306 (2014)

Birnbaum, M.: Semiconductor surface damage produced by ruby lasers. J. Appl. Phys. **36**, 3688–3689 (1965)

Bonse, J., Krüger, J.: Pulse number dependence of laser-induced periodic surface structures for femtosecond laser irradiation of silicon. J. Appl. Phys. **108**, 034903 (2010)

Bonse, J., Munz, M., Sturm, H.: Structure formation on the surface of indium phosphide irradiated by femtosecond laser pulses. J. Appl. Phys. **97**, 013538 (2005)

Bonse, J., Rosenfeld, A., Krueger, J.: Implications of transient changes of optical and surface properties of solids during femtosecond laser pulse irradiation to the formation of laser-induced periodic surface structures. Appl. Surf. Sci. **257**, 5420–5423 (2011)

Bonse, J., Krüger, J., Höhm, S., Rosenfeld, A.: Femtosecond laser-induced periodic surface structures. J. Laser Appl. **24**, 042006 (2012)

Bonse, J., Höhm, S., Rosenfeld, A., Krüger, J.: Sub-100-nm laser-induced periodic surface structures upon irradiation of titanium by Ti:sapphire femtosecond laser pulses in air. Appl. Phys. A **110**, 547–551 (2013)

Dostovalov, A.V., Korolkov, V.P., Terentyev, V.S., Okotrub, K.A., Dultsev, F.N., Babin, S.A.: Study of the formation of thermochemical laser-induced periodic surface structures on Cr, Ti, Ni and NiCr films under femtosecond irradiation. Quantum Electron. **47**, 631–637 (2017)

Dostovalov, A.V., Derrien, T.J.-Y., Lizunov, S.A., Přeučil, F., Okotrub, K.A., Mocek, T., Korolkov, V.P., Babin, S.A., Bulgakova, N.M.: LIPSS on thin metallic films: new insights from multiplicity of laser-excited electromagnetic modes and efficiency of metal oxidation. Appl. Surf. Sci. **491**, 650–658 (2019a)

Dostovalov, A.V., Okotrub, K.A., Bronnikov, K.A., Terentyev, V.S., Korolkov, V.P., Babin, S.A.: Influence of femtosecond laser pulse repetition rate on thermochemical laser-induced periodic surface structures formation by focused astigmatic Gaussian beam. Laser Phys. Lett. **16**, 026003 (2019b)

Gakovic, B., Radu, C., Zamfirescu, M., Radak, B., Trtica, M., Petrovic, S., Panjan, P., Zupanic, F., Ristoscu, C., Mihailescu, I.N.: Femtosecond laser modification of multilayered TiAlN/TiN coating. Surf. Coat. Technol. **206**, 411–416 (2011)

Golosov, E.V., Ionin, A.A., Kolobov, Yu.R., Kudryashov, S.I., Ligachev, A.E., Makarov, S.V., Novoselov, Yu.N., Seleznev, L.V., Sinitsyn, D.V., Sharipov, A.R.: Near-threshold femtosecond laser fabrication of one-dimensional subwavelength nanogratings on a graphite surface. Phys. Rev. B **83**, 115426 (2011)

Kautek, W., Rudolph, P., Daminelli, G., Kruger, J.: Physico-chemical aspects of femtosecond-pulse-laser-induced surface nanostructures. Appl. Phys. A **81**, 65–70 (2005)

Kovačević, A.G., Petrović, S.M., Bokić, B.M., Gaković, B.M., Bokorov, M.T., Vasić, B.Z., Gajić, R.B., Trtica, M.S., Jelenković, B.M.: Surface nanopatterning of Al/Ti multilayer thin films and Al single layer by a low-fluence UV femtosecond laser beam. Appl. Surf. Sci. **326**, 91–98 (2015)

Kovačević, A.G., Petrović, S., Lazović, V., Peruško, D., Pantelić, D., Jelenković, B.M.: Inducing subwavelength periodic nanostructures on multilayer NiPd thin film by low-fluence femtosecond laser beam. Appl. Surf. Sci. **417**, 155–159 (2017)

Majchrzak, E., Poteralska, J.: Two-temperature microscale heat transfer model. Part I: determination of electron parameters. Sci. Res. Inst. Math. Comput. Sci. Czestochowa Univ. Technol. **9**, 99–108 (2010a)

Majchrzak, E., Poteralska, J.: Two-temperature microscale heat transfer model Part II: Determination of lattice parameters. Sci. Res. Inst. Math. Comput. Sci. Czestochowa Univ. Technol. **9**, 109–119 (2010b)

Öktem, B., Pavlov, I., Ilday, S., Kalaycıoğlu, H., Rybak, A., Yavaş, S., Erdoğan, M., Ilday, F.Ö.: Nonlinear laser lithography for indefinitely large area nanostructuring with femtosecond pulses. Nat. Photonics **7**, 897 (2013)

Reif, J., Varlamova, O., Costache, F.: Femtosecond laser induced nanostructure formation: self-organization control parameters. Appl. Phys. A **92**, 1019–1024 (2008)

Shinoda, M., Gattass, R.R., Mazur, E.: Femtosecond laser-induced formation of nanometer-width grooves on synthetic single-crystal diamond surfaces. J. Appl. Phys. **105**, 053102 (2009)

Sipe, J.E., Young, J.F., Preston, J.S., van Driel, H.M.: Laser-induced periodic surface structure. I. Theory. Phys. Rev. B **27**, 1141–1154 (1983)

Ursu, I., Mihăilescu, I.N., Prokhorov, A.M., Konov, V.I., Tokarev, V.N.: On the role of the periodical structures induced by powerful laser irradiation of metallic surfaces in the energy coupling process. Phys. B+C **132**, 395–402 (1985)

Van Driel, H.M., Sipe, J.E., Young, J.F.: Laser-induced periodic surface structure on solids: a universal phenomenon. Phys. Rev. Lett. **49**, 1955–1958 (1982)

Varlamova, O., Martens, C., Ratzke, M., Reif, J.: Genesis of femtosecond-induced nanostructures on solid surfaces. Appl. Opt. **53**, I10–I15 (2014)

Von der Linde, D., Sokolowski-Tinten, K., Bialkowski, J.: Laser–solid interaction in the femtosecond time regime. Appl. Surf. Sci. **109–110**, 1 (1997)

Vorobyev, A.Y., Guo, C.: Femtosecond laser-induced periodic surface structure formation on tungsten. J. Appl. Phys. **104**, 063523 (2008)

Vorobyev, A.V., Guo, C.: Direct femtosecond laser surface nano/microstructuring and its applications. Laser Photonics Rev. **7**, 385–407 (2013)

Vorobyev, A.Y., Makin, V.S.: Periodic ordering of random surface nanostructures induced by femtosecond laser pulses on metals. J. Appl. Phys. **101**, 034903 (2007)

Wang, J., Guo, C.: Ultrafast dynamics of femtosecond laser-induced periodic surface pattern formation on metals. Appl. Phys. Lett. **87**, 251914 (2005)

Young, J.F., Sipe, J.E., van Driel, H.M.: Laser-induced periodic surface structure. III. Fluence regimes, the role of feedback, and details of the induced topography in germanium. Phys. Rev. B **30**, 2001–2015 (1984)

Materials Characterization 173 (2021) 110944

Contents lists available at ScienceDirect

Materials Characterization

journal homepage: www.elsevier.com/locate/matchar

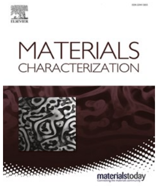

One-step preparation of gold nanoparticles - exfoliated graphene composite by gamma irradiation at low doses for photothermal therapy applications

D.P. Kepić [a,*], D.N. Kleut [a], Z.M. Marković [a], D.V. Bajuk-Bogdanović [b], V.B. Pavlović [c], A. J. Krmpot [d], M.M. Lekić [d], D.J. Jovanović [a], B.M. Todorović-Marković [a]

[a] *Vinča Institute of Nuclear Sciences - National Institute of the Republic of Serbia, University of Belgrade, P.O.B. 522, 11001 Belgrade, Serbia*
[b] *Faculty of Physical Chemistry, University of Belgrade, Studentski trg 12-16, 11158 Belgrade 118, P.O.B. 47, Serbia*
[c] *Faculty of Agriculture, Department of Agricultural Engineering, University of Belgrade, Nemanjina 6, 11080 Belgrade, Serbia*
[d] *Institute of Physics Belgrade, University of Belgrade, Pregrevica 118, 11080 Belgrade, Serbia*

ARTICLE INFO

Keywords:
Electrochemically exfoliated graphene
Gold nanoparticles
Composite nanomaterials
Gamma irradiation
Photothermal therapy
Cancer treatment

ABSTRACT

Graphene is an excellent material to anchor metal nanoparticles due to its large surface area. In this paper, we report the use of electrochemically exfoliated graphene as support to anchor gold nanoparticles (Au NPs). Au NPs are synthesized via the reduction of chloroauric acid under gamma irradiation at low doses of 1, 5, and 10 kGy and directly deposited onto the graphene surface, making this procedure simple and fast. Good water dispersibility of exfoliated graphene, due to the presence of oxygen-containing functional groups in the structure of graphene, provides long-term stability of Au NPs - graphene composite dispersions. The majority of the Au NPs obtained by this method have sizes of up to 40 nm, while the increase in the applied dose leads to an increase in the amount of smaller nanoparticles. The increase of temperature of the prepared composite material upon irradiation with an 808 nm continuous wave laser was monitored. All samples show a temperature increase between 21.5 and 25.6 °C for 10 min of the laser exposure, which indicates that Au NPs - graphene composite can effectively be used in photothermal treatment for cancer therapy.

1. Introduction

The unique structure of graphene put this material in the focus of scientific interest in the past years. Its fascinating electrical, mechanical, thermal, and optical properties are thoroughly investigated for the potential application in electronics as the new-generation electronic devices [1,2], sensors [3,4], and energy storage devices [5,6], as well as in biomedicine for bioimaging [7], drug delivery [8,9], and photothermal therapy [10], to name some. However, a major challenge in the processing of graphene lies in its poor dispersibility in water and other commonly used solvents. This issue can be solved by covalently modifying graphene's chemical structure by strong oxidants to introduce polar functional groups and make it water dispersible. The procedure generally involves the use of strong oxidants in acidic environments and elevated temperatures. As obtained material, denoted as graphene oxide (GO), is rich in oxygen-containing functional groups, but graphene sp^2 honeycomb structure becomes highly disrupted which negatively affects its performance. An additional step is required to reduce graphene oxide, but the structure becomes only partially restored leaving a large number of structural defects. A good alternative is electrochemical exfoliation of graphite [11,12], which reduces the oxidation degree of graphene and preserves its structural and electronic properties. Briefly, hydroxyl ions created from the reduction of water during electrochemical process bind to graphene edges and weaken van der Waals forces in graphite allowing the intercalation of electrolyte ions between graphene layers. In the next step, the reduction of intercalated ions and expansion of gas bubbles occur and graphene layers become detached. Since hydroxyl ions covalently bond graphene sheet only in the initial stage of the exfoliation, graphene structure is well preserved but with a sufficient number of attached polar groups to make graphene water dispersible. Following this approach, it is possible to obtain a high-yield of single- and few-layer graphene with large flake size. Compared to well-established methods for the production of graphene oxide, electrochemical exfoliation of graphite does not require harsh chemicals, making the procedure cost-efficient and environmentally friendly.

The large surface area of graphene could be easily used for the adsorption of various molecules and nanoparticles (NPs), creating graphene-based composites and hybrid materials [13,14]. Of particular

---

[*] Corresponding author.
E-mail address: d.kepic@vin.bg.ac.rs (D.P. Kepić).

https://doi.org/10.1016/j.matchar.2021.110944
Received 4 December 2020; Received in revised form 1 February 2021; Accepted 1 February 2021

interest are metal nanoparticles, which have mechanical, thermal, optical, and magnetic properties different from their bulk counterparts due to the effects that emerge from their size. Currently, various synthetic strategies are being developed for their production and a majority of them imply the reduction of metal ions to their zero-valent state. To prevent agglomeration and overgrowth of a freshly formed NPs, a stabilizing agent is introduced to the reaction mixture during synthesis. The role of the agent usually has sodium citrate, which deactivates the surface of formed nanoparticles, and polymers such as polyvinyl pyrrolidone (PVP) [15,16] or cetyltrimethylammonium bromide (CTAB) [17,18], which acts as a capping agent and anchors metal nanoparticles on its surface. Graphene oxide was used as a support for the synthesis of Ir NPs [19], as well as Pt—Ru NPs for the electro-oxidation of methanol and ethanol [20] and Au NPs for glucose biosensor [21,22] and for the development of surface-enhanced Raman spectroscopy (SERS) platforms [23]. Additionally, metal NPs have great potential to be applied in photothermal therapy for cancer treatment [24–26]. Photothermal therapy has emerged as a promising strategy for cancer treatment due to the selective hyperthermia of tumor tissue. The strategy involves selective delivery of various nanoparticles into tumor tissue and the irradiation of the tissue with wavelengths that correspond to the near-infrared or therapeutic window. The electrons in the conduction band tend to oscillate under the irradiation and the absorbed light is converted into heat, which further leads to the irreversible damage of the tumor tissue. Among different nanoparticles that can be implemented in this strategy, gold nanoparticles are of particular interest because they absorb light in the near-infrared region and their optical properties can be easily tuned by varying their dimensions and structure [27,28].

Compared to classical chemical approach, gamma irradiation provides fast and clean route to perform reduction reactions at room temperature. To date, various metal nanoparticles were synthesized following this method. Wang et al. prepared Ag NPs - reduced graphene oxide (RGO) hybrids at doses of 50 and 160 kGy [29]. RGO was used as a support for Pt—Au nanocomposite prepared a dose of 150 kGy [30], and Ag—Au alloy nanoparticles at doses in a range from 29 to 115 kGy [31]. Ag NPs - GO nanocomposite was prepared by Zhao et al. at a dose of 150 kGy [32]. Beside GO and RGO, there is no report in the literature of the use of electrochemically exfoliated graphene as a support for the synthesis of metal nanoparticles under gamma irradiation.

In this work, for the first time electrochemically exfoliated graphene was used as a support to anchor Au nanoparticles. Au NPs were synthesized in one step by means of gamma irradiation at low doses (1–10 kGy) from chloroauric acid as a precursor in graphene dispersion in the absence of any stabilizing agents. The absence of reductants and polymers as stabilizing molecules preserves the chemical environment of metal NPs and consequently their performance, which makes this procedure simple and fast. The morphology of the obtained composite material was thoroughly investigated and the size distribution of the synthesized Au NPs was determined. The temperature elevation under an 808 nm laser irradiation of the Au NPs - exfoliated graphene was measured and the potential of this composite material for photothermal therapy is demonstrated.

2. Experimental procedure

2.1. Sample preparation

Electrochemical exfoliation of highly oriented pyrolytic graphite (HOPG, Vinča Institute of Nuclear Sciences, Serbia) was performed in a two-electrode system using graphite rods as both the counter and the working electrode, with the constant distance of 4 cm between the electrodes. The electrolyte solution was prepared by dissolving ammonium persulfate (Alfa Aesar) in water to obtain a concentration of 0.1 M. Direct current (DC) voltage of +12 V was applied, and the voltage was kept constant until the exfoliation process was completed (indicated by the total consumption of the working electrode). Exfoliated product was collected by vacuum filtration and washed with a copious amount of deionized water to remove any residual salt. After washing, the product was dispersed in water using an ultrasound bath. To remove graphitic residuals, the dispersion was centrifuged at 2575 ×*g*, and supernatant was used for further procedure. Gravimetrically determined graphene concentration in the dispersion was 1 mg/ml. In a certain volume of graphene dispersion was added chloroauric acid (Sigma Aldrich) to obtain final concentration of 1.25×10^{-4} M and isopropyl alcohol (1:10 volume ratio), and the mixture was purged with argon for 15 min to remove dissolved oxygen. After that, the vials are hermetically sealed and irradiated. Irradiations were carried out by gamma-ray flux from ^{60}Co nuclide at a radiation dose rate of 10.5 kGy/h. Samples were exposed to the gamma irradiation source absorbing the doses of 1, 5, and 10 kGy. Irradiation treatment was followed by filtration (0.2 μm pore size, Isopore Membrane Filters), after which the samples were washed with deionized water, and dried at 60 °C.

2.2. Sample characterization

Transmission electron microscopy (TEM) analyses were performed on TEM-JEOL JEM-1400 microscope operated at accelerating voltage of 120 kV. All samples for TEM were dispersed in ethanol and a drop of dispersion was deposited on lacey carbon copper grids (200 mesh). The particle size distribution was determined using Gwyddion software (version 2.44).

Atomic force microscopy (AFM) measurements were performed on Quesant microscope operating in tapping mode in air at room temperature. 50 μl of sample was dispersed in 300 μl of water and well homogenized on an ultrasound bath. A drop of dispersion was drop-casted on Si substrate and imaged after drying. Silicon tips (purchased from Nano and More) with constant force of 40 N/m were used. AFM images were analyzed using Gwyddion software (version 2.44).

The UV–vis absorption spectra were measured using Avantes UV–vis spectrophotometer (Apeldoorn, The Netherlands). Samples were recorded in quartz cuvettes at room temperature.

Raman spectra were recorded by confocal Raman microscope (alpha 300 R+, WiTec, Ulm, Germany). The excitation laser of the 532 nm wavelength and 76 μW power was focused using 100 × (NA = 0.9) objective onto the sample surface. The confocal pinhole diameter was 50 μm and the accumulation time for a single Raman spectrum was set to 40 s. Constant background was subtracted from all measured Raman spectra.

Fourier transform infrared spectroscopy (FTIR) spectra were acquired on Avatar 370 Thermo Nicolet spectrometer. The spectral resolution was 4 cm^{-1}. Samples were recorded in a form of KBr pellets.

XPS was performed using a Thermo Scientific K-Alpha XPS system (Thermo Fisher Scientific, UK) equipped with a micro-focused, monochromatic Al Kα X-ray source (1486.6 eV). An X-ray beam of 400 μm in size was used at 6 mA × 12 kV. The spectra were acquired in the constant analyzer energy mode with pass energy of 200 eV for the survey. Narrow regions were collected with pass energy of 50 eV. Charge compensation was achieved with the system flood gun that provides low energy electrons (~0 eV) and low energy argon ions (20 eV) from a single source. Thermo Scientific Avantage software, version 5.952 (Thermo Fisher Scientific), was used for the digital acquisition and data processing. Spectral calibration was determined by using the automated calibration routine and the internal Au, Ag and Cu standards supplied with the K-Alpha system.

For the photothermal efficiency measurements, stable dispersions of the samples in water with concentration of 1 mg/ml were prepared. Irradiation was conducted in quartz cuvettes at room temperature (20.3 °C). The samples were exposed to 808 nm continuous wave laser radiation with TEM00 mode radial distribution, slightly elliptical, with major and minor axes of 7.14 mm and 6.35 mm, respectively. The total laser irradiance was 2.16 W/cm^2. The temperature was monitored by a thermocouple (accuracy 0.1 °C) every 30 s. After 10 min of laser

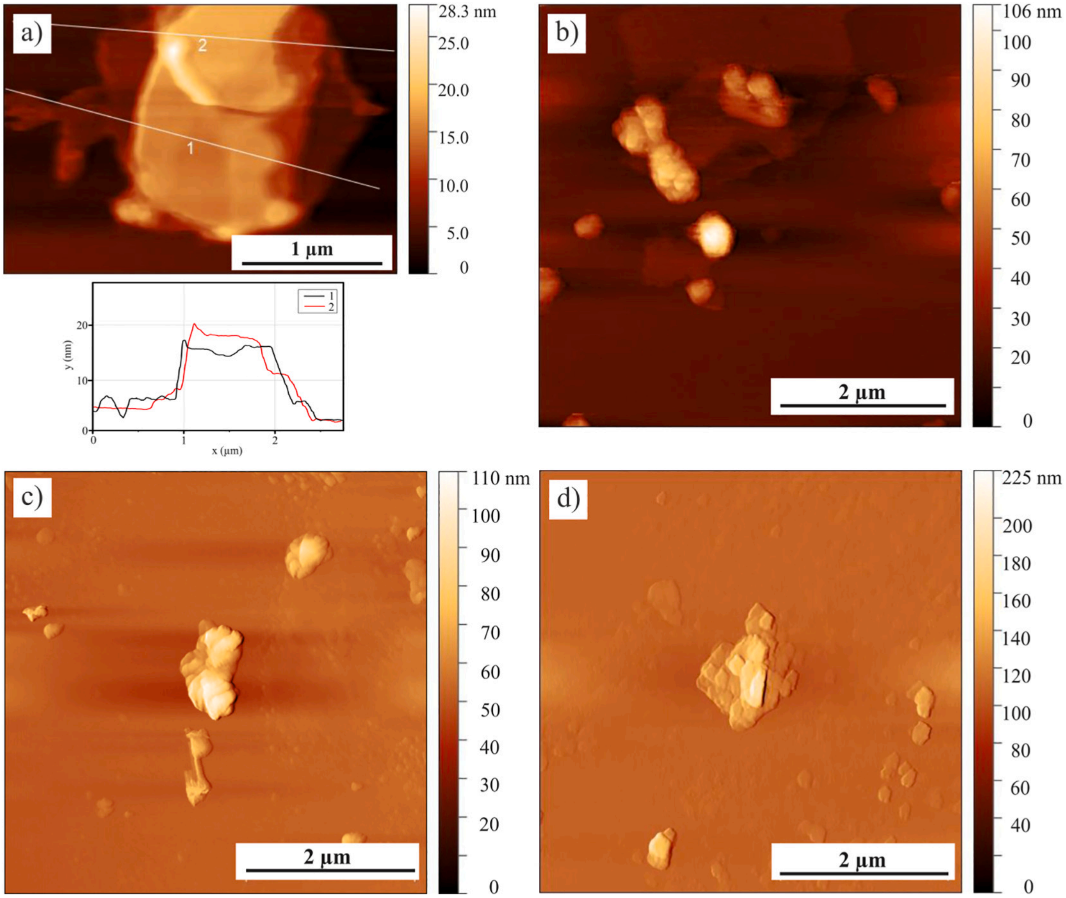

Fig. 1. Top view AFM images of (a) Au NPs - exfoliated graphene irradiated at 1 kGy and the corresponding height profiles (1 and 2) as indicated in the AFM image, (b) Au NPs - exfoliated graphene irradiated at 1 kGy, (c) Au NPs - exfoliated graphene irradiated at 5 kGy and (d) Au NPs - exfoliated graphene irradiated at 10 kGy.

irradiation laser was switched off and the temperature was monitored for the next 15 min. The photothermal efficiency (η) of the samples was calculated using Roper's method [33,34] according to the equation:

$$\eta = \frac{hS(T_{max} - T_{amb}) - Q_{loss}}{I\left(1 - 10^{-A_{808}}\right)} \tag{1}$$

where h is the heat transfer coefficient, S the surface area of the cuvette, and T_{max} and T_{amb} are the maximum and the ambient temperature, respectively. I represents the laser power, A_{808} the absorbance of the samples at 808 nm, and Q_{loss} is the heat dissipated from the light absorbed by the solvent and the cuvette. The value hS was calculated according to the equation:

$$hS = \frac{\Sigma_i m_i C_{pi}}{\tau_s} \tag{2}$$

where m_i and C_{pi} are the mass and the specific heat capacity of each component of the system, respectively. τ_s is the time constant that was calculated from Fig. 8b using the equations:

$$\theta = \frac{T - T_{amb}}{T_{max} - T_{amb}} \tag{3}$$

and

$$t = -\tau_s\, ln(\theta) \tag{4}$$

3. Results and discussion

3.1. Au NPs synthesis

Radiolysis of water induced by gamma irradiation generates both reductive and oxidative species [35]. In the presence of oxidation species scavenger, such as isopropyl alcohol, reactive species produced by water radiolysis generate isopropyl radical that is, among other generated reducing species, capable of reducing metal ions to metal in zero-valent state. The reduction of $[\mathrm{AuCl_4}]^-$ forms $\mathrm{Au^0}$ which combination further creates particle nuclei and leads to particle growth. The presence of a stabilizing agent such as polymers or surfactants plays an important role in the overall formation of nanoparticles. Functional groups from those molecules serve as anchoring sites for NPs nuclei. After the synthesis, it is often necessary to remove the stabilizing agent for the maximum performance of obtained NPs. Exfoliated graphene has a large surface area and a large number of functional groups that can anchor Au NPs nuclei and influence particle formation. The unique 2D structure of graphene can be effectively decorated with Au NPs to create novel composite material with good water dispersibility, making the removing step of the stabilizing agent redundant.

3.2. Morphology analyses

Morphology analyses were conducted by AFM and TEM. Fig. 1 shows representative AFM images of Au NPs - exfoliated graphene composite indicating that exfoliated graphene is mainly presented in a form of few-layer graphene. Statistical analysis based on AFM images shows that lateral sizes of exfoliated graphene flakes are in the range of several hundreds of nanometers up to several micrometers, without any

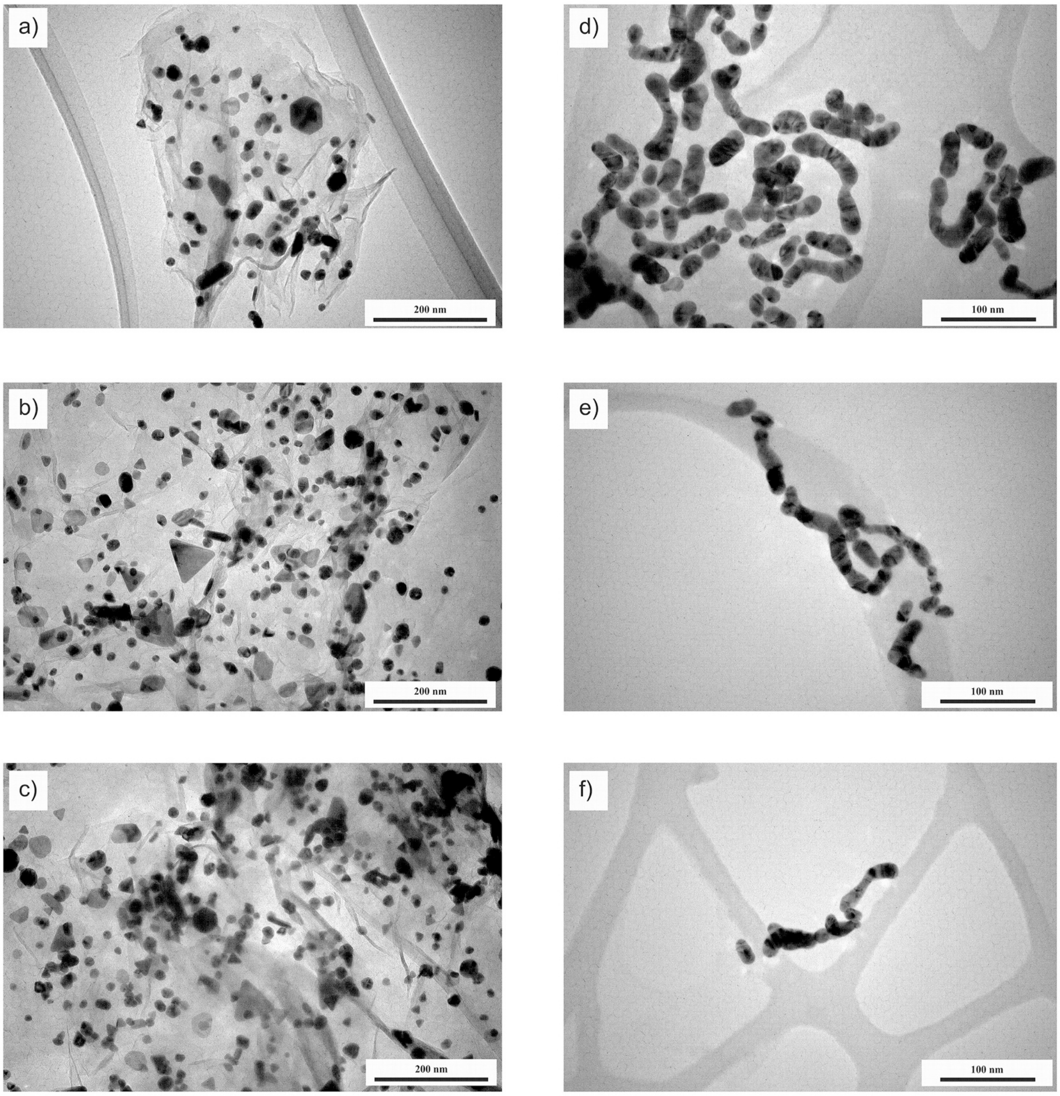

Fig. 2. TEM images of (a) Au NPs - exfoliated graphene irradiated at 1 kGy, (b) Au NPs - exfoliated graphene irradiated at 5 kGy, (c) Au NPs - exfoliated graphene irradiated at 10 kGy (d) Au NPs irradiated at 1 kGy, (e) Au NPs irradiated at 5 kGy and (f) Au NPs irradiated at 10 kGy.

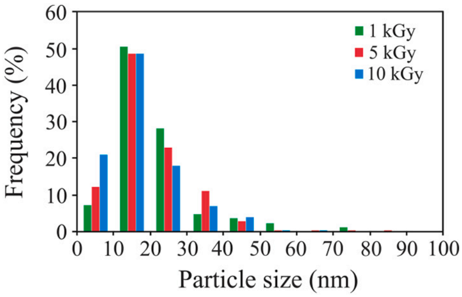

Fig. 3. Particle size distribution of Au NPs irradiated in the presence of graphene.

significant deviation caused by gamma irradiation at the applied doses.

TEM images of Au NPs - exfoliated graphene composites are presented in Fig. 2. As can be seen from the images, for the applied doses of 1, 5, and 10 kGy Au NPs are well distributed on the graphene surface. Also, for all the aforementioned doses gold nanoparticles of spherical, triangular, hexagonal, trapezoidal, and rod-shaped morphology are observed. A variety of Au NPs morphologies attached to the graphene sheet was previously reported and is related to the presence and the abundance of functional groups and defects on graphene layers [36]. To investigate this issue, we irradiated chloroauric acid at the same conditions in the absence of graphene and analyzed the morphology of obtained NPs. The reduction of chloroauric acid under gamma irradiation takes place, but the final result are irregularly shaped gold nanowires and, to a smaller extent, irregularly shaped gold nanospheres. Interestingly, similar Au formations were found as a product of quenched citrate reduction of chloroauric acid [37].

Gamma irradiation is found to be an efficient synthetic route for metal NPs because of the possibility to control the nanoparticles' sizes and size distribution by controlling the radiation dose [38]. According to the statistical analysis, nearly half of the prepared Au NPs have sizes in the 11–20 nm range for all the applied doses (Fig. 3). It is worth noting that the increase in the applied dose leads to the increase in the amount of smaller nanoparticles (up to 10 nm in size). The formation of Au NPs is composed of two consecutive steps - nucleation and aggregation. At low doses the concentration of formed nuclei is smaller than the concentration of the Au ions that participate in the growth step, therefore the synthesized Au NPs are larger in size. On the other hand, at the higher applied doses most of the Au precursor is consumed to form nuclei which concentration becomes larger than the concentration of

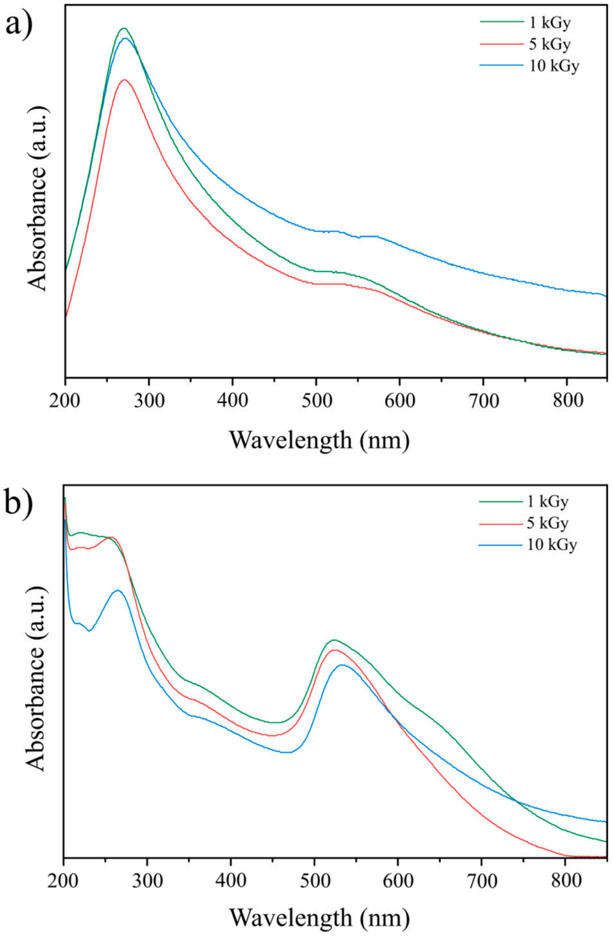

Fig. 4. UV–vis spectra of (a) Au NPs - exfoliated graphene and (b) Au NPs irradiated at different doses.

unreduced Au ions, which consequently leads to the growth of smaller NPs [39].

3.3. Spectroscopy analyses

While UV–vis spectrum of graphene oxide is dominated by the peak at 230 nm, originating from π-π* transition of aromatic C═C bonds, and a shoulder at ~300 nm attributed to n-π* transition of C═O bonds [40], exfoliated graphene displays only one broad peak at 270 nm [41]. The red shift of π-π* transition peak to the values of 270 nm is already documented and it is attributed to the restoration of graphene's electronic conjugation upon hydrazine reduction [42]. The peak at 270 nm for exfoliated graphene, along with the absence of a 300 nm shoulder peak, indicates that in the exfoliated graphene the graphene's structure is well preserved. UV–vis spectra of Au NPs - exfoliated graphene composite (Fig. 4a) show one large intensity peak at 270 nm and a smaller broad peak at 530 nm. The peak at 530 nm originates from the localized surface plasmon resonance of Au NPs. In the UV–vis spectra of Au NPs synthesized without graphene (Fig. 4b) this peak shows a slight red shift with the increase of the radiation dose. Interestingly, the same spectra show a peak at 261 nm from the electron transition from the occupied d-level states to empty states in the conducting band above the Fermi level [36] and is more prominent for the higher applied doses. In the spectra of Au NPs - exfoliated graphene composites this peak overlaps π-π* transition peak from graphene.

Reactive species produced by water radiolysis induce also the reduction of graphene materials [43]. Prepared exfoliated graphene dispersion in a concentration of 1 mg/ml shows long-term stability in water. Good graphene dispersibility in a polar solvent is due to the presence of polar oxygen-containing functional groups attached to the graphene surface, such as hydroxyl, carboxyl, epoxy, and carbonyl. The changes in graphene structure upon irradiation were investigated by means of FTIR, XPS, and Raman spectroscopy. Two dominant peaks in Raman spectra of Au NPs - graphene composite are located at 1351 cm^{-1} and 1591 cm^{-1} and are attributed to D and G band respectively (Fig. 5). The D band is attributed to disordered sp^3-hybridized carbon material from defects and functionalities, while the G band is related to well-ordered sp^2 graphite-type structures [44]. Besides, peaks at 2695 cm^{-1} and 2938 cm^{-1} are also observable and can be attributed to 2D band and (D + G) combination mode. For all the applied doses Raman peaks do not show any shift. The intensity ratio of D and G bands (I_D/I_G) gradually increases with the increase of the irradiation dose from 1.14 for non-irradiated graphene to 1.30 for Au NPs - graphene composite irradiated at 10 kGy. This could be the consequence of Au NPs bonding to the graphene sheets.

To get a better insight into the type of functional groups attached to the graphene structure, FTIR spectroscopy was performed (Fig. 6). The most prominent bands in FTIR spectra correspond to the stretching and

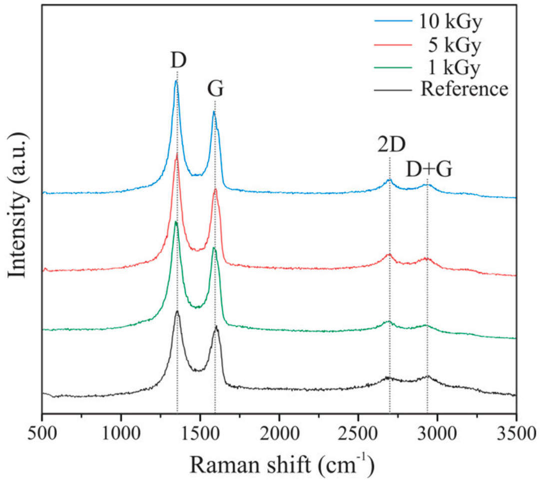

Fig. 5. Raman spectra of exfoliated graphene (reference) and Au NPs - exfoliated graphene irradiated at different doses.

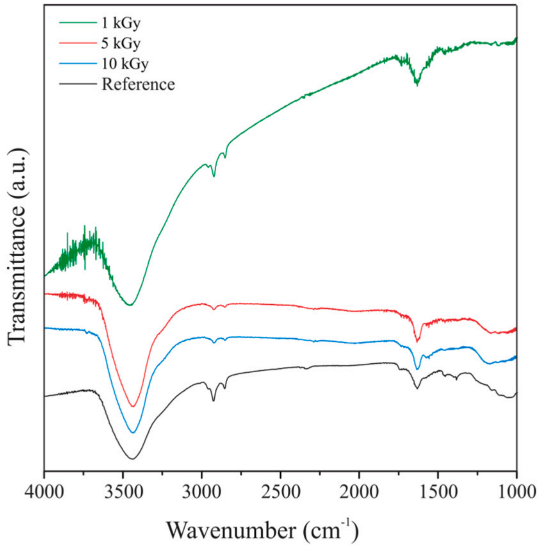

Fig. 6. FTIR spectra of exfoliated graphene (reference) and Au NPs - exfoliated graphene irradiated at different doses.

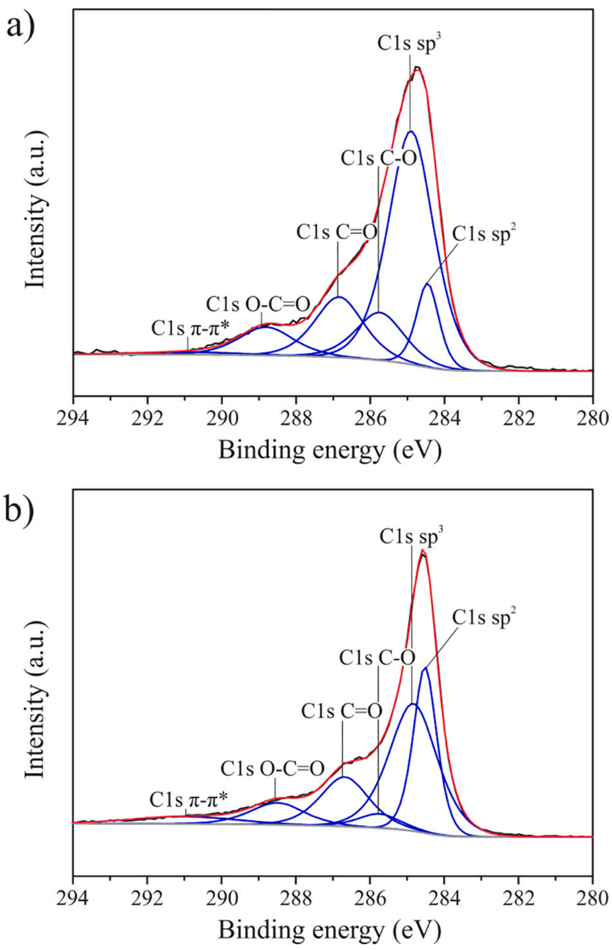

Fig. 7. XPS spectra of (a) non-irradiated graphene and (b) graphene irradiated at 10 kGy.

Table 1
XPS data of the characteristic bonds from deconvoluted C1s peak.

Name	Binding energy (eV)	Exfoliated graphene (at. %)	Graphene irradiated at 10 kGy (at.%)
C1s sp^2	284.5	9.7	26.0
C1s sp^3	284.9	54.4	41.1
C1s C-O	258.7	11.8	4.0
C1s C=O	286.8	14.9	16.0
C1s O-C=O	288.6	7.8	7.9
C1s π-π*	291.0	1.4	5.0

bending mode of hydroxyl groups (3400–3500 cm^{-1} and ~ 1633 cm^{-1}, respectively) [45]. Bands at 2930 and 2850 cm^{-1} indicate the presence of CH_2 groups. In addition, in the FTIR spectra of exfoliated graphene bands at ~1734 cm^{-1} (C═O groups), ~1574 cm^{-1} (C═C groups) and ~ 1177 cm^{-1} (C—O groups) can also be observed. As the irradiation dose increases, the band at ~1574 cm^{-1} becomes more prominent, while the bands in the range 2930–2850 cm^{-1} show a decrease, which implies the partial restoration of graphene structure.

The restoration of the graphene structure is further confirmed by means of XPS. Deconvoluted high-resolution XPS spectra of C1s peak of as-prepared exfoliated graphene and graphene irradiated at the dose of 10 kGy are shown in Fig. 7 and the data for the characteristic bonds are listed in Table 1. The deconvolution of C1s XPS spectra gives features at 284.5, 284.9, 258.7, 286.8, 288.6, and 291.0 eV which reveal the presence of sp^2 and sp^3 carbon, hydroxyl/epoxy groups, carbonyl, and carboxyl groups, and π-π* shake up band [46,47]. From the XPS data, it is evident the increase of the carbon sp^2 content after the irradiation. Simultaneously, the carbon sp^3 content decreases, along with the content of C—O bonds. The irradiation induces the change in C/O ratio from 1.8 for non-irradiated graphene to 3.5 for graphene irradiated at 10 kGy.

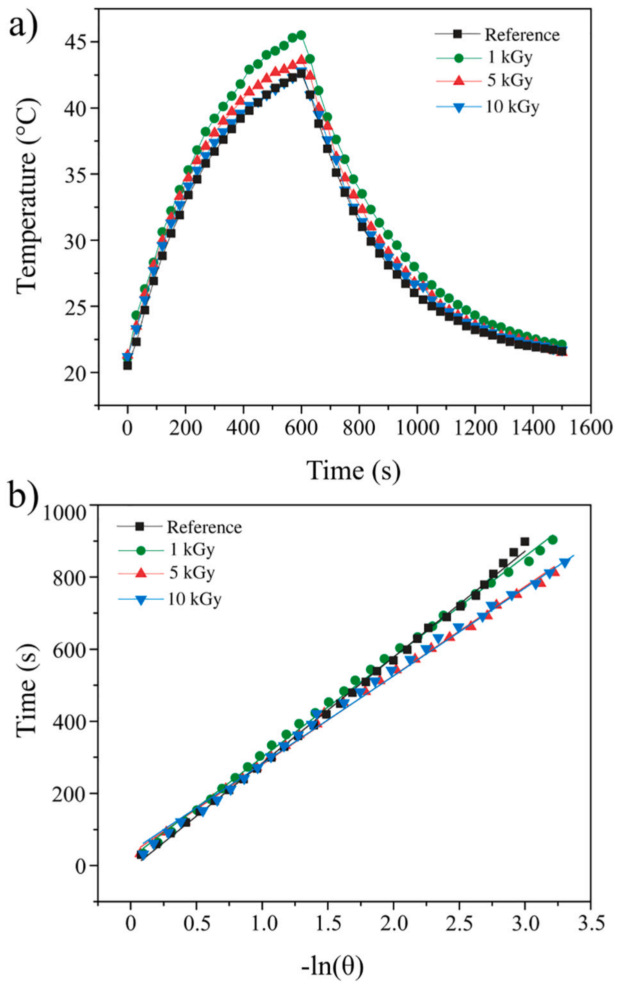

Fig. 8. (a) Temperature profiles of exfoliated graphene (reference) and Au NPs - exfoliated graphene composites under 808 nm continuous wave laser excitation and (b) linear fitting of time data versus -ln(*θ*) acquired from the cooling period.

3.4. Photothermal efficiency measurements

For the photothermal efficiency measurements, the prepared Au NPs - exfoliated graphene composites were irradiated with an 808 nm continuous wave laser and the temperature elevation was monitored for 10 min. After that time the laser was switched off and the temperature was monitored during the cooling period (15 min). The results of these measurements are presented in Fig. 8a.

For successful photothermal therapy, it is important to heat the tumor tissue at a minimum of 41 °C, which corresponds to the 4 °C temperature increase in the body [48]. Nanomaterials that are able to convert the absorbed light into heat and cause a temperature increase of a minimum of 4 degrees are considered suitable for photothermal therapy. As expected, the irradiation of pure medium (water) does not induce the temperature increase. On the other hand, the irradiation of exfoliated graphene, as well as Au NPs - exfoliated graphene composites, induce the temperature increase. The highest temperature elevation of 25.6 °C is observed for Au NPs - graphene irradiated at 1 kGy. With the increase of the irradiation dose, a slight decrease in the temperature elevation could be observed. To determine the photothermal efficiency

Table 2
Calculated photothermal efficiency of exfoliated graphene (reference) and Au NPs - exfoliated graphene composites irradiated at different doses.

Sample	Time constant τ_s	Absorbance at 808 nm	Photothermal efficiency (η)
Reference	293.77	0.13	58.26%
1 kGy	246.99	0.13	73.55%
5 kGy	278.66	0.12	72.16%
10 kGy	243.70	0.12	70.96%

of the samples, the temperature decrease was monitored with the laser switched off. The values of τ_s were calculated from Fig. 8b using eqs. (3) and (4). Taking into account the values of hS obtained from the eq. (2), laser incident power of 0.77 W, and the absorbances at 808 nm, photothermal efficiency (η) was calculated from the eq. (1) and listed in Table 2. As expected, the highest value of photothermal efficiency of 73.55% has Au NPs - graphene composite irradiated at 1 kGy, while the increase in the irradiation dose slightly decreases the photothermal efficiency of the material. These measurements demonstrate the efficient photothermal conversion of the incident laser light of Au NPs - graphene composites that have the potential to be used in photothermal treatment in cancer therapy.

4. Conclusion

In this paper, one-step synthesis of graphene supported Au NPs via gamma irradiation at low doses is demonstrated. Graphene, prepared by the electrochemical exfoliation of highly ordered pyrolytic graphite, is presented as few-layer graphene with lateral sizes that range from several hundred nanometers up to several micrometers. Au NPs were synthesized from chloroauric acid as a precursor in graphene dispersion in the absence of any stabilizing agents at doses of 1, 5, and 10 kGy. Polar oxygen-containing functional groups at the graphene surface provide good water dispersibility of Au NPs - graphene composites. Nearly half of the prepared Au NPs have sizes in the range from 11 to 20 nm, and the increase in the applied dose leads to an increase in the amount of smaller nanoparticles (up to 10 nm in size). For all the applied doses particles of spherical, triangular, hexagonal, trapezoidal, and rod-shaped morphology are observed. The prepared composite material shows the increase of temperature upon irradiation with an 808 nm continuous wave laser, which is the most prominent for Au NPs - graphene irradiated at 1 kGy. Consequently, the same sample shows the highest photothermal efficiency. Observed temperature elevation under laser irradiation can effectively be used in photothermal treatment for cancer therapy.

Declaration of Competing Interest

The authors declare that they have no known competing financial interests or personal relationships that could have appeared to influence the work reported in this paper.

Acknowledgements

The research was supported by the Ministry of Education, Science and Technological Development of the Republic of Serbia [451-03-2/2020-14/20] and by the Science Fund of the Republic of Serbia, PROMIS, [Grant No. 6066079, HEMMAGINERO]. D. Kepić acknowledges the COST Action CA15107 Multicomp, supported by the COST Association (European Cooperation in Science and Technology). A. Krmpot and M. Lekić acknowledge funding provided by the Institute of Physics Belgrade, through the grant by the Ministry of Education, Science and Technological Development of the Republic of Serbia.

References

[1] J. Yang, P. Hu, G. Yu, Perspective of graphene-based electronic devices: Graphene synthesis and diverse applications, APL Mater. 7 (2019), 020901.
[2] T.-H. Han, H. Kim, S.-J. Kwon, T.-W. Lee, Graphene-based flexible electronic devices, Mater. Sci. Eng. R. Rep. 118 (2017) 1–43.
[3] T. Yang, X. Zhao, Y. He, H. Zhu, 6 - graphene-based sensors, in: H. Zhu, Z. Xu, D. Xie, Y. Fang (Eds.), Graphene, Academic Press, 2018, pp. 157–174.
[4] J. Peña-Bahamonde, H.N. Nguyen, S.K. Fanourakis, D.F. Rodrigues, Recent advances in graphene-based biosensor technology with applications in life sciences, J. Nanobiotechnol. 16 (2018) 75.
[5] L. Bai, Y. Zhang, W. Tong, L. Sun, H. Huang, Q. An, N. Tian, P.K. Chu, Graphene for energy storage and conversion: synthesis and interdisciplinary applications, Electrochem. Energy Rev. 3 (2019) 395–430.
[6] M. Pumera, Graphene-based nanomaterials for energy storage, Energy Environ. Sci. 4 (2011) 668–674.
[7] C. Wang, J. Li, C. Amatore, Y. Chen, H. Jiang, X.-M. Wang, Gold nanoclusters and graphene nanocomposites for drug delivery and imaging of cancer cells, Angew. Chem. Int. Ed. 50 (2011) 11644–11648.
[8] L. Zhang, J. Xia, Q. Zhao, L. Liu, Z. Zhang, Functional graphene oxide as a nanocarrier for controlled loading and targeted delivery of mixed anticancer drugs, Small 6 (2010) 537–544.
[9] Z. Liu, J.T. Robinson, X. Sun, H. Dai, PEGylated nanographene oxide for delivery of water-insoluble cancer drugs, J. Am. Chem. Soc. 130 (2008) 10876–10877.
[10] K. Yang, S. Zhang, G. Zhang, X. Sun, S.-T. Lee, Z. Liu, Graphene in mice: ultrahigh in vivo tumor uptake and efficient photothermal therapy, Nano Lett. 10 (2010) 3318–3323.
[11] K. Parvez, Z.-S. Wu, R. Li, X. Liu, R. Graf, X. Feng, K. Müllen, Exfoliation of graphite into graphene in aqueous solutions of inorganic salts, J. Am. Chem. Soc. 136 (2014) 6083–6091.
[12] K. Parvez, R. Li, S.R. Puniredd, Y. Hernandez, F. Hinkel, S. Wang, X. Feng, K. Müllen, Electrochemically exfoliated graphene as solution-processable, highly conductive electrodes for organic electronics, ACS Nano 7 (2013) 3598–3606.
[13] V.B. Mohan, K.-t. Lau, D. Hui, D. Bhattacharyya, Graphene-based materials and their composites: a review on production, applications and product limitations, Compos. Part B 142 (2018) 200–220.
[14] Y. Ioni, E. Buslaeva, S. Gubin, Synthesis of graphene with noble metals nanoparticles on its surface, Mater. Today: Proc. 3 (2016) S209–S213.
[15] M.M. Chili, V.S.R.R. Pullabhotla, N. Revaprasadu, Synthesis of PVP capped gold nanoparticles by the UV-irradiation technique, Mater. Lett. 65 (2011) 2844–2847.
[16] S.K. Seol, D. Kim, S. Jung, W.S. Chang, Y.M. Bae, K.H. Lee, Y. Hwu, Effect of citrate on poly(vinyl pyrrolidone)-stabilized gold nanoparticles formed by PVP reduction in microwave (MW) synthesis, Mater. Chem. Phys. 137 (2012) 135–139.
[17] K. Okitsu, Y. Nunota, One-pot synthesis of gold nanorods via autocatalytic growth of sonochemically formed gold seeds: the effect of irradiation time on the formation of seeds and nanorods, Ultrason. Sonochem. 21 (2014) 1928–1932.
[18] J. Lai, L. Zhang, W. Niu, W. Qi, J. Zhao, Z. Liu, W. Zhang, G. Xu, One-pot synthesis of gold nanorods using binary surfactant systems with improved monodispersity, dimensional tunability and plasmon resonance scattering properties, Nanotechnology 25 (2014) 125601.
[19] J.V. Rojas, M.C. Molina Higgins, M. Toro Gonzalez, C.E. Castano, Single step radiolytic synthesis of iridium nanoparticles onto graphene oxide, Appl. Surf. Sci. 357 (2015) 2087–2093.
[20] L. Dong, R.R.S. Gari, Z. Li, M.M. Craig, S. Hou, Graphene-supported platinum and platinum–ruthenium nanoparticles with high electrocatalytic activity for methanol and ethanol oxidation, Carbon 48 (2010) 781–787.
[21] L. Cao, P. Wang, L. Chen, Y. Wu, J. Di, A photoelectrochemical glucose sensor based on gold nanoparticles as a mimic enzyme of glucose oxidase, RSC Adv. 9 (2019) 15307–15313.
[22] S.-K. Kim, C. Jeon, G.-H. Lee, J. Koo, S.H. Cho, S. Han, M.-H. Shin, J.-Y. Sim, S. K. Hahn, Hyaluronate–gold nanoparticle/glucose oxidase complex for highly sensitive wireless noninvasive glucose sensors, ACS Appl. Mater. Interfaces 11 (2019) 37347–37356.
[23] R. Britto Hurtado, M. Cortez-Valadez, L.P. Ramírez-Rodríguez, E. Larios-Rodriguez, R.A.B. Alvarez, O. Rocha-Rocha, Y. Delgado-Beleño, C.E. Martinez-Nuñez, H. Arizpe-Chávez, A.R. Hernández-Martínez, M. Flores-Acosta, Instant synthesis of gold nanoparticles at room temperature and SERS applications, Phys. Lett. A 380 (2016) 2658–2663.
[24] Y. Liu, B.M. Crawford, T. Vo-Dinh, Gold nanoparticles-mediated photothermal therapy and immunotherapy, Immunotherapy 10 (2018) 1175–1188.
[25] J.B. Vines, J.-H. Yoon, N.-E. Ryu, D.-J. Lim, H. Park, Gold nanoparticles for photothermal cancer therapy, Front. Chem. (2019) 7.
[26] A. Samadi, H. Klingberg, L. Jauffred, A. Kjær, P.M. Bendix, L.B. Oddershede, Platinum nanoparticles: a non-toxic, effective and thermally stable alternative plasmonic material for cancer therapy and bioengineering, Nanoscale 10 (2018) 9097–9107.
[27] H. Moustaoui, J. Saber, I. Djeddi, Q. Liu, A.T. Diallo, J. Spadavecchia, M. Lamy de la Chapelle, N. Djaker, Shape and size effect on Photothermal heat elevation of gold nanoparticles: absorption coefficient experimental measurement of spherical and urchin-shaped gold nanoparticles, J. Phys. Chem. C 123 (2019) 17548–17554.
[28] W. Yang, H. Liang, S. Ma, D. Wang, J. Huang, Gold nanoparticle based photothermal therapy: development and application for effective cancer treatment, Sustain. Mater. Technol. 22 (2019), e00109.
[29] S. Wang, Y. Zhang, H.-L. Ma, Q. Zhang, W. Xu, J. Peng, J. Li, Z.-Z. Yu, M. Zhai, Ionic-liquid-assisted facile synthesis of silver nanoparticle-reduced graphene oxide hybrids by gamma irradiation, Carbon 55 (2013) 245–252.

[30] X. Li, L. Liu, Z. Xu, W. Wang, J. Shi, L. Liu, M. Jing, F. Li, X. Zhang, Gamma irradiation and microemulsion assisted synthesis of monodisperse flower-like platinum-gold nanoparticles/reduced graphene oxide nanocomposites for ultrasensitive detection of carcinoembryonic antigen, Sensors Actuators B Chem. 287 (2019) 267–277.

[31] K. Hareesh, R.P. Joshi, D.V. Sunitha, V.N. Bhoraskar, S.D. Dhole, Anchoring of Ag-Au alloy nanoparticles on reduced graphene oxide sheets for the reduction of 4-nitrophenol, Appl. Surf. Sci. 389 (2016) 1050–1055.

[32] X. Zhao, N. Li, M. Jing, Y. Zhang, W. Wang, L. Liu, Z. Xu, L. Liu, F. Li, N. Wu, Monodispersed and spherical silver nanoparticles/graphene nanocomposites from gamma-ray assisted in-situ synthesis for nitrite electrochemical sensing, Electrochim. Acta 295 (2019) 434–443.

[33] D.K. Roper, W. Ahn, M. Hoepfner, Microscale heat transfer transduced by surface Plasmon resonant gold nanoparticles, J. Phys. Chem. C 111 (2007) 3636–3641.

[34] Z. Qi, J. Shi, Z. Zhang, Y. Cao, J. Li, S. Cao, PEGylated graphene oxide-capped gold nanorods/silica nanoparticles as multifunctional drug delivery platform with enhanced near-infrared responsiveness, Mater. Sci. Eng. C 104 (2019) 109889.

[35] A. Appleby, H.A. Schwarz, Radical and molecular yields in water irradiated by . gamma.-rays and heavy ions, J. Phys. Chem. 73 (1969) 1937–1941.

[36] D. Hernández-Sánchez, G. Villabona-Leal, I. Saucedo-Orozco, V. Bracamonte, E. Pérez, C. Bittencourt, M. Quintana, Stable graphene oxide–gold nanoparticle platforms for biosensing applications, Phys. Chem. Chem. Phys. 20 (2018) 1685–1692.

[37] B.-K. Pong, H.I. Elim, J.-X. Chong, W. Ji, B.L. Trout, J.-Y. Lee, New insights on the nanoparticle growth mechanism in the citrate reduction of gold(III) salt: formation of the au nanowire intermediate and its nonlinear optical properties, J. Phys. Chem. C 111 (2007) 6281–6287.

[38] N. Misra, J. Biswal, A. Gupta, J.K. Sainis, S. Sabharwal, Gamma radiation induced synthesis of gold nanoparticles in aqueous polyvinyl pyrrolidone solution and its application for hydrogen peroxide estimation, Radiat. Phys. Chem. 81 (2012) 195–200.

[39] A. Abedini, A.R. Daud, M.A. Abdul Hamid, N. Kamil Othman, E. Saion, A review on radiation-induced nucleation and growth of colloidal metallic nanoparticles, Nanoscale Res. Lett. 8 (2013) 474.

[40] J. Li, C.-y. Liu, Ag/graphene heterostructures: synthesis, characterization and optical properties, Eur. J. Inorg. Chem. 2010 (2010) 1244–1248.

[41] Z.M. Marković, D.P. Kepić, D.M. Matijašević, V.B. Pavlović, S.P. Jovanović, N. K. Stanković, D.D. Milivojević, Z. Spitalsky, I.D. Holclajtner-Antunović, D.V. Bajuk-Bogdanović, M.P. Nikšić, B.M. Todorović Marković, Ambient light induced antibacterial action of curcumin/graphene nanomesh hybrids, RSC Adv. 7 (2017) 36081–36092.

[42] D. Li, M.B. Müller, S. Gilje, R.B. Kaner, G.G. Wallace, Processable aqueous dispersions of graphene nanosheets, Nat. Nanotechnol. 3 (2008) 101–105.

[43] A. Ansón-Casaos, J.A. Puértolas, F.J. Pascual, J. Hernández-Ferrer, P. Castell, A. M. Benito, W.K. Maser, M.T. Martínez, The effect of gamma-irradiation on few-layered graphene materials, Appl. Surf. Sci. 301 (2014) 264–272.

[44] L.M. Malard, M.A. Pimenta, G. Dresselhaus, M.S. Dresselhaus, Raman spectroscopy in graphene, Phys. Rep. 473 (2009) 51–87.

[45] V. Ţucureanu, A. Matei, A.M. Avram, FTIR spectroscopy for carbon family study, Crit. Rev. Anal. Chem. 46 (2016) 502–520.

[46] D. Yang, A. Velamakanni, G. Bozoklu, S. Park, M. Stoller, R.D. Piner, S. Stankovich, I. Jung, D.A. Field, C.A. Ventrice, R.S. Ruoff, Chemical analysis of graphene oxide films after heat and chemical treatments by X-ray photoelectron and micro-Raman spectroscopy, Carbon 47 (2009) 145–152.

[47] A. Ganguly, S. Sharma, P. Papakonstantinou, J. Hamilton, Probing the thermal Deoxygenation of Graphene oxide using high-resolution in situ X-ray-based spectroscopies, J. Phys. Chem. C 115 (2011) 17009–17019.

[48] D. Jaque, L. Martínez Maestro, B. del Rosal, P. Haro-Gonzalez, A. Benayas, J. L. Plaza, E. Martín Rodríguez, J. García Solé, Nanoparticles for photothermal therapies, Nanoscale 6 (2014) 9494–9530.

Physica E 148 (2023) 115653

Contents lists available at ScienceDirect

Physica E: Low-dimensional Systems and Nanostructures

journal homepage: www.elsevier.com/locate/physe

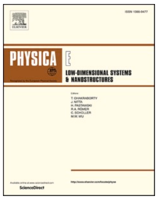

Structural properties of femtosecond laser irradiation induced bismuth oxide based nano-objects in $Bi_{12}SiO_{20}$ (BSO) single crystal

Nebojsa Romcevic, Marina Lekic, Aleksander Kovacevic, Novica Paunovic, Borislav Vasic, Maja Romcevic *

Institute of Physics Belgrade, University of Belgrade, 11080, Belgrade, Serbia

A R T I C L E I N F O

Handling Editor: M.W. Wu

Keywords:
Czochralski technique
Laser modification
Nanocomposites
Far-infrared spectroscopy

A B S T R A C T

Single crystal of $Bi_{12}SiO_{20}$ was grown from the melt by Czochralski technique. The crystal growth was in the [111] direction. The surface of the polished sample was irradiated by a femtosecond pulsed laser beam of various power. The influence of laser power on structural properties of $Bi_{12}SiO_{20}$ crystal, as well as on its phase composition, was studied. The surface morphology of our samples was investigated by AFM. The surface of unirradiated sample is rather smooth with no cracks observed. In sample modified by pulsed femtosecond beam, we registered the presence of small spherical islands on the surface. The dimensions of the islands and their density depend on the applied power. There were also significant changes in far-infrared spectra of irradiated sample in comparation to non-irradiated sample. Based on these results, the material obtained after femtosecond pulsed laser irradiation consisting of bismuth oxide based nano-objects, formed as nanocrystals (dimensions below 20 nm in diameter), which are arranged in a matrix of $Bi_{12}SiO_{20}$.

1. Introduction

Sillenites ($Bi_{12}MO_{20}$, M = Si, Ge, Ti) are optically active crystals exhibiting a lot of strong effects (optical rotation, electro-optical (Pockels), magneto-optical (Faraday) and photo-induced effects) and interesting properties such us remarkably large values of dielectric, piezo-electric and elasto-optic constants, very high values of the dark electric resistance, the index of refraction [1] etc. These crystals have application as active elements in many devices [2]. For these applications the materials are bulk single crystal samples.

On the other hand, due to their extremely small sizes, nanomaterials (one, two or three dimensions of less than 100 nm) cannot be used in large scale, particularly as long-bearing materials in engineering applications. For this it has long been a desire to develop bulk composites incorporating these nanomaterials (for example nanocomposites) to harness their extraordinary properties in bulk applicable materials. Initial ideas and principles are given in Ref. [3]. The most important fact is that the characteristics of the nanomaterials are fundamentally different in comparison with the bulk materials [4].

Lasers play an ever expanding role in material processing [5], as is the case with surface treatment of single crystals [6] where the energy of a laser beam interacts with a material to transform it in some way in a thin surface layer. This transformation (or laser process) is controlled by precisely regulating the wavelength, power, duty cycle and repetition rate of the laser beam. All materials have unique characteristics that dictate how the laser beam interacts and consequently modifies the material [7,8].

In our previous papers, we have investigated the influence of locally induced heating with increasing laser power densities on some nanomaterials such as stable hexagonal transition oxides ZnO doped with CoO [9] and cubic rock-salt MnO [10]. The influence of femtosecond pulsed laser power on the quality and optical characteristics of $Bi_{12}GeO_{20}$ single crystal was also studied [11].

The aim of this work is to continue our research with investigation influence of femtosecond pulsed laser irradiation on $Bi_{12}SiO_{20}$ single crystal using FTIR spectroscopy along with atomic force microscopy (AFM), but this time the focus is on modification of material and its structural characterization.

2. Experimental procedure

2.1. Preparation of crystal samples

Czochralski technique was applied to grow $Bi_{12}SiO_{20}$ single crystal,

---

* Corresponding author.
E-mail address: romcevic@ipb.ac.rs (M. Romcevic).

https://doi.org/10.1016/j.physe.2023.115653
Received 17 November 2022; Received in revised form 26 December 2022; Accepted 5 January 2023

where MSR 2 crystal puller controlled by a Eurotherm was used with temperature fluctuations of the experiment lower than 0.2 °C. Additional weighing set was used to monitor the crucible weight in order to keep a crystal diameter constant (absolute deviation was below 0.1 mm).

A platinum crucible was used to contain the melt, which was placed in an alumina vessel on a zircon – oxide wool. This system was constructed in order to stop the excessive radiation heat losses. Also, a cylindrical silica glass after heater was constructed around the system to reduce the thermal gradients in the crystal and in the melt. Crystal growth was occurred in an air atmosphere while iridium wires were used as initial crystal seeds. Later on, seed cuts from the produced $Bi_{12}SiO_{20}$ crystals were used for the growth of other crystals.

Bi_2O_3 and SiO_2 were used for synthesis of crystals. Starting materials were mixed in 6:1 stoichiometric ratio. Optimal pull rate was chosen in the range 5 – 6 mm/h. Equations of the melt hydrodynamics were used to calculate critical crystal diameter, $d_c = 10$ mm and critical rotation, $\omega_c = 20$ rpm. The crucible was not rotating during crystal growth. The crystal boule was cooled at ~50 °C/h down to a room temperature, after the crystal growth. Crystals grew in [111] direction, without core being observed. Finally, crystals were cut and polished.

2.2. *Crystal irradiation and characterization*

Crystal samples were exposed to a pulsed femtosecond laser beam (pulse width 90 fs, repetition rate 76 MHz) from Coherent Mira 900 F laser system pumped by a 532 nm continuous wave Coherent Verdi V-10 laser. The irradiating beam wavelength was monitored by an Ocean Optics HR2000CG UV-NIR spectrometer. The samples were irradiated along their longest axis, z, i.e., along the crystal growth direction. During irradiation, the crystal facet was partially exposed due to the oval shape of the beam profile. A graded filter was used to adjust the beam power on the sample from 50 to 800 mW (measured by Ophir Nova II powermeter with thermal and photometric heads), which corresponds to the fluence range of 75–1200 nJ/cm^2. Exposure time of each irradiation power was 3s, measured by a stopwatch of 0.2s of accuracy. The total irradiation time and energy were intentionally kept low to avoid significant contribution of an accumulative process caused by repopulation of the traps [12].

Far-infrared reflection spectra were recorded in the wave number range up to 650 cm^{-1} utilizing an A BOMEM DA - 8 FTIR spectrometer with a deuterated triglycine sulfate (DTGS) pyroelectric detector.

The surfaces of samples were examined in detail using Atomic Force Microscope (AFM), NTEGRA prima from NT-MDT. NSG01 probes with a typical resonant frequency of 150 kHz and 10 nm tip apex curvature radius were used.

The X-ray diffraction (XRD) data for $Bi_{12}SiO_{20}$ single crystals was measured using X-ray diffractometer (XRD) Rigaku Ultima IV, Japan, with filtered CuKα1 radiation ($\lambda = 0.154178$ nm). The X-ray diffraction data were collected over the 2θ range from 20° up to 80° with the step of 0.02° and scanning rate of 2°/min. The PDXL2 v2.0.3.0 software [13], with reference to the diffraction patterns available in the International Center for Diffraction Data (ICDD) [14] was used for the phase identification and data analysis.

3. Results and discussion

3.1. *Femtosecond pulsed laser modification*

In order to establish the behaviour of the sample material under the influence of femtosecond beam, three wavelengths from the common range of the Mira device (700–900 nm) have been chosen. The samples were exposed to femtosecond beam of 730, 800 and 830 nm, with input powers of 50–700, 50–800, and 50–550 mW, respectively. For each wavelength, the transmitted power vs input power has been monitored. The input power has been gradually increased and in this way the influence of possible strong modifications by higher power to the results of low power was diminished. Transmitted vs. input power dependency was established (Fig. 1).

Transmitted power dependence on the input power is in fact linear for each chosen wavelengths. The linear dependence shows uniform absorption during the input power change – there were no significant damages in the material of the samples caused by the beam during exposition. If present, strong or large-scale structural changes inside the material would change the absorption coefficient which would lead to the deviation of the Pout vs. Pin (Fig. 1) dependence from the linear one.

Because of that, in the further analysis in this paper, under treated sample we will consider the sample modified with a laser line of 730 nm and a power of 700 mW as a representative one. In Fig. 2, a sample treated with 730 nm and a power of 50 mW was analyzed for comparison.

3.2. *AFM*

Fig. 2 shows the results of AFM measurements of the $Bi_{12}SiO_{20}$ single crystal and the same sample after being irradiated by a femtosecond pulsed laser beam. The surface of unirradiated sample is rather smooth with no cracks observed, and only traces of mechanical polishing can be seen in Fig. 2a. Fig. 2b and c. Show the surface of the sample after irradiated by a femtosecond pulsed laser with 730 nm and power of 50 mW and 700 mW respectively. Full lines at Fig. 2 a-c present directions in which the structure dimensions were determined. Height prolife on the surface and in the shine dots is shown in Fig. 2 d. For the treated samples, the nanoobject clearly stands out in the selected direction. It could be said that the height of the nano-object for both samples is in the range of about 10–15 nm, and that the height of the nanoobject increases with the increase in the power of the femtosecond laser. On the other hand, the diameter of these nano-objects is about 20 nm (Figs. 2b) and 15 nm (Fig. 2c). In addition, we note that the density of nano-objects is significantly higher in Fig. 2c.

Average roughness (Ra) for the samples shown in Fig. 2 a, b, c is 1.25 nm, 1.57 nm and 1.6 nm, respectively. Although the value for Ra is relatively small, i.e. the surface of the samples is relatively smooth, we can conclude that as a result of the femtosecond laser treatment, as well as when increasing the laser power, the value for Ra also increases, which is expected.

3.3. *XRD measurements*

Phase analysis using XRD of single crystal BSO samples are presented

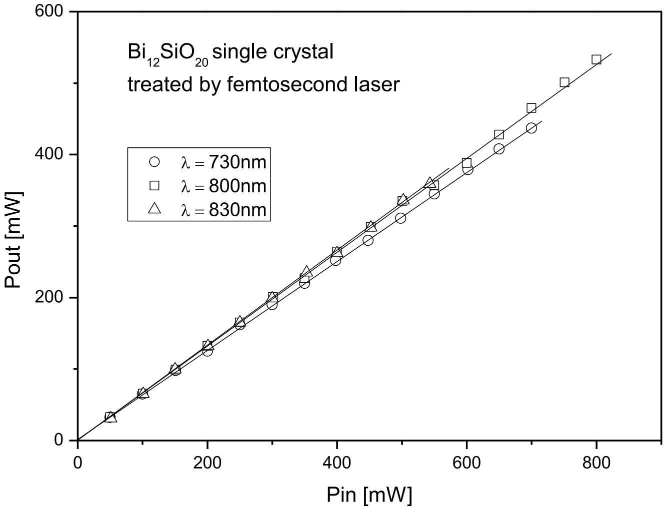

Fig. 1. Transmitted (Pout) vs. input (Pin) power for samples exposed to the beam of 730 nm, 800 nm and 830 nm.

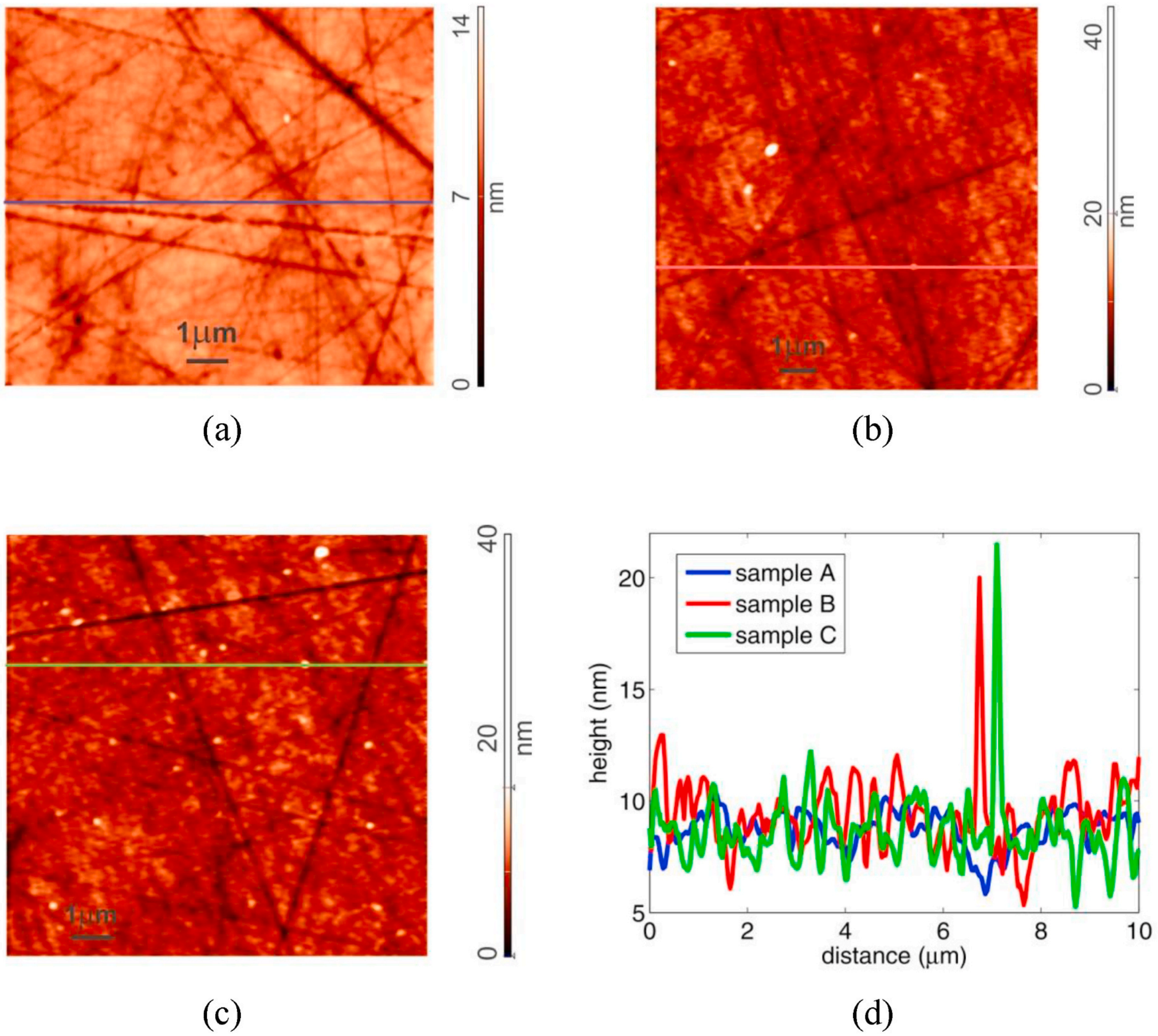

Fig. 2. AFM results of $Bi_{12}SiO_{20}$ single crystal: untreated (a); femtosecond laser treated sample: 730 nm, 50 mW (b) and 730 nm, 700 mW (c). Height prolife on the surface (d).

in Fig. 3. Phase analysis indicates that all peaks belong to the $Bi_{12}SiO_{20}$ phase, which is in good agreement with the JCPDF Card No. 37–0485.

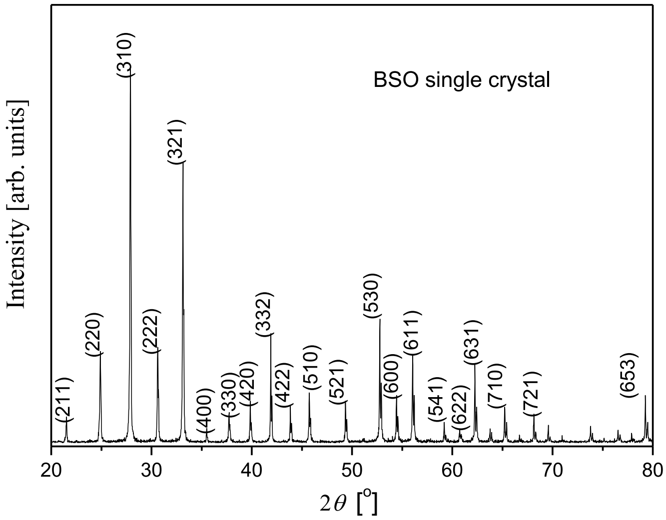

Fig. 3. X-ray diffraction results of untreated $Bi_{12}SiO_{20}$ single crystal, peaks of $Bi_{12}SiO_{20}$ phase marked with hkl.

The XRD for the treated sample is no different from that for the untreated.

3.4. Far-infrared spectroscopy

The experimental far-infrared spectrum of BSO single crystal was recorded in the spectral range of 70–650 cm^{-1} at room temperature and in Fig. 4 is presented as a blue line. The obtained spectrum shows all characteristics described in the literature [15,16]. The far-infrared spectrum of the femtosecond laser treated BSO, recorded in the spectral range of 70–650 cm^{-1} at room temperature, is presented in Fig. 4 as a red line. Even though the spectra given in Fig. 4 were recorded under the same conditions, differences in the BSO single crystal and femtosecond laser treated BSO spectra are clearly visible at in several places, such as about 130, 180, 280 cm^{-1} ….

$$\Gamma = 8A + 8E + 25F \quad (1)$$

Among these modes, only the F modes are infrared active.

Fig. 5, lower spectrum, shows the far-infrared spectra of BSO single crystal. The points are given the experimental results, and the solid line is obtained in the standard way by the procedure of fitting parameters [18,19]. Due to the large energy gap (Eg = 2,57eV) and accordingly very low concentrations of free carriers, a dielectric function was used which takes into account only the interaction of electromagnetic radiation with

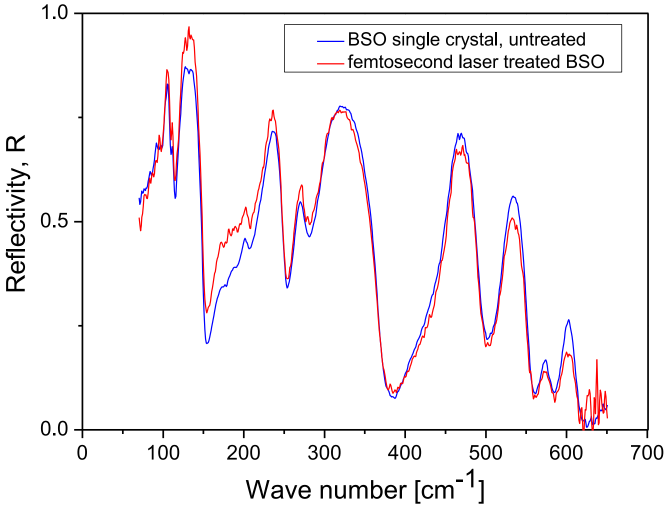

Fig. 4. Experimental far-infrared reflection spectra of $Bi_{12}SiO_{20}$ single crystal untreated (blue line) and treated by femtosecond beam (red line). First, in short about factor group analysis. Crystal BSO has a cubic unit with space group I23 (T3) [17].

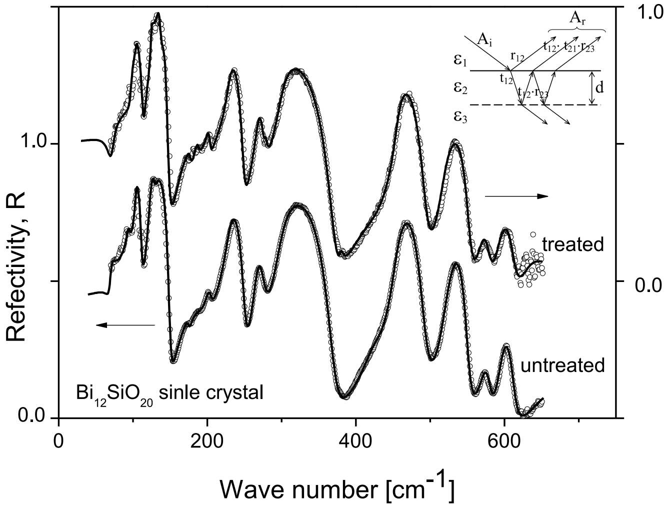

Fig. 5. Far-infrared reflection spectra of $Bi_{12}SiO_{20}$ single crystal and femtosecond laser-treated $Bi_{12}SiO_{20}$ sample. The experimentally obtained data points are depicted as circles. The theoretical spectrum obtained with the model defined by eqs. (2) and (3) and fitting procedure is given as solid line. Insert. Schematic overview of the femtosecond laser-treated $Bi_{12}SiO_{20}$ sample.

phonons:

$$\varepsilon(\omega) = \varepsilon_\infty \prod_{k=1}^{s} \frac{\omega^2 + i\gamma_{kLO} - \omega_{kLO}^2}{\omega^2 + i\gamma_{kTO} - \omega_{kTO}^2} \tag{2}$$

where ε_∞ is the bound charge contribution and is considered as a constant, ω_{LOk} and ω_{TOk} are the longitudinal and transverse optical – phonon frequencies, and γ_{TOk} and γ_{LOk} are the phonon dampings.

The results obtained for TO/LO frequencies (in cm^{-1}) are: 69/71, 94/95, 104/112, 123/150, 129.5/130, 142/143, 175.2/175.5, 187.5/192.5, 202.5/204.3, 229/251, 267/276.8, 297.5/371, 424/427, 453/494, 520/551.5, 572/581, 594/613, 647/658. The agreement with the literature data [15,16] is excellent. This result serves as an introduction to the spectrum analysis for the femtosecond laser treated BSO sample, where the situation is somewhat more complex. Fig. 5, upper spectrum, shows the far-infrared spectrum of femtosecond laser treated BSO single crystal. The points are given the experimental results, and the solid line is obtained in the following way.

Namely, as can be seen from Fig. 2b and c, laser treatment leads to a change in the surface of the samples. It seems that its composition changes in a very thin layer, but also that nanoobjects are formed inside the layer and on its surface. Therefore, we decided to use a model that takes into account the existence of a three-layer structure (see insert of Fig. 5), where.

(a) medium 1 is air ($\varepsilon_1 = 1$),
(b) medium 2 is a layer with thickness d present at the sample surface with dielectric constant ε_2 (eq. (2)), and
(c) lower optically thick layer, medium 3, practically single crystal BSO, described with ε_3 (eq. (2)).

In this case, the reflectivity can be determined as described in Ref. [20]:

$$R_A = \frac{A_r}{A_i} = \frac{\boldsymbol{r}_{12} e^{-i\alpha} + r_{23} e^{i\alpha}}{e^{-i\alpha} + \boldsymbol{r}_{12} \boldsymbol{r}_{23} e^{i\alpha}} \tag{3}$$

where $r_{ij} = (n_i - n_j)/(n_i + n_j) = (\sqrt{\varepsilon_i} - \sqrt{\varepsilon_j})/(\sqrt{\varepsilon_i} + \sqrt{\varepsilon_j})$ are the Fresnel coefficients, A_i and A_r represent amplitudes of the incident and reflection beams, respectively, n is the complex index of refraction, ε is the dielectric constant and $\alpha = 2\pi\omega d\,(\varepsilon_2)^{1/2}$ is the complex phase change related to the absorption in the crystal layer with the thickness d. Reflectance, R, is given as $R = |R_A|^2$.

The parameters of the treated sample were determined by the fitting procedure. In that manner, the parameters for the single crystal BSO layer (medium 3) remained the same as those determined from untreated sample. The surface layer (medium 2), besides them, has additional modes. The layer thickness is d = 1,9 μm. Comparison of our result with the values from the literature for the registered additional phonons is given in Table 1.

Some results from literature, for example [22], show that laser-induced oxidation of bismuth can occur, but the degree of oxidation and the formation of the crystalline phase strongly depend on the laser power. We think that in our case, due to laser heating, on the $Bi_{12}SiO_{20}$ single crystal, the formation of starting material phases occurs. It is known that bismuth oxide can exist in several polymorphic forms: α-Bi_2O_3, the only phase stable at room temperature, and three high-temperature phases, β-, δ- and γ-Bi_2O_3. The orthorhombic phase, α-Bi_2O_3, transforms to cubic δ-Bi_2O_3 at 729 °C, which may transform to tetragonal β-Bi_2O_3 or body-centered cubic γ-Bi_2O_3 upon cooling to 650 and 639 °C, respectively [24–27]. Both of these forms are metastable,

Table 1
Comparison between additional far-infrared frequencies registered in this paper and experimentally and calculated frequencies from the literature.

Phonon peaks This work [cm^{-1}]	Experimental literature values of phonon frequencies [cm^{-1}]	Calculated phonon frequencies [cm^{-1}]	Description
120	120 [21]	120 [21]	Bi_4O_7 [21]
	118 [22]		α-Bi_2O_3 [22]
		124 [21]	β-Bi_2O_3 [21]
161	157 [21]		γ-Bi_2O_3 [21]
	166 [23]		γ-Bi_2O_3 [23]
278	279 [22]		γ-Bi_2O_3 [22]
	281 [21]		γ-Bi_2O_3 [22]
380	381 [21]		γ-Bi_2O_3 [21]
		388 [21]	Bi_4O_7 [21]

but may be stabilized at room temperature by the addition of impurities [25].

Another metastable phase, which was also registered by our measurements, is Bi_4O_7. This phase is a fully chargeordered pseudo-binary bismuth (Bi^{3+}, Bi^{5+}) oxide [28,29]. This mixed valence and the optical gap within the visible range (1.9eV) turns the Bi_4O_7 interesting for applications in photocatalysis. Also, because of strong luminescence at about 420 nm Bi_4O_7 is a candidate as for purplish-blue light emitter [30]. One of the following directions of research can be dedicated to this topic as well.

It seems to us that in this way it is clearly shown that femtosecond laser treating produces nano-objects consisting of different phases based on bismuth oxide in a matrix of $Bi_{12}SiO_{20}$ single crystal. In the future, we will search for new functionalities, which would open up new topics and areas.

4. Conclusions

We used a femtosecond pulsed laser to modify the surface on a $Bi_{12}SiO_{20}$ single crystal growth by Czochralski technique. The treatment led to the formation of bismuth oxide based nanoobjects in the $Bi_{12}SiO_{20}$ matrix. These nanoobjects are formed as nanocrystals with dimensions below 20 nm in diameter and about 15 nm in height. By composition, they are α-, β-, and γ-Bi_2O_3 and Bi_4O_7. The concentration of nanoobjects increases when the power of the femtosecond laser increases. Application in optoelectronics and optical sensor industry is expected.

Author contributions

N. Romcevic: Conceptualization, Methodology, Formal analysis, Writing- Original draft preparation. **N. Paunovic, M. Lekic, A. Kovacevic, B. Vasic:** Investigation, Formal analysis. **M. Romcevic:** Investigation, Formal analysis, Writing—review and editing. All authors have read and agreed to the published version of the manuscript.

Funding

This research was supported by the Science Fund of the Republic of Serbia, Grant No. 7504386, Nano object in own matrix – Self composite – NOOM-SeC.

Declaration of competing interest

The authors declare that they have no known competing financial interests or personal relationships that could have appeared to influence the work reported in this paper

Data availability

Data will be made available on request.

References

[1] J.-C. Chen, L.-T. Liu, C.-C. Young, A study of the growth mechanism of bismuth silicon oxide during LHPG method, J. Cryst. Growth 198/199 (1999) 476–481, https://doi.org/10.1016/S0022-0248(98)01142-7.

[2] M.P. Petrov, A.V. Khomenko, in: P. Gunter, J.P. Huignard (Eds.), Photorefractive Materials and Their Applications II, Publicher, Springer, Berlin, 1989, pp. 325–352, https://doi.org/10.1007/BFb0120157.

[3] Y. Dzenis, Structural nanocomposites, Science 319 (2008) 419–420, https://doi.org/10.1126/science.1151434.

[4] T.E. Twardowski, Introduction to Nanocomposites Material Properties, Processing, Characterization, Publicher: Destech Publications, Lancaster, Pa, USA, 2007, pp. 1–532.

[5] P.M. Ossi, M. Dinescu, Laser processing of materials, in: P. Schaaf (Ed.), Springer Series in Materials Science (SSMATERIALS), vol. 139, 2010, pp. 131–167, https://doi.org/10.1007/978-3-642-13281-0.

[6] M.A. Montealegre, G. Castro, P. Rey, J.L. Arias, P. Vazquez, M. Gonzalez, Surface treatments by laser technology, Contemporary Materials I−1 (2010) 19–30, https://doi.org/10.5767/anurs.cmat.100101.en.019M.

[7] A.K. Roy (Ed.), Hybrid Atomic-Scale Interface Design for Materials Functionality, Publicher, Elsevier, 2021, https://doi.org/10.1016/C2018-0-05143-9.

[8] M.V. Shugaev, C. Wu, O. Armbruster, A. Naghilou, N. Brouwer, D.S. Ivanov, T.J.-Y. Derrien, N.M. Bulgakova, W. Kautek, B. Rethfeld, L.V. Zhigilei, Fundamentals of ultrafast laser–material interaction, MRS Bull. 41 (12) (2016) 960–968, https://doi.org/10.1557/mrs.2016.274.

[9] B. Hadzic, N. Romcevic, D. Sibera, U. Narkiewicz, I. Kurylisyn-Kudelska, W. Dobrowolski, M. Romcevic, Laser power influence on Raman spectra of ZnO (Co) nanoparticles, J. Phys. Chem. Solid. 91 (2016) 80–85, https://doi.org/10.1016/j.jpcs.2015.12.008.

[10] B. Hadzic, B. Vasic, B. Matovic, I. Kuryliszyn-Kudelska, W. Dobrowolski, M. Romcevic, N. Romcevic, Influence of laser induced heating on MnO nanoparticles, J. Raman Spectrosc. 49 (5) (2018) 817–821, https://doi.org/10.1002/jrs.5358.

[11] A. Kovacevic, J. Ristic-Djurovic, M. Lekic, B. Hadzic, G. Saleh Isa Abudagel, S. Petricevic, P. Mihailovic, B. Matovic, D. Dramlic, Lj Brajovic, N. Romcevic, Influence of femtosecond pulsed laser irradiation on bismuth germanium oxide single crystal properties, MRS Bull. 83 (2016) 284–289, https://doi.org/10.1016/j.materresbull.2016.06.023.

[12] B. Taheri, S.A. Holmstrom, R.C. Powell, J.J.F. Song, F. Antonio Munoz, I. Földvári, A. Péter, Nonlinear absorption of laser light in $Bi_{12}GeO_{20}$ single crystals, Opt. Mater. 3 (1994) 251–255, https://doi.org/10.1016/0925-3467(94)90037-X.

[13] PDXL Version 2.0.3.0 Integrated X-Ray Powder Diffraction Software, Rigaku Corporation, Tokyo, Japan, 2011, p. 196.

[14] Powder Diffraction File, PDF-2 Database, Announcement of New Database Release, International Centre for Diffraction Data (ICDD), 2012.

[15] A. Golubovic, S. Nikolic, R. Gajic, S. Duric, A. Valcic, The grown and optical properties of $Bi_{12}SiO_{20}$ single crystals, J. Serb. Chem. Soc. 67 (4) (2002) 279–289.

[16] D. Senuliene, G. Babonas, Far infrared reflection spectra of sillenite crystals and their solid solutions, phys. stat. solidi (b) 180 (2) (1993) 541–549, https://doi.org/10.1002/pssb.2221800225.

[17] G.N. Zhizhin, B.N. Mavrin, V.F. Shabanov, Opticheskie Kolebatelnye Spektry Kristallov, Pubisher: Nauka, Moskva, 1984.

[18] J. Trajic, M. Romcevic, N. Romcevic, B. Babic, B. Matovic, P. Balaz, Far-infrared spectra of mesoporous ZnS nanoparticles, Opt. Mater. 57 (2016) 225–230, https://doi.org/10.1016/j.optmat.2016.05.004.

[19] J. Trajic, M. Rabasovic, S. Savić-Sevic, D. Sevic, B. Babic, M. Romcevic, J. Ristic-Durovic, N. Paunovic, J. Krizan, N. Romcevic, Far-infrared spectra of dysprosium doped yttrium aluminium garnet nanopowder, Infrared Phys. Technol. 77 (2016) 226–229, https://doi.org/10.1016/j.infrared.2016.06.003.

[20] M. Gilic, J. Trajic, N. Romcevic, M. Romcevic, D.V. Timotijevic, G. Stanisic, I. S. Yahia, Optical properties of CdS thin films, Opt. Mater. 35 (2013) 1112–1117, https://doi.org/10.1016/j.optmat.2012.12.028.

[21] O. Depablos-Rivera, A. Martinez, S.E. Rodil, Interpretation of the Raman spectra of bismuth oxide thin films presenting different crystallographic phases, J. Alloys Compd. 853 (2021), 157245, https://doi.org/10.1016/j.jallcom.2020.157245.

[22] K. Trentelman, A note on the characterization of bismuth black by Raman microspectroscopy, J. Raman Spectrosc. 40 (2009) 585–589, https://doi.org/10.1002/jrs.2184.

[23] C. Rodriguez-Fernandez, K. Akius, M.M. de Lima Jr., A. Cantarero, J.M. van Ruitenbeek, C. Sabater, Raman signal revels the rhombohedral crystallographic structure in ultra-thin layers of bismut thermally evaporated on amprphous substrate, Maerials Sci. Eng. B 27 (2021), 115240, https://doi.org/10.1016/j.mseb.2021.115240.

[24] S. Venugopalan, A.K. Ramdas, Raman spectra of bismuth germanium oxide and bismut silicon oxide, Phys. Rev. B 8 (10) (1972) 4065–4079, https://doi.org/10.1103/PhysRevB.5.4065.

[25] B. Mihailova, M. Gospodinov, L. Konstantinov, Raman spectroscopy study of silenites. I. Comparasion between $Bi_{12}(Si,Mn)O_{20}$ single crystals, J. Phys. Chem. Solid. 60 (1999) 1821–1827, https://doi.org/10.1016/S0022-3697(99)00194-8.

[26] I.F. Vasconcelos, M.A. Pimenta, A.S.B. Sombra, Optical properties of $Bi_{12}SiO_{20}$ (BSO) and $Bi_{12}TiO_{20}$ (BTO) obtained by mechanical alloying, J. Mater. Sci. 36 (2001) 587–592, https://doi.org/10.1023/A:1004804000723.

[27] J.C. Alonso, R. Diamant, E. Haro-Poniatowski, M. Fernandez-Guasti, G. Munoz, I. Camarillo, M. Jouanne, J.F. Morhange, Raman characterization of $Bi_{12}SiO_{20}$ thin films obtained by pulsed laser deposition, App. Sur. Sci. 109/110 (1997) 359–361, https://doi.org/10.1016/S0169-4332(96)00674-5.

[28] B. Begemann, M. Jansen, Bi_4O_7, das erste definierte binare Bismut (III, V) - oxid, J. Less Common. Met. 156 (1989) 123–135, https://doi.org/10.1016/0022-5088(89)90412-8.

[29] R.E. Dinnebier, R.M. Ibberson, H. Ehrenberg, M. Jansen, The crystal structures of the binary mixed valence compound $Bi(III)_3Bi(V)O_7$ and isotypic Bi_3SbO_7 as determined by high resolution X-ray and neutron powder diffraction, J. Solid State Chem. 163 (2002) 332–339, https://doi.org/10.1006/jssc.2001.9427.

[30] H. Guan, Y. Feng, Facile synthesis and purplish blue luminescence of the binary mixed valence compound Bi_4O_7 microcrystals, Matter. Lett. 143 (2015) 269–272, https://doi.org/10.1016/j.matlet.2014.12.129.

PROCEEDINGS

IX International Conference IcETRAN
and LXVI ETRAN Conference,
Novi Pazar, Serbia, 6 - 9, June, 2022.

ЗБОРНИК РАДОВА

IX међународне конференције ИцЕТРАН
и LXVI конференције ЕТРАН,
Нови Пазар 6 - 9. јуна 2022. године

PROCEEDINGS IX International Conference IcETRAN and LXVI ETRAN Conference, Novi Pazar, Serbia, 6 - 9, June, 2022.

ЗБОРНИК РАДОВА IX међународне конференције ИцЕТРАН и LXVI конференције ЕТРАН, Нови Пазар 6 - 9. јуна 2022. године

Editor in Charge / Главни уредник
Vladimir Katić / Владимир Катић

Published by **/ ETRAN Society, Belgrade, Academic Mind, Belgrade**
Издавачи / **Друштво за ЕТРАН, Београд и Академска мисао, Београд**

Production / Израда
Academic Mind, Belgrade / Академска мисао, Београд

Place and year of publication / Место и година издања
Belgrade, 2022. / Београд, 2022.

Circulation / Тираж
300 copies / 300 примерака

ISBN 978-86-7466-930-3

**ETRAN – Society for electronics, telecommunication,
computing, automatics and nuclear angineering**

**ЕТРАН - Друштво за електронику, телекомуникације,
рачунарство, аутоматику и нуклеарну технику**

Kneza Milosa 9/IV, 11000 Belgrade / Кнеза Милоша 9/IV, 11000 Београд

Phone / Телефон: +381 (11) 3233 957

E-mail / Е-пошта: office@etran.rs

www.etran.rs

ORGANIZERS - ОРГАНИЗАТОРИ

ETRAN Society, Belgrade / Друштво за ЕТРАН, Београд

**State University of Novi Pazar, Novi Pazar, Serbia /
Државни универзитет у Новом Пазару, Нови Пазар, Србија**

**University of Priština temporarily settled in Kosovska Mitrovica, Faculty of Technical Sciences, Serbia /
Факултет техничких наука Косовска Митровица - Универзитет у Приштини са привременим седиштем у Косовској Митровици**

UNDER THE AUSPICES OF / ПОКРОВИТЕЉ

**Ministry of Education, Science and Technological Development
of the Republic of Serbia /**

Министарство просвете, науке и технолошког развоја републике Србије

SUPPORTED BY / ПОДРШКА

IEEE – Institute of Electrical and Electronics Engineers, USA

Power Electronics Society of Serbia / Друштво за енергетску електронику Србије

CIRED Serbia / CIRED Србија

CIP – Каталогизација у публикацији
Народна библиотека Србије, Београд

621.3(082)(0.034.2)
534(082)(0.034.2)
004(082)(0.034.2)
681.5(082)(0.034.2)
621.039(082)(0.034.2)
66.017(082)(0.034.2)
57+61(048)(0.034.2)
006.91(082)(0.034.2)

INTERNATIONAL Conference on Electrical, Electronic and Computing Engineering (9 ; 2022 ; Novi Pazar) Зборник радова [Електронски извор] / IX међународне конференције ИцЕТРАН и LXVI конференције ЕТРАН, Нови Пазар 6 % 9. јуна 2022. године = Proceedings / IX International Conference IcETRAN and LXVI ETRAN Conference, Novi Pazar, Serbia, 6 % 9, June, 2022. ; [главни уредник Владимир Катић = editor in charge Vladimir Katić]. - Београд : Друштво за ЕТРАН : Академска мисао = Belgrade : ETRAN Society : Academic Mind, 2022 (Београд : Академска мисао). - 1 електронски оптички диск (CD-ROM) ; 12 cm

Системски захтеви: Нису наведени. - Насл. са насловне стране документа. - Радови на срп. и енгл. језику. - Тираж 300. - Библиографија уз сваки рад. - Abstracts.

ISBN 978-86-7466-930-3 (AM)

1. Друштво за електронику, телекомуникације, рачунарство, аутоматику и нуклеарну технику (Београд). Конференција (66 ; 2022 ; Нови Пазар) а) Електротехника - Зборници b) Акустика - Зборници c) Рачунарска технологија - Зборници d) Системи аутоматског управљања - Зборници e) Нуклеарна техника - Зборници f) Технички материјали - Зборници g) Биомедицина - Зборници h) Метрологија - Зборници

COBISS.SR-ID 71309321

Суб-микрометарске паралелне површинске структуре индуковане фемтосекундним ласерским снопом у форензици

Александер Ковачевић, Сузана Петровић, Марина Лекић, Борислав Васић, Бранислав Салатић,
Јелена Поточник

*Апстракт***— Један од ефеката интеракције ултра-кратког ласерског снопа са материјалима је формирање паралелних структура на површини (laser-induced parallel surface structures - LIPSS), чији је период мањи од таласне дужине снопа. Уколико се ради о вишеслојним танким филмовима метала, квалитет формираних структура је бољи. Узорак од пет двослојних танких филмова Al и Ti на супстрату Si смо изложили фемтосекундном снопу и запазили формирање две врсте структура које се разликују по облику. Обе су врсте вероватно узроковане појавом површинског плазмона-поларитона на површини најгорњег слоја. Појава плазмона поларитона на површини танких металних филмова и наночестица може да ограничи простирање електромагнетног поља и да појача флуоресцентни сигнал из молекула хемикалије на површини. У зависности од структуре интерфејса за одређивање циљне хемикалије на металној површини флуоресценција побољшана плазмоном (plasmon-enhanced fluorescence, PEF) је привлачан метод за скраћење времена и појачање осетљивости разних аналитичких технологија које се користе у форензици.**

*Кључне речи***— фемтосекундни ласер; вишеслојни танки филмови; периодичне површинске структуре; флуоресценција.**

I. Увод

Интеракција ласерског снопа са површином проузрокује многе ефекте, међу којима је у последње време пажњу заокупило формирање паралелних структура (LIPSS – laser induced parallel surface structures) под дејством ултракратких снопова [1]. Због карактеристике да им је периодичност мања од таласне дужине снопа, поље примене је веома широко [2]. Интеракција са металима може побољшати триболошке карактеристике, а на ламеларним материјалима, као што су вишеслојни танки метални филмови, формирани LIPSS има добар квалитет и може да побољша особине површине [3-4]. Снопови различитих карактеристика (флуенца, таласна дужина, дужина импулса, поларизација, ...), разни материјали (диелектрици, полупроводници, метали, ...), али и стање амбијента током интеракције – све то утиче на карактеристике LIPSS [5]. Генерално, уочена је појава две врсте структура, са нижом просторном учестаношћу (LSFL – low spatial frequency LIPSS) и са вишом просторном учестаношћу (HSFL – high spatial frequency LIPSS) [6].

II. Експериментална поставка

Узорци који су коришћени су добијени депоновањем Al и Ti на подлогу од Si (1 0 0) помоћу Balzers Sputron II апарата који користи 1,3 keV аргонске јоне и са 99.9% чистоће Al и Ti мета. Две врсте узорака су подвргнуте интеракцији са фемтосекундним снопом. Први тип је био силицијумска подлога на којој је депоновано пет Al/Ti двослоја чиме је достигнута укупна дебљина од ~130 nm (сваки слој од ~13 nm). Други тип је такође био силицијумска подлога, али на којој је био депонован један слој Al дебљине ~130 nm.

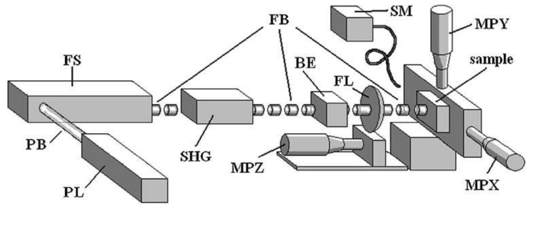

Сл. 1. Дијаграм експерименталне поставке за статичну интеракцију; PL – ласер за пумпање, PB – сноп за пумпање, FS – извор фемтосекундног снопа, FB – фемтосекундни сноп, SHG – удвајач учестаности, BE – проширивач снопа, FL – фокусирајуће сочиво, MPX/MPY/MPY - микропозиционери, SM – спектрометар, sample - узорак.

Извор фемтосекундног снопа је био Coherent Mira 900F систем чија је фреквенција удвојена са Inrad 5-050 ултрабрзим генератором другог хармоника. Карактеристике снопа су биле: таласна дужина 390 nm (удвојено) и 800 nm (основни хармоник), дужина импулса ~150 fs, репетиција 76 MHz (период између импулса ~13 ns), снага на мети 160–260 mW, линеарна поларизација у

Александер Ковачевић – Институт за физику Универзитета у Београду, Прегревица 118, 11080 Београд, Србија (e-mail: aleksander.kovacevic@ ipb.ac.rs).

Сузана Петровић – Институт за нуклеарне науке „Винча“ Универзитета у Београду, ПП 522, 11351 Београд-Винча, Србија (e-mail: spetro@ vin.bg.ac.rs).

Марина Лекић – Институт за физику Универзитета у Београду, Прегревица 118, 11080 Београд, Србија (e-mail: marina.lekic@ ipb.ac.rs).

Борислав Васић – Институт за физику Универзитета у Београду, Прегревица 118, 11080 Београд, Србија (e-mail: bvasic@ ipb.ac.rs).

Бранислав Салатић – Институт за физику Универзитета у Београду, Прегревица 118, 11080 Београд, Србија (e-mail: banes@ ipb.ac.rs).

Јелена Поточник – Институт за нуклеарне науке „Винча“ Универзитета у Београду, ПП 522, 11351 Београд-Винча, Србија (e-mail: jpotocnik@ vin.bg.ac.rs).

хоризонталној равни, Гаусов елиптични профил. Експозиције су биле од 1 до 10 s. Таласна дужина снопа је контролисана фибер-оптичким спектрометром Ocean Optics HR2000CG-UV-NIR. Интеракције су обављане у ваздуху фокусирањем фемтосекундног снопа под нормалним углом на површину првог слоја узорка (Al), сл. 1. Резултати су анализирани скенирајућим електронским микроскопима (SEM) JEOL JSM 6560 LV који има Oxford Instruments EDS анализатор и FEI SCIOS2, као и помоћу микроскопа атомских сила (AFM) NT-MDT NTEGRA Prima.

На сл. 2 је дијаграм поставке модификоване за потребе скенирања снопа преко узорка. Изостављен је удвајач учестаности, чиме је интеракција пренесена у блиску инфрацрвену област, ради скенирања се сноп уводи у огледални 2D скенер и у проширивач снопа, а фокусирање се обавља објективом модификованог микроскопа (40×, NA=0,65).

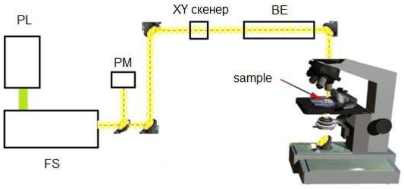

Сл. 2. Дијаграм експерименталне поставке за интеракцију уз скенирање снопом; PL – ласер за пумпање, FS – извор фемтосекундног снопа, PM – мерење снаге снопа, XY скенер – скенер снопа, BE – проширивач снопа, sample - узорак.

III. Резултати и дискусија

На сл. 3 је приказ слике SEM дела области интеракције са 5×(Al/Ti). Фемтосекундни сноп таласне дужине 460 nm је имао флуенцу од 13,6 mJ/cm^2 а време експозиције 10 s. У области интеракције се виде паралелне структуре са периодом од око 300 nm. Структуре су формиране у виду издигнућа на површини.

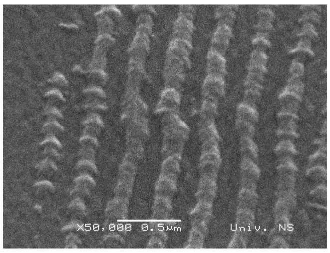

Сл. 3. Приказ слике SEM дела области интеракције са 5×(Al/Ti) на Si; флуенца 13,6 mJ/cm^2 и 10 s време експозиције.

На сл. 4 је приказана AFM слика области интеракције приказаној на сл. 2. Овде се боље види да су структуре формиране као издигнућа на површини.

Сл. 4. Приказ AFM слике дела области интеракције приказане на сл. 2: 5×(Al/Ti); флуенца 13,6 mJ/cm^2 и 10 s време експозиције.

Узорак другог типа – један слој танког филма (~130 nm) Al – је био изложен флуенци од 8,6 mJ/cm^2 исте таласне дужине и времену експозиције од 10 s. Резултати у виду слике SEM дела области интеракције су приказани на сл. 5. У централном делу је дошло до аблације топљењем, а аблирани материјал се распоредио у околини централне зоне интеракције. Дошло је до расподеле у виду LIPSS, али квалитет облика није тако добар као у случају првог узорка. Просторни период структура је око 300 nm.

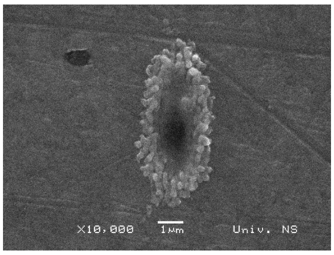

Сл. 5. Приказ слике SEM области интеракције са Al на Si; флуенца 8,6 mJ/cm^2 и 10 s време експозиције [4].

Упадни ултракратки сноп изазива на интерфејсу између металне и диелектричне површине појаву површинског плазмона (SP), а његовом интеракцијом са упадним снопом долази до формирања површинског плазмона поларитона (SPP) [2, 7], који узрокује статичну периодичну расподелу енергије на површини, периода мањег од таласне дужине упадног снопа. Дубина продирања ласерског снопа од 390 nm се израчунава [8] за Al на око 3 nm, а за Ti на око 9,3 nm.

Присуство подслоја Ti узрокује повећање прага оштећења првог (горњег) слоја, Al. Температура решетке се формира кроз два механизма: електронско-фононски (који узрокује локализацију загревања), и транспорт електронима везан за топлотну проводност електрона (који односи топлоту од зоне интеракције) [9]. Разлика у електронско-фононској спрези између два материјала води до стрме промене температуре решетке унутар подслоја (Ti). Као последицу, електрони из горњег слоја (Al) брзо преносе енергију следећем (подслоју) и тиме се термална енергија преноси кроз интерфејс Al/Ti, спреже са решетком и на тај начин односи из зоне интеракције. У првом следећем слоју (подслој, Ti) долази до гомилања термалне енергије периодично у латералном смеру, али због високе температуре топљења Ti не долази до топљења. Праг оштећења првог слоја је тиме повећан јер се енергија углавном гомила у првом подслоју, који већ има висок праг оштећења. Одсуство подслоја Ti омогућава гомилање енергије у слоју Al и изражено топљење (сл. 5).

У поређењу са Al/Ti вишеслојним узорком, оптичка дубина продирања за Al је нижа, што резултује већим вреностима апсорбоване енергије и акумулације топлоте. Топљење и аблација су израженији него код вишеслојног.

Осим статичког озрачивања, вршена су и динамичка, када је сноп скениран преко површине узорка. У овом случају је таласна дужина била 800 nm, а флуенца 153 mJ/cm^2. На одређеним правцима је скенирање извршено вишеструким прелетом снопа преко површине узорка; на сл. 6 је приказана област дела интеракције где је сноп скениран 8, 9 и 10 пута. Просторни период структуре је око 283 nm (мање од половине таласне дужине упадног снопа). У инсету на сл. 6 је приказана AFM слика дела интеракције, формирана по интензитету тунелске струје између врха пробе и узорка. Примећује се да је струја кроз формиране структуре (формиране у виду уздигнућа на површини) мања (еквивалентно тамнијој боји) него струја у деловима који нису трансформисани (светлија боја). То наводи на закључак да је дошло до смањења проводности у тим деловима, за које се може претпоставити да је узрок јача оксидација која је услед већег гомилања енергије.

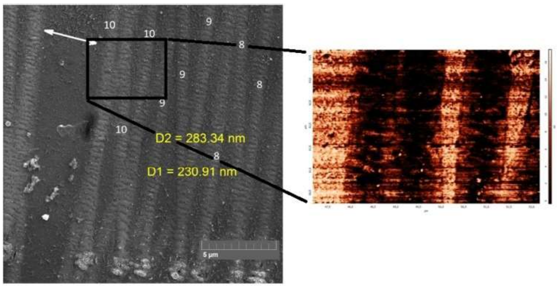

Сл. 6. Приказ слике SEM (лево) и AFM (инсет-десно) дела области интеракције 5×(Al/Ti) на Si; поновљено скенирање, 8—10 пролаза, флуенца 153 mJ/cm^2; бројеви 8, 9 и 10 представљају број прелета снопа преко истог правца; правац поларизације је означен белом стрелицом.

Модел изложен у [10] предлаже формирање једне врсте LIPSS на металним површинама интеракцијом са ултракратким снопом у ваздуху. У првом кораку расејање на површинским нерегуларностима индукује појаву SPP и периодичне расподеле енергије на површини. У другом кораку, на местима где се енергија акумулира долази до загревања и реакције метала са кисеоником из ваздуха. Због ултракратког импулса је оксидација бржа од термалне дифузије, и дебљина оксида расте на местима акумулиране енергије. Тиме се одржава нанометарска локализација. Како структура расте у висину, расејање се појачава и тиме је остварена позитивна повратна спрега. У трећем кораку – како структура расте – због све већег присуства оксида се смањује продирање кисеоника у структуру и тиме се цели процес зауставља. Трећи корак има негативну повратну спрегу.

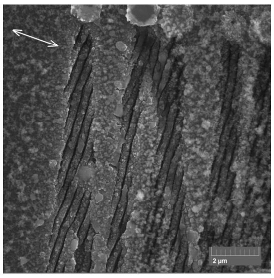

Сл. 7. Приказ слике SEM дела области интеракције 5×(Al/Ti) на Si; поновљено скенирање, 10 пролаза, флуенца 215 mJ/cm^2; правац поларизације је означен белом стрелицом.

На сликама 3 и 6 је приказано формирање једне врсте LIPSS, „гребен“, настале оксидацијом и надоградњом материјала. Правац простирања гребенских LIPSS је паралелан правцу поларизације упадног снопа (HSFL). За нешто веће флуенце снопа, сл. 7, долази до аблације материјала, а у аблираној области се појављује друга врста LIPSS, „канали“. Таласна дужина је 800 nm, флуенца 215 mJ/cm2, а као резултат је просторни период од 370 nm. Ширина канала је 80 nm. Аблација је наступила услед топљења/испаравања материјала. Правац каналских LIPSS управан на правац поларизације упадног снопа (LSFL).

Појава плазмона – колективне осилације наелектрисања и придруженог електромагнетног поља на површини металних филмова и наноструктура – омогућава ограничење простирања светлости у мале области и тиме је дало нова решења у оптичким спектроскопијама, као што су површински-побољшана Раманова спектроскопија (in surface-enhanced Raman spectroscopy, SERS) површински-побољшана инфрацрвена спектроскопија (surface-enhanced infrared spectroscopy, SEIRA) и плазмонски-побољшана флуоресцентна спектроскопија (surface plasmon-enhanced fluorescence spectroscopy, PEF), које се користе у низу форензичких аналитичких технологија за детекцију хемијских и биолошких агенаса релевантних у важним областима медицинске дијагностике, контроле хране и безбедности [12]. У PEF се флуорофорни означивачи спрежу са ограниченим пољем површинских плазмона што се може конструисати да веома појача интензитет емитованог флуоресцентног светла ради детектовања врло малих количина аналита са побољшаном границом детекције и скраћењем времена анализе. Просторно преклапање и усклађивање фазе између поларитона води до успостављања спрегнутих симетричних и антисиметричних модова површинског плазмона поларитона. Симетрични тип мода се може побудити на металним површинама са густим решеткама испод нивоа дифракције. Дифракција на таквој периодичној модулацији дозвољава да плазмони поларитони који се простиру у супротном смеру интерагују, стварајући појачане интензитете поља локализоване или у удубљењима (“канали“) решетке или на врховима („гребени“) периодичне модулације.

IV. ЗАКЉУЧАК

Приказано је испитивање површинских модификација индукованих на танким филмовима – узорци од пет (Al/Ti) бислојева (укупне дебљине 130 nm) на Si као и узорци од једнослојног Al (дебљине 130 nm) на Si – помоћу фемтосекундног ласерског снопа таласне дужине од 390 nm и 800 nm и репетиције 76 MHz (~13 ns између импулса). За статичку интеракцију су формиране површинске периодичне структуре (LIPSS) на вишеслојном Al/Ti при флуенци једног импулса од 10,3–14 mJ/cm^2, а на једнослојном Al при флуенци једног импулса од 8,6 mJ/cm^2. Присуство подслоја повећава праг оштећења најгорњег слоја, што побољшава квалитет формираних LIPSS. За динамичку интеракцију (скенирање снопа преко површине узорка) за 153 mJ/cm^2 је дошло до формирања гребенских LIPSS, а за већу флуенцу једног импулса, 215 mJ/cm^2, до каналских LIPSS. На основу правца простирања LIPSS се закључује њихова врста, LSFL (ниске просторне учестаности) или HSFL (високе просторне учестаности). За формирање LIPSS се механизам се види у појави површинског плазмона поларитона који изазива периодичну расподелу енергије. Присуство подслоја одговарајућих термичких карактеристика омогућава лако преношење термалне енергије у дубље слојеве. Код гребенских LIPSS има три корака везаних за продирање кисеоника из ваздуха у материјал (оксидација), док код каналских LIPSS долази до аблације топљењем/испаравањем и уклањања материјала.

Појава плазмона поларитона је важна при неким флуоресцентним техникама, као што је PEF, који је унапредио осетљивост и скратио време анализе процедура за детекцију важних аналита укључујући биомаркере, патогене и токсине. Ова једињења су детектована на ниским фемтомоларним концентрацијама, а анализа је веома скраћена. Једна од плазмона који се појављује је тесно везан са појавом периодичних структура са периодом мањим од таласне дужине (LIPSS). Индуковање LIPSS може бити интересантно у великом броју примена – медицинским, декоративним, триболошким, и др. – због појаве плазмона поларитона којим се светлост конфинира и омогућава побољшање у плазмонски побољшаној флуоресцентној спектроскопији.

ЗАХВАЛНИЦА

Овај рад је спроведен у оквиру реализације научних пројеката, које је финансирало Министарство науке и технолошког развоја Републике Србије под редним бројевима III45016, OI171005, OI171038. Аутори су захвални М. Бокорову са Техничког факултета Универзитета у Новом Саду, др Д. Перушку из Института за нуклеарне науке "Винча", као и др Б. Јеленковићу, др Д. Пантелићу, др Р. Гајићу, др А. Крмпоту, др М. Рабасовићу и В. Лазовићу из Института за физику Београд, за подршку.

ЛИТЕРАТУРА

[1] H. M. van Driel, J. E. Sipe and J. F. Young, "Laser-induced periodic surface structure on solids: A universal phenomenon", *Phys. Rev. Lett.*, vol. *49*, pp. *1955-1959*, Dec. 1982.

[2] A. Y. Vorobyev and C. Guo, "Direct femtosecond laser surface nano/microstructuring and its applications", *Laser Photonics Rev.*, vol. *7*, pp. *385-407*, May 2013.

[3] S. M. Petrović, D. Peruško, B. Salatić, I. Bogdanović-Radović, P. Panjan, B. Gaković, D. Pantelić, M. Trtica, B. Jelenković, "Laser induced damage/ablation morphology on the 8(Al/Ti)/Si system in different ambient conditions", *Opt. Laser Technol.*, vol. *54*, pp. *22-29*, Dec. 2013.

[4] A. G. Kovačević, S. Petrović, B. Bokić, B. Gaković, M. T. Bokorov, B. Vasić, R. Gajić, M. Trtica, B. M. Jelenković, "Surface nanopatterning of Al/Ti multilayer thin films and Al single layer by a low-fluence UV femtosecond laser beam", *Appl. Surf. Sci.*, vol. *326*, pp. *91-98*, 2015.

[5] A. G. Kovačević, S. Petrović, V. Lazović, D. Peruško, D. Pantelić, B. M. Jelenković, "Inducing subwavelength periodic nanostructures on multilayer NiPd thin film by low-fluence femtosecond laser beam", *Appl. Surf. Sci.*, vol. *417*, pp. *155-159*, Sep. 2017.

[6] J. Bonse, S. Hoehm, S. V. Kirner, A. Rosenfeld, J. Krueger, "Laser-Induced Periodic Surface Structures—A Scientific Evergreen", *IEEE J. Sel. Topics Quantum Electron.*, vol. *23*, no. *3*, a. *9000615*, 2017.

[7] A. Y. Vorobyev, V. S. Makin, Chunlei Guo, "Periodic ordering of random surface nanostructures induced by femtosecond laser pulses on metals", *J. Appl. Phys.*, vol. *101*, no. *3*, a. *034903*, 2007.

[8] D. Bauerle, *Laser Processing and Chemistry*, Berlin, Germany: Springer, 2000.

[9] G. D. Tsibidis, "Thermal response of double-layered metal films after ultrashort pulsed laser irradiation: The role of nonthermal electron dynamics", *Appl. Phys. Lett.*, vol. *104*, no. *5*, a. *051603*, 2014.

[10] B. Öktem, I. Pavlov, S. Ilday, H. Kalaycıoğlu, A. Rybak, S. Yavaş, M. Erdoğan, F. Ö. Ilday, "Nonlinear laser lithography for indefinitely large area nanostructuring with femtosecond pulses", *Nature Phot.*, vol. *7*, pp. *897-901*, 2013.

[11] H. Malekzad, P. S. Zangabad, H. Mohammadi, M. Sadroddini, Z. Jafari, N. Mahlooji, S. Abbaspour, S. Gholami, M. G. Houshangi, R. Pashazadeh, A. Beyzavi, M. Karimi, M. R. Hamblin, "Noble metal nanostructures in optical biosensors: Basics, and their introduction to anti-doping detection", *Trends Anal. Chem.*, vol. *100*, p. *116-135*, 2018.

[12] M. Bauch, K. Toma, M. Toma, Q. Zhang, J. Dostalek, "Plasmon-Enhanced Fluorescence Biosensors: a Review", *Plasmonics*, vol. *9*, pp. *781–799*, 2014.

ABSTRACT

One of the effects of the interaction of ultrashort laser beam with materials is the forming of laser-induced parallel surface structures (LIPSS), with period less than beam wavelength. For multilayer thin metal films, the quality of formed structures is better. The sample of five bilayers of Al and Ti on Si substrate was exposed to femtosecond beam and noticed the forming of of two types of structures different in shape. Both are most probably the product of surface Plasmon polariton on the surface of most top layer. The occurrence of Plasmon polariton on the surface of thin metal layers and nanoparticles can confine the propagation of electromagnetic field and to amplify the fluorescent signal from molecules of the chemical compound on the surface. Depending on the interface structure for determining the target chemical on metal surface, Plasmon enhanced fluorescence is an attractive method for shortening the time of detection and increasing the sensitivity of various analytical technologies used in forensics.

Sub-micrometer parallel surface structures induced by femtosecond laser beam in forensics

Aleksander Kovačević, Suzana Petrović, Marina Lekić,
Borislav Vasić, Branislav Salatić, Jelena Potočnik

SERBIAN ACADEMY OF
NONLINEAR SCIENCES

1st CONFERENCE ON NONLINEARITY

Editors

B. Dragovich, Ž. Čupić

Belgrade, 2020
SERBIA

Proceedings

of the

1st CONFERENCE ON NONLINEARITY

(October 11 – 12, 2019, Belgrade, Serbia)

Editors

B. Dragovich, Ž. Čupić

Publisher
Serbian Academy of Nonlinear Sciences
Belgrade, 2020
SERBIA

Modeling of experimental evidences for self-organization of soliton-tweezers in nanosuspensions[*]

Vladimir Skarka[†]
Laboratoire de Photonique d’Angers, EA 4464, Université d’Angers,
49045 Angers, France
Institute of Physics, University of Belgrade, 11000 Belgrade, Serbia
Marina Lekić[‡]
Institute of Physics, University of Belgrade, 11000 Belgrade, Serbia
Stephan Rokotoarimalala[§]
Laboratoire de Photonique d’Angers, EA 4464, Université d’Angers,
49045 Angers, France

ABSTRACT

The exhaustive experimental investigations allowed us to understand spontaneous self-organization of soliton-tweezers in pure water naturally containing suspended nanobubbles. The laser beam propagation modifies the medium, but due to feedback mechanisms beam is itself altered in a self-organized way generating soliton. In soft matter like body water, suspended nanoparticles are aspirated inside the beam if their refractive index is larger than the background one. In opposite case they are expelled making again soliton self-focusing, thus, compensating defocusing effects. The result is a spontaneously self-collimated soliton-tweezer with a conserved profile as demonstrated by experiments and numerical simulations of a novel complex intensity equation. Coefficients multiplying this equation terms are determined by experimental measurements allowing the predictability important for noninvasive medical applications in inactivation of viruses, bacteria, and cancer cells.

---

[*] This work has been supported by the Ministry of Education and Science of the Republic of Serbia, under Projects III 45016, OI 171038, and OI 171006.

[†] e-mail address: vskarka@yahoo.com
[‡] e-mail address: lekic@ipb.ac.rs
[§] e-mail address: stephan.rokotoarimalala@univ-angers.fr

1. Introduction

Biomedia like blood, myosin, kinesin, ribosomes, liposomes, and varieties of living cells suspended in body water can be manipulated, tweezed, and controlled using laser beams and pulses[1-7]. The laser beam propagates through the nonlinear medium and alter it. Simultaneously, the changed medium acts by feedback mechanisms to this laser light modifying it in turn. Therefore, the laser light is self-controlled by light through the interaction with nonlinear medium [7-14]. The laser stability and precision are of crucial importance for nondestructive medical applications, *e.g*. photobiomodulation using these feedback mechanisms [6, 15,16]. In order to improve this indispensable dynamical stability, the best way is to leave nature to act by self-organization of solitons localized in space and in time [17,18]. The laser beam becomes soliton whenever antagonist effects, *i.e*., beam focusing and defocusing are balanced [19-21]. In any medium, including vacuum, laser beam is diffracting. In rigid guides beams are confined in the region with higher optical index of refraction. In contrast, the particularity of the propagation in soft matter is that the easily moving fluids adapt their density distribution in such a way that the beams always propagate through the highest index of refraction. Following 2018 Nobel Prize winner Ashkin, the tweezing laser beam collects around its center micro- and nanoparticles with index of refraction n_p higher than the background medium one (n_b), *i.e*., positively polarized particles [1-4,22,23]. Consequently, the beam is always self-focuses. However, in opposite case, when the refractive index of nanoparticles is lower than the background one ($n_p<n_b$), the negatively polarized nanoparticles are expelled from the beam that focalizes too, propagating again through higher index of refraction. Therefore, such a redistribution of nanoparticles density following Gaussian laser intensity induces always the nonlinear beam self-focusing [24-28]. Taking into account that the same nonlinear nanoparticle density distribution causes also defocusing effects, it becomes plausible that self-focusing effects compensate defocusing ones in a self-organized way [29]. As a consequence, the beam is self-collimated and becomes soliton-tweezer with identical widths following two transverse coordinates x and y corresponding to a unique transverse coordinate $r_\perp = \sqrt{x^2+y^2}$ [19-21,30]. Using paraxial approximation and slowly varying envelop, A(r), the dynamics of electric field, $E=A(r)\exp(ik_0n_0z)$ can be described by two transverse dimensions (2D) nonlinear Schrödinger equation (NLS)

$$i\,\partial E/\partial z + \gamma\nabla_\perp^2 E + \eta E + (\sigma|I| - \nu|I|^2)E = 0 \qquad (1)$$

where$I=E^2$ is the complex intensity and the transverse Laplasian reads $\nabla_\perp^2 = \frac{\partial^2 E}{\partial x^2} + \frac{\partial^2 E}{\partial y^2}$. The only imaginary term corresponds to the field propagation. The unavoidable diffraction is given by the second one. The third term is linear. The nonlinear self-focusing is given by the fourth term. The higher order negative nonlinearity is necessary in order to avoid the catastrophic collapse [19-21]. Coefficients in front of terms have to be determined from experiment in order to connect it directly to the theory [31]. For this purpose, we realize the laser beam propagation in pure water.

2. Experiments of soliton-tweezers self-organizationin water suspension of nanoparticles:Equation connecting theory with experiments

Taking into account that the total body water volume estimated from simple anthropometric measurements is about 70%, the safety of medical applications of lasers depends on good knowledge of beam propagation in water [32]. The challenge is to investigate the possibility of spontaneous self-generation of soliton-tweezers in pure water. Following exhaustive literature, the pure water contains naturally gas microbubbles and nanobubbles [33-38]. For instance, collapsing microbubbles may generate free-radicals in body water [39]. It is reported recently that drug delivery plasmonic nanobubbles rapidly detect and destroy drug-resistant tumor [40]. It seems that nanobubbles of about 50 to 100 nm are the most stable [33-38]. Taking into account that the water has the index of refraction $n_b=1.33$ and air nanobubbles $n_p=1$, we investigate the case of negative polarizability of nanoparticles ($n_b>n_p$). In order to study soliton tweezing gas particles in body water, *e.g.*, blood transporting oxygen and carbon dioxide, the prerequisite are theoretical, numerical and experimental synergetic investigations of the pure water.

We investigate experimentally the propagation of laser beam in the 20 cm long optically clear u-cuvette filled by pure water [41]. A powerful near infrared Mira 900 laser in continuous regime with wavelength $\lambda_0=727$ nm is used as the light source. The laser beam is spontaneously self-structured and self-collimated propagating in water suspension of nanobubbles as can be seen in Figure 1a. Indeed, the laser beam has the same width along of the cuvette. The beam width conservation implies the zero wave front curvature, as a main property of Schrödinger solitons [19-21]. Therefore, this beam is a 2D spatial soliton that is self-organized due to the balance between the self-focusing tweezing effects due to redistribution of nanobubbles, from the one side, and self-defocusing effects, from the other side [29]. The experiment to establish optical properties of the investigated nanosuspension consists in measuring with precision the beam output intensity as a function of gradually increasing input one, charted in Figure 1e as dots with uncertainty bars [31]. The third order polynomial fit of the distribution of these dots furnishes the numerical factors in front of linear and quadratic focusing terms (x and x^2) and cubic defocusing term (x^3) in insert of Figure 1e giving respectively values of linear coefficient η, self-focusing coefficient σ, and self-defocusing coefficient ν of Eq.(1). The NLS describes the evolution of laser complex electric field E. However, in experiments is always measured the increase of laser complex intensity $I=E^2=A^2(r)\exp(i2k_0n_0z)$. Therefore, in order to obtain right description of experiment in paraxial approximation it is necessary to multiply Eq.(1) by complex electric field E

$$i\,\partial I/\,\partial z+\gamma\nabla_{\perp}^{2}I+\eta I+(\sigma|I|-\nu|I|^{2})I\;=0 \qquad (2)$$

obtaining a novel soliton-tweezer complex intensity equation (STCIE).This synergetic equation directly connects the measured quantities with

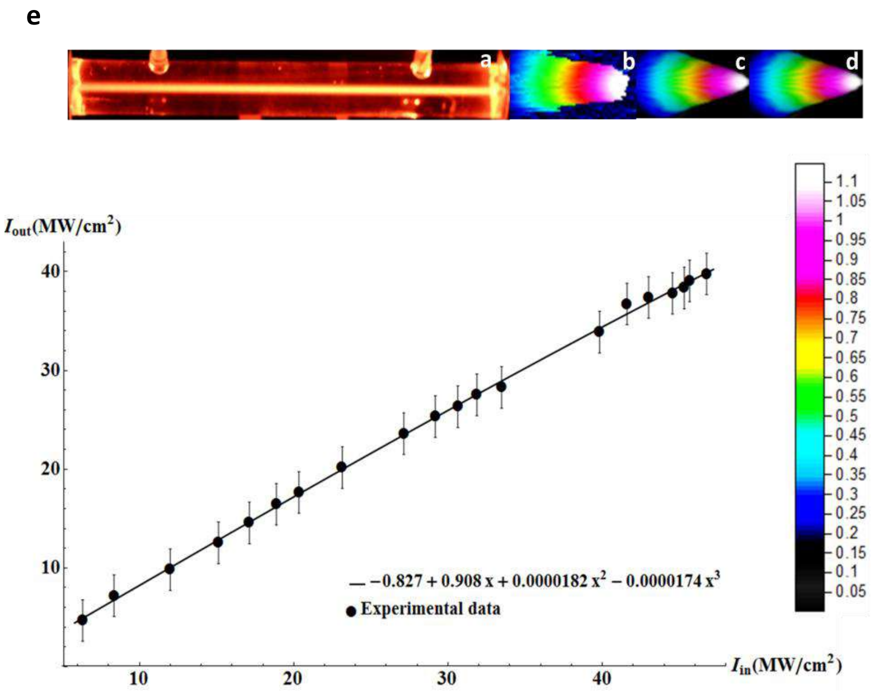

Figure 1a Self-collimated powerful red soliton-tweezer propagating through pure water in 20 cm cuvette. **e** Dots (with uncertainty bars) represent the measured soliton-tweezer output for various input intensities. The third order polynomial fit allows to obtain numerical values for coefficients in Eq.(2). Numerical propagations for z=1000 (**c**) and z=20000 steps (**d**) of this STCIE give identical soliton-tweezer profiles in very good agreement with the experimental one (**b**).

the theory. Indeed, the numerical factors in front of linear (x), quadratic (x^2), and cubic (x^3) terms in insert of Figure 1egive value of coefficients η, σ, and ν of linear (I), quadratic (|I|I), and cubic ($|I|^2I$) intensity terms of Eq. 2. The soliton-tweezers self-trapped propagation is limited by the cuvette length, but can be extended by numerical propagation of STCIE. Indeed, the camera positioned in the output of u-cuvette captured the soliton-tweezer profile (Figure 1b) that looks similar to profiles obtained by z=1000 (Fig. 1c) and z=20000 steps (Fig. 1d) numerical propagation of synergetic STCIE with coefficients from insert of Figure 1e.

Obviously, the beam intensity profile can be captured only in output of 20 cm u-cuvette, in order to visualize it in the middle, a twice shorter u-cuvette is irradiate by the identical laser beam under identical conditions. The laser beam is spontaneously self-collimated in 10 cm u-cuvette too (see Figure 2a). The intensity profiles after 10 cm and 20 cm propagations in pure water naturally containing suspension of nanobubbles are identical (compare Figures 1b and 2b). The third order polynomial fit, in insert of Figure 2f, gives different numerical values for coefficients η, σ, and ν, from those in Figure 1e. However, the

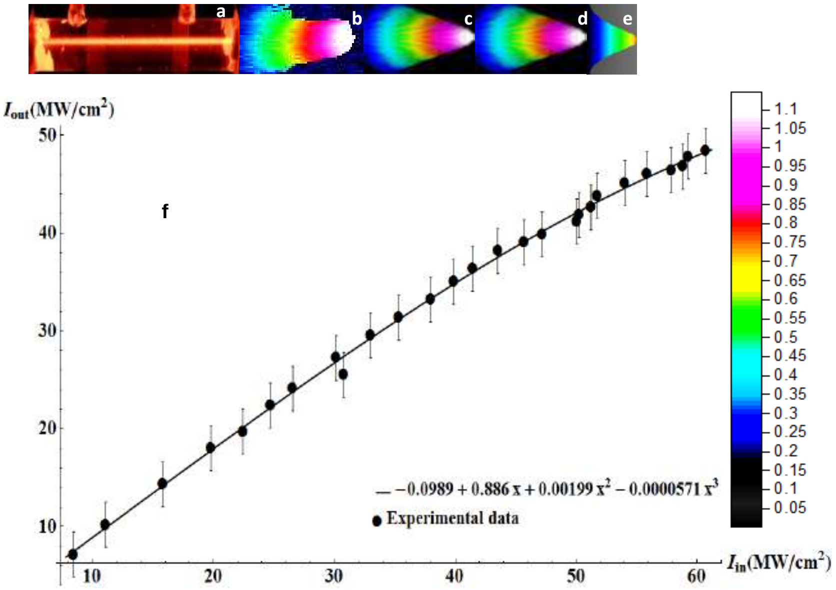

Figure 2a Self-organized propagation of soliton-tweezer in 10 cm cuvette. **b** The output profile resemble to beam profiles after self-trapped numerical propagation of z=600 (**c**) and z=20000 steps (**d**). **e** Diffracting low intensity beam profile. **f** Measured soliton-tweezer output intensities for increasing input ones represented by dots. The full line corresponds to third order polynomial fit furnishing numerical values for coefficients in STCIE. The color scale is common for all cuvettes.

numerical propagation of Eq. 2 with new values of coefficients, after z=600 (Figure 2c) and z=20000 steps (Figure 2d) give intensity profiles identical to those of Figures 1c and 1d and very similar to experimental profiles. Therefore, the feasibility of soliton-tweezers in the pure water is confirmed. In contrast, the low intensity beam is diffracting as in Figure 2e.

For security reasons, it is desirable to nondestructively tweeze and manipulate body water nanoparticles using laser of very low intensity, *i.e.*, low power density. Consequently, in order to demonstrate the soliton-tweezer feasibility even for three order of magnitude lower intensities, a weak continuous green laser beam with wavelength λ_0=532 nm is propagated through the pure water in 20 cm cuvette. From the beam lateral view in Figure 3a can be concluded that the width of the beam profile (Figure 3b) is maintained constant through the cuvette. In order to find equivalent of beam profile in the center of 20 cm u-cuvette, the same green beam is now propagated through the 10 cm u-cuvette. It becomes self-collimated due to the soliton-tweezer self-trapping too (see Figure 4a).

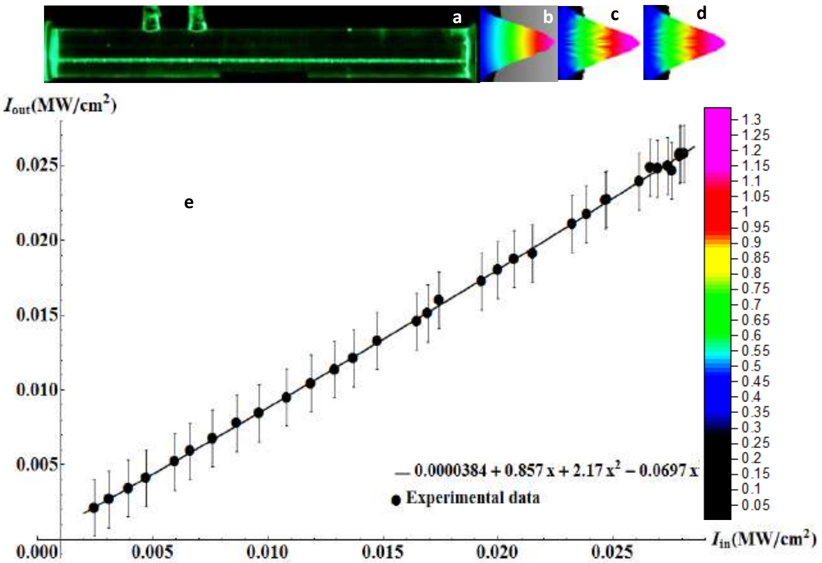

Figure 3a The propagation of a weak green laser beam through the same 20 cm cuvette becomes self-collimated due to the interaction with nanobubbles suspended in water. **b** Its output profile coincide with those obtained numerically after z=800 (**c**) and z=20000 steps(**d**). **e** The curve that fit experimental data corresponds to a third order polynomial with coefficients that are integrated in Eq.(2) allowing the soliton-tweezer numerical propagation.

Therefore, this beam keeps always the same profile as in Figure 4b. This output profile is identical to the output one of 20 cm u-cuvette in Figure 3b. In contrast, in Figure 4e is shown the profile of a very low intensity beam that is diffracting. The variation of output intensities in function of input intensities for 20 cm and 10 cm cuvettes are charted respectively in Figures 3e and 4f. Although fitting of these curves gives different coefficients in front of terms in Eq.(2) its long numerical simulations till z=20000 steps, charted in Figures 3c,d and 4c,d keep the identical form of profile that is the signature of a soliton. These numerical profiles are in very good agreement with experimental profiles in Figures 3b and 4b. Therefore, even for very low intensities, soliton-tweezers self-trapped in water suspension of nanobubbles remain robust allowing photobiomodulation and other noninvasive medical applications in body water colloidal nanosuspensions.

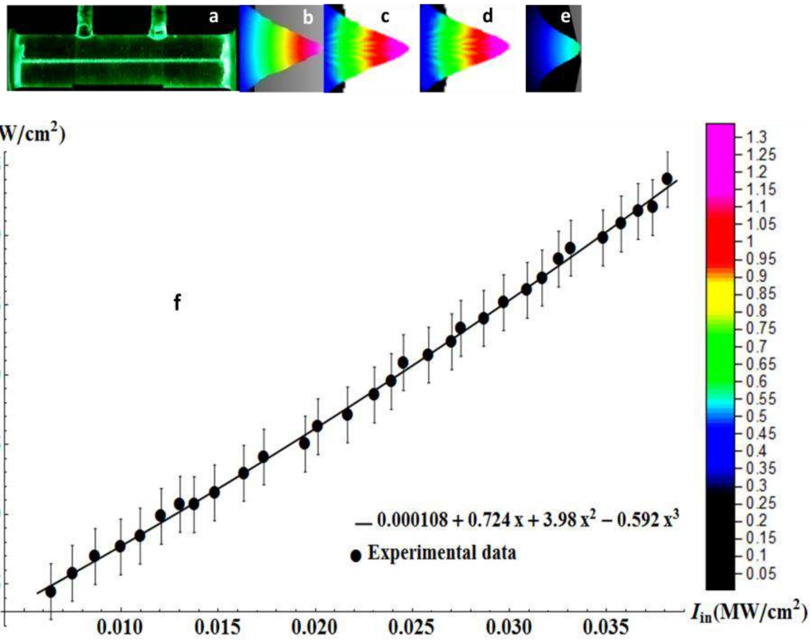

Figure 4a Lateral view of the same green laser beam propagation in 10 cm cuvette shows the self-collimation caused by the self-organized interaction with nanobubbles in water suspension, even though intensities in the self-trapping range are three orders of magnitude lower than those of red laser. **f** Coefficients of the STCIE, experimentally obtained from fitted input-output data, allow long numerical simulations of soliton-tweezer profiles that are conserved without any modification, not only after z=1000 steps as in (**c**), but also after z=20000 steps as in (**d**). **b** These profiles coincide with the experimental one, and those in Figure 6. **e** Out of trapping range the beam is diffracting.

Our synergetic approach establishes a very useful bridge between the theory and experiment via numerical simulations of novel STCIE allowing a security test of non destructibility prior every medical application.

3. Dissipative soliton-tweezers self-trapped in water suspensions of nanobubbles

The nonlinear Schrödinger equation and the established soliton-tweezer complex intensity equation, both describe conservative systems. However, the energy losses are unavoidable in real dynamical systems and can disintegrate solitons unless gain is also present. Such systems are well described by the complex cubic-quintic Ginsburg-Landau equation (CQGLE) governing complex electric field E[9,14,21,29]

$$\frac{i\,\partial E}{\partial z} + (\eta + \sigma|I| - \nu|I|^2 + \gamma\nabla_\perp^2)E = i(\delta + \varepsilon|I| - \mu|I|^2 + \beta\nabla_\perp^2)E. \quad (3)$$

The left hand side of this equation corresponds to conservative NSL. The dissipative, thus, imaginary right hand side contains the same terms but with different coefficients to be fixed from the experiment. The parameter δ of the first imaginary term must be negative, in order to ensure the stability of the system [5,9]. It corresponds to linear loss giving with propagation term the linear absorption equation. This term and negative nonlinear quintic term are both compensated by cubic gain, similarly as real terms of self-defocusing and self-focusing. We demonstrated that the self-organized dynamical balance of antagonist effects is in reality more complex, with second order derivatives compensation playing central role [9,42,43]. The positive β diffusive term corresponds to gain. In order to connect this theory with experiments, all terms are multiplied by coefficients. Their values are measured in experiments [31]. Recently, B.N. Aleksić, *et al.* showed that the competing cubic-quintic nonlinearity represents a very good approximation of saturable nonlinearity [44].

For the sake of comparative investigations we propagate through 20 cm u-cuvette again 727 nm Mira laser beam, but this time in femtosecond regime. This beam is spontaneously self-collimated during propagation, having a constant width along u-cuvette, as can be seen in Figure 5a.

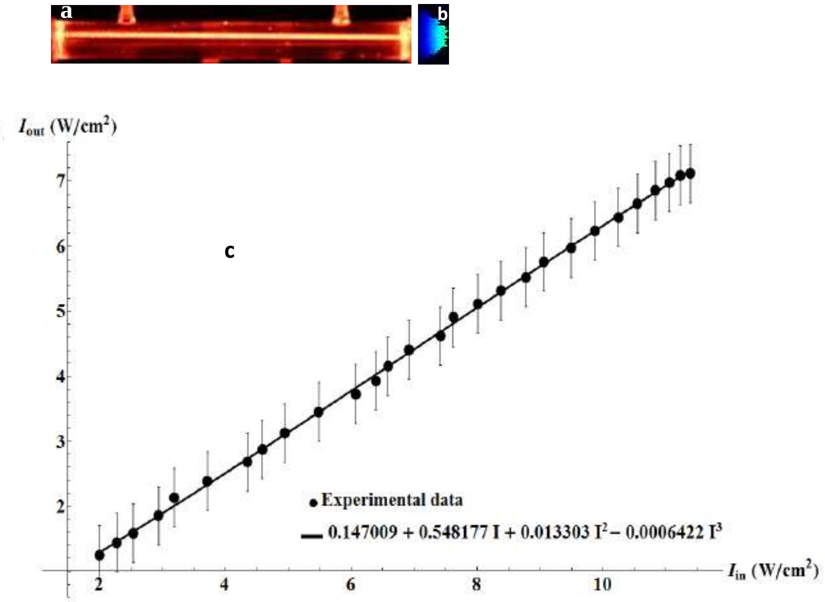

Figure 5 **a** Self-trapped and self-collimated femtosecond soliton-tweezer propagating through nanosuspension in 20 cm cuvette. **b** Experimentally obtained output profile. **c** Dots represent the measured output for various input intensities. The third order polynomial fit allows to obtain in front of I, I^2,and I^3in insert, numerical values for coefficients η, σ, and ν in left hand side of Eq. (3).

A camera capture from the output of u-cuvette is presented in Figure 5b.In fact, for each increase of input intensity it is taken picture of the output.

Each camera capture is then analyzed using MATLAB in order to extract output intensity from each pixel. The addition of intensities of all pixels in a square framework fitting the light spot gives the value of corresponding global intensity charted as a dot in Figure 5c.Then, the ensemble of dots is fitted by a third order polynomial. The coefficients of this polynomial in insert give experimental values of coefficients in front of terms on the left hand side of Eq. (3) (CQGLE) in the same way as it was done for Eq. (1) (NSL). The imaginary right hand side of CQGLE is related to the balance between gain and loss of power density. The coefficients multiplying corresponding terms can be find from power density diagram in Figure 6 obtained by systematic measure of input and output power after each camera capture. The global power is divided by the surface of the same square framework fitting the light spot, providing the same units of W/cm^2 in both side of CQGLE. These input-output dots are fitted using the same third order polynomial. Indeed, right hand side terms are of the similar order of magnitude as left hand side terms. In the insert of Figure 6 are charted experimental values for the coefficients in front of CQGLE imaginary terms. Our aim is to establish a direct correspondence between the experiment and the theory. However, theoretical approaches use electrical field, E to describe laser beam, while in experiments is measured the complex intensity, $I=E^2$ [31]. Therefore, the direct correspondence between experiment and theory is established multiplying Eq. (3) by electrical field, E in order to recover the complex intensity

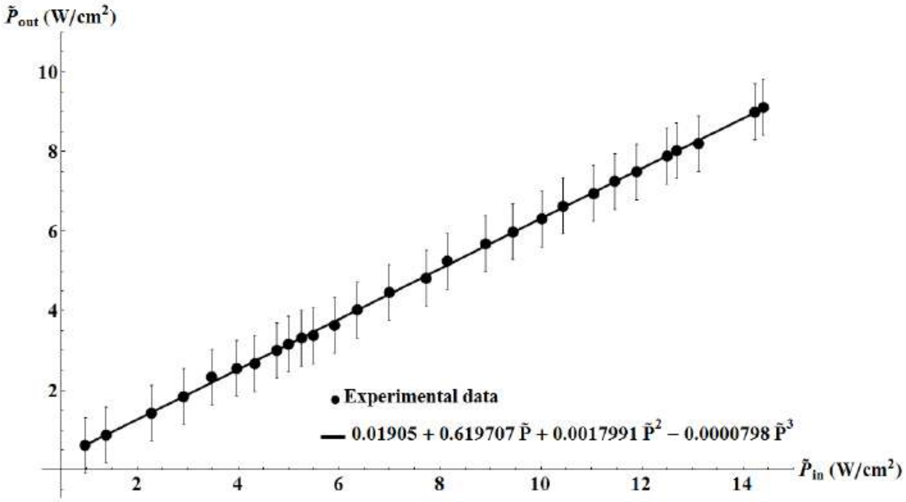

Figure 6 Measures of output versus input power densities of self-trapped dissipative soliton-tweezer, charted by ensemble of dots (with uncertainty bars). Their third order polynomial fit provides us in insert with numerical values in front of $\dot{P}$, $\dot{P}^2$,and $\dot{P}^3$ corresponding to coefficients δ, ε, and μ in the right hand side of Eq. (3).

$$\frac{i\,\partial I}{\partial z} + (\eta + \sigma|I| - \nu|I|^2 + \gamma\nabla_\perp^2)I \;= i(\delta + \varepsilon|I| - \mu|I|^2 + \beta\nabla_\perp^2)I. \quad (4)$$

This dissipative soliton-tweezer complex intensity equation (DSTCIE) is astonishingly symmetric. The imaginary and real quadratic terms increase intensity that is decreased by cubic terms in a self-organized balance. More generally, the compensation of antagonist effects is what keep the nature in dynamic equilibrium. The advantage of this novel approach is not only to describe correctly experiments but also to predict their results, which is of particular importance for medical applications. Numerical propagation of DSTCIE allows to test the feasibility of dissipative soliton-tweezers.

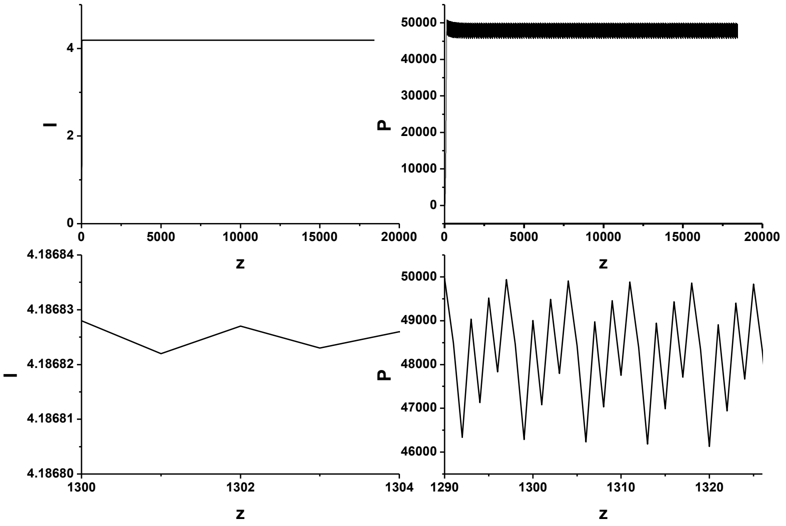

Figure 7 Femtosecond dissipative soliton-tweezer is propagated numerically z=19000 steps using DSTCIE with coefficients from inserts of Figures 5 and 6 showing stability of intensity and power. Only strong zooming revel weak breathing.

A long numerical evolution till z=20000 shows in Figure 7, a very good stability of intensity, I and power, P. A strong zooming revel very weak breathing of intensity and little bit stronger of the power due to its quadratic dependence on beam width in 2D systems[9,14,21,29]. This breathing is more obvious in Figure 8 where the soliton-tweezer 3D profile oscillates between a dome and a "millstone".

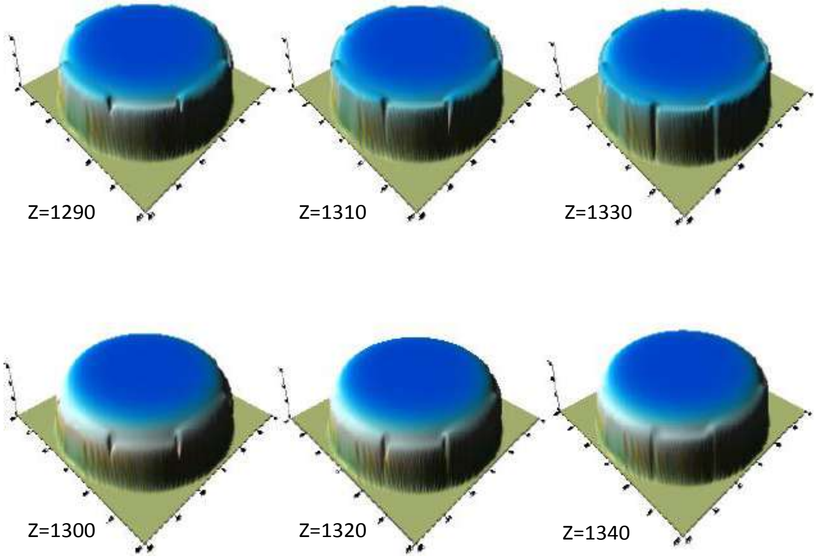

Figure 8 Breathing alternation of soliton-tweezer profiles (in arbitrary units) in form of "millstones" (first row)and domes (second row) corresponding to power maxima and minima in Figure 7.

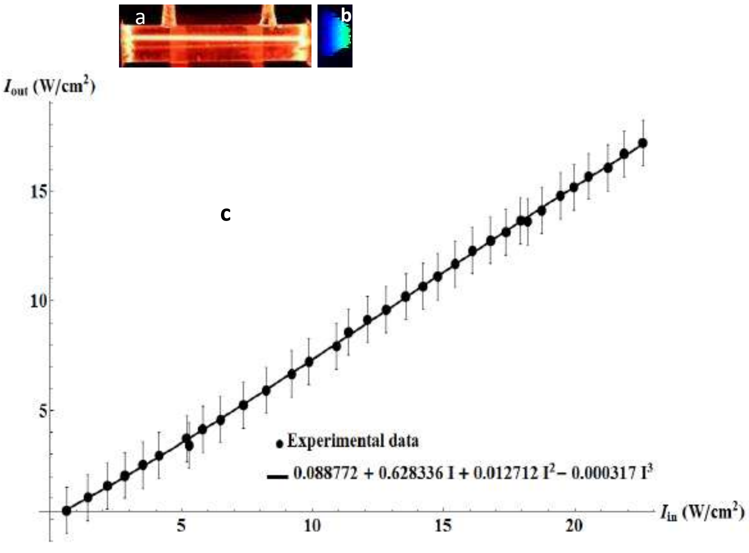

Figure 9a Same self-collimated 727 nm dissipative soliton-tweezer propagating through nanobubbles suspension in 10 cm cuvette. **b** Output profiles after propagation of 10 and 20 cm are identical. **c** Fitting input-output intensity dots yields coefficients in front of linear, quadratic, and cubic intensity to be replaced in dissipative soliton-tweezer complex intensity Eq. (4) that can predict ulterior numerical propagation.

We remarked the same behavior in a previous theoretical publication concerning self-structuring of stable dissipative breathing vortex solitons in a colloidal nanosuspension [29]. It is amazing that such a breathing is confirmed by our approach that connect directly the theory with experiments. The inertia of nanobubbles may be the reason of this breathing.

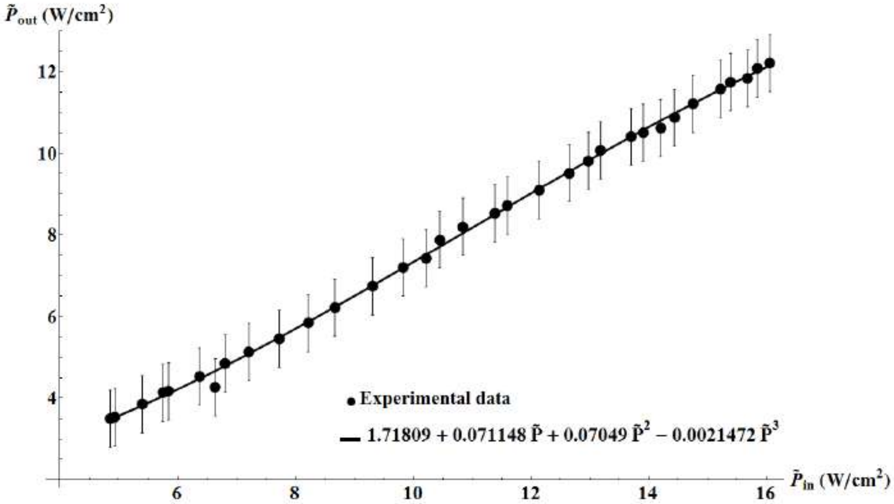

Figure 10 Measured input-output dissipative power density provides values for coefficients of imaginary polynomial terms in Eq. (4).

The self-trapping of spontaneously self-collimated soliton-tweezers is confirmed using a twice shorter u-cuvette under the identical conditions (see Figure 9a). The camera capture of soliton profile in the output of 10 cm cuvette (Figure 9b) corresponds to the profile of twice longer u-cuvette in Figure 5b. Measured output intensities and powers divided by square surface in Figure 9c and Figure 10 lead to the determination of coefficients in DSTCIE using the third order polynomial fits of corresponding input-output dots. The numerical propagation of DSTCIE gives the same results as in case of 20 cm cuvette (Figures 5 and 6). Therefore, this novel equation correctly describes behavior of dissipative solitons-tweezers in experiments of propagation in water suspension of nanobubbles.

4. Self-generation of vortexsoliton-tweezers in nanosuspensions

Vortex soliton-tweezers are robust steady-state structures with nonzero angular momentum and phase singularity in zero intensity center [14,21,30,45-47]. In conservatives systems v are governed by STCIE (Eq. 2). The propagation of dissipative vortex soliton-tweezers is described by DSTCIE (Eq. 4). We use a weak Thorlabs HeNe laser beam of 632.8 nm in order to generate vortex in 10 cm u-cuvette containing nanobubbles naturally suspended in pure water. Indeed, a vortex soliton-tweezer is spontaneously self-collimated maintaining along u-cuvette the same width, as shown in Figure 11a. Figure 11b is the camera capture of output vortex profile. Dots with uncertainty bars in Figure 11c are result of systematic and precise measurement of output intensity for each gradually increasing input intensity. The already established procedure of fitting yields the values for STCIE coefficients in insert of Figure 11c. The same values can be used for left hand side DSTCIE coefficients. Those of right hand side are obtained fitting input-output power dots in Figure 12. Hence, the feasibility of vortex soliton-tweezers is established.

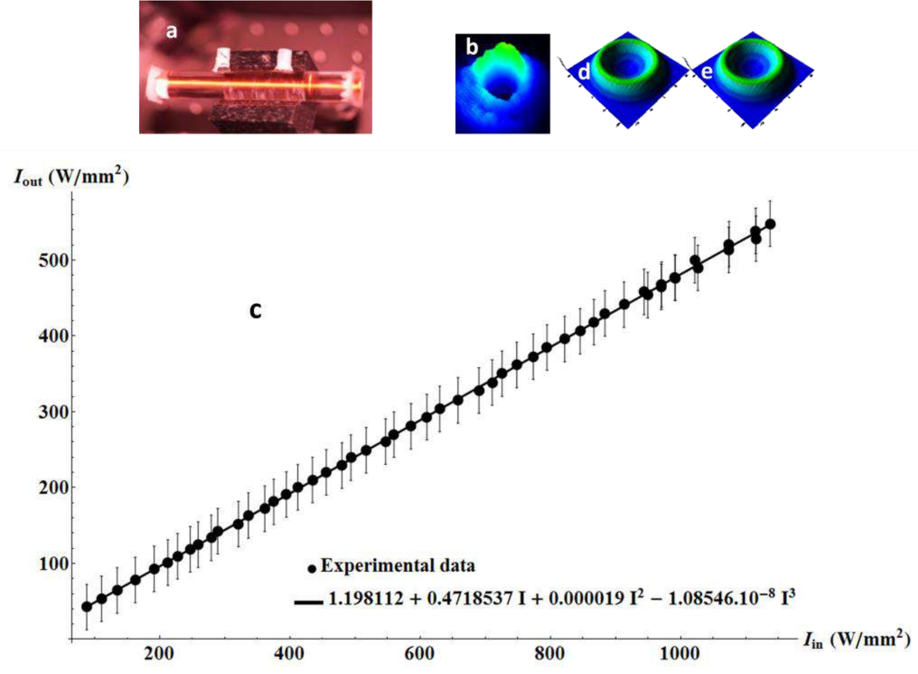

Figure 11a Vortex soliton-tweezer spontaneously self-collimated in 10 cm u-cuvette. **b** Experimentally obtained vortex output profile is similar to profiles obtained by z=1800 (**d**) and z=10000 steps (**e**) numerical simulations of STCIE with coefficients from insert (**c**).

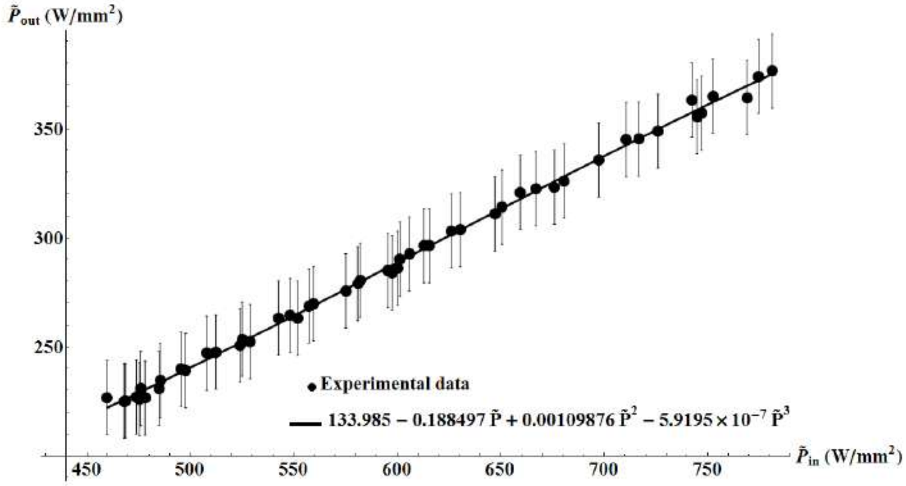

Figure 12 Output versus input power density of self-organized vortex soliton-tweezer fitted in order to obtain, in insert, values for coefficient in imaginary terms in DSTCIE.

5. Novel intensity equation for spatiotemporal tweezing light bullets

Light bullets are spatiotemporal solitons completely localized in space and time [9,19,20,48,49]. In conservative systems they are governed by three transverse dimensions (x, y, and t) NSL

$$\frac{i\,\partial E}{\partial z} + \gamma\Delta E + \eta E + (\sigma|I| - \nu|I|^2)E = 0 \qquad (5)$$

where the Laplacian$\Delta = \partial^2/\partial t^2 + \nabla_\perp^2$ is associated to the time variable t and the transverse coordinate $r_\perp$. The propagation of light bullets in dissipative systems is described using 3D Ginsburg-Landau equation [9, 48,49].

$$\frac{i\,\partial E}{\partial z} + (\eta + \sigma|I| - \nu|I|^2 + \gamma\Delta)E = i(\delta + \varepsilon|I| - \mu|I|^2 + \beta\Delta)E. \qquad (6)$$

In order to establish the direct connection between this spatiotemporal theory involving electric field, E and experiments measuring input and output intensities we multiply Eq. (5) by electric field, E in paraxial approximation

$$\frac{i\,\partial I}{\partial z} + \gamma\Delta I + \eta I + (\sigma|I| - \nu|I|^2)I = 0 \qquad (7)$$

establishing cubic-quintic tweezing light bullet complex intensity equation (TLBCIE). In this novel equation not only diffraction, but also dispersion is compensated by competing cubic-quintic nonlinearity.

In reality, experiments are always localized in three spatial dimensions and in time. They involve always losses and sometimes gain. The adequate theoretical and numerical approaches are the prerequisites for experimental realization of light bullets. Therefore, the complex intensity is the right variable in an equation that pretends to describe the experiment in a realistic way. Therefore, Eq. (6) is in paraxial approximation multiplied by electric field

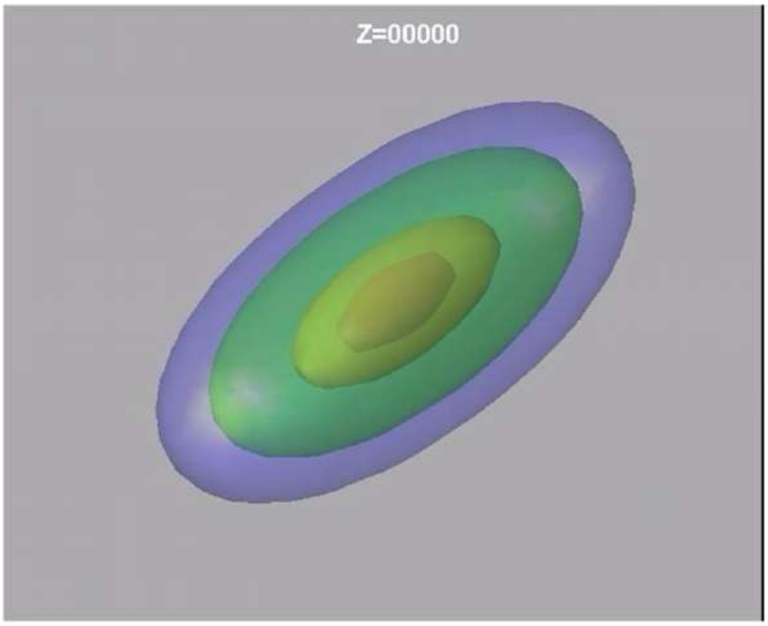

Figure 13 Dissipativelight bullet from non-spherically-symmetric input pulse becomes in the end of propagation spherically-symmetric like in Figure 14.

$$\frac{i\,\partial I}{\partial z} + (\eta + \sigma|I| - \nu|I|^2 + \gamma\Delta)I \;= i(\delta + \varepsilon|I| - \mu|I|^2 + \beta\Delta)I. \qquad (8)$$

In such a way we establish dissipative tweezing light bullet complex intensity equation (DTLBCIE). This equation represent the most general expression of self-organized description of 3D spatiotemporal soliton propagation, taking into account that the competing cubic-quintic nonlinearity represents a very good approximation of saturable nonlinearity [9,44,48,49]. The DTLBCIE is astonishingly symmetric.

Figure 14 Dissipative light bullet with topological singularity in center is effectively a soliton-tweezing shell transporting small energy suitable for secure medical applications.

The quadratic terms amplify the complex intensity through self-focusing and gain. They compensate the linear and cubic losses. The gain diffusive term with positive β balances the diffraction and dispersion. We demonstrated that in reality a cross compensation occurs between the excess of the self-focusing, losses, and gain making the system self-organized [9,48,49]. Numerically simulated light bullet from non-spherically-symmetric input pulse is shown in Figure 13. The light bullet with topological singularity is the light shell (in Figure 14). The powerful femtosecond bullet consisting of ultra-thin light shell transports a very small energy suitable for nondestructive and secure medical applications.

6. Conclusions

The prerequisites for understanding phenomena in nanophotonics are exhaustive experimental investigations coupled with theoretical advances using tools of numerical simulations. Object of our investigations is the water as the essential substance for the life in the earth. On the first glance it is astonishing that water contains naturally air nanobubbles. However, it is to forget that fishes breathe in water. Therefore, the pure water is in fact, nonlinear suspension of relatively stable nanobubbles. The nonlinear behavior of water is revealed using interactions with lasers. Propagating through water laser beams and pulses are spontaneously self-organized into soliton-tweezers that collect positively polarized nanoparticles with index of refraction larger than the water one. In opposite case, negatively polarized nanoparticles, with smaller refractive index, are expelled out, allowing laser light to propagate again through the higher index, thus to be in both cases self-focused. This self-focusing compensates all defocusing effect, spontaneously self-collimating the soliton-tweezer as our experiments and numerical simulations confirm. To be able to make the numerical simulations, it is necessary to have an adequate equation describing this phenomenon. We solved the paradox that the theoretical descriptions use the electric field, while in experiments is measured the electric intensity, by introducing a novel complex intensity equation for conservative and dissipative systems. Terms of this equation contain coefficients determined from the experimental measurements. Soliton-tweezers profiles obtained by numerical propagation of established equation, coincide with experimentally obtained profiles, confirming the correspondence between experiment and theory. In such a way, the feasibility of soliton-tweezers to control and manipulate nanoparticles in water suspension, is established. The corresponding applications are multiples. They may be medical, biological, industrial... The blood in living organisms can be considered as water suspension of nanoparticles. Soliton-tweezers can be useful in fight against viruses, bacteria, and cancer cells in blood without damaging healthy tissues. The blood passing through our u-cuvette can be irradiate by laser. Depending of their frequency soliton-tweezers or tweezing light bullets can selectively destruct some viruses, bacteria, or cancer cells [50-52]. For instance, if Coronaviruses-19 (COVI-19) have higher resonant frequencies than the frequency of soliton-tweezer they can be inactivated in its centre due to high intensity, heat, and vibrations. If viruses have lower resonant frequencies, they can be expelled out of soliton on the wall of u-cuvette where they stay bind by monoclonal antibodies [53-55]. As a consequence, the blood is purified. It is important to note that the purification is efficient even though we do not know the viruses resonant frequencies. Indeed, for the same frequency of soliton-tweezer, viruses with higher resonant frequency are inactivated in soliton center by high heat, and vibrations. Simultaneously, those viruses with lower resonant frequencies are stick on wall by monoclonal antibodies [53-55]. Viruses are much smaller than other nanoparticles in body water, so that they have much higher resonant frequencies than other. The safe use of low power soliton-tweezers for noninvasive medical applications is in such a way reinforced.

References

[1] A. Ashkin, J. M. Dziedzic and T. Yamane, *Nature***330**(1987) 769.
[2] A. Ashkin, *Science* **210** (1980) 1081.
[3] A. Ashkin *et al*. *Nature* **348** (1990) 346.
[4] R. A. L. Jones, *Soft Condensed Matter*, Oxford University Press, 2002.

[5] N. N. Akhmediev, A. Ankiewicz, *Dissipative Solitons: From Optics to Biology and Medicine*, *Lect. Notes Phys*.751 Springer-Verlag: Berlin, 2008.

[6] L. Santana-Blank *et al.Water as a Photoacceptor, Energy Transducer, and Rechargeable Electrolytic Bio-battery in Photobiomodulation*. In *Handbook of Low-Level Laser Therapy*, (2017) 119.

[7] C. Conti, G. Ruocco and S. Trillo, *Phys. Rev.Lett.***95** (2005) 183902.

[8] Y. S. Kivshar and G. P. Agrawal, *Optical Solitons: From Fibers to Photonic Crystals*; Academic Press: San Diego, 2003.

[9] V. Skarka and N. B. Aleksić, *Phys. Rev. Lett*. (2006) 0139031.

[10] Z. Chen, M. Segev and D. N. Christodoulides, *Rep. Prog. Phys*. **75** (2012) 086401.

[11] I. S. Aranson and L. Kramer, *Rev. Mod. Phys*. **74** (2002) 99.

[12] F. T. Arecchi, S. Boccaletti and P. L. Ramazza, *Phys. Rep*. **318** (1999) 1.

[13] D. Mihalache *et al.Phys. Rev. Lett.* **97** (2006) 0739041.

[14] V. Skarka *et al.Phys. Rev. Lett.***105** (2010) 213901.

[15] M. Sato, M. Ishihara, M. Kikuchi, and J. Mochida, *Lasers Surg. Med*. **43** (2011) 421.

[16] G. R. Schweinsberger *et al*. *Lasers Surg. Med*. **43** (2011) 443.

[17] R. W. Boyd, *Nonlinear Optics*; Academic Press: San Diego, 1992.

[18] G. Nicolis and I. Prigogine, *Self-organization in Nonequilibrium Systems* Wiley: New York 1977.

[19] V. Skarka, V. I. Berezhiani and R. Miklaszewski, *Phys. Rev. E***59** (1999) 1270.

[20] V. Skarka, V. I. Berezhiani and R. Miklaszewski, *Phys. Rev. E Rev. E***56** (1997) 1080.

[21] V. Skarka *et al. Phys. Rev. A***90**(2014)0238451.

[22] A. Ashkin, *Phys. Rev. Lett.* **24** (1970) 156.

[23] P. W. Smith, A. Ashkinand W. I. Tomlinson, *Opt. Lett*. **6** (1981) 284.

[24] S. Fardad *et al*. *Nano Lett*.**14**(2014) 2498.

[25] R. El-Ganainy *et al.Opt. Express***15**(2007) 10207.

[26] M. Matuszewski, W. Krolikowski and Y. S. Kivshar, *Opt. Express* **16** (2008) 1371.

[27] M. Matuszewski, W. Krolikowski and Y. S. Kivshar, *Phys. Rev. A***79** (2009) 023814.

[28] R. El-Ganainy *et al.Phys. Rev. A***80** (2009) 053805.

[29] V. Skarka *et al. Opt. Express***25** (2017) 10090.

[30] B. N. Aleksić, N. B. Aleksić, V. Skarka and M. R. Belić, *Physical Review A***91** (2015) 043832.

[31] V. Skarka, M. M. Lekić, A. G. Kovačević, B. Zarkovand N. Ž. Romčević, *Opt. Quant.Electron*.**50** (2018) 37.

[32] P. E. Watson, I. D. Watsonand R. D. Batt, *Am. J. Clin. Nutr*.**33** (1980) 27.

[33] S. A. Thorpe, A. R. Stubbs, A. J. Hall and R. J. Turner, *Nature* **296** (1982) 636.

[34] N. Ishida *et al. Langmuir* **16** (2000) 6377.

[35] F.Y. Ushikubo*et al. Colloids and Surfaces A*: *Physicochem. Eng. Aspects* **361** (2010) 31.
[36] R. M. Pope and E.S. Fry, *App. Opt*. **36** (1997) 8710.
[37] B. H. Tan, H. An and C.-D. Ohl, *Phys. Rev. Lett*. **120** (2018) 164502.
[38] M. Chaplin, Nanobubbles in *Water Structure and science*, *Water Site Map*, London South Bank University 2000.
[39] M. Takahashi, K. Chiba and P. Perry, *J. Phys. Chem*. **111**(2007) 1343.
[40] , E. Y. Lukianova-Hleb *et al.Theranostics***2**(2012) 976.
[41] E. L. Falcao-Filho, C. B. de Araujo, G.Boudebs, H. Leblond and V. Skarka, *Phys. Rev.Lett.***110** (2013) 0139011.
[42] V. Skarka, D. V. Timotijević, N. B. Aleksić, *J. Opt. A: Pure Appl. Opt.* **10** (2008) 075102.
[43] D. Mihalache *et al.Phys. Rev. A***82** (2010) 023813.
[44] B. N. Aleksić, L. A. Uvarova, N. B. Aleksić and M. R. Belić, *Opt. Quant. Electron.***52** (2020) 175.
[45] V. Skarka, N. B. Aleksić, M. Derbazi and V.I. Berezhiani, *Phys. Rev. B***81** (2010) 035202.
[46] I. Berezhiani, V. Skarka, and N. B. Aleksić, *Phys. Rev. E***64** (2001) 057601.
[47] V. Skarka, V. I. Berezhiani, and N. B. Aleksić, *Phys. Lett. A***291** (2001) 124.
[48] N. B. Aleksić, V. Skarka, D. V. Timotijević, D. Gauthier, *Phys. Rev. A***75** (2007) 061802(R).
[49] V. Skarka, N. B. Aleksić and V. I. Berezhiani, *Phys. Rev. A***81** (2010) 045803.
[50] A. Ashkin *et al. Nature* **348** (1990) 346.
[51] A. R. Singh, A. Košmrlj and R. Bruinsma, *Phys. Rev. Lett*. **124** (2020) 158101.
[52] Szu-Chi Yang *et al*. *Scientific. Reports* **5** (2016) 18030.
[53] R. G. H. Cotton, and C. Milstein, *Nature* **244** (1973) 42.
[54] Lingshu Wang, *et al*. *Journal of Virology* **92**(2018) e02002.
[55] S. Balamurugan, S. Konlavat, W. Kittikhun and P. Waranyoo, *Asian Pac J Allergy Immunol*.**38** (2020) 10.

SERBIAN ACADEMY OF
NONLINEAR SCIENCE

2nd CONFERENCE ON NONLINEARITY

Editors

B. Dragovich, Ž. Čupić

Belgrade, 2022
SERBIA

Proceedings

of the

2nd CONFERENCE ON NONLINEARITY

(October 18 – 22, 2021, Belgrade, Serbia)

Editors

B. Dragovich, Ž. Čupić

Publisher
Serbian Academy of Nonlinear Sciences
Belgrade, 2022
SERBIA

Self-organized bridge connecting THEORY to EXPERIMENTS*

Vladimir Skarka†
Laboratoire de Photonique d'Angers, EA 4464, Université d'Angers,
49045 Angers, France
Institute of Physics, University of Belgrade, 11000 Belgrade, Serbia
Marina Lekić ‡
Institute of Physics, University of Belgrade, 11000 Belgrade, Serbia

ABSTRACT

Laser tweezing stability is crucial for selective inactivation of viruses, bacteria, and cancer tissues preserving healthy cells in body water. However, laser beam propagates modifying the medium, simultaneously altering itself by feedback mechanisms, thus, jeopardizing the control. Using multidisciplinary synergy between theoretical, experimental, and numerical results, we demonstrate the feasibility of novel soliton-tweezers controlling nanoparticles in water suspensions. In soft matter like body water, suspended nanoparticles are aspirated inside the soliton-tweezers, if their refractive index is larger than the background one. They are expelled whenever their index is lower. In both case, the nonlinear density distribution of nanoparticles induces beam self-focusing that compensates self-defocusing effects, generating soliton-tweezer. Experimentally measured self-focusing and self-defocusing coefficients are incorporated in established novel synergetic soliton-tweezer complex intensity equation describing experiments realistically. Virus-nanoparticles with resonant frequencies higher than the one of soliton-tweezer would be possibly inactivated paraxially.

---

* This work has been supported by the Ministry of Education and Science of the Republic of Serbia, under Projects III 45016, OI 171038, and OI 171006. Najdan Aleksić, Vazha Berezhiani, and Stephan Rakotoarimalala are acknowledged for their contributions.

†e-mail address: vskarka@yahoo.com
‡e-mail address: lekic@ipb.ac.rs

1. Introduction

First and second law of equilibrium thermodynamics are the foundations of physics. However, every action involves utilization, hence, loss of energy, but this is only a transformation to another energy. Macroscopic laser light, *i.e.*, electromagnetic wave is transformed into heat, *i.e.*, nanoscopic agitation of interacting atoms and molecules. Following the second low, interacting nanoparticles are trying to reach the thermodynamic equilibrium, which cannot be reached since the system cannot be isolated. However, this strong attraction to the equilibrium organizes the system, making it self-organized (harmonized). Following 1977 Nobel Prize winner Ilya Prigogine, nonlinear dissipative structures are self-organized far from thermodynamic equilibrium, due to the intake of energy and/or matter (mainly nanomatter) [1]. The self-organization is the compensation of antagonist effects. The fight and the collaboration of antagonist effects, *e.g.* yin and yang, are the universal principles of dialectic. Fortunately for us, in nature yin and yang mainly cooperate generating even the self-organized life. Living organisms are mainly composed of soft nanomatter including body cells, bacteria, viruses, and other nanoparticles in water suspensions. The total human body water volume estimated from simple anthropometric measurements is about 70% [2]. Healthy human body has ten times more bacteria than cells and countless viruses. Biomedia like blood, myosin, kinesin, ribosomes, liposomes, and varieties of living cells suspended in body water can be manipulated, tweezed, and controlled using laser beams and pulses [3-7]. The safety of any laser manipulation depends on good knowledge of its propagation in water with nanoparticles [8]. A laser beam propagates in nonlinear way through a nanosuspension modifying it. Doing this, beam is simultaneously altering itself by feedback mechanisms, thus, jeopardizing its control on nanoparticles [9]. The laser stability and robustness are of crucial importance for medical and biological applications *e.g.* photobiomodulations [7]. The laser dynamical stability and precision are of crucial importance, not only for brain

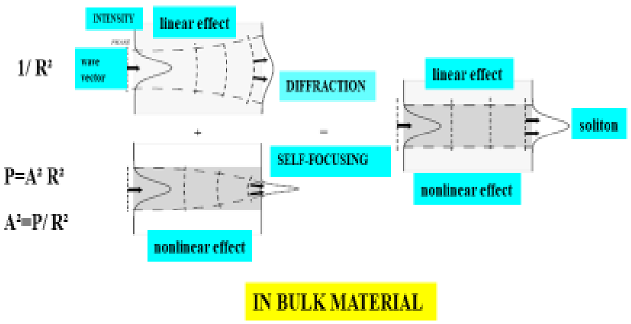

$$i\frac{\partial E}{\partial z}+\frac{\partial^2 E}{\partial x^2}+\frac{\partial^2 E}{\partial y^2}+|E|^2 E=0$$

UNSTABLE

DIFFRACTION CUBIC NONLINEARITY

$$i\frac{\partial E}{\partial z}+\frac{\partial^2 E}{\partial x^2}+\frac{\partial^2 E}{\partial y^2}+|E|^2 E-v|E|^4 E=0 \qquad (1)$$

STABLE

DIFFRACTION CUBIC - QUINTIC NONLINEARITY

Figure 1 Self-collimated soliton becomes stable whenever the cubic self-focusing nonlinearity is compensating diffraction and quintic self-defocusing nonlinearity described by two-dimension saturating Schrödinger equation.

surgery but also for nondestructive medical diagnostics [10]. The very promising mechanism to achieve the necessary stability and control of nanoparticles is the self-organization of the laser light inside nanosuspensions into solitons localized in space and in time [11-17]. The laser beam becomes soliton whenever antagonist effects, *i.e.*, beam focusing and defocusing are balanced in self-organized dynamical equilibrium far from the thermodynamic one (cooperation of yin and yang) [18-20]. In any medium, including vacuum, laser beam is diffracting. In Kerr media, in rigid slab guides beam is confined into soliton, in the region with higher optical index of refraction due to the compensation of diffraction by cubic self-focusing (see Figure 1). Such a soliton is described by the one transverse dimension (1D) nonlinear Schrödinger equation (NLS) for electric field $E=A(r)\exp(ik_0n_0z)$ where A(r) is slowly varying amplitude envelop propagating following z direction with wave vector k_0 and vacuum index of refraction n_0. However, 2D NLS is unstable in bulk media where both linear and nonlinear effects have the same width R dependence $1/R^2$ (see Figure 1). Indeed, initially dominating diffraction cannot be arrested by self-focusing, contrary to the 1D case where the focusing is proportional to 1/R. Therefore, amplitude decreases and soliton disappears. In opposite case, the self-focusing domination leads to increase of amplitude till the catastrophic collapse. To be stable, solitons need to be in Kerr media with quintic self-defocusing nonlinearity too. Such a reinforcement of yin, together with diffraction compensates self-focusing cubic nonlinearity self-generating a soliton described by saturable 2D NLS Eq. (1).

In contrast, the particularity of the laser propagation in soft matter is that the easily moving nanoparticles in fluid adapt their density distribution in such a way that the laser beam always propagates through the highest index of refraction. In experimental biophysics, 2018 Nobel Prize winner A. Ashkin used this property in order to tweeze bionanoparticles using lasers [3-5]. The high frequency pressure force of the laser field either attracts or repels suspended nanoparticles from the field region, depending if the nanoparticles optical index of refraction (n_p) is either larger or smaller than the background one (n_b). The tweezing laser beam collects paraxially, around its central axes, positively polarized nanoparticles having the index of refraction n_p higher than the background medium one ($n_p>n_b$). Therefore, such a redistribution of nanoparticles density following laser Gaussian intensity profile always induces the nonlinear beam self-focusing [3-5,8]. In opposite case beam is self-focusing too, taking into account that negatively polarized nanoparticles with lower index ($n_p< n_b$) are expelled from the beam. In both cases, the nanoparticles density modifications result in the nonlinear increase of effective index of refraction inside a tweezer making it always self-focusing and potentially collapsing [8,9]. Only solitons are stable and self-collimated due to the compensation of all self-defocusing effects by self-focusing in a self-created precarious guide corresponding to a dynamical equilibrium far from thermodynamic one.

In recent studies of the laser beam propagation in diluted noniteracting nanoparticles suspensions, the balance between the optical gradient force and particles diffusion due to Brownian motion is achieved for long duration pulses [21]. For nanoparticles with positive polarizability ($n_p > n_b$) the nonlinear Schrödinger equation (NLSE) has exponentially growing nonlinearities that lead to a catastrophic collapse [21,22]. In real nanosuspensions the wave collapse cannot take place since nonlinear Rayleigh scattering losses grow dramatically with increase of nanoparticles concentration invalidating the diluted suspension model. To overcome these difficulties more realistic formalisms with particle-particle interactions were suggested [8,23-26]. In contrast to the positive polarizability, negatively polarized nanoparticles, having refractive index smaller than the background one ($n_p < n_b$), are expelled from the laser beam minimizing Rayleigh scattering losses. The corresponding nonlinearity in NLSE is saturable leading to the formation of stable self-trapped transversely localized beam, *i.e.*, spatial soliton [8,11-13, 18-20].

The usual approach to tweezing of nanoparticles in suspensions is to artificially focalize laser tweezer in order to trap few nanoparticles in its beam waist, *i.e.*, in a very small region where the beam is precariously self-collimated in a local dynamical equilibrium (see Refs. [3] and [4]). In contrast, in our innovating experiments, this tweezing self-collimation is extended paraxially along the entire beam in solitonic dynamical equilibrium, called soliton-tweezer. In this case, not only few nanoparticles but all nanoparticles are tweezed collectively. In order to establish soliton-tweezing of nanoparticles in body water, the prerequisites are synergetic multidisciplinary theoretical, numerical and experimental investigations of nanoparticles in pure water suspensions.

A very difficult task is to describe essentially nonlocal tweezing experiments measuring electric intensity I=EE, by a partial differential equation like NLSE that generally gives electric field E in one point in space and time. Therefore, in our innovating description of tweezing experiments in water suspensions of nanoparticles we introduce the nonlocality through the coupling between the heat equation and the generalized higher order NSL. Taking into account the estimated total body water volume of about 70%, the biosafety of any laser manipulation depends on good knowledge of solitons propagation in water with nanoparticles [2]. Consequently, our theoretical model in a multidisciplinary synergetic approach, needs confirmation by experiments and numerical simulations as the prerequisite for safe medical and biological applications.

2. Nonlocal model of self-organized soliton-tweezers

Coupling light pressure and thermal self-action, we establish a nonlocal variational model of soliton-tweezers self-trapped propagation in nanoparticles suspensions. The soliton-tweezers self-organization and nonlinear guiding are investigated starting from the Helmholtz equation

$$\Delta\check{\mathrm{E}} + \mathrm{k}_0^2\mathrm{n}^2\check{\mathrm{E}} = 0 \qquad (2)$$

where $k_0=\omega/c$ is the wavevector and $\bar{E}$ is the amplitude of monochromatic electric field $\check{E}=\bar{E}(Z, r_\perp)$ *exp* $(i\omega t)$+cc denoting by cc complex conjugate [12,22,26]. The Laplasian $\Delta = \partial^2/\partial Z^2 + \nabla_\perp^2$ with the transverse one $\nabla_\perp^2 = \frac{\partial^2 E}{\partial x^2} + \frac{\partial^2 E}{\partial y^2}$ is associated to the field propagation variable Z and the transverse coordinate $r_\perp = \sqrt{x^2 + y^2}$. The complex medium effective index of refraction, n depends not only on refractive indices of background (n_b) and nanoparticles (n_p), but also on the volume filling factor $f=V_p\, dN_p/dV$, where N_p stands for the number of nanoparticles and $V_p=4\pi a^3/3$ is the volume of a spherical nanoparticle with radius a. The effective refractive index of composed medium reads $n = (1-f)n_b + fn_p$ [22]. Optical indices $n_b=n_{0b} + \delta n_b(J)$ and $n_p=n_{0p} + \delta n_p(J)$, as well as the filling factor $f=f_0 + \delta f(J)$ depend on the laser intensity $J=(cn_0/2\pi)|\bar{E}|^2$. Consequently, the effective index in Eq. (2) is also perturbed $n=n_0 + \delta n(J)$, where $n_0=(1-f_0)n_{0b} + f_0 n_{0p}$ and $\delta n=(n_{0p}-n_{0b})\delta f + (1-f_0)\delta n_b + f_0\delta n_p$. The filling factor reads $f=f_0$ *exp* $(-\beta|\bar{E}|^2)$ where $\beta=|\alpha|/4k_BT$ with temperature, T and k_B as Boltzmann constant [12,21]. The polarizability α of nanoparticles is given by $\alpha=3V_p n_b^2\xi/(4\pi)$ where $\xi=(n_{0p}^2- n_{0b}^2)/(n_{0p}^2 + 2n_{0b}^2)$.

Importance of thermal nonlinear effects modifying laser beam dynamics in suspensions of nanoparticles is well recognized [22,27,28]. Indeed, the temperature of background liquid (*e.g.* body water) increases absorbing part of radiation energy, hence, the thermal nonlinearity of host medium can modify the nonlinear dynamics of soliton in a nonlocal way [17,29,30]. The electromagnetic laser waves induced temperature change obeys the heat transport equation $C\partial\delta T/\partial t-\chi\Delta\delta T=\mu J$ where C is the heat capacity per unit volume, χ is the thermal conductivity, while the coefficient μ characterizes linear absorption losses due to the background liquid heating [17]. Such a heat transfer equation reduces to

$$\chi\Delta\delta T = -\mu J \tag{3}$$

under steady state conditions, *i.e.*, when temporal variation in laser intensity profile can be neglected [17,27]. Indeed, one of the main characteristics of solitons is their high temporal and spatial stability [11-13,18-20,31,32].

In order to elucidate experiments that have essentially a nonlocal character, we construct, starting from Eqs. (2)-(3), a novel nonlocal theoretical model of self-organized soliton-tweezers propagation in suspensions of nanoparticles. Assuming the electric field, $\bar{E}=\bar{A}(r_\perp)$ *exp* (ik_0n_0Z), the slowly varying envelop $\bar{A}(r_\perp)$ approximation is applied to both equations simultaneously. Using paraxial approximation, the following set of coupled nonlinear equations is obtained

$$i\frac{\partial\bar{E}}{\partial Z}+\frac{\nabla_\perp^2\bar{E}}{2k_0n_0}+k_0|\,n_{0p}-n_{0b}|f_0(1-e^{-\beta|\bar{E}|^2})\bar{E}-k_0(1-f_0)\left|\frac{\partial n_b}{\partial T}\right|\delta T\bar{E}=0 \tag{4}$$

and

$$\nabla_\perp^2\delta T=-\frac{cn_0\mu}{2\pi\chi}|\bar{E}|^2. \tag{5}$$

Besides the propagation and diffraction terms, in Eq. (4) appear the exponential focusing term as well as the defocusing one that insure the coupling with Eq. (5). In most of liquids, like body water, the thermal nonlinearity has a defocusing character $\partial n_b/\partial T<0$. Taking into account that nanoparticles are expelled from the laser beam, the Rayleigh scattering losses are neglected [8, 21]. Eqs. (4)-(5) are rewritten as

$$i\,\partial E/\,\partial z+\nabla_\perp^2E+(1-exp(-|E|^2))E-\Theta E=0 \tag{6}$$

and

$$\nabla_\perp^2\Theta=-K|E|^2=-K|I| \tag{7}$$

using dimensionless variables: the propagation and transverse coordinates $z=Zk_0|n_{0p}-n_{0b}|f_0$ and $r=(2k_0^2 n_0|n_{0p}-n_{0b}|f_0)^{1/2}r_\perp$, envelop electric field $E=\beta^{1/2}\bar{E}$, real intensity $|I|=|E|^2$, and generalized thermal index $\Theta=K_1(\delta T/T)$, with the coefficient $K_1=|n_{0p}-n_{0b}|^{-1}(f_0^{-1}-1)T|\partial n_b/\partial T|$ and the coupling parameter $K=K_1K_2$ where $K_2=\mu c n_0 k_B/(2\pi|\alpha|\chi k_0^2|n_{0p}-n_{0b}|f_0)$. The thermal conductivity of water at T=300 K° is $\chi=0.6071$ $K^\circ W/m$ and $\partial n_b/\partial T=-10^{-4}$ $(K^\circ)^{-1}$.

3. Nonlocal variational approach of soliton-tweezers

Starting from Eqs. (6)-(7) a novel nonlocal variational approach adapted to nonlocal experiments, is established [33,34]. The Lagrangian density corresponding to Eqs. (6)-(7) reads

$$L=\frac{i}{2}\left(\frac{\partial E^{cc}}{\partial z}E-\frac{\partial E}{\partial z}E^{cc}\right)+|\nabla_\perp E|^2-(|E|^2-1+exp[-|E|^2])-\frac{|\nabla_\perp\Theta|^2}{2K}+\Theta|E|^2 \tag{8}$$

The appropriate variations of Lagrangian, $\delta L/\delta E^{cc}=0$ and $\delta L/\delta\Theta=0$ yield Euler-Lagrange equations associated to Eqs. (6)-(7). Suitably chosen trial functions are optimized. For the laser field envelop the natural trial function is a Gaussian [8,16,18-20]

$$E=A(z)exp[-r^2/(2R(z)^2)+iC(z)r^2+i\Psi(z)], \tag{9}$$

where A, R, C, and Ψ are respectively amplitude, beam width, wave front curvature and phase [8,13,16,20]. The trial function for the nonlocal heat response of the medium reads

$$\Theta=B(z)\{Ei[-r^2/R_T(z)^2]-ln[r^2/d^2]\}, \tag{10}$$

where B is the amplitude and R_T is the width [33,34]. Here, *Ei* is the exponential integral function. The trial function Θ corresponds to radially-symmetric solution of Eq. (7) with zero boundary conditions on a circle of radius d>>R. The trial functions are substituted into Eqs. (6)-(7) and Lagrangian is averaged over radial coordinate

$$< L >= P\left[\frac{d\psi}{dz} + \left(\frac{dC}{dz} + 4C^2\right)R^2 + \frac{1}{R^2}\right] - PBln[\frac{d^2e^{\gamma}}{R^2+R_T^2}] - \frac{2\pi B^2}{K} ln[\frac{d^2e^{\gamma}}{2R_T^2}] + \pi R^2 G(A^2) \qquad (11)$$

with the nonlinearity

$$\mathrm{G}(\mathrm{A}^2) = \int_0^{\infty}(1 - \mathrm{A}^2 exp[-\rho] - exp[-\mathrm{A}^2 exp[-\rho]])\mathrm{d}\rho = ln[\mathrm{A}^2] - \mathrm{A}^2 + \Gamma[0, \mathrm{A}^2] + \gamma, \qquad (12)$$

where $\gamma \simeq 0.577216$ is Euler's constant, $\Gamma[s, w] = \int_w^{\infty} y^{s-1} exp(-y)dy$ is the incomplete gamma function, and $\rho = r^2/R^2$. The beam power is $P=\pi A^2 R^2$. The following set of ordinary differential equations is obtained under the condition of zero variation with respect to each of unknown functions $Q=(A, B, R, R_T, C, \Psi)$ in trial functions, $\delta<L>/\delta Q=0$

$$dA/dz = -4\, A\, C, \qquad (13)$$

$$C = 1/(4R)\, dR/dz, \qquad (14)$$

$$\mathrm{d}^2\mathrm{R}/\mathrm{dz}^2 = 4[1/\mathrm{R}^3 + \mathrm{B}/2\mathrm{R} - 1/\mathrm{R}(\mathrm{G}/\mathrm{A}^2 - G')] = \mathrm{F}, \qquad (15)$$

$$\mathrm{d}\Psi/\mathrm{dz} = -2/\mathrm{R}^2 + \mathrm{G}/\mathrm{A}^2 - 2G' + \mathrm{B}\, ln[2\mathrm{R}^2/(\mathrm{d}^2 e^{\gamma+1/2})], \qquad (16)$$

where $G' = \partial G(A^2)/\partial A^2$, along with two algebraic relations $B=KP/4\pi$, and $R_T = R$. The beam power conservation follows immediately from Eqs. (14)-(15). The generalized force, F is given by Eq. (15) [11]. To steady state solutions, $dA/dz=dR/dz=dC/dz=C=0$ of Eqs. (13)-(16) correspond soliton-tweezer widths $R_{\pm} = 2\left[A^2\sqrt{K}\sqrt{(G - G'A^2) \pm \sqrt{(G - G'A^2)^2 - \frac{KA^6}{2}}}\right]^{-1}$. This equation exists providing the coupling parameter $K<K_{cr}\approx 0.056$, as follows from expressions $G - A^2 G' = -1 + exp[-A^2] + ln[A^2] + \Gamma[0, \mathrm{A}^2] + \gamma$ and $G' = -1 + (1 - exp[-A^2])/A^2$. The influence of thermal effects on the laser beam propagation depends on the value of the coupling parameter K that is very small [17,27]. The relation between power, P and amplitude, A, obtained solving Eqs. (13)-(15), is charted in Figure 2 for different small parameters K. Indeed, the influence of background heating is

present but small. Full curves correspond to stable steady state soliton-tweezer solutions, while the dotted ones stand for unstable solutions.

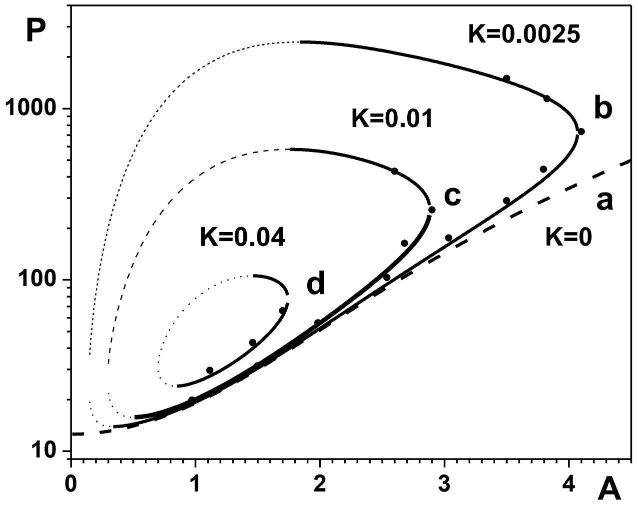

Figure 2 Power, P as a function of amplitude, A for various coupling parameters, K. For K=0 (dashed line) there are no heating effects. Full lines correspond to stable analytical solutions and dotted lines to unstable ones. Heavy dots are obtained by numerical simulations.

The soliton-tweezer stability is confirmed by numerical simulations represented by heavy dots in Figure 2. Without heating effects (K=0), the system of two coupled Eqs. (6)-(7) reduces to the one higher order NSLE corresponding to the Eq. (6) without coupling linear term. Such a case is charted in in Figure 2 by dashed strait line.

The potential, U, shown in Figure 3, is obtained integrating the generalized force F from Eq. (15)

$$\mathrm{U} = -\int \mathrm{F}(\mathrm{R})\mathrm{dR} = \frac{2}{\mathrm{R}^2} + \frac{2\pi\mathrm{R}^2}{\mathrm{P}}\left(\Gamma\left[0,\frac{\mathrm{P}}{\pi\mathrm{R}^2}\right] + ln\left[\frac{\mathrm{P}e^{\gamma}}{\pi\mathrm{R}^2}\right]\right) - 2 - \frac{\mathrm{KP}ln\mathrm{R}^2}{4\pi}. \quad (17)$$

Using the analogy with a bullet in a potential well, a deeper physical understanding of "light bullet" dynamics around equilibrium width, R_{eq}, can be acquired [13,16,20]. Indeed, dynamically stable soliton-tweezers are self-trapped in minima of U-potential well corresponding to the novel analytical stability criterion

$$\left(\frac{\partial^2 \mathrm{U}}{\partial \mathrm{R}^2}\right)_{\mathrm{R}=\mathrm{R}_{\mathrm{eq}}} = \frac{8}{\mathrm{R}^2}\left(\frac{2}{\mathrm{R}^2} + \frac{\mathrm{KP}}{8\pi} - \frac{\pi \mathrm{R}^2}{\mathrm{P}} + \left(1 + \frac{\pi \mathrm{R}^2}{\mathrm{P}}\right) exp\left[-\frac{\mathrm{P}}{\pi \mathrm{R}^2}\right]\right)_{\mathrm{R}=\mathrm{R}_{\mathrm{eq}}} > 0\,. \tag{18}$$

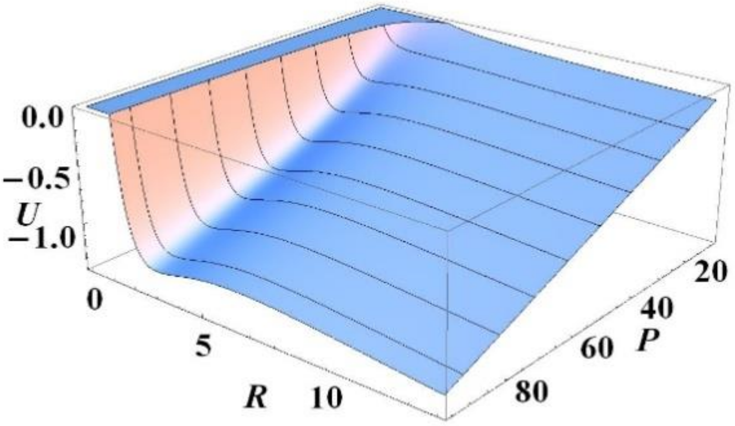

Figure 3 Stable steady state soliton-tweezer solutions are in the bottom of U-potential well for small widths, R, and self-trapping powers, P.

Therefore, the stable propagation of soliton-tweezer is analytically established for full line intervals of self-trapping in Figure 2 corresponding to the bottom of potential well in Figure 3.

In experiments only global self-focusing and self-defocusing effects are measured [32]. Therefore, the exponential of Eq. (6) is formally expanded and the dominating self-focusing cubic nonlinearity term is weighted by the coefficient σ that takes into account the formal sum of all smaller positive higher-order self-focusing terms in the expansion. Similarly, the dominating negative, self-defocusing quintic nonlinearity is weighted by the coefficient ν regrouping all smaller negative terms of higher order

$$i\,\partial E/\partial z + \nabla_{\perp}^{2}E + (\sigma|I| - \nu|I|^{2})E - \Theta E = 0. \tag{19}$$

The established nonlocal variational model of self-organized soliton-tweezer propagation in nanosuspensions has to be confirmed by experiments.

4. Experimentally self-generated soliton-tweezers confirmed by numerical simulations

In order to establish soliton-tweezing of nanoparticles in body water, the prerequisites are synergetic multidisciplinary theoretical, numerical and experimental investigations of the suspension of nanoparticles in pure water [8,35-39]. Here we consider, as a representative example, the continuous laser interaction with negatively polarized nanoparticles ($n_b > n_p$) in pure water suspension. Without loss of generality, we investigate the self-organized propagation of a near infrared laser beam of wave length λ_0=727 nm in u-cuvette with 100 mL pure water suspension of 0.05 mg gold nanoshells. Such hybrids are surface plasmon resonant nanoparticles consisting of a nanoscale silica core surrounded by an ultra-thin gold shell [22,37,39,40]. In experiments we use gold nanoshells of 240 nm diameter that have a strong plasmon resonance at wave length λ_0=980 nm [37,41]. In laser light of lower wave length λ_0=727 nm, hence, higher frequency, these nanoparticles are negatively polarized [22]. Their capping agent is the polyethylene glycol (PEG) ligand that is covalently bound to the particles surface [37,42]. It is a safe polyether compound consisting of repeating units of ethylene oxide. The PEG is used as a stealth coating in biomedical applications in order to evade the body immune system and to reduce non-specific binding [37,42]. Its surface functionality disperses very well in water increasing biocompatibility for *in-vivo* and *in-vitro* toxicology experiments, radionanomedicine, nanobiodiagnostic, as well as photothermal applications [5,10,35,37-42]. Such a surface is very stable in buffers containing high salt concentrations found in culture media and body water like blood.

The established nonlocal variational model of soliton-tweezer self-trapped propagation controlling collectively tweezed nanoparticles in plasmonic suspensions is confirmed by experiments using appropriate setup with Mira 900 laser of wavelength λ_0=727 nm in continuous regime. The spontaneous self-collimation of laser beam due to its self-trapped propagation in 20 cm long optically clear u-cuvette filled with pure water suspension of collectively tweezed gold nanoshells, is shown in Figure 4a. Corresponding camera captured output beam intensity profile is charted in Fig. 4b. The constant beam width during the propagation is the signature of stable soliton-tweezer self-trapping. Indeed, the beam width conservation implies the zero wave front curvature that is the main property of solitons [12,18,31,32]. In contrast to usual diffracting laser beams, the nonlinear soliton-tweezer is spontaneously self-collimated due to the compensation of self-defocusing by the self-focusing tweezing effect [8,13,16,18-20,31,32]. Therefore, experiments

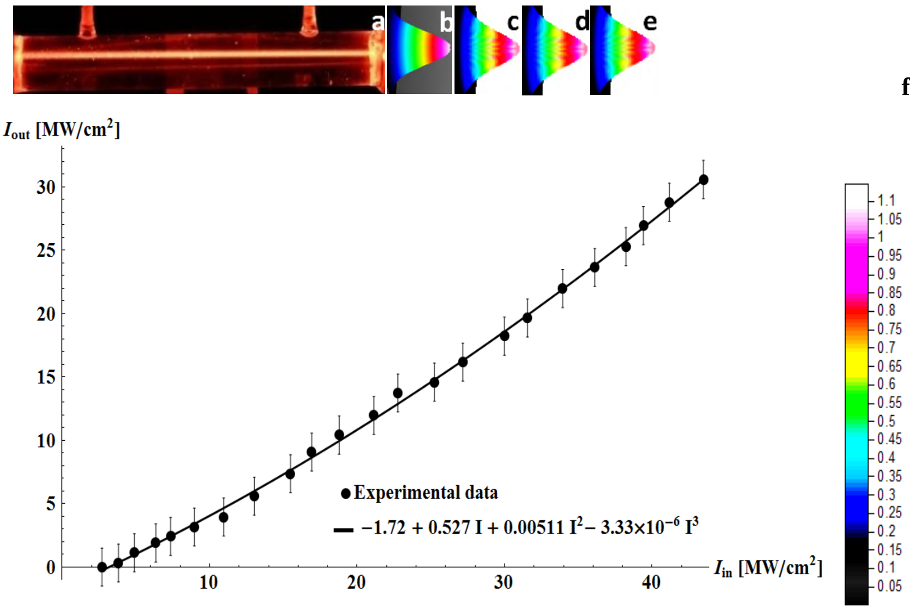

Figure 4 Matching of experimental and numerical results of soliton-tweezer propagation in u-cuvette of 20 cm. **a** Spontaneously self-trapped and self-collimated soliton-tweezer propagating through plasmonic suspension of collectively tweezed nanoshells. **f** Dots with uncertainty bars represent measured soliton-tweezer output intensities for increasing input intensities. In insert, their third order polynomial fit determines positive numerical values of coefficients **η** and **σ** in front of intensities I, and I^2 of Eq. (20), as well as the negative value of **ν** in front of I^3. **b** The soliton-tweezer output profile, camera captured in experiment, is matching numerical profiles that stay same after propagations of (**c**) z=1000, (**d**) z=20000, and (**e**) z=30000 arbitrary unit. The color scale is common.

confirm that soliton-tweezers stay in dynamical equilibrium in the bottom of the U-potential well in Figure 3, as predicted by the established analytical stability criterion, Eq. (18). Dots in Figure 4f correspond to measured values of output intensities, I_{out} as functions of gradually increasing input intensities, I_{in}. Their third order polynomial fit gives $\eta I + \sigma I^2 - \nu I^3$ with concrete values of coefficients in insert of Figure 4f. The quadratic intensity term, σI^2 corresponding to the concave part of curve for small intensities, is focusing, like the self-focusing term in usual nonlinear Schrödinger equation (NLSE) for electric field, E. The negative cubic intensity term, $-\nu I^3$ corresponding to the convex part of curve for big intensities, is defocusing, like the negative self-defocusing term in NLSE. The linear intensity term, ηI does not have a counterpart in ordinary local NLSE. It corresponds to the linear term in Eq. (19) that couple this equation with heat equation Eq. (7). As can be seen from Figure 2 the parameter K is very small. As a consequence, Eq. (7) can be formally integrated contributing a coefficient η to this coupling term in Eq. (19). Therefore, the nonlocal influence of the heat can be included in the linear term of Eq. (19) rewriting it as ηE in our model equation. Therefore, the coefficient η as well as coefficients σ and ν have to be determined from experiments by fitting measured input-output intensity $I=E^2$ curve, as in Figure 4f. Usually in theoretical approaches, laser electromagnetic wave is represented only by the electric field E, taking into account that the corresponding magnetic field is proportional to its complementary electric radiation E [6,12]. However, the experimental data force us to take into account intensity $I=E^2$ if we want to establish a realistic theoretical description of laser electromagnetic field that necessary includes complementary magnetic field. Indeed, the self-generation of laser electromagnetic light is the consequence of the universal principle of dialectic: the cooperation of electric (yang) and magnetic (yin) fields. As a consequence, rewritten Eq. (19) for complex electric field E is multiplied by the same E in order to model the experimentally measured complex intensity $I=E^2$, giving the synergetic soliton-tweezer equation

$$i\,\partial I/\partial z + \varepsilon\nabla_{\perp}^{2} I + \eta I + (\sigma|I| - \nu|I|^2)I = 0. \tag{20}$$

This equation model the influence of heat nonlocality, self-focusing, and self-defocusing in experiment, respectively, through the measured coefficient η, σ, and ν. Both experimental results and theoretical model confirm the solitonic nature of soliton-tweezers. Consequently, self-focusing balances self-defocusing and diffraction, implying $\varepsilon = \sigma - \nu$. Therefore, the coefficient ε is also determined from the same experiment. This novel synergetic soliton-tweezer complex intensity equation (STCIE) establishes the missing bridge between nonlocal experiments and their direct theoretical description.

The output intensity profile after a propagation of z=1000 arbitrary units (a.u.), is obtained in Figure 4c as a numerical solution of STCIE with experimentally measured coupling, self-defocusing and tweezing self-focusing coefficients. It coincides with numerical profiles in Figures 4d and 4e after very long propagations of z=20000 a.u. and 30000 a.u. This is numerical confirmation of a spontaneous self-collimation of soliton-tweezer with conserved width. The striking similarity of experimental and numerical profiles in Figures 4b-4e helps to establish the feasibility and numerical predictability of soliton-tweezers based on the synergy of the multidisciplinary theoretical, experimental, and numerical approaches.

Soliton-tweezer robustness is also confirmed in Figures 5 by a stable behavior of its width, R, complex intensity, I, and power, P during a 30,000 a.u. long numerical evolution. The light breathing is the signature of soliton-tweezer dynamic stabilization in the bottom of U-potential well of Figure 3, through collective tweezing of nanoparticles that have inertia.

In order to see the beam profile in the center of u-cuvette of 20 cm, the same experiment is repeated with the u-cuvette of 10 cm. Obtained spontaneously self-collimated soliton-tweezer is camera captured in Figures 6a-6b. It has the same width as the one in Figs. 4a-4b. Numerical values of coefficients in Eq. (20) are extracted from the third order polynomial fit of experimentally obtained input-output dots in insert of Fig. 6f. STCIE with these values is solved numerically yielding identical soliton-tweezer output profiles after z=1000 a.u. (Figure 6c), z=20000 a.u. (Fig. 6d) and z=30000 a.u. (Fig. 6e) numerical propagations. These profiles are matching those of the 20 cm u-cuvette in Figures 4c-4e, although the fitting coefficients for STCIE in inserts of Figs. 4f and 6f are quite different. Essential is that both curves start as concave causing tweezing self-focusing with positive I^2 and finish as convex inducing self-defocusing with negative I^3, confirming the feasibility of soliton-tweezers.

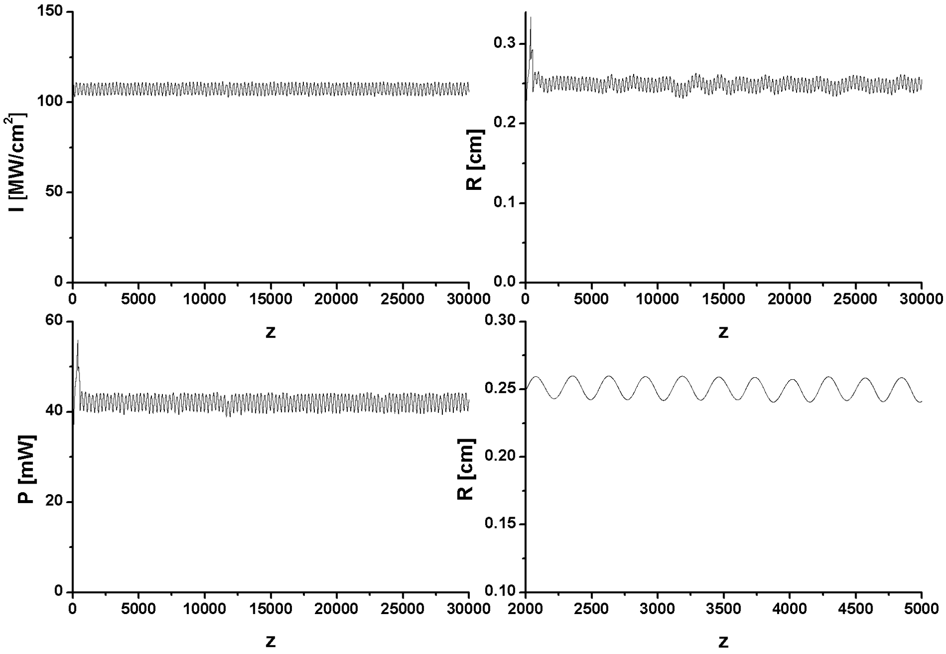

Figure 5. Numerical propagation of STCIE with fitting parameters of Figure 4f, during z=30,000 a.u. shows stable and robust regular breathing of soliton-tweezer complex intensity, **I** power, **P,** and beam width, **R** (with two different resolutions) in the dynamical equilibrium in the bottom of U-potential well of Figure 3.

Coefficients coming from insert of Figure 6f are introduced in STCIE in order to obtain stable numerical evolutions of width, R, complex intensity, I, and power, P during more than z=30,000 a.u. (see Figure 7). Their behavior

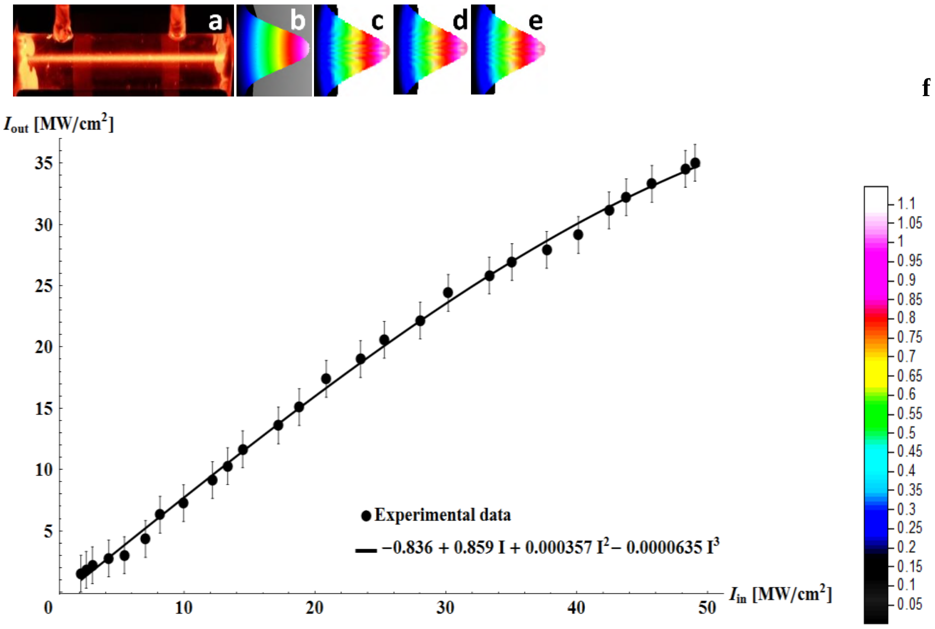

Figure 6 Spontaneously self-collimated propagation of soliton-tweezer in 10 cm u-cuvette. **a** The camera captured beam is the same as the one in 20 cm u-cuvette. **b** Its experimental output profile coincides with those obtained by numerical propagation of Eq. (20) after (**c**) z=1000, (**d**) z=20000, and (**e**) z=30000 a.u., as well as with those of Fig. 4a-4e. The color scale is common for both experiments. **f** Measured soliton-tweezer output intensities for increasing input ones are represented by dots with uncertainty bars. In insert, their third order polynomial fit gives numerical values of coefficients in front of linear and nonlinear intensities in Eq. (20).

is similar to the one in Figure 5, confirm robustness of soliton-tweezer and its predictability important for medical applications.

Therefore, identical experimental and numerical results of self-trapping in both u-cuvettes and in theoretical model, charted in Figures 2-7, confirm the feasibility, stability, robustness, and predictability of soliton-tweezer controls of collectively tweezed nanoparticles in plasmonic suspensions.

Behavior of soliton-tweezer self-trapped in suspension of positively polarized nanoparticles is investigated using femtosecond laser of wavelength λ_0=1037 nm. In experiments we use gold nanoshells of 240 nm diameter that have a strong plasmon resonance at wave length λ_0=980 nm. Indeed, in laser light of higher wave length λ_0=1037 nm, these nanoparticles are positively polarized [22]. The experiment is of the same conception with the same cuvette of 10 cm as in previous experiments, but the soliton-tweezer is invisible at this wavelength. However, it is possible to investigate the structure of soliton-tweezer and its propagation using our innovative approach. In Figure 8 are charted data of measured output complex intensities as function of increasing input intensities, in form of dots. Their third order polynomial fit gives $\eta I + \sigma I^2 - \nu I^3$ in inset of Figure 8 with concrete values of coefficients η, σ, and ν. As in previous examples, the positive sign of the quadratic self-focusing term implies that the first part of the curve for the smaller intensities is parabolic, *i.e.*, convex. The second part of the curve for higher intensities is concave due to negative sign of the cubic self-defocusing term. We see here the collaboration of

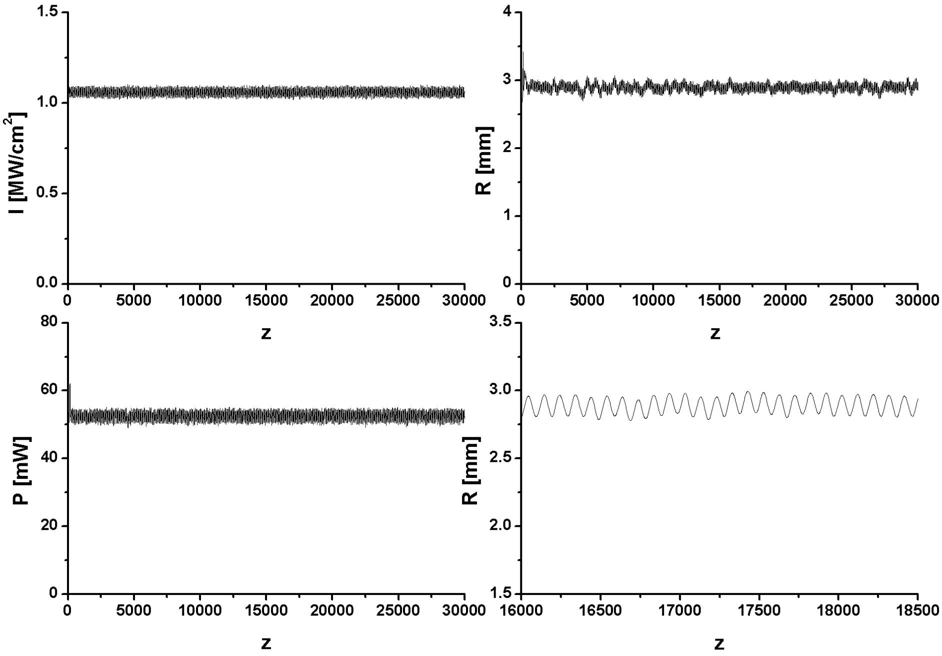

Figure 7. Soliton-tweezer stability in 10 cm cuvette is confirmed numerically. Numerical values of coefficients, obtained by fitting experimental data, are included in Eq. (20), in order to perform 30,000 steps long stable numerical propagation of complex intensity, **I**, power, **P**, and width, **R,** resulting in their conservation that confirm soliton-tweezer stability.

antagonist effects of self-focusing (yang) and self-defocusing (yin) that is responsible for the self-organization of stable soliton-tweezer in Figure 8. We have intention to investigate the universal character of convex-concave curves that appear in the increasing part of Gaussian and sinusoid too.

Obtained values of coefficients η, σ, and ν are introduced in our innovative STCIE, Eq. (20). This equation is then numerically propagated from z= 0 a.u. till z=90520 a.u. (see Figure 9). Such an exceptionally long propagation has for purpose to demonstrate the perfect stability and robustness of soliton-tweezer. This is due to the compensation of all self-defocusing effects by self-focusing nonlinearity induced by collective modification of nanoshells density following the soliton-tweezer profile. This compensation in STCIE comes from the synergetic yin-yang self-cooperation of theory and experiments making the bridge between them. Although STCIE is local in space as any nonlinear partial differential equation, it includes, in its linear term, the essence of nonlocality through

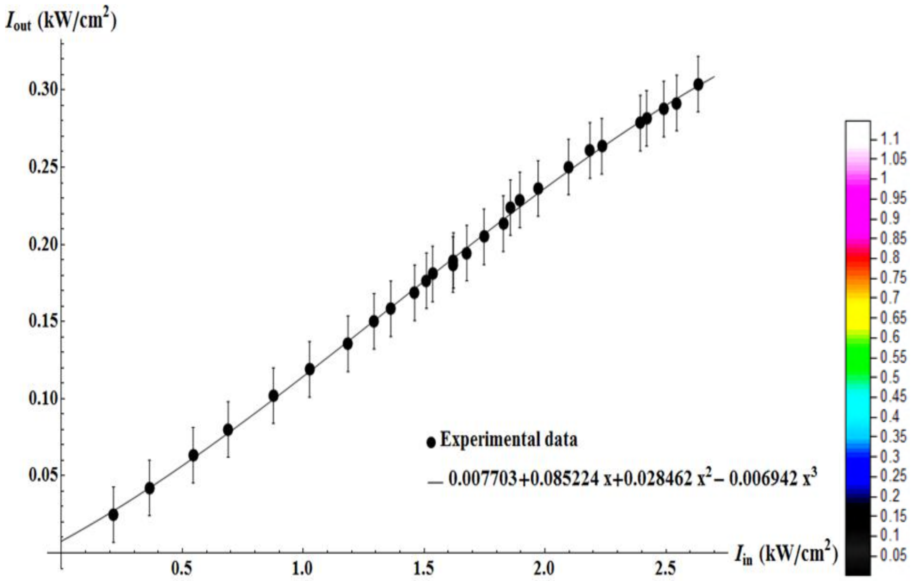

Figure 8 Soliton-tweezer self-trapped and self-collimated in suspension of positively polarized nanoparticles is investigated using femtosecond laser of wavelength λ_0=1037 nm. Heavy dots output intensities are charted in function of increasing input intensities.

the coefficient η that take formally into account the coupling with heat equation. The value of η comes from experimental measurements. Indeed, our synergetic STCIE is a hybrid equation with values of coefficient σ in self-focusing term and coefficient ν in self-defocusing term, come directly from the measurements too. In such a way, a realistic theoretical description of the experiment is established for the first time.

The stability and robustness as well as the predictability are demonstrated in figure 10 where the soliton-tweezer intensity, I, power, P, and width, R are constant. Nearly imperceptible breathing of intensity is seen in Figure 10 only with very big resolution of 30 a.u. This breathing appears in Figure 9 as the transformation of dome soliton-tweezer into millstone one.

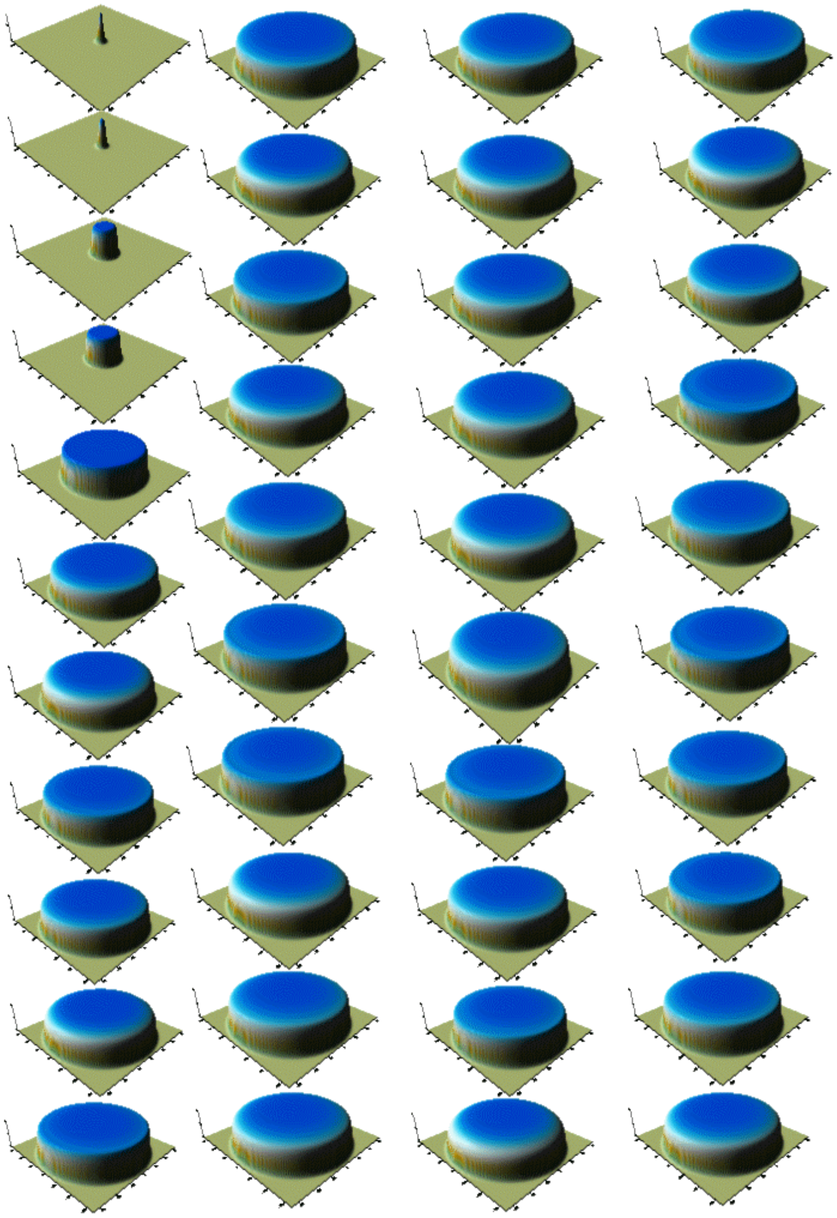

Figure 9 Exceptionally long numerical propagation of STCIE with fitting parameters of Figure 8, charted for z=0, 20, , 40, 50, 100, 300, 400, 430, 440, 450, 460, 1600, 1750, 2690, 2700, 2710, 3250, 5000, 8000, 10000, 15000, 16900, 17370, 17880, 18120, 18400, 18420, 21280,21800, 24450, 27000, 32550, 33000, 46400, 49960, 60500, 90510, and z=90,520 a.u. shows stable and robust regular breathing of soliton-tweezer consisting of the change of its shape from millstone to dome and vice versa.

5. Conclusions

As demonstrated, the self-trapped and self-collimated soliton-tweezer is perfectly stable in water suspensions of both positively and negatively polarized nanoparticles. Therefore, we established the feasibility of self-organized soliton-tweezers controlling collectively nanoshells in water suspension using multidisciplinary theoretical, experimental, and numerical results obtained synergistically. The stability, predictability and robustness of soliton-tweezers suggest the possibility of safe medical applications, *e.g.* selective inactivation of viruses, bacteria or cancer cells in body water without damaging healthy tissues [4,10,35-41,43,44]. Indeed, an efficient and safe inactivation of human coronaviruses by far-UVC light (222 nm) is recently demonstrated [45]. The fact that both golden nanoshells and

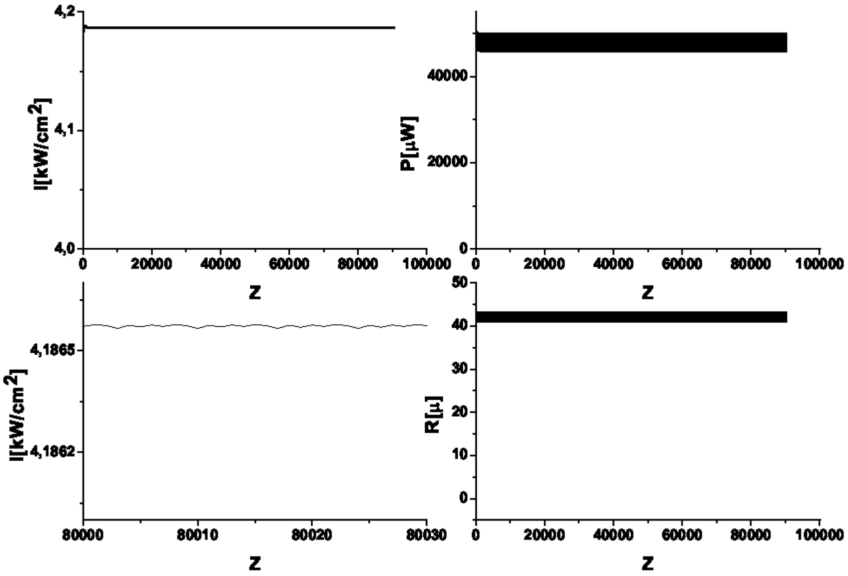

Figure 10 Numerical propagation of STCIE with fitting parameters of Figure 4f, during z=30,000 a.u. shows stable and robust regular breathing of soliton-tweezer complex intensity, **I** power, **P,** and beam width, **R** (with two different resolutions) in the dynamical equilibrium in the bottom of U-potential well of Figure 3.

viruses, despite their fundamental difference, belong to the same category of nanoparticles due to their similar size, encourage us to suggest experimental studies on the possibility to inactivate SARS-CoV-2 in blood using our novel soliton-tweezers. Indeed, the presence of SARS-CoV-2 was detected recently in human blood [46]. The size of nanoparticles determines the plasmon resonance frequencies that are crucial for efficient applications of soliton-tweezers. The glycoprotein membrane of SARS-CoV-2 is rich of electric dipoles susceptible to generate some surface resonances [48,49]. In soliton-tweezer field, all nanoparticles, including virus-nanoparticles, with higher resonant frequency than laser one, behave as positively polarized as in Figures 8-10. In contrary, if their resonant frequency is lower than soliton-tweezer one, they are effectively negatively polarized as in Figures 4-7. If SARS-CoV-2 in blood filling u-cuvette is positively polarized, it would be squeezed paraxially in a soliton-tweezer. Consequently, it may be supposed that in the central part of soliton-tweezer field, viruses would be inactivated suffering simultaneously enhanced heat and resonant vibrations, [43-45]. The inactivation temperature of about 60°C can be easily achieved increasing the soliton-tweezer intensity (see Figures 4-10). Therefore, we suggest to incorporate our u-cuvette in *extracorporeal membrane oxygenation system* (ECMOS) used for medical treatment of SARS-CoV-2 by blood extraction from human body in order to provide input of oxygen and output of carbon dioxide. In order to collect all such positively polarized SARS-CoV-2, the soliton-tweezer width has to be enlarged in order to match the radius of redesigned u-cuvettes in ECMOS. Negatively polarized viruses are expelled out of beam and may be stick on the u-cuvette wall by monoclonal antibodies that have the high level capacity to bind them [47-49]. In such a way viruses are mechanically removed from the blood without need of their inactivation. SARS-CoV and MERS-CoV monoclonal antibodies can be used for binding SARS-CoV-2 in absence of specific antibodies [48,49]. Taking into account that the blood processing in ECMOS is in vitro, *i.e.*, out of human body, easily produced mouse monoclonal antibodies can be used too for binding SARS-CoV-2 without danger of inducing body immunologic reactions [47-49].

We stress that it is not necessary to know the resonant frequencies of SARS-CoV-2 in order to purify the blood efficiently. Indeed, viruses with resonant frequencies higher than the frequency of soliton-tweezer are attracted toward its central axe and inactivated there by high intensity, heat, and vibrations [43-45]. Simultaneously, viruses with resonant frequencies lower than soliton-tweezer one, are expelled toward the wall where they stay bind by monoclonal antibodies [47-49]. Notice that viruses with the refracting index larger that blood one, are negatively polarized if their resonant frequency is below soliton-tweezer one [22].

Resonant frequencies of viruses, related to their small size, are much higher than those of other nanoparticles in body water [43-49]. This is crucial for selective and secure medical applications. In contrast to the Kerr solitons generated above an intensity threshold, soliton-tweezers always control nanoparticles concentration independently of their intensity [8,13,18]. The lack of the threshold allows use of very low intensity soliton-tweezers that do not affect other nanoparticles in blood increasing safety in medical applications [45]. However, thorough experimental studies involving SARS-CoV-2 are needed in order to confirm our hypothesis.

Soliton-tweezers exist in nature in the form of vortices as e.g. tornado. This violent meteorological event is tweezing air and water nanoparticles, hence, can be modeled as soliton–tweezer. Indeed, we generated, for the first time up to our knowledge, a self-trapped vortex soliton-tweezer in 65 cm air column, using simultaneously red, blue, and green lasers. Such a multicolor combination of lasers gives a novel white spot. Tornado and laboratory soliton-tweezer are both big solitary waves that may be considered as concrete examples of rotating rogue waves (see Figure 11). The similarity of camera captions of tornado and our soliton-tweezer encourage us to suggest safe experimental studies of tornado on the model of laboratory soliton-tweezer.

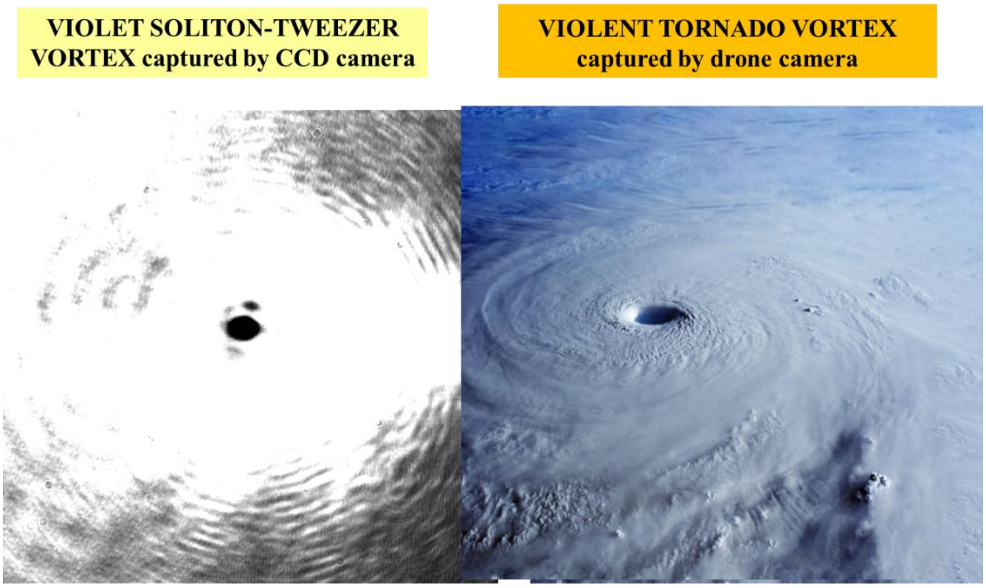

VIOLET SOLITON-TWEEZER VORTEX captured by CCD camera

VIOLENT TORNADO VORTEX captured by drone camera

Figure 11 Vortex soliton-tweezer is realized in 65 cm of air using red, green, and blue lasers simultaneously, giving white spot. It is similar to the tornado captured by drone camera.

In conclusion, the innovative is threefold in establishing direct multidisciplinary synergetic bridge between theory and experiments via numerical simulations. 1. We established an original theoretical model of self-trapping of soliton-tweezers in suspensions of nanoparticles by extending variational approach to nonlocal systems. 2. Soliton gradient forces tweeze nanoparticles collectively inducing density gradient that produces, in turn, self-focusing and self-trapping of soliton-tweezer in a stable dynamical equilibrium that we realized experimentally in very long cuvettes. 3. Using synergy between our experimental and theoretical results, we established a direct description of soliton-tweezer self-trapping by an innovating partial differential equation for complex intensity that includes experimentally measured coefficients. Numerical simulations of this equation together with self-collimation experiments confirm feasibility, stability, robustness, and predictability of soliton-tweezers.

References

[1] G. Nicolis and I. Prigogine, *Self-organization in Nonequilibrium Systems* Wiley: New York 1977.

[2] P. E. Watson, I. D. Watson and R. D. Batt, *Am. J. Clin. Nutr.* **33** (1980) 27.

[3] A. Ashkin, *Phys. Rev. Lett.* **24** (1970) 156.

[4] A. Ashkin, J. M. Dziedzic and P. W. *Opt. Lett*. **7** (1982) 276.

[5] A. Ashkin *et al*. *Nature* **348** (1990) 346.

[6] N. N. Akhmediev, A. Ankiewicz, *Dissipative Solitons: From Optics to Biology and Medicine*, *Lect. Notes Phys*. 751 Springer-Verlag: Berlin, 2008.

[7] L. Santana-Blank *et al*. *Water as a Photoacceptor, Energy Transducer, and Rechargeable Electrolytic Bio-battery in Photobiomodulation*. In *Handbook of Low-Level Laser Therapy*, (2017) 119.

[8] V. Skarka *et al. Opt. Express* **25** (2017) 10090.

[9] R. El-Ganainy *et al. Opt. Express* **15** (2007) 10207.

[10] G. R. Schweinsberger *et al*. *Lasers Surg. Med*. **43** (2011) 443.

[11] C. Conti, G. Ruocco and S. Trillo, *Phys. Rev. Lett.* **95** (2005) 183902.

[12] Y. S. Kivshar and G. P. Agrawal, *Optical Solitons: From Fibers to Photonic Crystals*; Academic Press: San Diego, 2003.

[13] V. Skarka and N. B. Aleksić, *Phys. Rev. Lett*. (2006) 0139031.

[14] Z. Chen, M. Segev and D. N. Christodoulides, *Rep. Prog. Phys.* **75** (2012) 086401.

[15] F. T. Arecchi, S. Boccaletti and P. L. Ramazza, *Phys. Rep*. **318** (1999) 1.

[16] V. Skarka *et al*. *Phys. Rev. Lett.* **105** (2010) 213901.

[17] R. W. Boyd, *Nonlinear Optics*; Academic Press: San Diego, 1992.

[18] V. Skarka, V. I. Berezhiani and R. Miklaszewski, *Phys. Rev. E***56** (1997) 1080.

[19] V. Skarka, V. I. Berezhiani and R. Miklaszewski, *Phys. Rev. E***59** (1999) 1270.

[20] V. Skarka *et al. Phys. Rev. A***90** (2014) 023845.

[21] R. El-Ganainy *et al. Opt. Express* **15** (2007) 10207.

[22] S. Fardad *et al*. *Nano Lett*. **14** (2014) 2498.

[23] M. Matuszewski, W. Krolikowski and Y. S. Kivshar, *Opt. Express* **16** (2008) 1371.

[24] M. Matuszewski, W. Krolikowski and Y. S. Kivshar, *Phys. Rev. A***79** (2009) 023814.

[25] R. El-Ganainy *et al. Phys. Rev. A***80** (2009) 053805.

[26] R. Gordon and J. T. Blakely, *Phys. Rev. A***75** (2007) 055801.

[27] S. A. Akhmanov *et al. IEEE J. Quantum Elect*. **4** (1968) 568.

[28] Y. Lamhot, A. Barak, O. Peleg and M. Segev, *Phys. Rev. Lett.* **105** (2010) 163906.

[29] C. F. Bohren and D. R. Huffman, *Absorption and Scattering of Light by Small Particles* Wiley: New York 1983.

[30] A. I. Yakimenko, V. M. Lashkin and O. O. Prikhodko, *Phys. Rev. E***73** (2006) 066605.

[31] E. L. Falcao-Filho, C. B. de Araujo, G. Boudebs, H. Leblond and V. Skarka, *Phys. Rev. Lett.* **110** (2013) 0139011.

[32] V. Skarka, M. M. Lekić, A. G. Kovačević, B. Zarkov and N. Ž. Romčević, *Opt. Quant. Electron.* **50** (2018) 37.

[33] N. B. Aleksić, N. B. Petrović, M. S. Strinić and M. R. Belić, *Phys. Rev. A***85** (2015) 043832.

[34] B. N. Aleksić, N. B. Aleksić, N. B. Petrović, M. S. Strinić and M. R. Belić, *Opt. Express* **22** (2014) 31842.

[35] G. Makey *et al. Nat. Phys.* **4,** (2020) 1.

[36] C. N. Likos, *Phys. Reps.* **348** (2001) 267.

[37] A. S. Schwartz-Duval *et al. Nat Commun* **11** (2020) 4530.

[38] Kai Yang *et al. Adv. Mater.* **24** (2012) 1868.

[39] R. S. Riley and E. S. Day**,** *WIREs Nanomed Nanobiotechnol* **9** (2017) 1449.

[40] R. A. Sperling *et al. Chem. Soc. Rev.* **37** (2008) 1896.

[41] Minho Kim, Jung-Hoon Lee and Jwa-Min Nam, *Science* **6** (2019) 17.

[42] Jiang Wu *et al. J. Mater. Chem. B* **2** (2014) 2983.

[43] A. R. Singh, A. Košmrlj and R. Bruinsma *Phys. Rev. Lett.* **124** (2020) 158101.

[44] Szu-Chi Yang *et al. Sci. Rep.* **5** (2016) 18030.

[45] M. Buonanno *et al. Sci. Rep.* **10** (2020) 10285.

[46] Wenling Wang *et al. JAMA.* **10** (2020) 10285.

[47] R. G. H. Cotton and C. Milstein, *Nature* **244** (1973) 42.

[48] Lingshu Wang, *Journal of Virology* **92** (2018) e02002.

[49] S. Balamurugan, S. Konlavat, W. Kittikhun and P. Waranyoo, *Asian Pac J Allergy Immunol*. **38** (2020) 10.

IV International School and Conference on Photonics
August 26 - 30. 2013, Belgrade, Serbia

www.photonica.ac.rs

PHOTONICA'13

and joint COST actions BM1205 and MP1204

training school

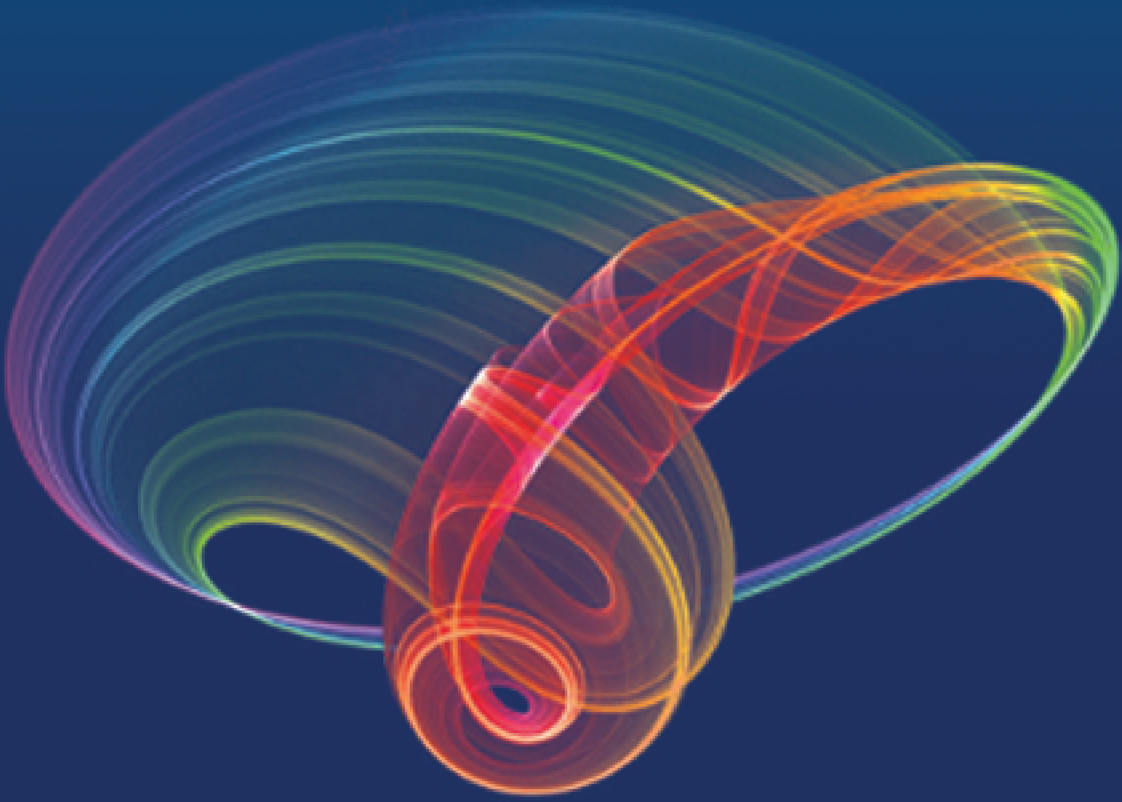

Organized by the Institute of Physics, University of Belgrade,
Pregrevica 118, 11080, Belgrade, Serbia

Influence of Ramsey interference in space and time domains on electromagnetically induced coherent resonances

M. Radonjiĺ, Z. Grujiĺ, M. Lekiĺ, S. Nikoliĺ, A. Krmpot, N. Luļiĺ, B. Zlatkoviĺ, I. Radojiļiĺ,
D. Arsenoviĺ and B. M. Jelenkoviĺ
Institute of Physics, Belgrade, Serbia
e-mail: milan.radonjic@ipb.ac.rs

Here we report on recent progress on the Ramsey effect on electromagnetically induced absorption/transparency (EIA/EIT) and nonlinear magneto-optical rotation (NMOR) resonances. In space domain, experimental and theoretical investigations show the strong effect of the pump beam, spatially separated from the probe beam, on the probe's EIA and NMOR [1]. Linearly polarized pump and probe laser beams are locked to appropriate transitions of the ^{87}Rb D_2 line and pass a vacuum Rb gas cell coaxially in Hanle configuration. Variation of the angle between pump and probe linear polarizations strongly influences the phases of atomic coherences generated by the pump beam and consequently the line-shapes of the probe EIA and NMOR resonances. Complete change of the resonance sign is possible if the phases of the ground state coherences, $\varphi m_g = 2$, are altered by ´. The central EIA fringe becomes less pronounced if the probe intensity increases, due to the larger probe contribution to atomic evolution. We also found that linewidths of the probe EIA and EIT resonances are independent on the probe laser intensity and diameter, but depend only on the size of the dark region between pump and probe lasers.

In time domain, we investigated tllehe effects of repeated interaction between Rb atoms and different polarization components of a single laser beam on temporal build-up of EIT resonances in Hanle configuration. After a sufficiently long preparation ů$^{+}$ light pulse two delayed and weak step-like pulses of ů$^{-}$ light are sent through heated Rb buffer gas cell. The dependence of the transmission of the ů$^{-}$ polarization component for different values of applied longitudinal magnetic field during the pulse sequence provides the EIT curves at a particular time instant. The influence of the first pulse on the temporal build-up of EIT resonances in the second pulse is demonstrated. It is shown that higher overall transparency and off-resonant transmission are obtained for the second pulse. On the other hand, slightly higher contrast and narrower resonances were measured for the first pulse.

REFERENCES

[1] Z. D. Grujiĺ, M. M. Lekiĺ, M. Radonjiĺ, D. Arsenoviĺ and B. M. Jelenkoviĺ, J. Phys. B: At. Mol. Opt. Phys. **45** 245502 (2012).

Ramsey effect on linewidth of coherent resonances in vacuum Rb cell

I. S. Radojičić[1], M. M. Radonjić[1], Z. D. Grujic[1,2], M. M. Lekić[1], D. V. Lukić[1], B. M. Jelenković[1]
[1]*Institute of Physics,*
Belgrade, Serbia
[2]*Department of Physics, University of Fribourg,*
CH-1700 Fribourg, Switzerland
e-mail: ivanrad@ipb.ac.rs

Ramsey's method of separated excitation fields of an atomic transition is often used in atomic and molecular high precision spectroscopy. Ramsey fringes that are induced by the two spatially or temporally separated excitation fields lead to a considerable narrowing of the corresponding coherent resonances. We studied electromagnetically induced transparency (EIT) and electromagnetically induced absorption (EIA) of the probe laser that is surrounded by the counter-propagating hollow pump beam, as in [1]. The diameter of the probe beam is smaller than the diameter of the hole of the hollow pump, allowing successive excitation of Zeeman coherences in Rb atom, between which atom is in a dark for some time, as required by the Ramsey method. Both laser beams are linearly polarized and locked to appropriate EIT and EIA transitions of the ^{87}Rb D_2 line. We have measured Zeeman EIT by measuring transmission of the laser locked to the EIT or EIA atomic transition through the vacuum Rb gas cell as a function of the external magnetic field.

We have shown for the first time in the vacuum Rb cell the probe EIT that is entirely due to scattering of the weak probe on the atomic coherences generated in the pump beam. As such, EIT line widths are nearly independent of both probe laser intensity, up to 0.75 mW/cm^2, and on the probe laser diameter. We have used two diameters, 0.8 mm and 2.8 mm for the probe beam keeping the same length of the dark region, i.e. the distance between pump and probe. Indeed, in the Ramsey method linewidths of atomic resonances depend only on the time between two excitations. Very similar behavior of the EIA for two probe diameters indicates similar excitation mechanism for the two types of atomic coherences, EIT and EIA. The EIA resonances are broader than EIT, as expected since the coherence time for the former is shorter (assuming all parameters are equal) because mechanism for the EIA involves spontaneous emission.

REFERENCES

[1] Z. D. Grujić, M. Mijailović, D. Arsenović, A. Kovačević, M. Nikolić, and B. M. Jelenković, Phys. Rev. A **78**, 063816 (2008).

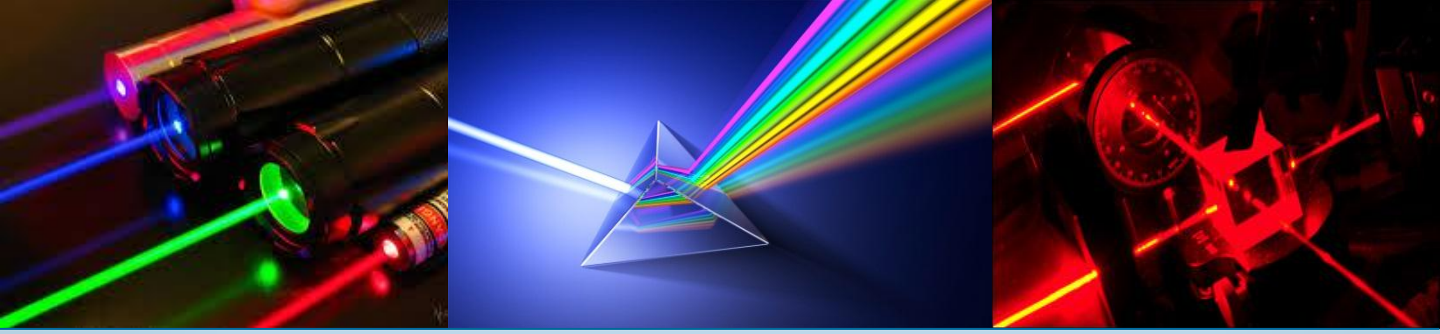

18th International School on Quantum Electronics

LASER PHYSICS AND APPLICATIONS

Book of abstracts

29 September – 03 October 2014
Sozopol, Black sea, Bulgaria

In this contribution we investigate the generalized Λ-system based on the $5S_{1/2}(F=2)$, $5S_{1/2}(F=3)$, $5P_{3/2}(F'=4, 3, 2)$ levels of the cold ^{85}Rb atoms interacting with the polarized laser beams: the stronger one (coupling or the pump) and the weaker one (the probe). The sample is produced in the magneto-optical trap. Cold atom environment is used to overcome limitations of conventional systems. Dependence of the probe transmission on the polarizations and detunings of both the probe and pump beams is studied. Results and discussion will be presented.

PB9

ROBUST NARROWING OF DARK RESONANCES IN RB VAPOR WITH COAXIAL COUNTER-PROPAGATING LASER BEAMS

I. Radojičić, M. Radonjić, Z. Grujić, M. Lekić, D. Lukić and B. M. Jelenković

Institute of Physics, University of Belgrade, Pregrevica 118, 11080 Belgrade, Serbia
e-mail: milan.radonjic@ipb.ac.rs

Counter propagating spatially separated hollow pump and coaxial probe laser beams generate narrow Zeeman electromagnetically induced transparency (EIT) resonances in vacuum Rb cell. The lasers were locked to $F_g=2 \rightarrow F_e=1$ transition of either D1 or D2 line of ^{87}Rb. This Ramsey type configuration yields dual-structured resonances having narrow peak on top of broader pedestal [1]. The pedestal becomes more prominent with increase of the probe beam intensity. Interestingly, we observed weak dependence of the narrow peak line-widths on the probe beam intensity and diameter provided dark region between the two beams is kept fixed [2]. Accompanying theoretical model showed good agreement with the measurements and enabled explanation of differences in line shapes for the two D-lines. We also found that very weak probe beam can be transmitted through the Rb cell only if the pump beam is present.

References:

[1] Z. D. Grujić, M. Mijailović, D. Arsenović, A. Kovačević, M. Nikolić and B. M. Jelenković, "Dark Raman resonances due to Ramsey interference in vacuum vapor cells", Phys. Rev. A 78, 063816, (2008).

[2] I. S. Radojičić, M. Radonjić, Z. D. Grujić, M. M. Lekić, D. V. Lukić and B. M. Jelenković, In preparation

Acknowledgements: This work was supported by the Ministry of Education and Science of Serbia, under Grants No. III45016 and OI171038 and also by SCOPES JRP IZ73Z0_1

Book of abstracts

PHOTONICA2017

The Sixth International School and Conference on Photonics

& COST actions: MP1406 and MP1402

&H2020-MSCA-RISE-2015 CARDIALLY workshop

28 August – 1 September 2017

Belgrade, Serbia

Editors

Marina Lekić and Aleksandar Krmpot

Institute of Physics Belgrade, Serbia

Belgrade, 2017

Solitons generated by self-organization in bismuth germanium oxide single crystals during the interaction with laser beam

V. Skarka[1,2,3], M. Lekić[1], A. Kovačević[1], B. Zarkov[4], and N. Z. Romčević[1]

[1]*Institute of Physics, University of Belgrade, Pregrevica 118, 11080 Belgrade, Serbia*
[2]*Science Program, Texas A&M University at Qatar, P.O. Box 23874, Doha, Qatar*
[3]*Laboratoire de Photonique d'Angers, EA 4464, University of Angers,2 Boulevard Lavoisier 49045 Angers Cedex 01, France*
[4]*Directorate of Measures and Precious Metals, Mike Alasa 14, 11000 Belgrade, Serbia*
e-mail:vladimir.skarka@univ-angers.fr

The self-organization is based on the balance of antagonistic effects, with nonlinearity-induced self-contraction arresting diffraction and/or dispersion in order to generate stable localized nonlinear optical structures called solitons [1]. Spatial Kerr solitons correspond to the compensation of diffraction by a cubic Kerr nonlinearity. However, in two- and three-dimensional systems, the laser beam or pulse undergo a catastrophic collapse unless a saturating nonlinearity is also present, as it was established using synergy of variational method and numerical simulations [2-5]. Such Kerr solitons are hard to obtain experimentally especially in solid state systems. The generation of 2D optical solitons has been recently demonstrated only in liquid carbon disulfide [6].

We present here the experimental, theoretical, and numerical investigations of Kerr solitons generated by self-organization in black and yellow high quality bismuth germanium oxide (BGO) single crystals. A laser beam of increasing power induces competing cubic and quintic nonlinearities. The numerical evolution of 2D complex cubic-quintic nonlinear Schrödinger equation with measured values of nonlinearities shows the compensation of diffraction by competing cubic and quintic nonlinearities of opposite sign, i.e., the self-generation of stable solitons. Experiments as well as numerical simulations show higher nonlinearity in the black BGO than in the more transparent yellow one. Experimentally obtained solitons are in good agreement with numerical results.

REFERENCES
[1] Y. S. Kivshar and G. P. Agrawal, Optical Solitons: From Fibers to Photonic Crystals (Academic, 2003).
[2] V. Skarka, N. B. Aleksić, Phys. Rev. Lett. 96, 013903 (2006).
[3] V. Skarka, N. B. Aleksić, H. Leblond, B. A. Malomed, and D. Mihalache, Phys. Rev. Lett. 105, 213901 (2010).
[4] V. Skarka, N. B. Aleksić, M. Lekić, B. N. Aleksić, B. A. Malomed, D. Mihalache, and H. Leblond, Phys. Rev. A 90 (2), 023845 (2014).
[5] V. Skarka, N. B. Aleksić, W. Krolikowski, D. N. Christodoulides, S. Rakotoarimalala, B. N. Aleksić, M. Belić, Opt. Express 25, 284183 (2017).
[6] E. L. Falcao-Filho, C. B. de Araújo, G. Boudebs, H. Leblond, and V. Skarka, Phys. Rev. Lett. 110, 013901 (2013).

Book of Abstracts

International Conference on Ultrafast Optical Science

UltrafastLight-2018

October 1-5, 2018, Moscow
Lebedev Physical Institute

ФАНО
России
ФЕДЕРАЛЬНОЕ
АГЕНТСТВО
НАУЧНЫХ
ОРГАНИЗАЦИЙ

RFBR
RUSSIAN
FOUNDATION
FOR BASIC
RESEARCH

ОЭС
СПЕЦПОСТАВКА

hv
photonics

Inducing LIPSS by multi-pass and cross-directional scanning of femtosecond beam over surface of thin metal films

A.G. Kovačević[1], S. Petrović[2], M. Lekić[1] and B.M. Jelenković[1]

[1]Institute of Physics, University of Belgrade, Belgrade, Serbia;
[2]Institute of Nuclear Sciences "Vinča", University of Belgrade, Belgrade, Serbia
e-mail: Aleksander.Kovacevic@ipb.ac.rs

During interaction of femtosecond laser beam with metal surfaces, laser induced periodic nanostructures, LIPSS can be formed, which may improve properties of materials. Having excellent mechanical properties, multilayer thin films, like 5x(Al/Ti)@Si, are convenient for forming of high quality LIPSS [1] due to their multilayer structure. We have exposed the multilayer thin film metal systems 5x(Al/Ti)@Si with femtosecond beam from the laser system Coherent Mira 900 in NIR with various scanning configurations [2]. The irradiated samples have been analyzed by Tescan Mira3 SEM. The beam scanned over the surface of the samples with multi-pass and cross-directional scanning configurations with the change of polarization direction. The formation of LIPSS is most probably due to the occurence of surface plasmon polariton, which leads to the periodic distribution of energy on the sample surface. The orientation of the LIPSS is related to the direction of the beam polarization. During multi-pass scanning, LIPSS maintained its configuration. The preservation of structures occured to some extent. Depending on the accumulated energy, two forms of LIPSS were generated: "hills", for less accumulation, and "trenches" for greater accumulation. "Hills" are non-ablative, probably are due to the build-up of the material and are parallel to the polarization direction. "Trenches" are formed by ablation and are perpendicular to the polarization direction. During cross-directional scanning, LIPSS of orthogonal directions have been generated. The value of the "hills" period was around 360 nm and the width was ∼285 nm. The values of "trenches" period fluctuated between 320 and 380 nm, while width was between 85 and 45 nm. Proposed mechanism is that, for less accumulated energy, "hills" formed, while more accumulated energy leads to the ablation and formation of "trenches".

The work has been supported by the Ministry of Science, Republic of Serbia, under № III45016, OI171038 and OI171005. The authors deeply thank dr. Dejan Pantelć and dr. Radoš Gajić, both of Institute of Physics, University of Belgrade, for valuable support.

REFERENCES

[1] A.G. Kovačević, S. Petrović et al., Appl.Surf. Sci. 326 , 91 (2015).

[2] A.G. Kovačević, S. Petrović et al., Appl.Surf. Sci. 417 , 155 (2017).

Inducing LIPSS on multilayer thin metal films by femtosecond laser beam of different orientations

A. G. Kovačević[1], S. M. Petrović[2], B. Salatić[1], M. Lekić[1], B. Vasić[1], R. Gajić[1],
D. Pantelić[1] and B. M. Jelenković[1]
[1]*Institute of Physics, University of Belgrade, Belgrade, Serbia*
[2]*Institute of Nuclear Sciences "Vinča", University of Belgrade, Belgrade, Serbia*
e-mail: Aleksander.Kovacevic@ipb.ac.rs

The occurrence of laser-induced periodic surface structures (LIPSS) has been known for a while [1]. Multilayer thin films, like Al/Ti, are suitable for LIPSS formation and attractive for applications – due to their wearing behavior and corrosion resistance; LIPSS generation may improve their properties as well [2, 3]. LIPSS properties depend not only on the material but also on the beam characteristics, like wavelength, polarization and scanning directions, etc. [4].

After exposing with NIR femtosecond pulses from Coherent Mira 900 laser system in several beam exposures, we have analyzed the samples of thin metal film systems with Tescan Mira3 SEM and NTegra AFM. The formation of LIPSS is most probably due to the generation of surface plasmon polariton, through the periodic distribution of energy in the interaction zone which lead to thermal processes in layers and interfaces. Two types of LIPSS were generated, which differ in shape, orientation and in ablation pronounced or not. For consecutive interactions in the same direction, LIPSS maintained its orientation, while for orthogonal passes LIPSS with mutually orthogonal orientation were generated. LIPSS period fluctuated between 320 and 380 nm and structures with pronounced ablation have significantly smaller width. Probable mechanism is that for greater accumulated energy pronounced ablation takes place giving LIPSS in the form of "trenches", while for less accumulated energy the buildup of the material – probably due to pronounced oxidation – lead to LIPSS in the form of "hills".

ACKNOWLEDGEMENT: The work was supported by the Ministry of Science of the Republic of Serbia under No. III45016, OI171038 and OI171005.

REFERENCES

[1] H. M. van Driel et al., Phys. Rev. Lett. 49, 1955 (1982).
[2] S. M. Petrović et al., Opt. Laser Technol. 54, 22 (2013).
[3] A. Kovačević et al., Appl. Surf. Sci. 326, 91 (2015).
[4] A. Kovačević et al., Appl. Surf. Sci. 417, 155 (2017).

Self-organization of soliton-tweezers in suspensions of nanocomposites and graphens

M. Lekić[1], I. Milosević[1] , S. Rokotoarimalala[2] and V. Skarka[1,2,3]
[1]*Institute of Physics, University of Belgrade, Pregrevica 118, Belgrade, Serbia*
[2]*Laboratoire de Photonique d'Angers, EA 4464, University of Angers,*
2 Boulevard Lavoisier, 49045 Angers, France
[3]*Science Program, Texas A&M University at Qatar, P.O. Box 23874, Doha, Qatar*
e-mail: lekic@ipb.ac.rs

Laser beams and pulses are powerful tools for tweezing, photobiomodulation, and manipulation of soft matter including colloidal nanosuspensions, emulsions, foams, as well as all kinds of biomedia like myosin, kinesin, ribosomes, liposomes, bacterias, viruses, blood, and a variety of living cells in body water [1]. The laser modifies the nonlinear mater passing through. Simultaneously, the modified mater acts to the light altering it by a feedback mechanism. Therefore, light is controlled by light through interaction with nonlinear mater. Laser stability and precision are of crucial importance not only for brain surgery but also for nondestructive diagnostics using this feedback mechanism. In order to achieve the necessary dynamical stability, the promising mechanism is the self-structuring of the light into localized solitons via nonlinear interaction inside the colloidal nanosuspensions and other varieties of soft matter. Tweezing solitons stable propagation is self-organized by the balance of antagonist effects, *i.e.*, beam self-focusing and self-defocusing [2]. The high frequency pressure force of the laser field either attracts or repels the nanoparticles from the field region, depending if their optical index of refraction is larger or smaller than the background one [3]. In both cases, the nanoparticles density modification results in the nonlinear increase of effective index of refraction inside the beam making it self-focusing. We use this self-focusing effect to establish theoretically, numerically and experimentally the self-organization of soliton-tweezers as a novel kind of dynamically reconfigurable self-collimated tweezing facilities. Such soliton-tweezers will be able to photobiomodulate and manipulate, in a noninvasive way, micro and nanoparticles in body water and other soft mater of interest for medical and biological applications. Based on the synergy between theory and experiment via numerical simulations, other nanocomposites and colloidal nanosuspensions involving graphene and various two-dimensional materials will be tweezed using spatiotemporal dissipative solitons and multidimensional vortex solitons [4, 5].

REFERENCES

[1] A. Ashkin, J. M. Dziedzic, T. Yamane, Nature 330, 769 (1987).
[2] V. Skarka, N. B. Aleksic, Phys. Rev. Lett. 96, 013903 (2006).
[3] V. Skarka et al., Opt. Express 25, 10090 (2017).
[4] V. Skarka et al., Opt. Quant. Electron. 50, 37 (2018).
[5] V. Skarka et al., Phys. Rev. A 90, 023845 (2014).

Inducing LIPSS on multilayer thin metal films by ultrashort laser beam in different ambient conditions

Aleksander G. Kovačević[1], Suzana Petrović[2], Branislav Salatić[1], Marina Lekić[1], Borislav Vasić[1], Dejan Pantelić[1], Branislav Jelenković[1]

(1) *Institute of Physics – University of Belgrade, Pregrevica 118, 11080 Belgrade, Serbia*

(2) *Institute of Nuclear Sciences "Vinča" – University of Belgrade, P.O.Box 522, 11000 Belgrade, Serbia*

Contact: A. Kovačević (aleksander.kovacevic@ipb.ac.rs)

Abstract. Laser induced periodic surface structures (LIPSS) may be induced during the interaction of ultrashort laser pulses with surfaces [1]. Having periods below the wavelength of the laser beam, the area of their application is wide, particularly on metal surfaces [2]. Due to lamellar structure, multilayer thin metal films are suitable for high quality LIPSS formation which can improve their characteristics [3, 4]. The beam, the material, and the ambient/environment meet during the interaction and their properties and states/conditions (polarization and scanning directions, temperature, electrical current, composition, …) influence the characteristics of the LIPSS [5]. We have exposed multilayer thin films of various metals (Al, Ti, Ni, Zr, …) to Coherent Mira 900 laser system in different conditions of beam, ambient and material; the irradiated samples have been analyzed by Tescan Mira3 SEM and NTegra AFM. Two forms of LIPSS were generated, differing in shape, pronounced ablation, orientation and period. During multi-pass scanning, LIPSS maintained the configuration. During orthogonal scanning, orthogonal LIPSS occurred at some areas. The occurrence of surface plasmon polariton (SPP) is the most probable cause which led to periodic distribution of energy on the surface and thermal processes.

Acknowledgements. The work was supported by the Ministry of Science of the Republic of Serbia under No. III45016, OI171038 and OI171005. The authors also thank dr Davor Peruško from the Institute of Nuclear Sciences "Vinča" of the University of Belgrade and to dr R. Gajić, dr A. Krmpot, dr M. Rabasović and V. Lazović, all from the Institute of Physics of the University of Belgrade, for their valuable support.

REFERENCES

[1] H. M. van Driel, J. E. Sipe and J. F. Young, *Phys. Rev. Lett.* **49**, 1955 (1982).
[2] A. Y. Vorobyev and C. Guo, *Laser Photonics Rev.* **7**, 385 (2013)..
[3] S. M. Petrović, D. Peruško, et al., *Opt. Laser Technol.* **54**, 22 (2013).
[4] A. G. Kovačević, S. Petrović, et al., *Appl. Surf. Sci.* **326**, 91 (2015).
[5] A. G. Kovačević, S, Petrović, et al., *Appl. Surf. Sci.* **417**, 155 (2017).

Narrowing of laser beam propagating through biological suspension

A. Kovacevic[1], T. Pajic[2], D. Pavlovic[1], M. Stanic[3], M. Lekic[1], S. Nikolic[1], B. Jelenkovic[1]
[1] *Institute of Physics Belgrade, University of Belgrade, Pregrevica 118, 11080 Belgrade, Serbia*
[2] *Faculty of Biology, University of Belgrade, Studentski trg 16, 11000 Belgrade, Serbia*
[3] *Institute for Multidisciplinary Research, University of Belgrade, Bulevar Despota Stefana 142, 11060 Belgrade, Serbia*
e-mail:aleksander.kovacevic@ipb.ac.rs

Recent demonstration of nonlinear self-action of laser beams in suspension of biological materials, like marine bacteria and red blood cells, has been reported [1-3]. In this work, we demonstrate nonlinear optical effects of laser beam propagation through the freshwater green microalga *Chlorela sorokiniana*, cultivated in Bold basal medium with 3-fold nitrogen and vitamins (3N-BBM+V).

Chlorella sorokiniana is a species of single-celled freshwater green microalga in the division *Chlorophyta*. Its spherical or ellipsoidal cells (3 x 2 µm in small cells to 4.5 x 3.5 µm in large cells, sometimes >5 µm) divide rapidly to produce four new cells every 17 to 24 hours [4]. The non-pathogenic species has been chosen as a model organism due to its small cell dimension, rapid growth, non-mobility and non-toxicity. The algae were kept in the light chamber and the temperature was maintained at 22°C. Mid-exponential growth phase of algal culture was used for the experiments.

In the experiments, the 532 nm CW laser beam is directed to the glass cuvette that is filled either with the medium or with algae suspended in the medium. We have monitored the laser beam diameter at the entrance and exit of the cuvette, and its axial profile through entire cell length. The concentration has been determined by optical microscopy and optical density and has been varied between 10^6 and 10^8 cm^{-3}.

The concentration of the algae and the laser beam power affect the beam radius. Our preliminary results have shown the effect of light self-trapping, i.e., the decrease of laser diameter when the algae concentration exceeds 10^6 cm^{-3} while laser power is above 1 W. The difference of the refractive indexes of the algae and the medium can induce optical trapping of algae, which subsequently changes the concentration of the algae within the laser beam. This in turn can explain different behavior of the beam in the medium with and without algae.

We discuss the mechanisms which led to narrowing of the beam including nonlinear effects as well as potential applications in waveguiding, medical imaging and optimal propagation of laser beam in biological suspensions.

Acknowledgments. The authors appreciate valuable and helpful comments of Dr. Najdan Aleksic from the Moscow State Technological University "STANKIN".

REFERENCES

[1] A. Bezryadina, T. Hansson, R. Gautam, et al. Phys. Rev Lett. 119, 058101 (2017).
[2] R. Gautam, Y. Xiang, J. Lamstein, et al., Light: Sci. Appl. 8, 31 (2019).
[3] R. Gautam, A. Bezryadina, Y. Xiang, et al., Adv. Phys. X 5 (2020), doi: 10.1080/23746149.2020.1778526.
[4] I. Shihira, R. W. Krauss. *Chlorella*. Physiology and taxonomy of forty-one isolates, pp.1-97. Maryland: University of Maryland, College Park (1965).

Laser-induced parallel structures on multilayer thin films of Ni, Pd, Ti, Ta and W

Aleksander G. Kovačević[1], Suzana Petrović[2], Jelena Potočnik[2], Marina Lekić[1], Branislav Salatić[1], Vladimir Lazović[1], Dejan Pantelić[1], Branislav Jelenković[1]

(1) *Institute of Physics, University of Belgrade, Pregrevica 118, 11080 Belgrade, Serbia*

(2) *Institute of Nuclear Sciences "Vinča", University of Belgrade, POBox 522, 11001 Belgrade, Serbia*

Contact: A. Kovačević (aleksander.kovacevic@ipb.ac.rs)

Abstract. The interaction of ultrashort laser beam with metal surfaces may induce the generation of periodic structures (LIPSS) with period less than the incoming wavelength, opening wide area of application [1, 2]. The presence of the underneath layer influences the quality of the LIPSS [3] . We have exposed multilayer thin films Ni/Ti, Ni/Pd, W/Ti, Ti/Ta to femtosecond beams of various wavelengths and powers. The interactions have been performed by Mira900 fs laser of Coherent. Detailed surface morphology after irradiation was examined firstly by optical microscopy, and then by scanning electron microscopy (JEOL JSM-7500F, Tokyo, Japan). Two types of structures have been noticed. Their appearance differ in the direction against the polarization direction, in pronounced ablation and in the spatial period, enabling their grouping into LIPSS of higher and lower spatial frequencies. Surface plasmon polariton is seen as the most probable cause of periodic distribution of energy at the surface and consequently to LIPSS.

Acknowledgements. The work was supported by the Ministry of Science of the Republic of Serbia under No. III45016 and OI171038. The authors also thank dr Davor Peruško from the Institute of Nuclear Sciences "Vinča" (University of Belgrade), dr V. Pavlović from the Faculty of Agriculture (University of Belgrade), dr Đ. Veljović and dr Ž. Radovanović from the Faculty of Technology and Metallurgy (University of Belgrade) and dr A. Krmpot and dr M. Rabasović from the Institute of Physics (University of Belgrade), for their valuable support.

REFERENCES

[1] H. M. van Driel, J. E. Sipe and J. F. Young, *Phys. Rev. Lett.* **49**, 1955 (1982).
[2] A. Y. Vorobyev and C. Guo, *Laser Photonics Rev.* **7**, 385 (2013).
[3] A. G. Kovačević, S. Petrović, et al., *Appl. Surf. Sci.* **326**, 91 (2015).

Laser beam waveguiding capabilities of the suspension of Chlorella sorokiniana in water

Aleksander G. Kovačević[1], Tanja Pajić[2], Danica Pavlović[1], Marina Stanić[3], Marina Lekić[1], Olga Fedotova[4], Stanko N. Nikolić[1], Oleg Khasanov[4], Ryhor Rusetski[4], Najdan Aleksić[5], Branislav M. Jelenković[1]

(1) *Institute of Physics of the University of Belgrade, Pregrevica 118, 11080 Belgrade, Serbia*

(2) *Faculty of Biology of the University of Belgrade, Studentski trg 16, 11000 Belgrade, Serbia*

(3) *Institute for Multidisciplinary Research of the University of Belgrade, Bulevar Despota Stefana 142, 11060 Belgrade, Serbia*

(4) *Scientific and Practical Materials Research Centre of the National Academy of Sciences of Belarus, Minsk, Belarus*

(5) *Moscow State University of Technology "STANKIN", Vadkovskiy per. 1, 127055 Moscow, Russia*

Contact: A. Kovačević (aleksander.kovacevic@ipb.ac.rs)

Abstract. Controlled light guiding to target regions in biological and biomedical systems is important for applications like sensing and diagnosis. The penetration depth in tissues, limited due to scattering, is increased by using conventional optical waveguides, built on materials like silica glass and hard plastics. More potential for formation of biophotonic waveguides having higher biocompatibility and biodegradability have natural biomaterials, like living cells.

Strong scattering and absorption loss in cells is overcome by nonlinear effects arising during laser light propagation through suspensions of living cells, like marine bacteria [1]. Microalga *Chlorella* shows more attractiveness due to robustness, simple structure, high growth rate and ability to grow in various conditions, and its species *Chlorela sorokiniana* is most robust and most resistive to heat and intense light [2, 3].

We examined the propagation of the 532 nm CW laser beam of various powers through the suspension of freshwater green microalga *C. sorokiniana* of various concentrations. Due to nonlinear effects, like thermo-optical, scattering, optical gradient forces, the beam modified. Self-guiding and the changing of cross-section occurred for chosen parameters of power and concentration. Some of the outcomes might be of interest for applications in biophotonics and biomedicine: waveguiding, medical imaging and optimal propagation of laser beam in biological suspensions.

REFERENCES

[4] A. Bezryadina, T. Hansson, R. Gautam et al., *Phys. Rev Lett.* **119** (2017), 058101 (2017). Lj. Author, *Book title*, Publisher, New York (2018).

[5] I. Shihira, R. W. Krauss. *Chlorella. Physiology and taxonomy of forty-one isolates*, pp.1-97. Maryland: University of Maryland, College Park (1965).

[6] L. E. de-Bashan, A. Trejo et al., *Bioresource Technol.* **99** (2008), 4980–4989 (2008).

Beam modification during propagation through aqueous microalgae suspension of interest to waveguiding

Aleksander Kovačević[1], Tanja Pajić[2], Djordje Jovanović[1], Marina Stanić[3], Danica Pavlović[1], Olga Fedotova[4], Oleg Khasanov[4], Rygor Rusetski[4], Marina Lekić[1], Branislav Salatić[1], Branislav Jelenković[1]

(1) *Institute of Physics, University of Belgrade, Pregrevica 118, 11080 Belgrade, Serbia*

(2) *Faculty of Biology, University of Belgrade, Studentski trg 16, 11000 Belgrade, Serbia*

(3) *Institute for the multidisciplinary Research, University of Belgrade, 11060 Belgrade, Serbia*

(4) *Scientific and Practical Materials Research Centre of the National Academy of Sciences of Belarus, Minsk, Belarus*

Contact: A. Kovačević (aleksander.kovacevic@ipb.c.rs)

Abstract. *Chlorella sorokiniana* Shih. et Krauss [1], due to its highest resistivity to heat and high light intensity among all *Chlorella* species [2], is a good candidate in the applications of light generation, waveguiding and modulation. Relative refractive index with respect to water is makes the cells the positive polarizability particles and lowest absorption in the green region of the visible spectrum [3] reduces the thermal effects generated from the propagating high power laser beam.

During laser beam propagation through aqueous suspensions of metal nanoparticles or microscopic marine bacteria, nonlinear effects, like thermo-optical, scattering, optical gradient forces take place in shaping the beam [4, 5]. However, strong thermal absorption of metal and sensitivity to strong light of cells limit the range of beam power. We examined the propagation of the 532 nm CW laser beam of various powers through the suspension of freshwater green microalga *C. sorokiniana* of various concentrations, placed in a glass vessel. For two concentrations of algae (0.5×10^{7} cm^{-3} and 1×10^{7} cm^{-3}) and several selected values of beam power (2-4 W) the beam experiences self-guiding and changes in exit cross section [6]. In this work, we pay attention to broader range of powers (0.1-5 W) and concentrations and investigate the diameter change during propagation and the cross-section change at exit wall of the vessel due to nonlinear effects, which might be interesting for waveguiding and optimal laser propagation in biological suspensions.

Acknowledgements. The authors appreciate the help of prof. M. Živić (Faculty of Biology), dr N. Aleksić and dr S. N. Nikolić (Institute of Physics). T.P. acknowledges the support of the Ministry of Science of the Republic of Serbia contract No. 451-03-68/2022-14/ 200178. O.F, O.K and R.R. acknowledge the support of the Belarussian republican foundation for fundamental research No. F20SRBG-007. M.S. acknowledges the support of the NATO Science for Peace and Security Programme No. G5320. A.K, D.J, D.P, M.L, B.S, B.J acknowledge the support from the Ministry of Science of the Republic of Serbia through the Institute of Physics.

REFERENCES

[15] I. Shihira, R. W. Krauss. *Chlorella. Physiology and taxonomy of forty-one isolates*, pp.1-97. Maryland: University of Maryland, College Park (1965).
[16] L.E. de-Bashan, A. Trejo, V.A.R. Huss, et al. *Bioresource Technol.* **99** (2008), 4980–4989.
[17] Emerson, R. and Lewis, C. M. *Am. J. Bot.* **30** (1943), 165-178.
[18] V. Shvedov, K. Cyprych, M.Y. Salazar-Romero, et al., *Opt. Express* **26** (2018), 23196-23206.
[19] A. Bezryadina, T. Hansson, R. Gautam et al., *Phys. Rev Lett.* **119** (2017), 058101 (2017).
[20] A.G. Kovačević, T. Pajić, D. Pavlović, et al., *Proc. 15th Photonics Workshop* (2022), 55 (abstract).

PHOTONICA2011

International School and Conference on Photonics

29 August – 02 September 2011

Belgrade, Serbia

ABSTRACTS OF TUTORIAL, KEYNOTE AND INVITED LECTURES AND CONTRIBUTED PAPERS

Editors

Jovana Petrović, Milutin Stepić and Ljupčo Hadžievski

Vinča Institute of Nuclear Sciences

Belgrade, Serbia

Belgrade, 2011

A quantum phase operator on the von Neumann lattice

Lj. Davidović[1], M Davidović[2] and M. Davidović[3]
[1]*Institute of Physics, University of Belgrade, Serbia*
[2] *Vinca Institute of Nuclear Sciences, University of Belgrade, Serbia*
[3]*Faculty of Civil Engineering, University of Belgrade, Serbia*
e-mail: milena@grf.bg.ac.rs

Using the results from [1], where some difficulties related to the definition of non entire functions of the creation and annihilation operators present in the literature - were avoided, we analyze a new quantum phase operator defined on the von Neumann lattice- as proportional to the difference of logarithms of creation and annihilation operators. We compare phase distributions for some characteristic states obtained with this new operator and some other results for phase distributions obtained with earlier approaches. We discuss the obtained results.

REFERENCES

[1] Lj. Davidovic, D. Arsenovic, M. Davidovic, D. Davidovic, J. Phys. A: Math. Theor. 42, 23 (2009).

Narrowing of EIT resonance in the configuration of counter-propagation laser beams

I. S. Radojičić[1], Z. D. Grujić[1,2], M. M. Lekić[1], D. V. Lukić[1] and B. M. Jelenković[1]
[1]*Institute of Physics, Belgrade, Serbia*
[2]*Department of Physics, University of Fribourg,CH-1700 Fribourg, Switzerland*
e-mail: ivanrad@ipb.ac.rs

We present effects of Ramsey method of separated oscillatory fields (pump and probe) on electromagnetically induced transparency (EIT). Both pump and probe lasers are locked to the $F_g = 2 \rightarrow F_e = 1$ in D_1 line transitions of ^{87}Rb. Effects are analyzed in the Hanle configuration and in a room temperature Rb vapor cell. The pump laser beam is used for creation and the probe laser beam for detection of the coherence between ground-state Zeeman sublevels.

We show that EIT can be obtained with spatially separated and counter-propagating pump and probe beams. In comparison with the single laser beam, substantial narrowing of the probe Hanle EIT is obtained due to temporal evolution of the pump induced Zeeman coherence and later probed by the probe laser. The interference between atomic coherences and the probe laser are confirmed from changes of the resonances line shape with the angle between linearly polarized pump and probe laser beams, i.e., due to different initial phases of the atomic coherences. These results are compared with results obtained with co-propagating pump and probe laser beam [1], and in counter-propagating scheme we have overcome problems due to scattered pump beam light that was mixed with probe beam on photo detector. This allowed us to use lower light power in probe beam and to obtain slightly narrower resonances.

REFERENCES

[1] Grujić, M. Mijailović, D. Arsenović, B. M. Jelenković, Phys. Rev. A 78, 063816-1 (2008).